

**THERMAL STRESS ANALYSIS OF FUSED-CAST
MONOFRAX-S REFRACTORIES**

by

STEVEN LEE COCKCROFT

B.Sc., University of British Columbia, 1980

B.A.Sc., University of British Columbia, 1984

M.A.Sc., University of British Columbia, 1986

A THESIS SUBMITTED IN PARTIAL FULFILLMENT OF
THE REQUIREMENTS FOR THE DEGREE OF
DOCTOR OF PHILOSOPHY

in

THE FACULTY OF GRADUATE STUDIES
(Department of Metals and Materials Engineering)

We accept this thesis as conforming
to the required standard

THE UNIVERSITY OF BRITISH COLUMBIA

September 1990

© Steven Lee Cockcroft

In presenting this thesis in partial fulfilment of the requirements for an advanced degree at the University of British Columbia, I agree that the Library shall make it freely available for reference and study. I further agree that permission for extensive copying of this thesis for scholarly purposes may be granted by the head of my department or by his or her representatives. It is understood that copying or publication of this thesis for financial gain shall not be allowed without my written permission.

Department of METAL AND MATERIAL ENGINEERING

The University of British Columbia
Vancouver, Canada

Date Dec 05, 1990

ABSTRACT

Mathematical models of heat flow and elastic stress generation based on the finite-element method have been developed and utilized to analyze the Epic-3 Monofrax-S casting process (Monofrax-S is primarily composed of 47-57% Al_2O_3 , 34-41% ZrO_2 and 10-15% SiO_2). The results of the mathematical analysis, in conjunction with information obtained from a comprehensive industrial study, has led to the development of mechanisms for the formation of the various crack types found in this casting process. Thermal stresses have been predicted to be generated early in the solidification process in association with rapid cooling of the refractory surface as it contacts the initially cool mould and again later in the solidification process in conjunction with the tetragonal-to-monoclinic phase transformation which occurs in the zirconia component of Monofrax-S. The mathematical analysis has also helped to identify indirectly a potential mechanism for the generation of mechanical stresses. Based on an understanding of the generation of tensile stresses, recommendations have been made for modifications to the moulding and casting procedures in order to reduce the propensity for the formation of cracks. The modifications have included changes to the mould construction and geometry to reduce the generation of mechanical stresses and changes to the moulding materials to impact on the flow of heat at key times during solidification and cooling. With the recommendations in place, the casting process has been re-examined with the mathematical models to verify the impact of the modifications. The predictions show that the modifications have acted to reduce tensile stresses associated with the formation of Type-A and -B cracks. Preliminary industrial trials with the modified mould have yielded blocks free of these defects.

Table of Contents

INTRODUCTION AND BACKGROUND	1
2.1 Introduction	1
2.2 Background	4
LITERATURE REVIEW	14
2.1 General	14
2.2 Monofrax-S	16
SCOPE AND OBJECTIVES	25
3.1 Scope of the Research Programme	25
3.2 Objectives of the Research Programme	29
INDUSTRIAL MEASUREMENTS	30
4.1 Experimental Technique	30
4.2 Experimental Procedure	33
4.3 Results	35
4.3.1 Initial Conditions	35
4.3.2 Re-pour Data	37
4.3.3 In-Mould Temperature Responses	37
4.3.4 Refractory Autopsy	49
4.4 Summary	50
MATHEMATICAL MODELS	52
5.1 Development of Mathematical Model of Heat Flow	52
5.1.1 Formulation	53
5.1.1.1 Finite Element Discretization of Spatial Derivatives	54
5.1.1.2 Solution	56
5.1.1.3 Selection of Element Type	57
5.1.1.4 Numerical Integration	59
5.1.1.5 Temperature-Dependent Material Properties	60

5.1.1.6 Latent Heat Evolution	61
5.1.1.7 Boundary Conditions.	63
5.1.2 Verification of Basic Model Formulation and Computer Code.	64
5.1.2.1 One-Dimensional Heat Conduction with Heat-Transfer Coefficient Boundary Condition.	65
5.1.2.2 One-Dimensional Heat Conduction with Phase Change.	69
5.1.2.3 Two-Dimensional Heat Conduction with Fixed-Temperature Bound- ary Condition.	78
5.1.2.4 Summary of Basic Heat-Flow Code Verification	81
5.2 Development of Mathematical Model of Stress Generation	82
5.2.1 Formulation	83
5.2.1.1 Finite-Element Solution by Displacement Method	85
5.2.1.2 Solution	89
5.2.1.3 Selection of Element Type	89
5.2.1.4 Numerical Integration	90
5.2.1.5 Temperature-Dependent Material Properties	90
5.2.1.6 Boundary Conditions	91
5.2.2 Verification of Basic Model Formulation and Computer Code	91
5.2.2.1 Iso-Thermal Beam Deflection Problem	92
5.2.2.2 Non-isothermal Body Problem	95
5.2.2.3 Summary on Basic Stress Analysis Code Verification	98
ANALYSIS OF EPIC-3 MONOFRAX-S CASTING PROCESS	100
6.1 Application of Thermal Model	100
6.1.1 Epic-3 Boundary Conditions	100
6.1.2 Initial Conditions	106
6.1.3 Material Properties	107
6.1.3.1 Thermophysical Properties of Monofrax-S (AZS-CS3)	108
6.1.3.2 Thermophysical Properties of Bonded and Annealing Sand	117

6.1.4 Finite-Element Spatial Discretization.	123
6.1.5 Sensitivity Analysis, Comparison to Industrial Data and Alignment of the Heat-Flow Model to the Industrial Process.	125
6.1.5.1 Sensitivity Analysis	126
6.1.5.2 Comparison of Model Predictions to Industrial Data	137
6.1.5.3 Alignment of Model to the Epic-3 Casting Process.	139
6.2 Application of Stress Model.	145
6.2.1 Boundary Conditions.	146
6.2.2 Initial Conditions	148
6.2.3 Thermomechanical Properties of Monofrax-S (AZS-CS3)	148
6.2.4 Finite Element Spacial Discretization.	155
6.2.5 Sensitivity Analysis.	155
MODEL PREDICTIONS AND DISCUSSION	163
7.1 Model Predictions	163
7.1.1 Mechanisms for Crack Formation.	166
7.2 Recommendations for the Control of Cracking.	201
7.2.1 Critical Aspects of Mould Design.	201
7.2.2 Critical Casting Variables.	213
7.2.3 Industrial Trials with Modified Mould.	213
SUMMARY AND CONCLUSIONS	214
8.1 Recommendations for Future Work.	216
REFERENCES.....	216

Table of Tables

Table 4.1.	Times at which data logger scan frequency was shifted.....	34
Table 4.2.	Ambient air temperature measurements.	36
Table 4.3.	Pour stream temperature measurements (initial pour).	36
Table 4.4.	Pour stream temperature measurements (re-pour).	37
Table 5.1.	Model input parameters and initial conditions.....	68
Table 5.2.	Model input parameters and initial conditions.....	73
Table 5.3.	Model input parameters and initial conditions.....	81
Table 5.4.	Mechanical properties for beam deflection problem.	94
Table 5.5.	Mechanical properties for non-isothermal beam problem.	97
Table 6.1.	Thermophysical Properties of Monofrax-S (AZS-CS3).	109
Table 6.2.	Thermal conductivity bonded sand.	119
Table 6.3.	Thermal conductivity of annealing sand.	119
Table 6.4.	Typical composition of base sand.	119
Table 6.5.	Thermomechanical properties for Monofrax-S (AZS-CS3).	151
Table 7.1.	Measured modulus of rupture of Monofrax-S (AZS-CS3) in tension as a function of temperature.	168
Table 7.2.	Thermophysical properties of additional moulding materials utilized in the modified mould.	205

Table of Figures

Figure 1.1.	Thermal expansion/contraction of zirconia in air ⁴	3
Figure 1.2.	Schematic illustration of cracks found in 1220 x 254 x 457mm (48 x 10 x 18in) Epic-3 Monofrax-S refractory.	4
Figure 1.3.	Mould/flasking lay-up for 1220 x 254 x 457mm (48 x 10 x 18in) Epic-3 Monofrax-S casting.	6
Figure 1.4.	Schematic illustration showing frequency distribution of Type-A cracks in 1220 x 254 x 457mm (48 x 10 x 18in) Epic-3 casting.	7
Figure 1.5.	Photomicrograph of cold fracture surface of Monofrax-S taken with an SEM at a magnification of 80X for reference.....	9
Figure 1.6.	Photomicrograph of Type-A crack surface taken near surface of the refractory with an SEM at a magnification of 80X showing smooth regions indicative of the presence of molten and/or viscous material at the time of crack formation.	10
Figure 1.7.	Photomicrograph of Type-A fracture surface taken near the centre of the refractory with an SEM at a magnification of 80X showing morphology indicative of the surface of shrinkage cavity.	11
Figure 1.8.	Photomicrograph of Type-B fracture surface taken near the surface of the refractory with an SEM at a magnification of 80X showing granular morphology indicative of brittle failure and smooth morphology indicative of molten and/or viscous material at the time of crack formation.	12
Figure 1.9.	Photomicrograph of Type-B crack surface taken 50.8mm(2.0in) to 76.2mm(3in) below the surface of the refractory with an SEM at a magnification of 80X showing regions of brittle fracture and smooth morphology indicative of the presence of molten and/or viscous material at the time of crack formation.	13
Figure 2.1.	Thermal conductivity, thermal expansion and typical composition of Monofrax-S (AZS-CS3).	18
Figure 2.2.	Thermal conductivity, thermal expansion and typical composition of Monofrax-S (AZS-CS4).	19
Figure 2.3.	Thermal conductivity, thermal expansion and typical composition of Monofrax-S (AZS-CS5).	20
Figure 2.4.	Alumina-Zirconia-Silica phase diagram.	22

Figure 2.5.	Fracture toughness of fused cast Monofrax-S and α -Alumina vs. temperature.	24
Figure 4.1.	Schematic diagram illustrating thermocouple placement in Epic-3 mould.	32
Figure 4.2.	In-mould temperature response from thermocouples adjacent to the broad face located 1181mm(46.5in) above the base of the refractory.	41
Figure 4.3.	In-mould temperature response from thermocouples adjacent to the broad face located 705mm(27.8in) above the base of the refractory.....	42
Figure 4.4.	In-mould temperature response from thermocouples adjacent to the broad face located 705(27.8) and 1181mm(46.5in) above the base of the refractory, 51mm(2.0in) from the refractory/mould interface.	43
Figure 4.5.	In-mould temperature response from thermocouples adjacent to the broad and narrow faces located 705mm(27.8in) above the base of the refractory 51mm(2.0in) from the refractory/mould interface.	44
Figure 4.6.	In-mould temperature response from thermocouples adjacent to the broad face located 1181mm(46.5in) above the base of the refractory.	45
Figure 4.7.	In-mould temperature response from thermocouples adjacent to the broad face located 70mm(2.75in) above the base of the refractory..	46
Figure 4.8.	In-mould temperature response from thermocouples located 51mm(2in) from the broad face.	47
Figure 4.9.	Temperature 51mm(2in) from the broad face at various distances from the base of the refractory at 15hrs elapsed time.	48
Figure 4.10.	Variation in temperature with distance from the broad face at 2, 4 and 8hrs elapsed time.	49
Figure 4.11.	Schematic illustration of the results of the autopsy on the instrumented Epic-3, Monofrax-S refractory.	51
Figure 5.1.	Eight-node isoparametric quadratic element depicted in rectilinear form in local coordinate system(u,v,w) and in global coordinate system(x,y,z).	58
Figure 5.2.	Twenty-node isoparametric quadratic element depicted in rectilinear form in local coordinate system(u,v,w) and in global coordinate system(x,y,z).	59
Figure 5.3.	Schematic illustration of one-dimensional, semi-infinite, transient heat conduction problem.	66

Figure 5.4.	Schematic illustration of finite element representation of one-dimensional, semi-infinite, transient heat conduction problem.	67
Figure 5.5.	Comparison of model-predicted temperature response to exact solution for one-dimensional transient heat conduction problem with a specified heat transfer coefficient boundary condition.	69
Figure 5.6.	Schematic illustration of one-dimensional heat conduction problem.	71
Figure 5.7.	Schematic illustration of finite element representation of one-dimensional heat conduction problem.	72
Figure 5.8.	Comparison of model-predicted temperature response to exact solution for one-dimensional transient heat conduction problem with a fixed temperature boundary condition.	74
Figure 5.9.	Comparison of model predicted temperature response to exact solution for one-dimensional transient heat conduction problem with phase change and fixed temperature boundary condition.	76
Figure 5.10.	Comparison of model predicted temperature response to exact solution for one-dimensional transient heat conduction problem with phase change and fixed temperature boundary condition. For this analysis the mesh density has been increased over the standard case. ...	77
Figure 5.11.	Schematic illustration of two-dimensional, transient heat conduction problem with fixed temperature boundary condition.	79
Figure 5.12.	Schematic illustration of finite element representation of two-dimensional, transient heat conduction problem with fixed temperature boundary condition.	80
Figure 5.13.	Comparison of model predicted temperature response to exact solution for two-dimensional, transient heat conduction problem with fixed temperature boundary condition.	82
Figure 5.14.	Schematic illustration of beam bending problem employed for verification of load deflection calculation.	92
Figure 5.15.	Schematic illustration of finite element representation of beam bending problem employed for verification of load deflection calculation.	93
Figure 5.16.	Schematic illustration of non-isothermal problem employed for verification of thermal-load/thermal-stress calculation.	95
Figure 5.17.	Schematic illustration of finite element representation of non-isothermal problem employed for verification of thermal-load/thermal-stress calculation.	96

Figure 5.18.	Comparison of model prediction of σ_x distribution to results of analytical solution.	98
Figure 6.1.	Schematic illustration of mould/flasking lay-up for Epic-3 casting technique showing coordinate system and centre-planes of symmetry utilized in thermal model analysis.	102
Figure 6.2.	Measured heat capacity data as a function of temperature and polynomial fit for Monofrax-S (AZS-CS3).	111
Figure 6.3.	Measured density data as a function of temperature and polynomial fit for Monofrax-S (AZS-CS3).	112
Figure 6.4.	Measured thermal conductivity data as a function of temperature and polynomial fit for Monofrax-S (AZS-CS3).	113
Figure 6.5.	Measured thermal diffusivity data as a function of temperature and polynomial fit for Monofrax-S (AZS-CS3).	114
Figure 6.6.	Enthalpy function for Monofrax-S (AZS-CS3), employed in thermal model.	116
Figure 6.7.	Measured thermal conductivity data as a function of temperature and polynomial fit for bonded sand.	120
Figure 6.8.	Measured thermal conductivity data as a function of temperature and polynomial fit for annealing sand.	121
Figure 6.9.	Heat capacity as a function of temperature for silica sand, input to the model.	122
Figure 6.10.	Schematic illustration of section of Epic-3 casting analyzed with heat-flow model.	124
Figure 6.11.	Schematic illustration of transverse (x/y) section of three-dimensional mesh employed in the thermal analysis.	125
Figure 6.12.	Location of nodes utilized in the sensitivity analysis.	127
Figure 6.13.	Model sensitivity to latent heat of fusion of Monofrax-S.	128
Figure 6.14.	Model sensitivity to liquidus-solidus gap, T_{gap}	130
Figure 6.15.	Model sensitivity to magnitude of refractory/mould interfacial heat-transfer coefficient, h_{cond}	132
Figure 6.16.	Model sensitivity to time for gap formation at refractory/mould interface.	133

Figure 6.17.	Model sensitivity to magnitude of rate of decrease of refractory/mould interfacial heat-transfer coefficient, f_{ramp}	134
Figure 6.18.	Model sensitivity to thermal conductivity of moulding sand.	135
Figure 6.19.	Model sensitivity to maximum temperature change per time step.	137
Figure 6.20.	Comparison between model predictions and industrial thermocouple data.	138
Figure 6.21.	Model fit to industrial thermocouple data using an adjusted thermal conductivity of moulding sand.	141
Figure 6.22.	Model fit to industrial thermocouple data using an adjusted latent heat of fusion of Monofrax-S.	142
Figure 6.23.	Model fit to industrial thermocouple data using an adjusted value for f_{ramp}	144
Figure 6.24.	Model fit to industrial thermocouple data using adjusted values for input parameters.	145
Figure 6.25.	Schematic illustration of boundary conditions applied to the two-dimensional transverse quarter-section of Epic-3 refractory.	147
Figure 6.26.	Measured elastic modulus data as a function of temperature and polynomial fit for Monofrax-S (AZS-CS3).	152
Figure 6.27.	Measured Poisson ratio data as a function of temperature and polynomial fit for Monofrax-S (AZS-CS3).	153
Figure 6.28.	Measured thermal linear strain as a function of temperature and polynomial fit for Monofrax-S (AZS-CS3).	154
Figure 6.29.	Location of nodes utilized in sensitivity analysis.	156
Figure 6.30.	Model sensitivity to elastic modulus (σ_y at centre of broad face).	158
Figure 6.31.	Model sensitivity to elastic modulus (σ_x at centre of narrow face).....	159
Figure 6.32.	Predicted temperature response for selected nodes.	160
Figure 6.33.	Model sensitivity to Poisson ratio (σ_y at centre of broad face).	161
Figure 6.34.	Model sensitivity to Poisson ratio (σ_x at centre of narrow face).	162
Figure 7.1.	Predicted distributions of temperature and axial stress (σ_x) on the surface of the lower quarter-section of the Epic-3 cast refractory at 23 hrs elapsed time.	165

Figure 7.2.	Predicted distributions of temperature and axial stress (σ_z) on the y-z centre plane of the lower quarter-section of the Epic-3 cast refractory at 23 hrs elapsed time.....	169
Figure 7.3.	Schematic illustration of mould/flasking lay-up showing region of casting analyzed with heat-flow model and location of nodes utilized in the investigation of Type-A1 cracks.	171
Figure 7.4.	Axial stress (σ_z) predicted by the model for three nodes located along a line perpendicular to the centre of the broad face at roughly mid-height in the refractory.....	172
Figure 7.5.	Comparison between axial stress (σ_z) predicted by the model and the modulus of rupture of Monofrax-S plotted as a function of temperature.	175
Figure 7.6.	Comparison between axial stress (σ_z) predicted by the model at the centre of the broad and narrow faces and the modulus of rupture of Monofrax-S plotted as a function of temperature.	176
Figure 7.7.	Comparison between temperature predicted by the model at the centre of the broad and narrow faces.....	179
Figure 7.8.	Predicted distributions of temperature and axial stress σ_z on the surface of the lower quarter-section of the Epic-3 cast refractory at 20 hrs elapsed time.....	180
Figure 7.9.	Predicted distributions of temperature and axial stress (σ_z) on the surface of the lower quarter-section of the Epic-3 cast refractory at 20 hrs elapsed time. The quarter-section has been truncated by removing 24.5mm(1in) in a direction normal to the broad-face.	182
Figure 7.10.	Schematic illustration of the mould/flasking lay-up showing region of casting analyzed with thermal model and location of nodes utilized in the investigation of Type-A2 cracks.....	184
Figure 7.11.	Axial stress (σ_z) predicted by the model at the centre of the broad face.....	185
Figure 7.12.	Comparison between axial stress (σ_z) predicted by the model and the measured modulus of rupture data for Monofrax-S for node located at the centre of the broad face 14mm(5.5in) from the base.	186
Figure 7.13.	Comparison between axial stress (σ_z) predicted by the model at the centre of the broad and narrow faces near the base and near mid-height.	187
Figure 7.14.	Comparison between temperatures predicted by the model at the centre of the broad face near the base and near mid-height.....	188

Figure 7.15.	Predicted distribution of temperature, σ_x and σ_y on the surface of the lower quarter-section of the Epic-3 cast refractory at 20 hrs elapsed time.	190
Figure 7.16.	Predicted transverse stresses acting parallel to the broad and narrow faces. The nodes are located at the centre of each face at mid-height. ...	193
Figure 7.17.	Schematic illustration of beam bending analogy as applied to a quarter transverse-section of the Monofrax-S refractory. The refractory is depicted as being only partially solidified.	194
Figure 7.18.	Predicted σ_y variation at the centre of the broad face at 0mm, 13mm(0.5in) and 51mm(2in) below the surface at mid-height in the refractory.	195
Figure 7.19.	Comparison between σ_y predicted by the model at the centre of the broad face at mid-height and the measured modulus of rupture data as a function of temperature.	196
Figure 7.20.	Predicted distributions of temperature and σ_z stress on the surface of the lower quarter-section of the Epic-3 cast refractory at 5 hrs elapsed time.....	198
Figure 7.21.	Predicted σ_z at intersection between the broad and narrow faces at mid-height of the refractory.	199
Figure 7.22.	Comparison between σ_z predicted by the model at the intersection between the broad and narrow faces at mid-height and the measured modulus of rupture data as a function of temperature.	200
Figure 7.23.	Proposed mould design for control of cracking in the Epic-3 casting process.	206
Figure 7.24.	Comparisons between axial stress predicted by the model at the centre of the broad face at mid-height in the refractory for the standard mould and for the modified mould.	207
Figure 7.25.	Comparisons between axial stress predicted by the model at the centre of the refractory at mid-height for the standard mould and for the modified mould.	208
Figure 7.26.	Comparisons between temperature responses predicted by the model at the centre of the broad face at mid-height in the refractory for the standard mould and for the modified mould.....	209
Figure 7.27.	Comparisons between axial stress predicted by the model at the centre of the broad face 140mm(5.5in) from the base of the refractory for the standard mould and for the modified mould.....	210

- Figure 7.28. Comparisons between transverse σ_y predicted by the model at the centre of the broad face at mid-height in the refractory for the standard mould and for the modified mould. 211
- Figure 7.29. Comparisons between axial stress predicted by the model at the intersection of the broad and narrow faces at mid-height in the refractory for the standard mould and for the modified mould. 212

TABLE OF SYMBOLS

LATIN SYMBOLS

A	surface area	m^2
B_j, B_i^T	matrix of differential operators	
Bi	Biot number	
C, C^e	global and elemental heat capacitance matrices	
$C_p, C_{p,i}$	heat capacity, heat capacity of species i	$J/g \cdot ^\circ C$
D	elasticity matrix	
E, E_i	elastic modulus, elastic modulus of species i	MPa
F_i	body force vector in direction i	MN
F_0	Fourier number	
f, \mathbf{f}	global and elemental load vector	MN
f	function (Eqs 5.17 and 5.18)	
f_{ramp}	rate at which refractory/mould interfacial heat transfer coefficient h_{gap} is reduced	$W/m^2 \cdot ^\circ C \cdot s$
H	enthalpy	J/g
ΔH_f	latent heat of solidification (fusion)	J/g
h	height (Eq. 5.60)	m
h, h_i	vector of heat transfer coefficients global and nodal	$W/m^2 \cdot ^\circ C$
$h_{conv}, h_{cond}, h_{rad}$	heat transfer coefficients due to convection, conduction and radiation	$W/m^2 \cdot ^\circ C$
h_c, h_{gap}, h_{ext}	heat transfer coefficients, generic, refractory/mould gap, and exterior	$W/m^2 \cdot ^\circ C$
I	moment of inertia	m^4
K, K^e	global and element stiffness matrix	
k_i	thermal conductivity of species i or thermal conductivity in direction i	$W/m \cdot ^\circ C$
N_i	row vector of shape or interpolation functions for node i	
N_j	column vector of shape or interpolation functions for node j	
n_i	normal to direction i	
Q	heat flux per unit volume	W/m^3
q	heat flux per unit area	W/m^2
S_i	surface i	

T, T^e	global and elemental temperature vector	°C
T_{amb}, T_{∞}	ambient temperature and temperature at infinity	°C
$T_0, T_{i,j}$	temperature at time 0, temperature on surface i at time j	°C
T_i	temperature at node i (Eq. 5.5), temperature at time i (Eqs. 5.14, 5.15, and 5.16)	
T_{max}	maximum temperature change per time-step	
T	surface traction (Eq. 5.49)	
t, t_{gap}	time, time for interfacial gap formation	s
t	thickness (Eq. 5.60)	m
Δt_i	time step at time i used in numerical integration	s
U_p	strain energy	N·m
u, v, w	local cartesian coordinate system	
u_i, v_i, w_i	displacements for node i in the x, y and z directions (Eq. 5.52)	m
V_p	work done by applied loads during displacement changes	N·m
V	volume	m ³
W_i	weighting coefficients for Gauss quadrature integration	
x, y, z	global cartesian coordinate system	

GREEK SYMBOLS

α	symbol for ferrite phase in steel (Chapter 1)	
α_i	thermal diffusivity	s·m
α, α_i	thermal linear expansion coefficient (Eq. 5.54, 5.64), thermal linear expansion coefficient of species i	°C ⁻¹
γ	symbol for austenite phase in steel (Chapters 2 and 7)	
$\gamma_{i,j}$	shear strain perpendicular to i in direction j	
$\delta, \{\delta\}, \{\delta\}^e$	displacement, displacement vector global, displacement vector elemental	m
$\epsilon_i, \{\epsilon\}, \{\epsilon\}_0$	strain in direction i , strain vector initial strain vector	
ϵ	emissivity (Eq. 6.5, 6.13)	
μ	kinematic viscosity	N·s/m ²
ν	Poisson's ratio	
Π_p	total potential energy	N·m

ρ, ρ_∞	density, density at infinity	g/m^3
σ_i	stress in direction i	MPa
σ	Stefan-Boltzmann constant (Eq. 6.5, 6.13)	$\text{W/m}^2 \cdot \text{C}^4$
T_{ij}	shear stress normal to i in direction j	MPa
ϕ	function	

MATHEMATICAL SYMBOLS

∂	differential operator	
,d		
Σ	sum of terms	

ACKNOWLEDGEMENTS

I would like to express my sincere indebtedness to Dr. Keith Brimacombe for his untiring support and friendship throughout this project. I would also like to thank Mr. Thomas Myles and Mr. Dennis Walrod for their guidance and assistance during my stay at the Falconer plant in New York. The financial support and co-operation of Carborundum Engineered Materials Company was greatly appreciated.

Many thanks are also in order to Dr. Greg Richards for always having his door open. His encouragement and the many hours of time he spent discussing this project over the last three years did not go unnoticed.

It is impossible to assess the contribution of John Hogg of University Computing Services. His help on the use of workstations and data visualization software were critical to the success of the project. Thanks also to Tom Nicol and Helen Salter of University Computing Services. The "boys" in the office must be commended for putting up with me and my noisy computers.

Finally, a special thanks to my wife Susan for the sacrifices and emotional support she has given me.

CHAPTER 1

INTRODUCTION AND BACKGROUND

1.1 Introduction

As ceramic material are placed in more demanding applications greater emphasis is placed on the production of defect free components. The ability to achieve a high level of quality control is critical to a wide variety of applications ranging from fused cast refractories to sintered silicon nitride engine components. A portion of the blame for the difficulties encountered in achieving reproducible quality lies with the manner in which processing problems have been addressed traditionally. In the past, rule-of-mixture and strength-of-material approaches have prevailed. What is required is a fundamental understanding of the factors which impact on the ability to produce defect free ceramic materials.

The Monofrax Plant of the Carborundum Engineered Materials Company, located in Falconer, N.Y., produces a wide range of fused cast ceramic components for various applications. One class of product, Monofrax-S, which contains primarily alumina (47-57%), zirconia (34-41%) and silica (10-15%), is used extensively in the glass industry for lining furnaces. Refractory components of Monofrax-S are made by first melting the raw materials in an electric-arc furnace and then pouring the resulting liquid into bonded sand moulds. The moulding and casting procedures are analogous in many respects to those used in a typical iron/steel foundry. About 5000 tonnes of Monofrax-S was produced at the Falconer plant in 1989.

The Monofrax-S3 through S5 (increasing ZrO_2/SiO_2 ratio) class of refractories is advertised to provide exceptional erosion-corrosion resistance to molten glass at elevated temperatures¹. This material solidifies into what is described as a complex fine grained composite of

crystalline zirconia and alumina in a glassy matrix¹. The glassy phase is reported² to be the key to the ability of the refractory to withstand the thermal cycling encountered in service. The siliceous matrix softens at temperatures in the vicinity of 650°C helping to dampen thermally induced stresses² such as those caused by the erratic thermal expansion/contraction behaviour of the zirconia phase. (At around 1000°C ZrO_2 undergoes a monoclinic - tetragonal phase change which is accompanied by a 3% change in volume³⁻⁷, see Figure 1.1⁴). Unfortunately, however, the glassy phase is the least resistant component of the Monofrax-S structure, dissolving first followed by crystalline alumina and finally crystalline zirconia¹.

Although well suited for use as a lining in glass tanks, the Monofrax-S products are not without problems. Most notably, castings of this grade of refractory suffer from cracks which occur during the solidification process. Those cracks which reach the surface may occur in a variety of locations and orientations. For example, in the Epic-3 castings (described later) transverse cracks (Type-A) are often observed near the middle and/or bottom of a face; longitudinal cracks (Type-B) are frequently found running down the mid-face; and transverse-corner cracks (Type-E) may form at the corners. Figure 1.2 illustrates schematically the orientations and locations of the various crack types. In service, these cracks act to provide a larger surface area for chemical attack thus reducing the overall erosion-corrosion resistance of Monofrax-S. In addition, the cracks can act as stress raisers which lower the ability of the refractory to withstand thermal cycling. Depending on the willingness of the customer to accept a cracked product, blocks may have to be recycled at a considerable cost. Hence, there is a strong incentive to determine the origin(s) of these cracks and to eliminate them.

1.2 Background

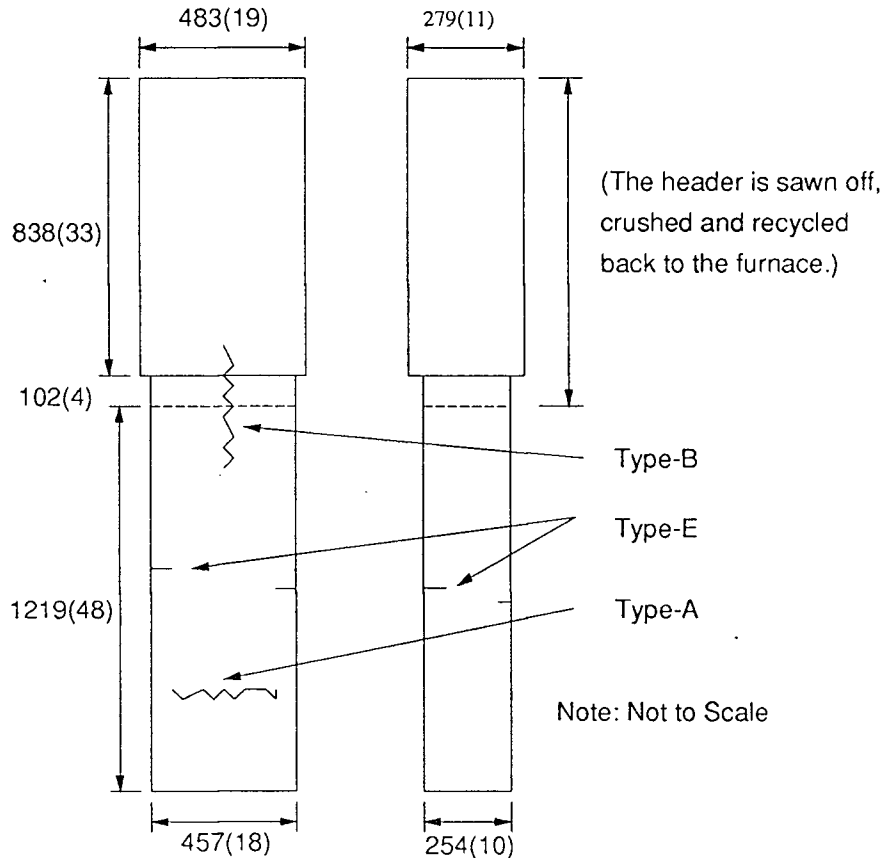


Figure 1.2. Schematic illustration of cracks found in 1220 x 254 x 457 mm (48 x 10 x 18in) Epic-3 Monofrax-S refractory. Note: units are mm (inches).

Traditionally, at Falconer, casting processes have been designed and optimized by trial and error incorporating historical experience whenever possible. Unfortunately, the ability of this approach to address specific problems, such as the occurrence of a particular crack, is time consuming, costly and often unsuccessful. Thus a knowledge intensive approach, commencing with an in-house study of the Monofrax-S cracking problem was initiated in 1985. There were three main objectives to the study: firstly, to attempt to establish links between

the types of cracks observed and process variables such as, pour rate, pour composition, block dimensions, etc.; secondly, to study the morphology of the crack surface to establish at what time(s) during the solidification process the cracking occurred; and thirdly, to examine and compare the structure and segregation observed in cracked and uncracked castings. The Epic-3 casting technique was selected for the study owing to its high susceptibility to crack formation. This casting technique involves an end-pour with a timed re-pour into an oversized header - see Figure 1.3 for a typical mould lay up. The re-pour is usually scheduled one-half hour after pouring, after which, the top of the casting is then covered with annealing (loose) sand. The mould may be stripped from five to ten days later depending on production schedules.

The first two objectives of the Monofrax-S, Epic-3 casting study have essentially been met. The analysis of 1,233 castings has indicated no singular cause-and-effect relationship correlating crack frequency with a process variable. Instead, several of the process variables studied have been found to influence cracking to some extent. The following observations were made⁸:

- (1) Type-A and E crack occurrences tend to coincide;
- (2) Type-A and B crack occurrences tend not to coincide;
- (3) Type-A cracking occurs on the broad-face most often at mid-height in the casting, just below the header ledge, and at the base of the casting - see Figure 1.4 which illustrates schematically the frequency distribution of Type-A cracks;
- (4) The ZrO_2 content of the pour stream tends to correlate inversely with Type-A crack frequency;
- (5) Pour rate into the mould correlates weakly with Type-B crack frequency, and;

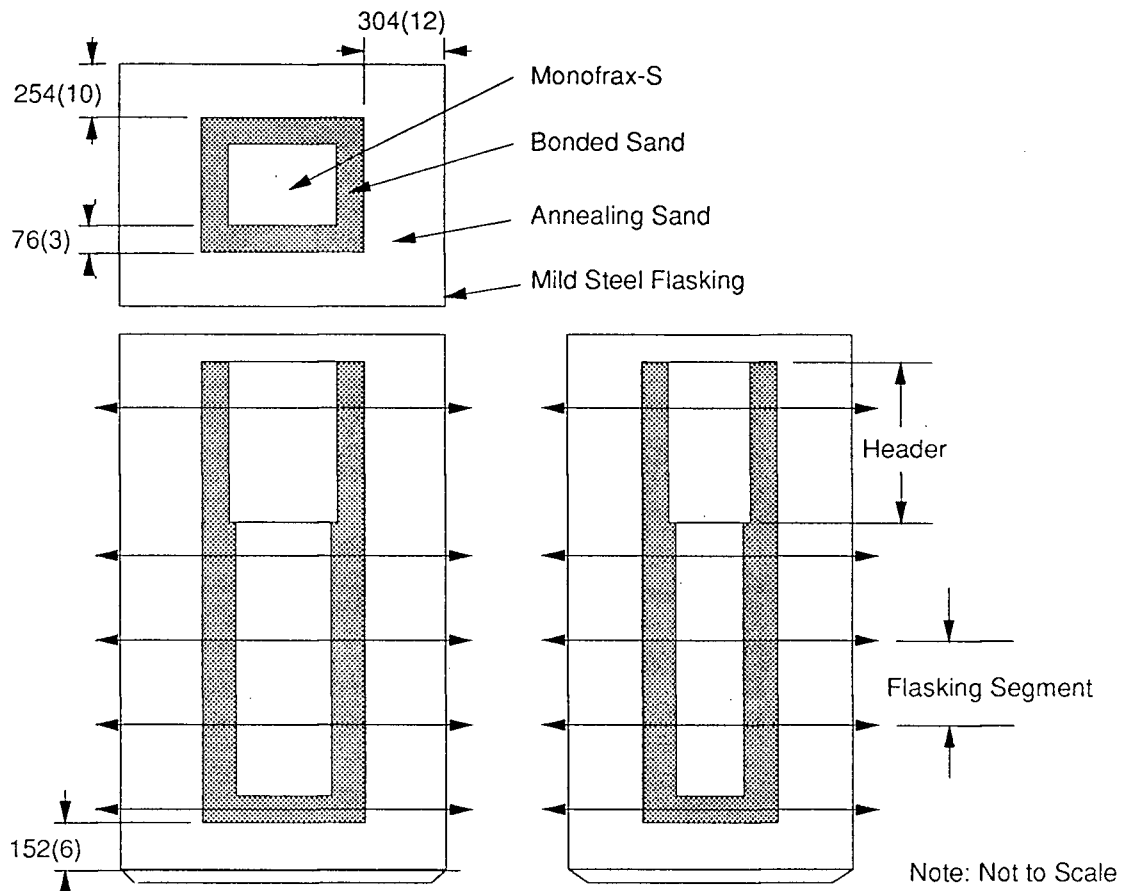


Figure 1.3. Mould/flasking lay-up for 1220 x 254 x 457 mm (48 x 10 x 18in) Epic-3 Monofrax-S casting. The dimensions are mm(inches).

(6) Block thickness influences Type-B frequency and to a lesser extent Type-A frequency.

The results of a study⁸ of fracture surface morphology with a scanning electron microscope (S.E.M.) have proven to be difficult to interpret. S.E.M. photographs have revealed that Type-A and B crack surfaces exhibit both smooth regions and regions of sharply defined granular morphology (the former is believed to be associated with the presence of molten and/or viscous material during crack formation, whereas the latter is more typical of brittle

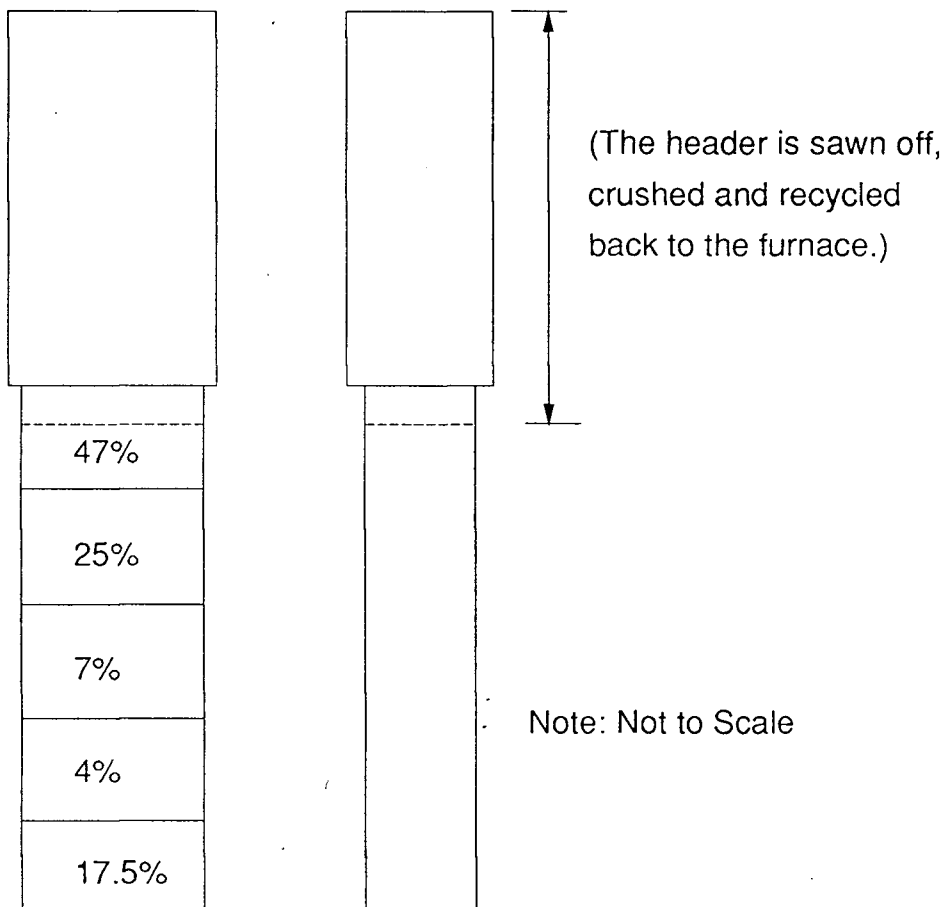


Figure 1.4. Schematic illustration showing the frequency distribution of Type-A cracks in 1220 x 254 x 457 mm (48 x 10 x 18in) Epic-3 refractory.

low temperature failure - see Figure 1.5, typical cold fracture). Interpretation is further complicated by the fact that all drill core samples of the cracks studied had to be thermally shocked open in order to expose the crack surfaces for viewing. The separation procedure involved heating the samples to approximately 300°C and then quenching them. This obviously added additional low temperature fracture surfaces not associated with the casting process.

In general, however, the S.E.M. photographs of the Type-A crack surfaces show a smooth, less angular fracture morphology near the block surface (see Figure 1.6) which changes to a structure indicative of the surface of shrinkage cavities toward the interior of the block (see Figure 1.7). Some regions exhibiting brittle failure are also evident in the interior photographs. However, these are likely associated with thermal shock separation of the cracks as discussed earlier. This evidence suggests that the Type-A cracks initiate at the block surface early in the solidification process and continue to propagate inwards through the zone of shrinkage porosity as the casting cools. The photographs taken at various locations on the Type-B crack surface, Figures 1.8 and 1.9, exhibit essentially the same features. On the basis of fracture surface morphology it is difficult to resolve which of the two cracks is the first to form. The fact that at points where Type-A and B cracks intersect, the Type-B cracks are routinely observed to be discontinuous indicates that they were the last to form⁸.

The data gathered during the Epic-3 Monofrax-S casting study has produced a comprehensive data base. Moreover, the results of the study have revealed several correlations of varying strength linking process parameters to the formation of various cracks and has tentatively established the timing for the formation of Type-A and B cracks. Unfortunately however, no clear picture emerges concerning the cause of the cracks and the remedies to eliminate them. A more fundamental approach is required.

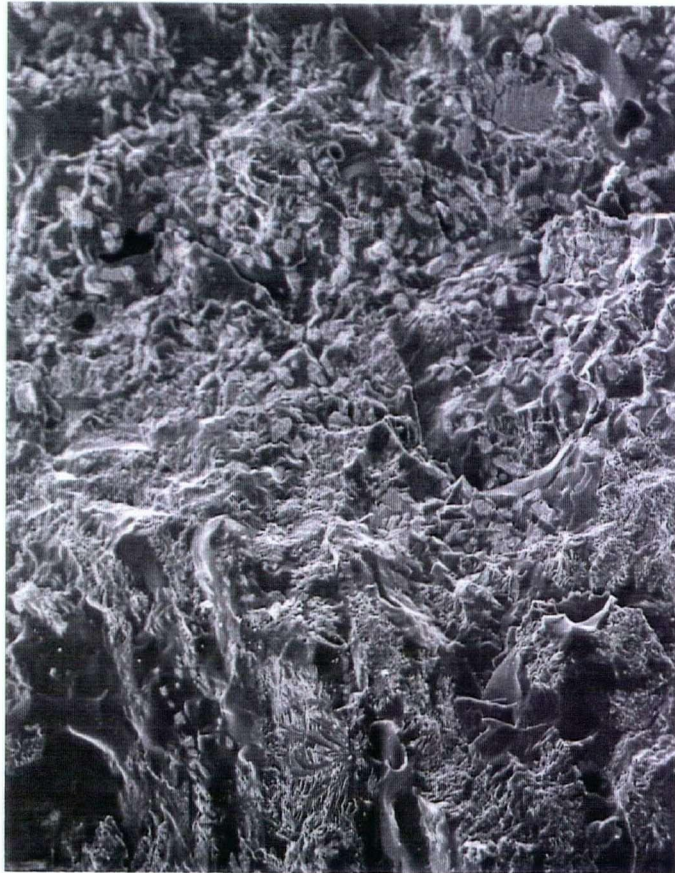


Figure 1.5. Photomicrograph of cold fracture surface of Monofrax-S taken with an SEM at a magnification of 80X for reference.



Figure 1.6. Photomicrograph of Type-A crack surface taken near the surface of the refractory with an SEM at a magnification of 30X showing smooth regions indicative of the presence of molten and/or viscous material at time of crack formation.

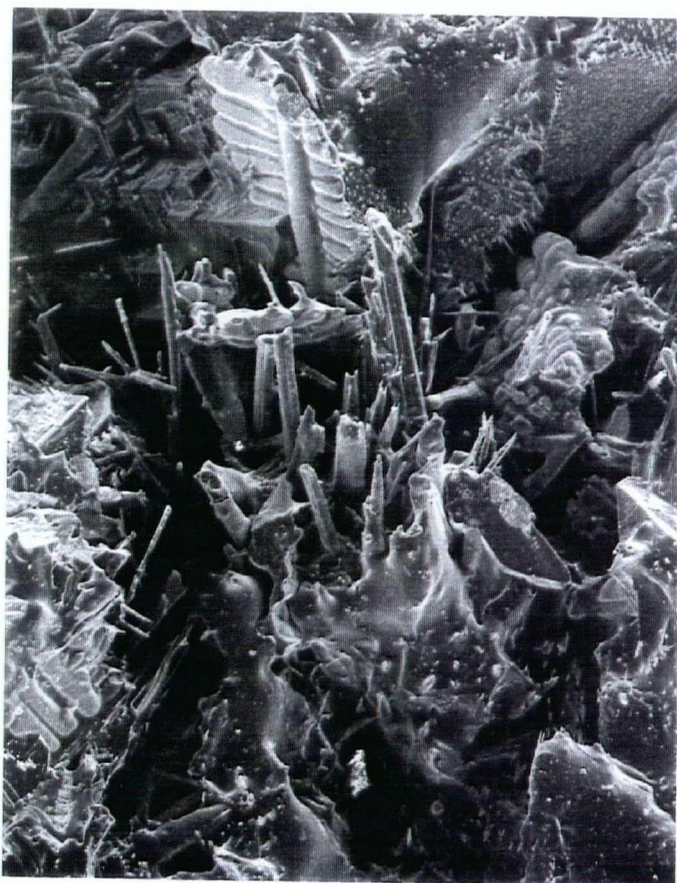


Figure 1.7 Photomicrograph of Type-A crack surface taken near the center of the refractory with an SEM at a magnification of 80X showing morphology indicative of the surface of a shrinkage cavity.

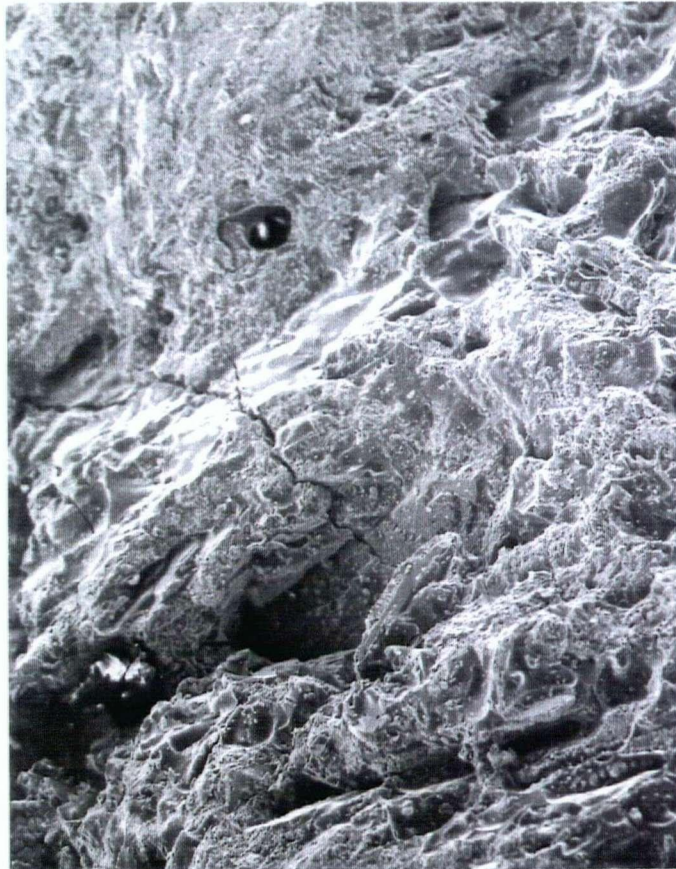


Figure 1.8. Photomicrograph of Type-B crack surface taken near the edge of the refractory with an SEM at a magnification of 80X showing granular morphology indicative of brittle failure and smooth surfaces indicative of molten and/or viscous material at the time of crack initiation.

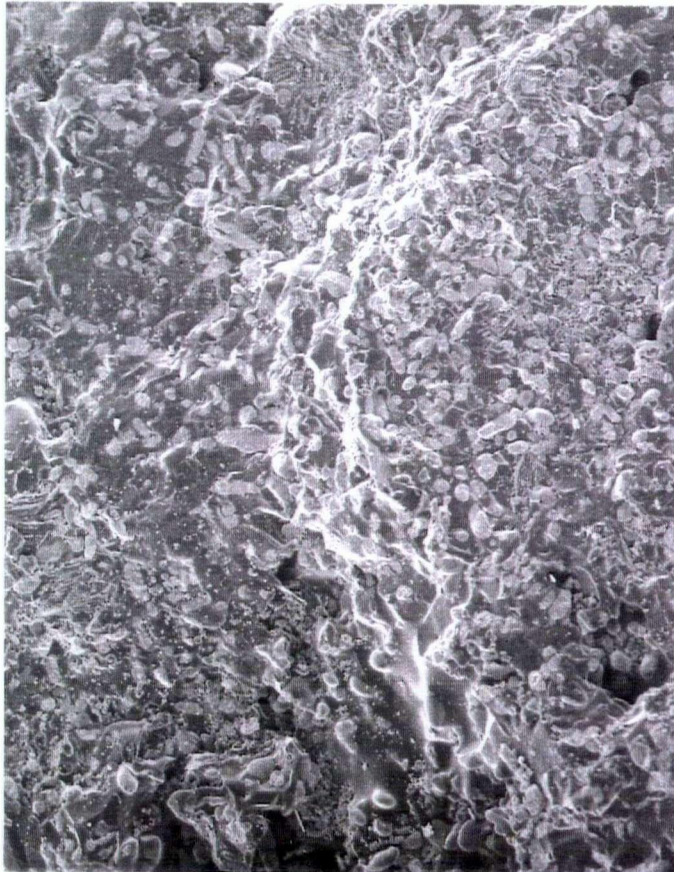


Figure 1.9. Photomicrograph of Type-B crack surface taken 50.8mm(2in) to 76.2mm(3in) below the surface of the refractory with an SEM at a magnification of 80X showing regions of brittle fracture and smooth morphology indicative of the presence molten and/or viscous material at the time of crack formation.

CHAPTER 2

LITERATURE REVIEW

A review of the literature has revealed a paucity of information on the processing of fused cast ceramics. A brief review of the literature on the behaviour of ceramic materials in transient thermal fields is present below together with some relevant material on metals casting processes.

2.1 General

Ceramic materials in general exhibit a high degree of susceptibility to thermal shock failure owing to their low thermal conductivity and low strain-to-failure. For example, refractory linings used in high temperature industrial furnaces often fail due to thermal stresses arising from thermal cycling⁹⁻¹⁵. A number of reported studies have attempted to establish design and operating criteria for these components. Early work involved the development of various "strength-of-material" type models⁹⁻¹³ to evaluate the thermal shock resistance of refractory components. The analytical models of Kingery⁹, Kienow¹⁰, and Hasselman¹⁰⁻¹² yield useful selection criteria which account for material behaviour albeit to a limited extent. Unfortunately, by necessity, their treatment of the thermal and geometric aspects of the problem restricts the application of these models to the analysis of furnace linings. The complex heat transfer and geometric aspects of the Epic-3 casting process dictates a more sophisticated approach.

More recently, the availability of greater computational power has permitted numerical techniques to be employed. Chang et al.¹⁴ have investigated thermal stress failure in thick-walled refractory structures. Two- and three-dimensional thermoelastic stress analyses based on the finite element method were conducted on refractory structures with length in the

direction of heat flow larger than height or width. In their analysis heating was assumed to occur at a linear rate over the front face defined by the smaller dimensions. For moderate heating rates they found that the maximum value of tensile stress occurred along the centre-line parallel to the longest dimension. Whereas, for high heating rates, the maximum component was to occur parallel to the face being heated. Moreover, the magnitude of tensile stress was found to be proportional to the heating rate and inversely proportional to the thermal diffusivity. Maximum values of stress were found for intermediate values of width.

A similar investigation of thermal stress fracture in rectangular refractory lining components has also been completed by Bradley et al.¹⁵. A two-dimensional thermoelastic constant heating model¹⁵ based on the finite element method has been employed in their analyses. The results are similar to the findings of Chang et al.¹⁴, and emphasize that the orientation and magnitude of tensile stresses are dependent on the geometry, thermal and mechanical properties and, heating and cooling rates.

Despite a more sophisticated treatment of stress, these models remain too restrictive in their characterization of heat flow to be of much use in the more complex Epic-3 casting problem. Owing to the fact that the temperature profiles are determined analytically, the Chang¹⁴ and Bradley¹⁵ models are limited to the analysis of problems involving one-dimensional heat conduction with linear heating rate and constant heating rate boundary conditions, respectively.

Metal castings also suffer from defects which arise due to thermal stresses¹⁶⁻²³. The continuous casting processes are particularly susceptible owing to the high heat-extraction rates¹⁷⁻¹⁹. For example, in the continuous casting of steel, "mid-way" or "half-way" cracks are observed in billets¹⁷⁻¹⁸ and "longitudinal mid-face" cracks are found in slabs¹⁹. Mathematical

models of heat transfer, and an understanding of stress generation and the mechanical properties of steel at elevated temperatures have been brought to bear to elucidate the mechanisms of crack formation¹⁶⁻¹⁹. These analyses indicate that large thermal strains acting on zones of low ductility are responsible for crack formation.

Thermal processing defects can also occur in static cast steel ingots²⁰⁻²³. One such defect, the "mid-face panel crack", is similar in many respects to the Type-B cracks (described earlier) found in Epic-3 Monofrax-S castings. Both are longitudinal in orientation, located in the mid-face and occur after solidification is complete²¹. A comprehensive investigation of steel ingot thermal processing has recently been completed by Thomas et al.^{22,23} The major thrust of their work was to develop a two-dimensional mathematical model to predict stress and understand the role of stress generation in the formation of panel cracks. Two separate mathematical models of heat flow and stress were formulated and solved using variations of the finite-element technique. The models were validated by comparison of results to simplified problems for which analytical solutions are available and, in the case of the heat transfer model, comparison of predictions to industrial data. Two relevant observations can be made from the work of Thomas et al.^{22,23}: firstly, it is essential to incorporate the effect of phase transformations into the model as it has been shown that major regions of tensile and compressive stress generation are linked to the expansion/contraction which accompany the γ - α phase transformation in steel; and secondly, it is essential to include the effects of time-dependent viscoplastic flow, as it has been shown to have a profound influence on the magnitude and qualitative development of stress. The first point is particularly noteworthy in view of the phase transformation which ZrO_2 undergoes at around 1000°C (previously described).

2.2 Monofrax-S

Any attempt to formulate mechanisms for the formation of cracks in Monofrax-S refractories requires an understanding of the high temperature behaviour of this material. Unfortunately, very little information is available in the literature. Some thermophysical and thermomechanical data can be obtained from product brochures¹. For example, typical data for the thermal conductivity and thermal expansion of Monofrax-S3, S4, S5 are presented along with their compositions in Figures 2.1-2.3¹. As illustrated in Figures 2.1-2.3, Monofrax-S undergoes an approximately 0.6% volume change at around 1100°C due to the monoclinic - tetragonal transformation of ZrO₂. The magnitude of the volume change is similar to that of the γ - α transformation in steel²³. In ZrO₂ this transformation exhibits a large thermal hysteresis, see Figure 1.1³. The monoclinic-to-tetragonal (forward) transformation occurs at approximately 1170°C^{3,4} on heating and the reverse between 850 and 1000°C on cooling. The magnitude of the thermal hysteresis is reported³ to be dependent on the amount of strain energy associated with the forward transformation. There is some uncertainty in the literature regarding the exact magnitude of the volume change associated with this transformation. A value of 3% volume change has been determined from linear expansion data⁴ which is consistent with the value determined by Patil and Subbarao^{5,6}. In contrast, a value of 9% volume change results from a comparison of the theoretical densities - 5560 kg/m³ for monoclinic and 6100 kg/m³ for tetragonal ZrO₂⁷.

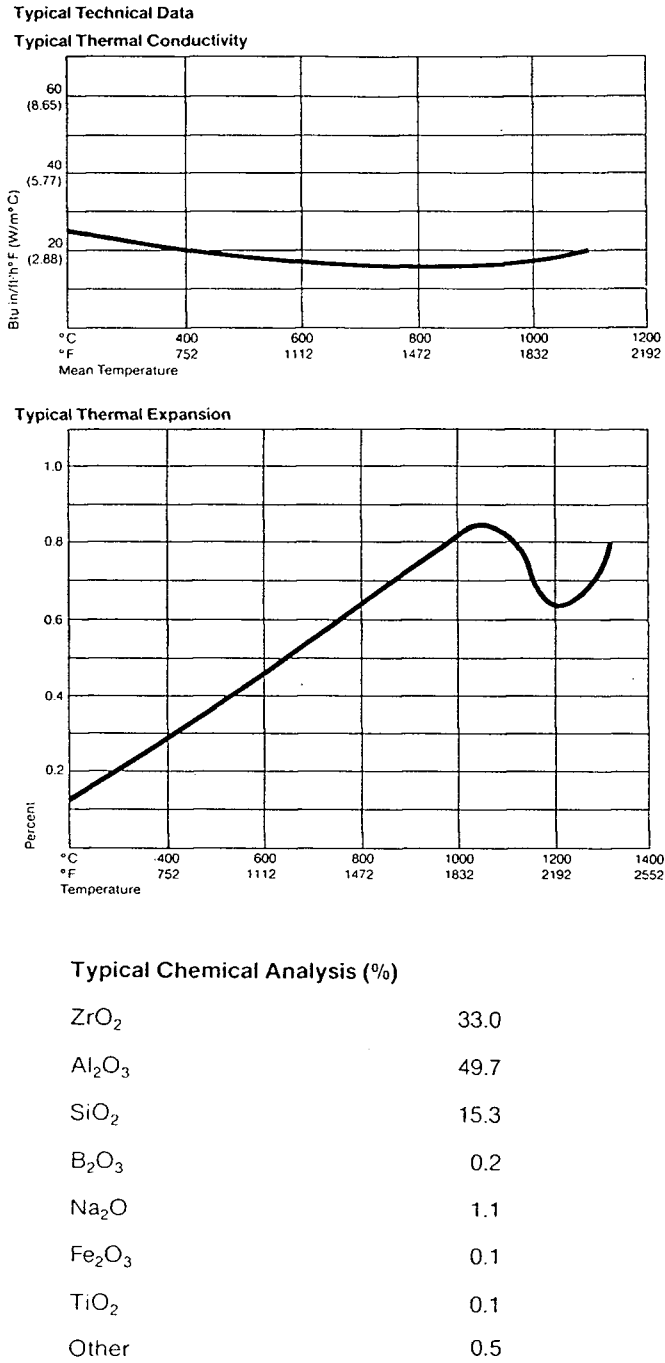
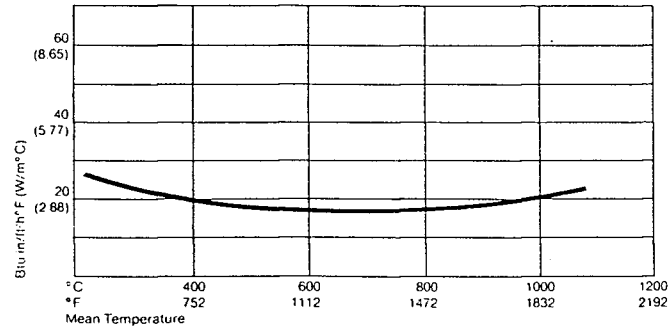


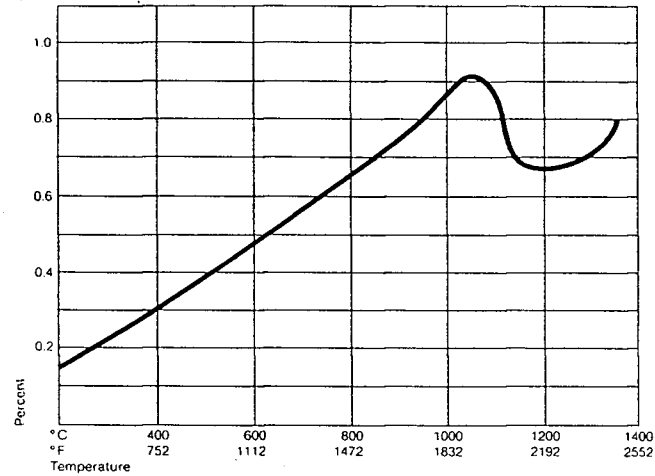
Figure 2.1. Thermal conductivity, thermal expansion and typical composition of Monofrax-S(AZS-CS3)¹.

Technical Data

Typical Thermal Conductivity



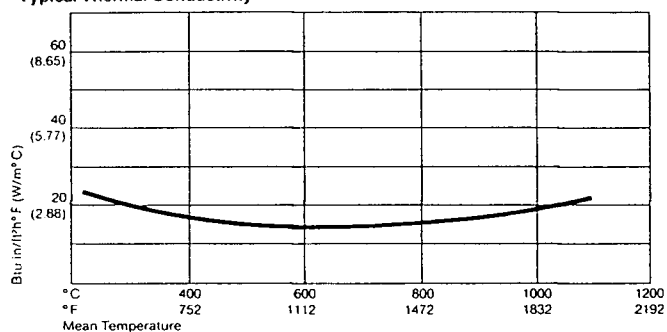
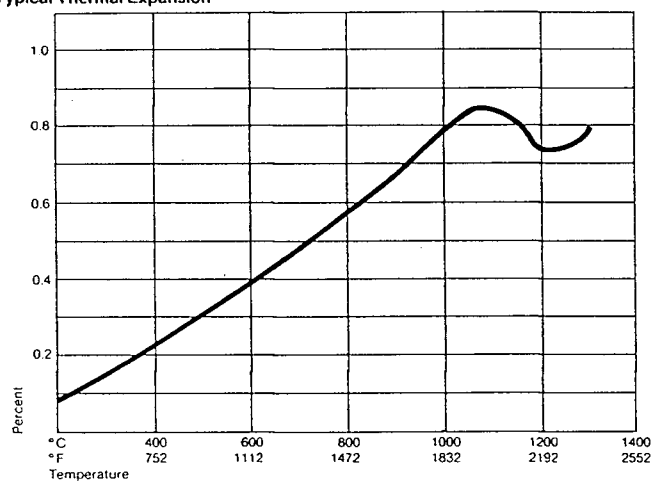
Typical Thermal Expansion



Typical Chemical Analysis (%)

ZrO ₂	36.4
Al ₂ O ₃	47.8
SiO ₂	14.0
B ₂ O ₃	0.2
Na ₂ O	1.1
Fe ₂ O ₃	0.1
TiO ₂	0.1
Other	0.3

Figure 2.2. Thermal conductivity, thermal expansion and typical composition of Monofrax-S(AZS-CS4)¹.

Technical Data**Typical Thermal Conductivity****Typical Thermal Expansion****Typical Chemical Analysis (%)**

ZrO ₂	39.5
Al ₂ O ₃	45.8
SiO ₂	12.9
B ₂ O ₃	0.2
Na ₂ O	1.1
Fe ₂ O ₃	0.1
Other	0.4

Figure 2.3. Thermal conductivity, thermal expansion and typical composition of Monofrax-S(AZS-CS5)¹.

The solidified structure of Monofrax-S has been described earlier as a complex fine-grained composite of crystalline zirconia and alumina in a glassy matrix¹. Hence, the solidification sequence for this material is expected to be complex. Nevertheless, from the Al_2O_3 - ZrO_2 - SiO_2 ternary phase diagram, Figure 2.4²⁴, it should be possible to tentatively establish the sequence starting with the material in a liquid state. On cooling the first material to precipitate is ZrO_2 at approximately 1810°C - the liquidus temperature - followed by Al_2O_3 , and then finally $3\text{Al}_2\text{O}_3$ - 2SiO_2 would precipitate at the solidus temperature (approximately 1780°C). Presumably any liquid remaining below the solidus temperature cools to form the glassy matrix. (In this sequence of events, the solidus is defined as the point at which latent heat ceases to be released on cooling. Strictly speaking glasses maintain a liquid-like structure when they are solid and hence do not release any latent heat associated with crystallization²⁵. This then, could lead to the presence of liquid material below the so-called solidus temperature.) As the glassy phase cools its viscosity increases to a point where it behaves more like a solid than a liquid. Based on recommended service temperatures, this transition would be expected to occur in the vicinity of 1650°C .

Some aspects of the thermomechanical behaviour of Monofrax-S have been examined by Chan and Nicolson². Effective fracture toughness values for Monofrax-S (AZS) and α - Al_2O_3 fused cast refractories have been determined as a function of temperature and are reproduced in Figure 2.5² (constant elastic moduli of $1.29(10^{11})\text{N/m}^2$ for Monofrax-S and $2.95(10^{11})\text{N/m}^2$ for α - Al_2O_3 have been assumed for the calculation of stress intensity factor). For Monofrax-S an increase in the fracture toughness can be seen as the glass phase begins to soften around 400°C followed by a maximum at about 650°C . At temperatures above 650°C the fracture toughness rapidly decreases as the glassy phase loses strength becoming more

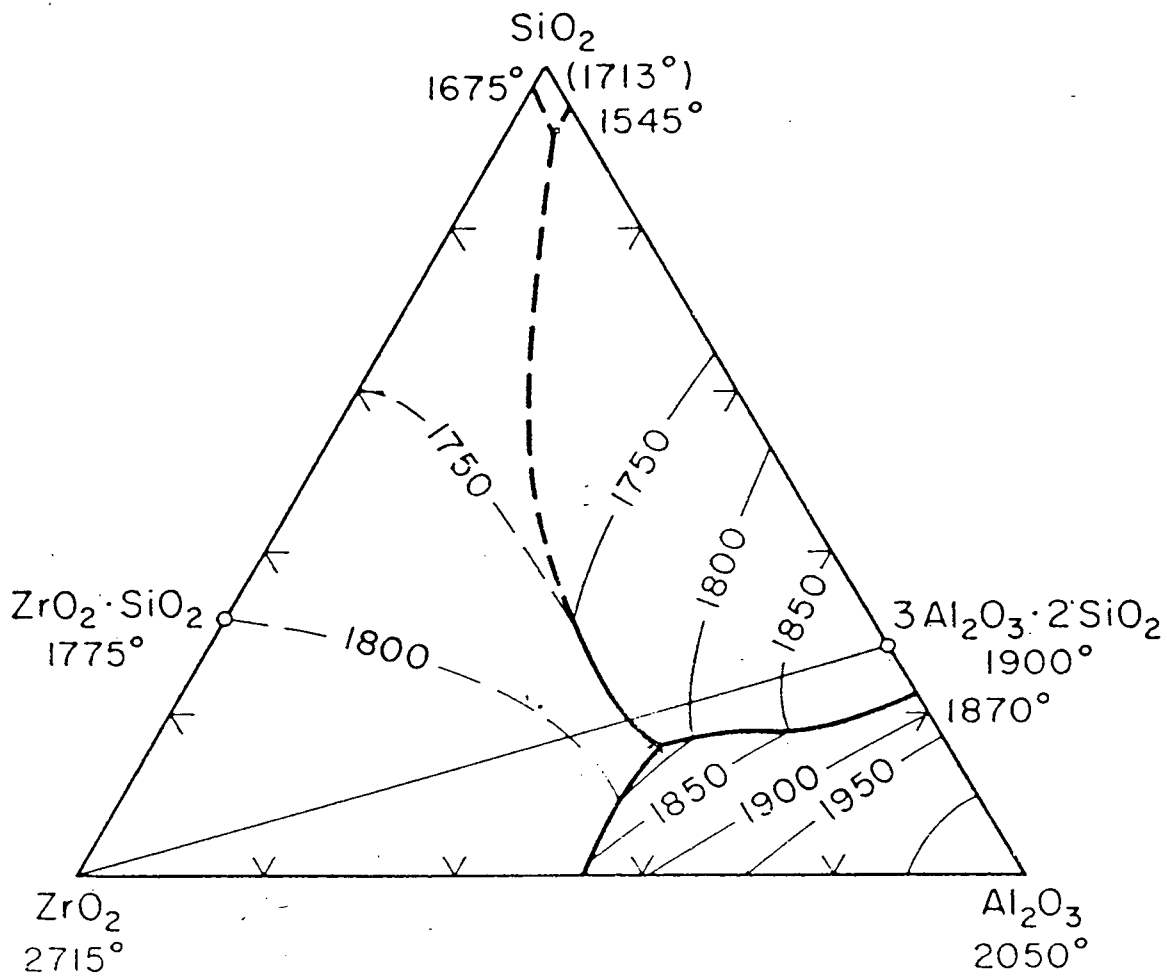
$\text{Al}_2\text{O}_3\text{-SiO}_2\text{-ZrO}_2$


Figure 2.4. Alumina-Zirconia-Silica phase diagram²⁴.

liquid like. Microstructural examination of a specimen tested at 1000°C is reported to indicate that the fracture occurs entirely by tearing of the glassy phase². On the basis of this evidence, it is clear that the viscoelastic behaviour of Monofrax-S will have a significant influence on the generation of stresses during the solidification process.

A review of the literature has revealed several potential sources for the tensile stresses in Monofrax-S refractories. The elimination of the cracking problem requires an understanding of the development of stress during solidification and throughout the subsequent cooling period. This can only be achieved with a mathematical model which simulates the flow of heat and generation of stress.

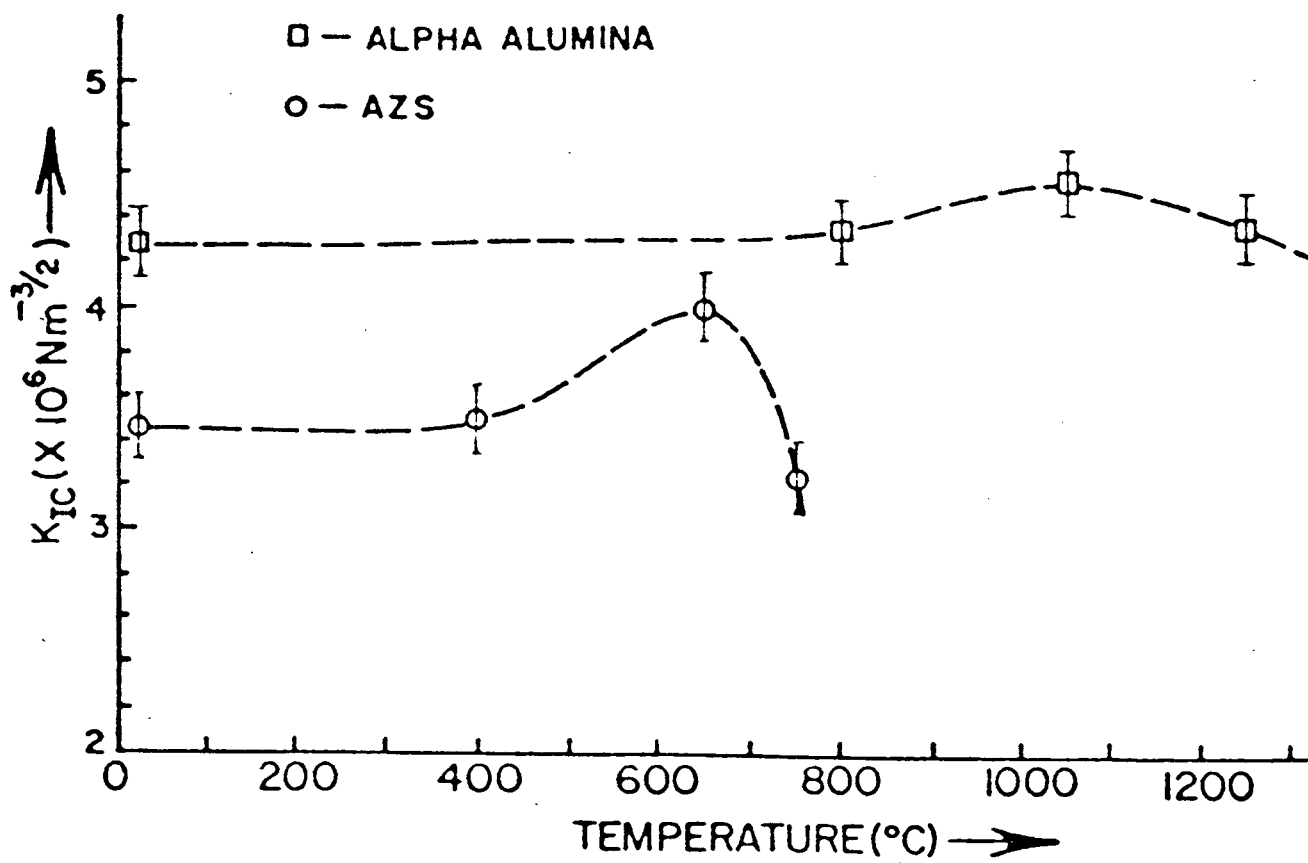


Figure 2.5. Fracture toughness of fused cast Monofrax-S and α -Alumina vs. temperature².

CHAPTER 3

SCOPE AND OBJECTIVES

3.1 Scope of the Research Programme

A major thrust of this research was the development of a mathematical model capable of calculating the temperature distribution and stresses generated during the solidification and subsequent cooling of Epic-3 Monofrax-S castings. Once developed and properly supported by industrial measurements, the mathematical model has been employed as a tool for both understanding how the cracks form in the castings and prescribing means for production of defect-free fused cast blocks.

Variations of the approach adopted for this work have been applied successfully by others in the investigation of crack formation in the direct chill casting of zinc-jumbos¹⁶, the continuous casting of steel¹⁷⁻¹⁹ and the static casting of steel ingots^{20,23}. As previously outlined, the principal focus of the work has been to develop a heat-flow/stress generation model of the Monofrax-S casting process. The numerical techniques that have been employed in the mathematical model are still relatively new and comprise important areas of research in their own right.

The geometric aspects of the problem dictate a three-dimensional analysis in order to calculate the stresses which give rise to both longitudinal and transverse cracks - Types-B and A respectively. The heat flow analysis has had to be transient in order to be capable of predicting the thermal field as a function of time. Moreover, owing to the fact that heat is extracted from the exterior surface of the mould the thermal model has had to calculate the temperature distribution in the bonded sand mould and annealing sand as well as in the

refractory itself - see Figure 1.3 mould/flasking lay-up for Epic-3 casting. A time-independent elastic formulation has been chosen for the stress model despite evidence² which indicates that Monofrax-S is capable of behaving in a time-dependent, visco-elastic manner at elevated temperatures. The simpler elastic analysis has been capable of qualitatively predicting stresses and meeting the objectives of this research programme as outlined previously. The stress analysis, in contrast to the thermal analysis, has been limited to the Monofrax-S refractory alone.

Following Thomas et al.^{22,23}, versions of the finite element technique (traditionally used for the stress analysis of structures) have been adopted for both the heat-flow model and uncoupled stress model. (An uncoupled formulation may be employed in this case since casting processes are dominated by sensible heat evolution. Any heat associated with deformation is insignificant in comparison.) The choice of the finite element technique over the more cost effective finite difference technique²⁶⁻²⁸ allows for a more direct input of the thermal model results into the stress model. In addition, the finite element method is more general in its formulation and hence is more easily applied to different shapes.

As mentioned earlier, a good understanding of the high-temperature behaviour of this ceramic material is necessary to formulate crack formation mechanisms. Owing to a paucity of this information in the literature, most of the input parameters for the thermal and stress model have had to be evaluated. This was accomplished in a parallel programme for thermo-physical and thermomechanical property determination initiated at Carborundum. This programme has focused on those data necessary for the time-dependent heat flow analysis and elastic stress analysis. In order to expedite the evaluation process most of the work has had to be contracted to independent research laboratories (this data will be presented later in Chapter 6).

The mathematical models described thus far are computationally intensive and expensive to run. Consequently, selection of an accurate and efficient numerical formulation and optimization of the resulting computer code were priorities. Thomas et al.²⁶ have compared numerical techniques for the solution of complex, two-dimensional, transient heat conduction problems involving a phase change. Of the methods tested, the Dupont²⁹ - Matrix³⁰ formulation with a lumped boundary condition coupled with the Lemmon³¹ latent-heat technique was found to have the best accuracy and stability. (Two problems^{32,33} for which analytical solutions are available were analyzed and served as a basis for assessing the accuracy of the numerical techniques tested.) Based on their findings, the two and three-dimensional formulations employed for model development have utilized the Dupont²⁹ time-stepping technique and the Lemmon latent-heat formulation. The details of the formulation of the heat conduction model are presented later in Chapter 5.

Optimization of the elastic stress formulation also figured importantly in development of the stress model described in Chapter 5. In addition, three dimensional stress analysis problems can often be reduced to more tractable two dimensional problems by recognizing that the essential aspects of the geometry and the loading require only two independent coordinates. For example, a two-dimensional heat-flow/plane stress analysis in a transverse quarter section can be applied to the region where Type-B longitudinal cracks are observed²³ - see Figure 1.2. Wherever possible, this approach has been adopted to minimize the computational severity of the analysis. The application of the mathematical models to the Epic-3 casting process is presented in detail in Chapter 6.

Once formulated, coded and debugged, the models were validated. In this procedure, analytical solutions³²⁻³⁴ to simplified problems were employed to validate the basic model formulation and coding for the two and three-dimensional heat transfer and stress generation

models - details are presented in Chapter 5. In addition, formulation of the heat transfer model was validated by comparison to industrial plant data. Thermocouples embedded in the mould at key locations - including close to the mould/refractory interface - were used to obtain local thermal histories. The temperatures have been recorded commencing with the pour and continuing until solidification was completed and the block was ready to be removed from the mould. As well as being necessary for model validation, these measurements were vital to check assumptions made in formulating the boundary conditions at the mould/refractory interface. The experimental procedure, equipment and results are discussed in detail in Chapter 4. The heat transfer model has been validated by comparing the predicted and measured thermal histories. Results of the comparison are presented in Chapter 6.

Having validated the thermal model, computer runs were then made with the stress model. The three-dimensional stress distributions predicted have been examined carefully in order to link regions of tensile stress with the locations of cracks observed in the actual castings. By following this procedure for the different crack types (longitudinal and transverse) a picture of how stresses are generated has been constructed. These findings have also been compared to the statistical correlations between crack type and process variables, and to the results of a microstructural examination of crack surface morphology which appear in the Epic-3 Monofrax-S crack survey study⁸ (previously outlined). At this stage, the results of the computer analysis and the crack survey report have been combined to formulate mechanisms for the formation of the various crack types. Measures to eliminate the cracks have then become evident and a modified mould design has been proposed. Finally, a computer run has been made to verify the impact of manipulation of mould heat fluxes. The results of the three-dimensional stress analysis as well as the model design analysis are presented in Chapter 7.

3.2 Objectives of the Research Programme

The objectives of this research programme can be summarized as follows:

- [1] To formulate, develop and verify a mathematical computer model capable of computing the transient thermal field and stress field in solidifying Epic-3 Monofrax-S blocks.
- [2] To calculate the temperature and stress distributions in solidifying blocks under typical process conditions which have led to the formation of the various crack types.
- [3] To develop mechanisms for crack formation based on links between the computer predictions and the comprehensive crack data base.
- [4] To formulate measures to eliminate the different cracks based on the mechanisms of crack formation.

All of the above objectives have been met.

CHAPTER 4

INDUSTRIAL MEASUREMENTS

As outlined in the Chapter 3, an industrial trial was conducted at the Monofrax Plant in Falconer, New York to collect in-mould temperature profiles for an Epic-3 casting commencing with the pour and continuing through the normal cooling period. Once collected, this data was then employed to validate the two- and three-dimensional heat-transfer models. Owing to the fact that the in-mould temperature data could also serve as a guide in the numerical formulation of boundary conditions (particularly those which describe the refractory/mould interface), the in-plant trial was conducted early in the research programme prior to completion of the mathematical models.

4.1 Experimental Technique

As described earlier, the experimental technique was relatively straightforward and involved instrumenting a 1220 x 254 x 457 mm (48 x 10 x 18in) Epic-3 mould with thermocouples. The thermocouples were strategically placed in key locations bearing in mind the following objectives: firstly, to collect a representative sample of the temperature distribution in the mould; and secondly, to investigate the heat transfer behaviour of the refractory/mould interface. In order to simplify the installation of the thermocouples, the mould was kept free of graphite chills which are often placed at various locations in or around the bonded sand mould to provide structural strength and suppress bulging in the casting. This difference will have to be kept in mind when bringing to bear the results of the statistical crack survey. Unfortunately, in the survey, the presence or absence of graphite chills was not documented.

Based on a review of the literature³³, preliminary analysis with a crude heat-transfer model and some preliminary thermocouple trials conducted at Carborundum, a combination

of Type-B, Platinum-6% Rhodium vs. Platinum-30% Rhodium, and Type-K, Nickel-Chromium vs. Nickel-Aluminum, thermocouples were selected. The Type-B thermocouples were chosen for those areas close to the mould/refractory interface owing to their ability to withstand brief exposures to temperatures in the vicinity of 1800°C under mildly oxidizing conditions³³. For locations where the temperature would be lower (distances greater than or equal to 51mm(2in), from the refractory face) less expensive Type-K thermocouples were selected. These thermocouples are capable of withstanding temperatures up to approximately 1350°C under slightly oxidizing conditions and have a higher mV output than the Type-B thermocouples (0-13.814mV Type-B, -6.458 to 54.875mV Type-K³³).

A total of 60 thermocouples were installed for the purpose of mould instrumentation - 12 Type-B and 48 Type-K. The assembly method essentially involved placing groups of thermocouples at varying heights in between additions of annealing sand - see Figure 4.1. The following is a description of the strategy employed for thermocouple placement.

Referring to Figure 4.1, the two groups of thermocouples inserted in the base of the casting were located 89mm(3.5in) and 203mm(8in) below the bottom surface of the refractory and consisted of two thermocouples each. One of the two thermocouples was located at the vertical centre-line of the casting; the second was displaced 102mm(4in) from the centre-line in a direction parallel to the broad-face. The remaining transverse groups each contained a total of either four or six thermocouples - see plan view in Figure 4.1 which illustrates thermocouple positioning for groups containing six thermocouples. The planar groups were stacked in a repetitive pattern of first four then six thermocouples in an alternating fashion. In those groups containing four thermocouples, one was placed in the mould 51mm(2.0in) from the narrow-face of the refractory and three were placed in the mould,

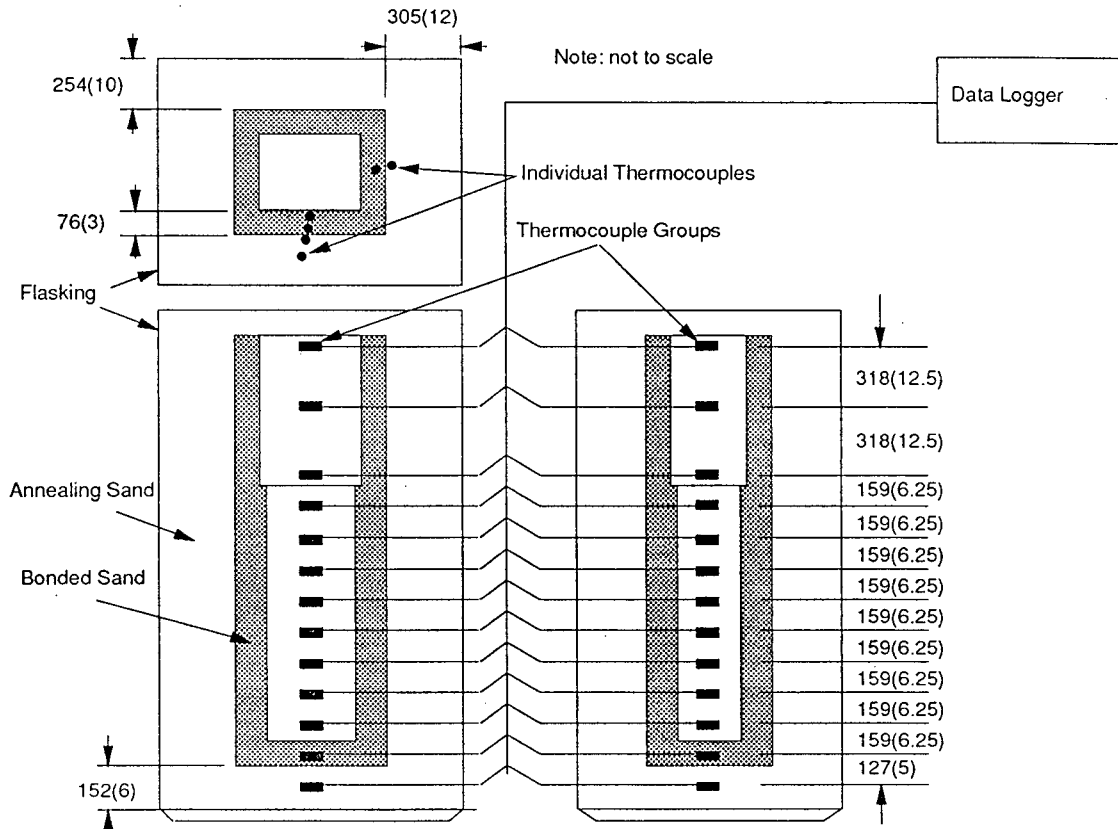


Figure 4.1. Schematic diagram illustrating thermocouple placement in Epic-3 mould.

Note: units are mm(inches).

51(2.0), 89(3.5) and 203mm(8.0in) respectively, from the broad-face. For the groups containing a total of six thermocouples, two were placed in the mould, 13(0.5) and 51mm(2.0in) respectively, from the narrow-face of the refractory and four were placed in the mould adjacent to the broad-face (these four thermocouples were placed either, 13(0.5), 51(2.0), 89(3.5) and 203mm(8.0in) respectively, or 6.4(0.25), 51(2.0), 89(3.5) and 203mm(8.0in) respectively, from the refractory face - this pattern repeated itself every four layers). Finally, two thermocouples were inserted into the mould at roughly mid-height in order to study heat

transfer at the refractory/mould interface. These Type-B thermocouples were placed at the inside surface of the bonded sand mould, on the broad-face, displaced approximately 13mm(0.5in) from the vertical centre-line of the face.

As a final step, during mould assembly, the location of all mould seams was recorded. At Falconer, the silica boards which make up the sides of the bonded sand mould are glued together to provide the necessary height. The result is a glue joint which runs in a transverse orientation, often at about mid-height. During casting, there can be intrusion of liquid Monofrax-S into this joint.

4.2 Experimental Procedure

Once fully instrumented, the next step involved recording the voltage output of the thermocouples in the mould over the course of the casting sequence. The procedure was straightforward. Approximately five minutes prior to pouring, the programmable data logger was switched on to begin recording data which was sampled periodically and stored throughout the first pour, re-pour and subsequent cooling over a period approximately nine days.

The capability of the programmable data logger to sample and record the thermocouple output periodically was critical to reduce the amount of data collected to a manageable volume (it can take up to 10 days for an Epic-3 casting to fully cool). Initially, the data logger was programmed to scan and store the thermocouple data every five seconds to better resolve the rapid temperature increase occurring in the mould close to the mould/refractory interface when the molten refractory first contacts the mould. The scan interval was later decreased in stages throughout the cooling period- see Table 4.1 for scan frequency and times of shift in scan frequency.

TABLE 4.1
Times at which Data Logger Scan Frequency was Shifted

Data Logger Scan Frequency (sec)	Scan Interval Start Time (days:hrs:mins:sec)
5.0	0:0:0:0
15.0	0:2:22:14
30.0	0:8:24:45
60.0	0:16:36:03
300.0	1:8:36:19
600.0	6:6:36:19

To permit a comparison between the model predictions and the plant data, the initial pour temperature and ambient air temperature were measured and recorded for later input to the model. Obtaining an accurate value for the pour temperature proved to be difficult owing to the high temperatures involved. The only option available at the time was a hand-held, single-colour optical pyrometer. An estimate of the pour stream temperature was obtained by pointing the optical pyrometer directly at the molten stream as it issued from the furnace.

In addition to monitoring the initial pour, the re-pour time and temperature also were measured and recorded. In the re-pour, the casting is re-positioned under the furnace pour-spout after it has been permitted to cool for a while in order that the shrinkage cavity may be filled with liquid. The top of the casting is normally rammed several times with a steel bar

prior to pouring to better access the shrinkage cavity. The re-pour may be scheduled anywhere from one to two hours after the original pour. The technique for recording the re-pour temperature was identical to that employed for measuring the initial pour data.

Finally, once the casting was fully cooled, the refractory was carefully removed from the mould and checked for cracks. The procedure involved removing the mild steel flasking - refer to Figure 1.3 for mould/flasking lay-up. Any annealing or bonded sand remaining after removal of the flasking then was carefully detached from the solidified refractory while checking for evidence of fusion between the sand and the refractory. Once removed, an autopsy was performed on the refractory to reveal the extent of the cracking. The autopsy included recording the location of surface and internal cracks. The location of the internal cracks was established by sectioning the refractory.

4.3 Results

The results of the industrial trial are presented below in four subsections: initial conditions, re-pour data, temperature responses and post-cast refractory autopsy.

4.3.1 Initial Conditions

The ambient air temperatures recorded over the course of the casting sequence are presented in Table 4.2. The air temperature ranged from a low of 17.8°C to a high of 26.8°C with an average value of 22.2°C (standard deviation of 2.8°C). During the pour, an air temperature of 24.5°C was recorded and serves as the initial condition for the mould and surrounding air. Using the hand-held, single-colour optical pyrometer the pour stream temperature was recorded as it issued from the furnace and is presented in Table 4.3. An average value of 1875°C (standard deviation 7.0°C) serves as an estimate of the initial pour temperature. The accuracy of the pyrometer has not been formally assessed and the emissivity of Monofrax-S

was assumed to be equal to 1^{34} .

TABLE 4.2
Ambient Air Temperature Measurements

Temperature (°C)	Elapsed Time (days:hrs:mins:sec)
24.5	0:0:0:0
26.8	0:0:11:0
24.8	0:0:29:0
23.4	0:20:42:0
24.7	1:21:07:0
17.8	3:0:25:0
20.4	3:1:27:0
20.4	3:2:25:0
20.4	4:4:4:0
18.5	5:8:11:0
24.0	5:21:7:0
20.4	6:8:0:0
Average 22.2°C Standard Deviation 2.8°C	

TABLE 4.3
Pour Stream Temperature Measurements (Initial Pour)

Temperature (°C)	Elapsed Time (days:hrs:mins:sec)
1870 1880	0:0:0:0
Average 1875°C Standard Deviation 7.0°C	

4.3.2 Re-pour Data

The re-pour was carried out 1 hr: 43 mins after the initial pour was complete. Based on the optical pyrometer measurement, the pour stream was estimated to be 1870°C. Only one measurement was taken.

TABLE 4.4

Pour Stream Temperature Measurements (Initial Re-pour)

Temperature (°C)	Elapsed Time (days:hrs:mins:sec)
1870	0:1:43:0

4.3.3 In-Mould Temperature Responses

Once collected and stored, the thermocouple voltage data was processed at UBC to yield in-mould temperature responses. Unfortunately, after processing, it was apparent that there were problems with a significant amount of the data collected. Of the 60 thermocouples installed, 2 failed completely, 7 yielded completely nonsensical output, 18 gave marginal output and 33 provided good, or reasonable, output. (Nonsensical output was characterized by continuous, rapid fluctuations in mV output clearly unrelated to any physical phenomena. Marginal output, in contrast, was characterized by intermittent periods of rapid fluctuations in voltage output mixed with periods of more reasonable response). Further investigation traced the source of the problem to faulty hook-up of the thermocouple leads to the data logger input boards. Fortunately, from the 33 thermocouples that performed well, it was possible to construct an adequate picture of the thermal behaviour of most of an Epic-3 mould with the exception of a region directly below the base of the refractory. Problems encountered

with the thermocouples located in this region resulted in useless data. Nonetheless, overall, sufficient data was obtained to permit the two- and three-dimensional heat transfer models to be verified.

A sampling of thermocouple temperature responses is presented in Figures 4.2-4.8.

From a close inspection of all of the data collected a few key observations have been made:

- [1] In general, the temperature responses show an initial rapid increase in temperature associated with the arrival of the heat pulse from the hot refractory casting followed by a relatively slow decline in temperature as the entire mould cools - see example of typical in-mould temperature responses up to 1.6 and 24 hours elapsed time presented in Figure 4.2 and 4.3-4.8, respectively. As would be anticipated, the rate of increase in temperature and peak temperature attained are both inversely related to distance from the refractory/mould interface.
- [2] From a comparison of in-mould temperatures obtained with thermocouples located 705(27.7) and 1181mm(46.5in) above the base of the refractory (89mm(3.5in) from the broad face) it is apparent that there is little or no axial temperature gradient in a zone at mid-height in the mould - see Figure 4.4. This indicates that heat flows predominantly in the two-dimensional transverse plane over the corresponding mid-height zone in the refractory. The extent of this zone has been established by plotting the temperature 51mm(2in) from the broad-face as a function of vertical distance from the base of the refractory at 15 hrs elapsed time. The results, presented in Figure 4.9, indicate that the region of two-dimensional heat transfer extends over about the middle two-thirds of the refractory. Below 762mm(30in) and above 1397mm(55in) axial heat flow becomes a factor. A two-dimensional heat-transfer model orientated in the transverse plane should be capable of simulating the thermal behaviour within this zone.

- [3] There appears to be a significant difference between the in-mould temperature distributions adjacent to the broad and narrow faces of the refractory. Referring to Figure 4.5, within two hours, the in-mould temperature adjacent to the broad face is significantly hotter than the equivalent position adjacent to the narrow face (the thermocouples are located 50.8mm(2.0in) from each face). The temperature difference increases to a maximum value of 100°C at approximately four hours. These measurements indicate a difference in the rate of supply and/or removal of heat from the mould adjacent to the minor and major faces of the refractory. A comparison of the relative thickness of annealing sand (mould insulation) adjacent to each of the faces suggests that the opposite behaviour would be expected. (There is 305mm(12in) of annealing sand adjacent to the narrow face as compared to 254mm(10in) for the broad-face - see Figure 1.3, Chapter 1, mould/flasking lay-up.) However, the fact that this temperature difference arises within the first two hours indicates that this behaviour is not related to the relative amount (thickness) of insulating material. Plotting the variation in temperature with distance from the broad face at various elapsed times, Figure 4.10, reveals that the heat-pulse has not reached the exterior surface within 2 hrs elapsed. The difference in temperature must therefore be tied to the supply of heat. It is conceivable that a larger gap could open up between the narrow-face mould and the refractory. The effect of this would be to reduce the supply of heat to the mould adjacent to the narrow-face which would result in a lower mould temperature. Alternately, the lower mould temperature could be tied to the cross-sectional geometry of the block. This question will be addressed later in the thesis in Chapter 6 where model predictions are presented.
- [4] The in-mould temperature response of a thermocouple 51mm(2in) from the header 1657mm(65in) above the base of the refractory is presented in Figure 4.8. The temperature response of thermocouples 70mm(2.7in) and 705mm(27.8in) above the refractory

base have also been presented to help elucidate the effect of the re-pour on the temperature response. The results suggest that the effect of the re-pour is to narrow the peak and to increase the peak temperature attained. At slightly over 2hrs elapsed time there is a perceptible increase in the slope of the temperature response adjacent to the header. This is consistent with the arrival of the heat-pulse from the re-pour at 1hr:43mins elapsed time.

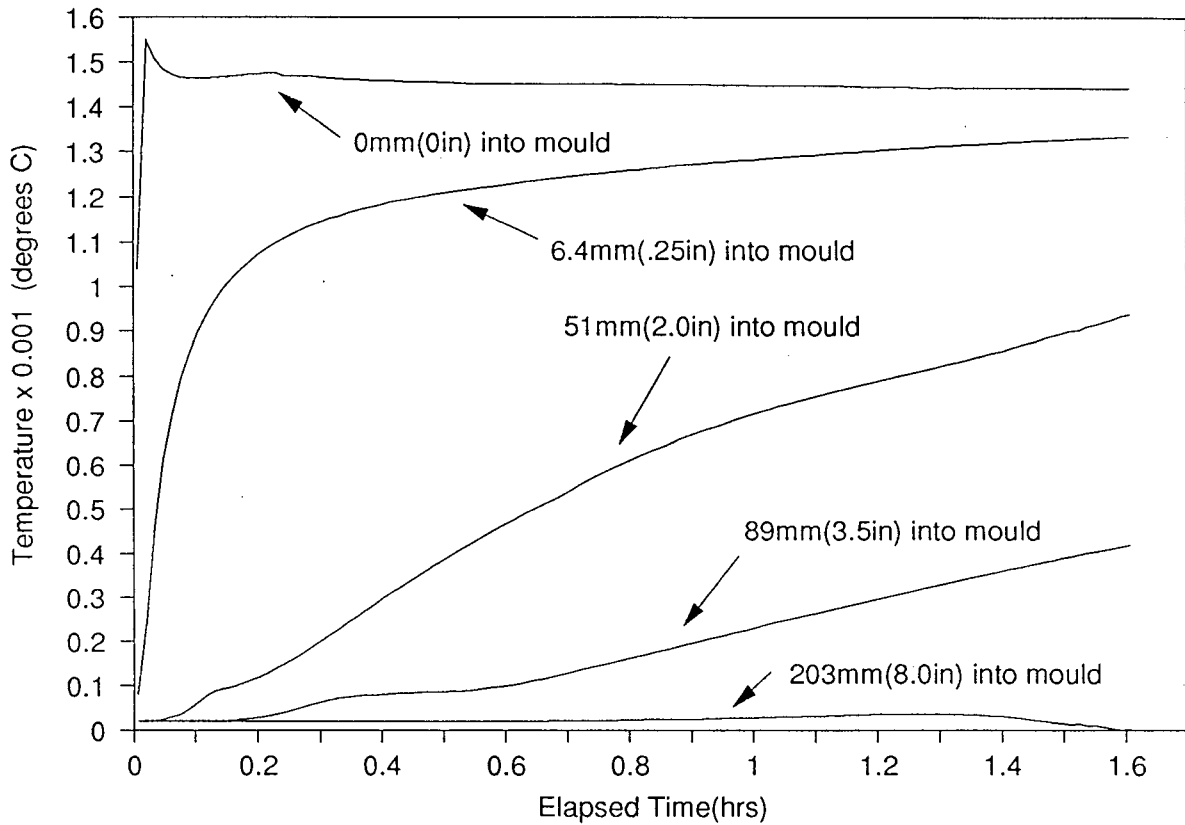


Figure 4.2. In-mould temperature response from thermocouples adjacent to the broad face located 1181mm(46.5in) above the base of the refractory. Note: distances are measured from the refractory/mould interface.

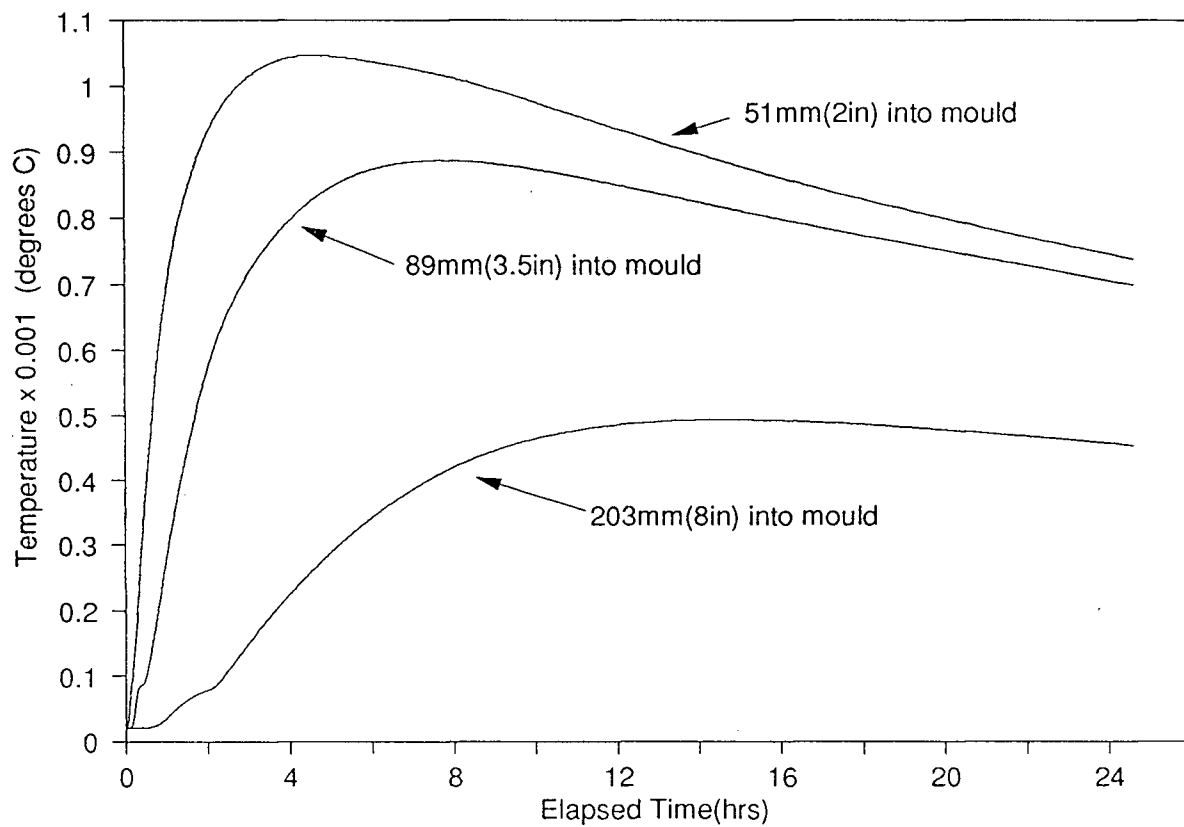


Figure 4.3 In-mould temperature response from thermocouples adjacent to the broad face located 705mm(27.8in) above the base of the refractory. Note: distances are measured from the refractory/mould interface.

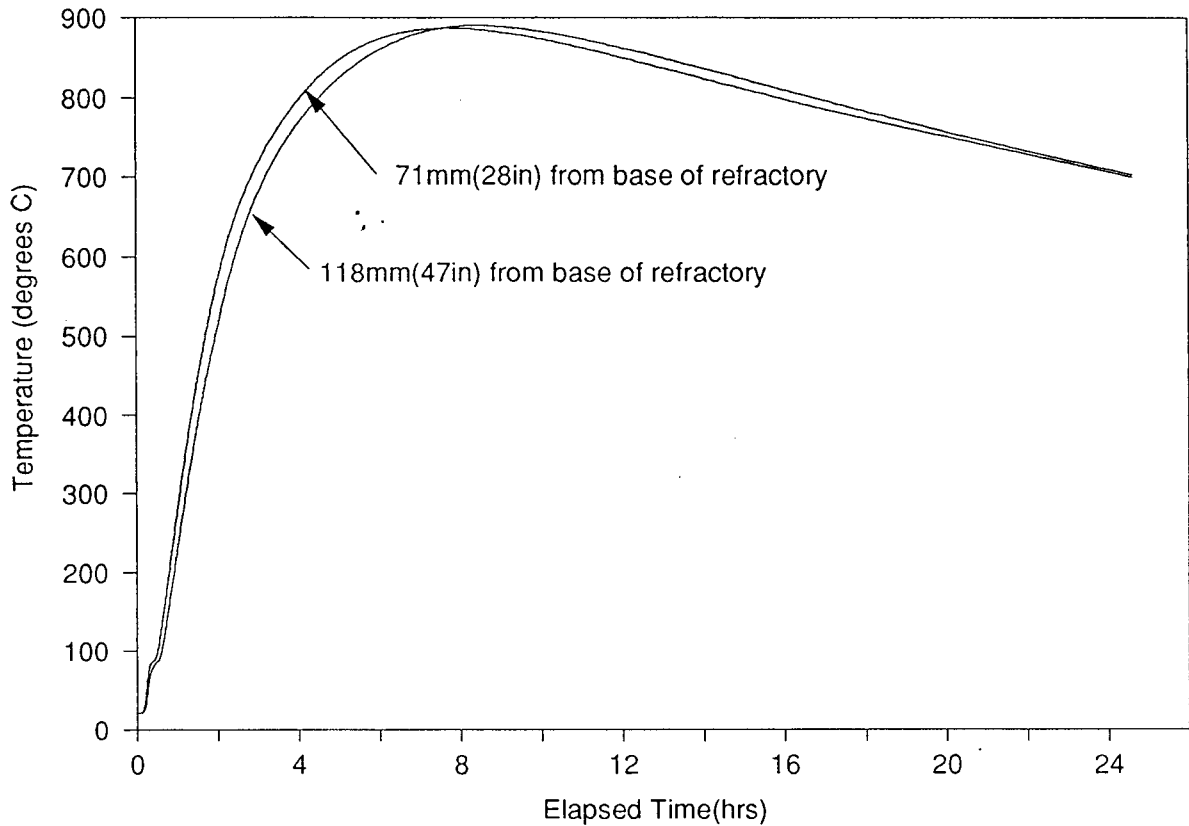


Figure 4.4. In-mould temperature response from thermocouples adjacent to the broad face located 705(27.8) and 1181mm(46.5in) above the base of the refractory, 51mm(2.0in) from the refractory/mould interface.

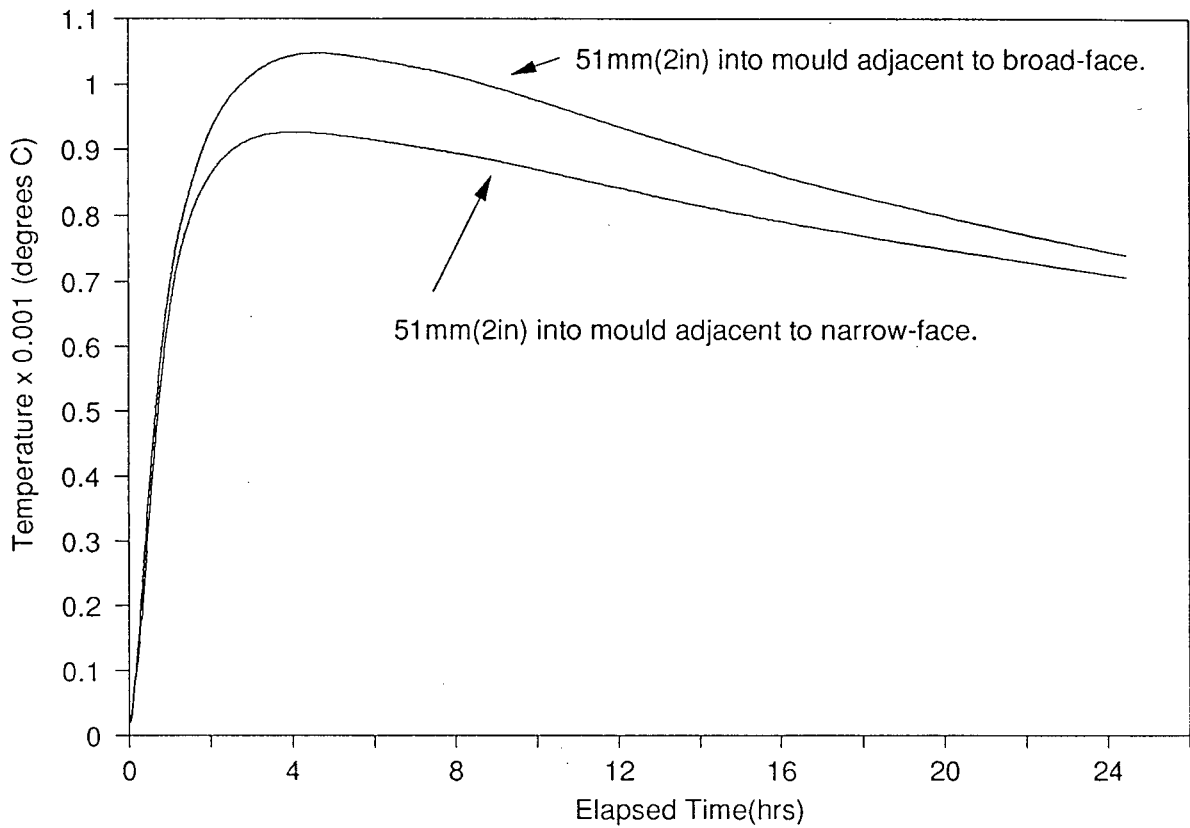


Figure 4.5. In-mould temperature response from thermocouples adjacent to the broad and narrow faces located 705mm(27.8in) above the base of the refractory, 51mm(2.0in) from the refractory/mould interfaces.

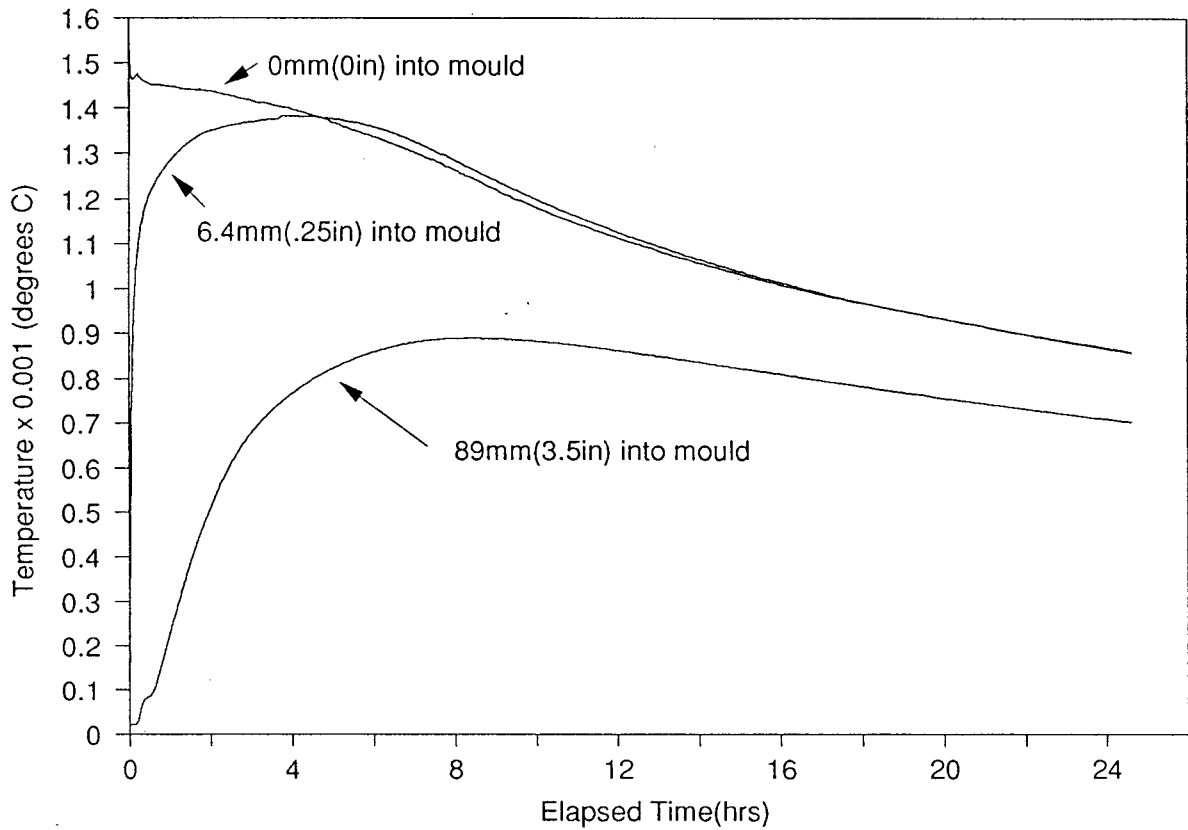


Figure 4.6. In-mould temperature response from thermocouples adjacent to the broad face located 1181mm(46.5in) above the base of the refractory. Note: distances are measured from the refractory/mould interface.

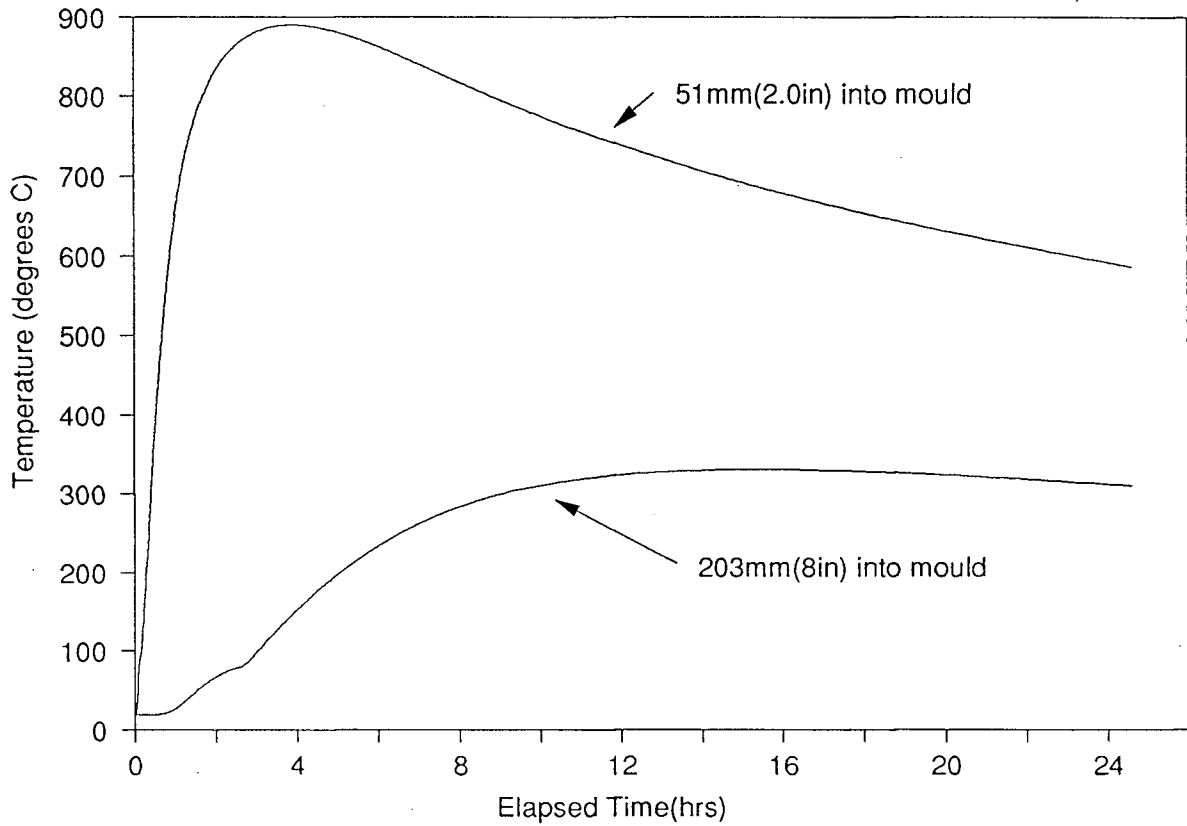


Figure 4.7. In-mould temperature response from thermocouples adjacent to broad face located 70mm(2.75in) above the base of the refractory. Note: distances are measured from the refractory/mould interface.

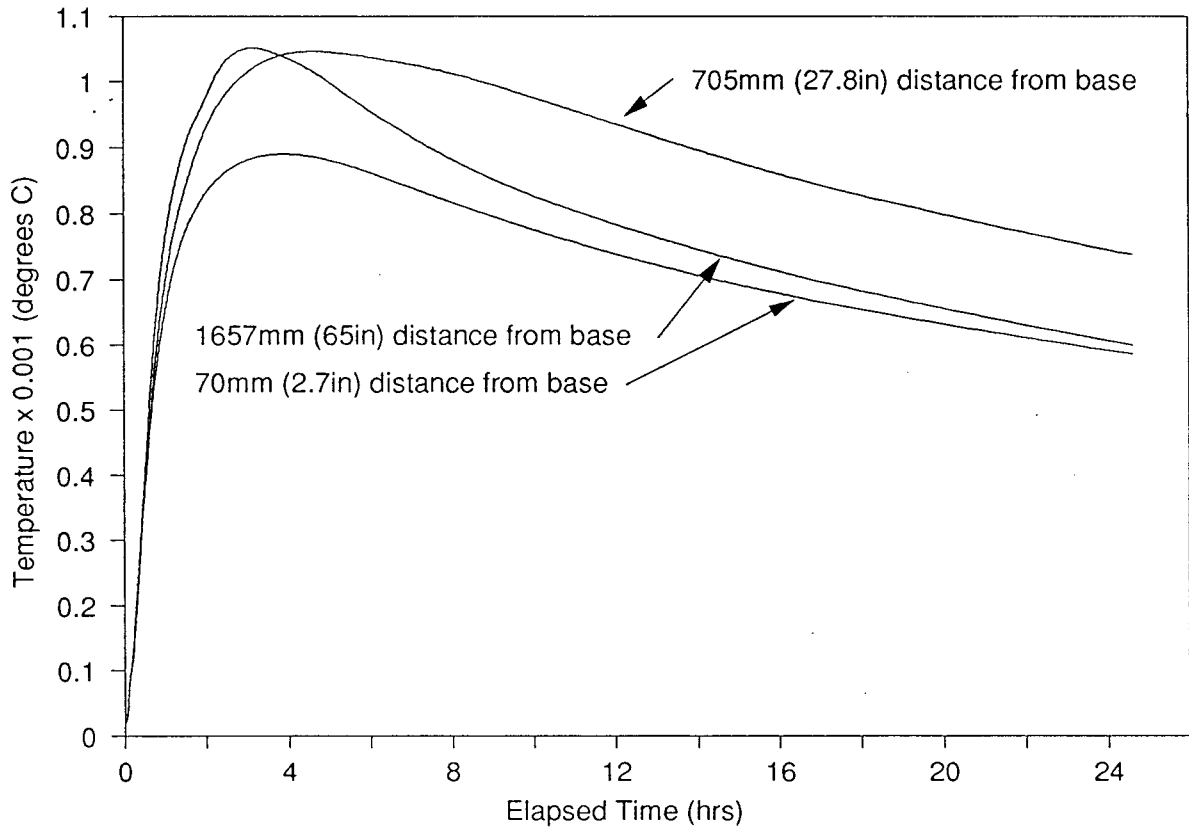


Figure 4.8. In-mould temperature response from thermocouples located 51mm(2in) from the broad face. Note: distances are measured from the base of the refractory.

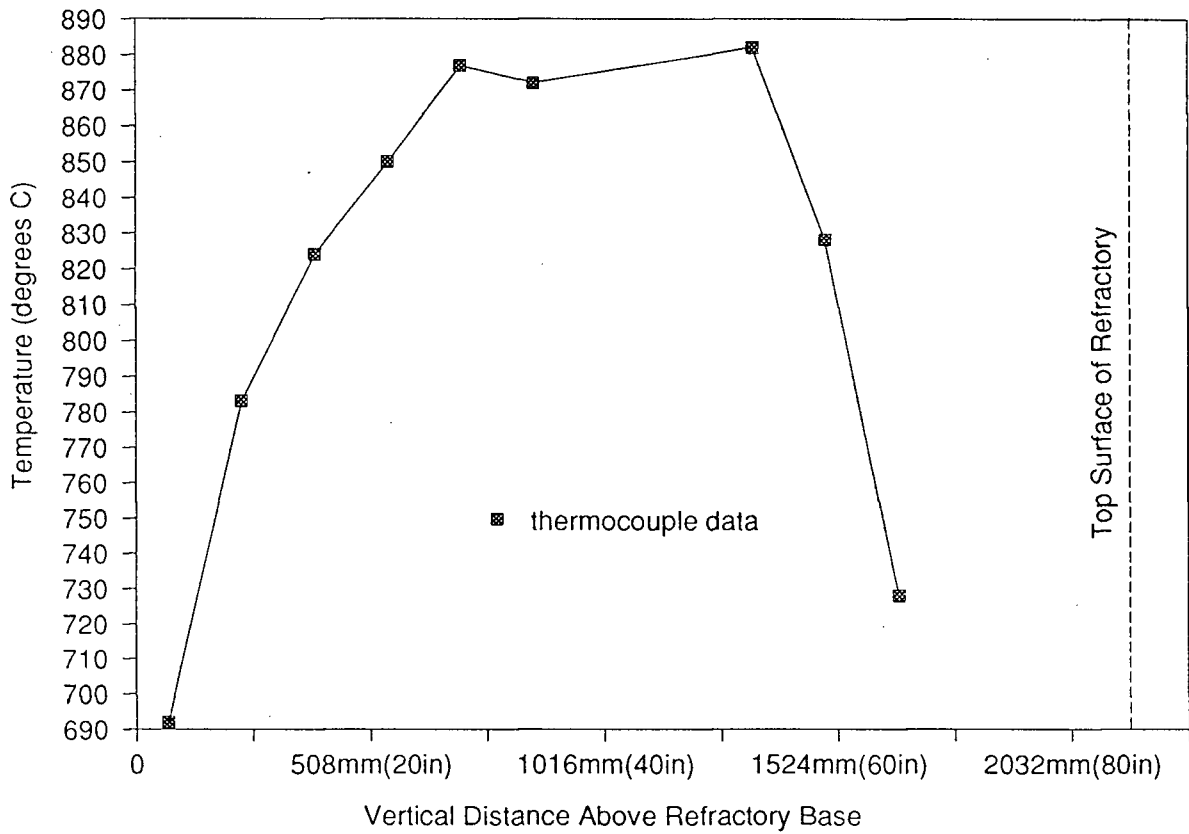


Figure 4.9. Temperature 51mm(2in) from broad face at various distances from the base of the refractory at 15hrs elapsed time.

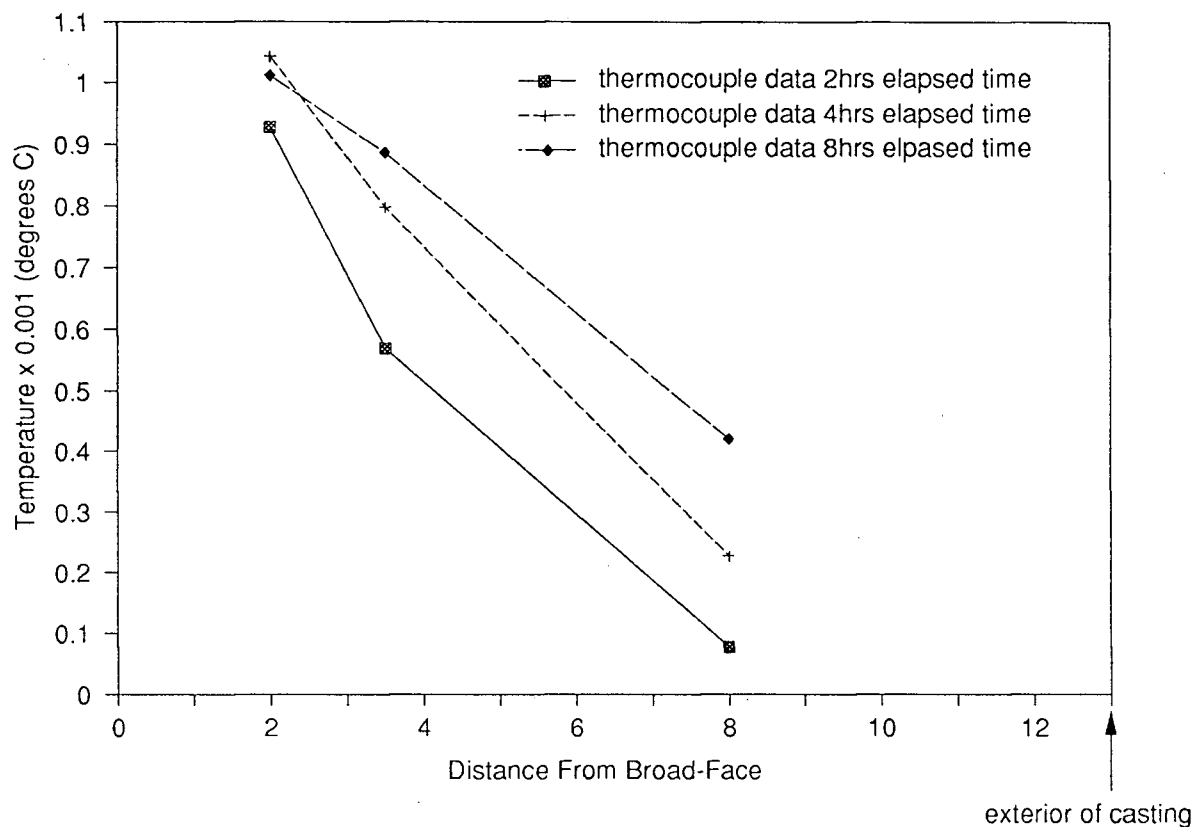


Figure 4.10. Variation in temperature with distance from broad face at 2, 4 and 8 hrs elapsed time.

4.3.4 Refractory Autopsy

The results of the casting autopsy are presented schematically in Figure 4.11. Most obvious were the three large Type-A transverse cracks in a zone at roughly mid-height of the cast block. Two of these cracks are classified as "show-through" (appearing on opposite sides) and would warrant rejection of the refractory. The third, revealed by sectioning the

block, does not intersect the surface and hence would have been missed by normal inspection practices. It is interesting to note that these three Type-A cracks lie in a zone bounded by the header ledge at the top and the mould seam at the bottom. A fourth Type-A crack was found located near the base of the refractory, Figure 4.11. In contrast to the other three Type-A cracks, the lower Type-A is limited to the surface of one face only and is significantly different in shape, tending to be more curved in profile (often Type-A cracks occurring in this region are referred to as "smiles"). Based on Walrod's study⁸ a distinction should be made between the upper and lower Type-A cracks as they are clearly different. Thus Type-A transverse cracks occurring in a zone at roughly mid-height are referred to as Type-A1, whereas, those located at the base of the refractory are designated as Type-A2. Also found on the test casting were four transverse Type-E corner cracks, shown in Figure 4.11. It should be noted that no Type-B longitudinal cracks were observed in this casting.

Finally, as mentioned previously, during refractory excavation, particular attention was paid to the material removed from the refractory/mould interface in order seek evidence of mould/refractory fusion. Unfortunately, no conclusive evidence was found in that the mould material was easily separated from the cast block and generally crumbled away.

4.4 Summary

Of the observations made from the industrial trial, there are several which are noteworthy. In particular, the asymmetry observed in the rates of heat removal from the broad and narrow faces, and the occurrence of three Type-A1 cracks in a zone between the header ledge and mould seam. Unfortunately, on their own, these observations are not sufficient to develop mechanisms for crack formation. However, when examined in conjunction with a mathematical analysis of stress generation, these observations will help to establish potential mechanisms for the generation of tensile stresses and hence cracks.

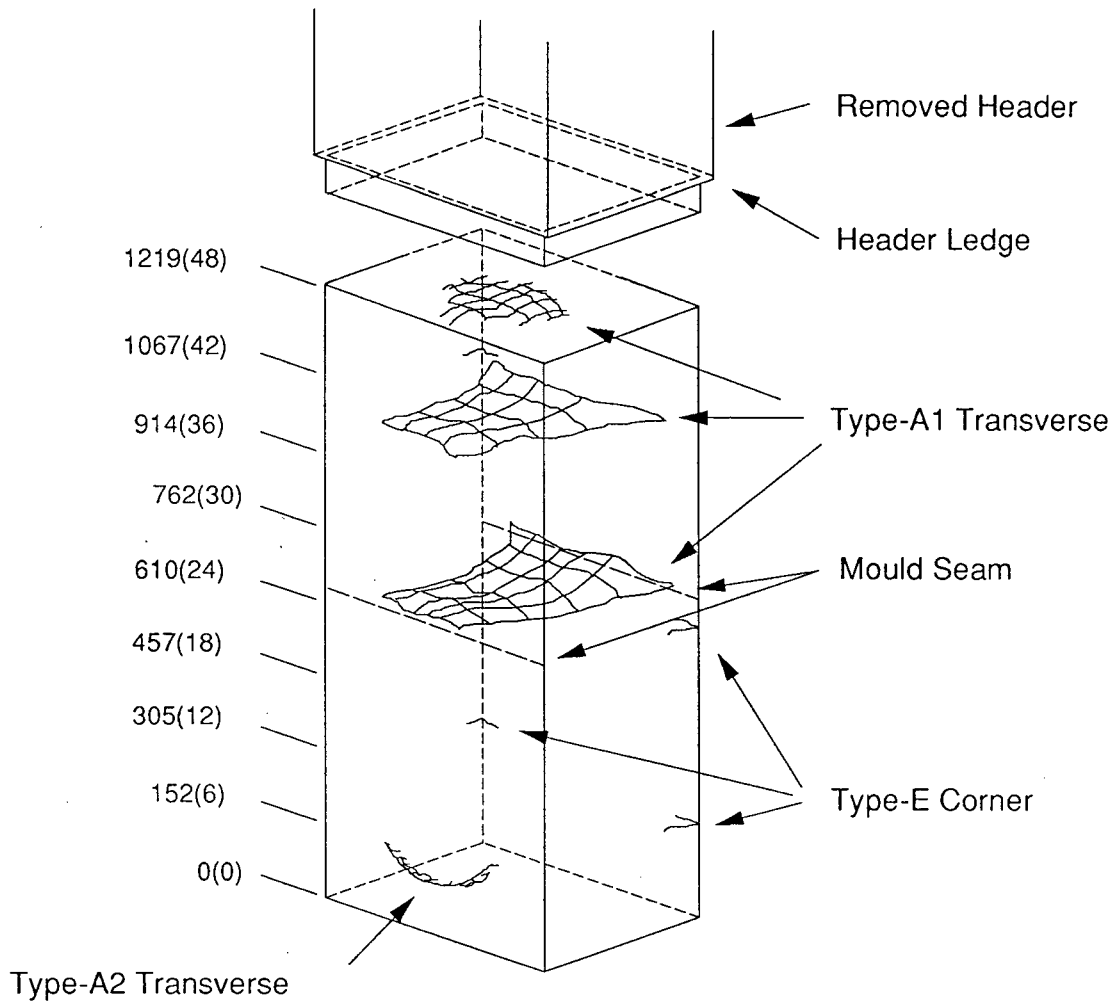


Figure 4.11. Schematic illustration of the results of the autopsy performed on the instrumented Epic-3, Monofrax-S refractory. Note: units are mm(inches).

CHAPTER 5

MATHEMATICAL MODELS

As outlined in the Chapter 3, one of the major thrusts of this research programme was to develop a heat-flow/stress generation model of the Monofrax-S casting process in order to solve the cracking problem. For the reasons outlined in the Chapter 3, the approach to be taken involves the formulation of separate, uncoupled mathematical models of heat-transfer and stress generation in two and three dimensions. The following Chapter discusses in detail the formulation of these models.

5.1 Development of Mathematical Model of Heat Flow

The finite-element technique - traditionally employed for stress analysis - has been adopted for formulation of the mathematical model of heat flow. The reasons for choosing the finite-element formulation over the more cost-effective finite-difference formulation²⁶⁻²⁸, are two-fold: firstly, employing the same numerical technique for heat-transfer as for the stress analysis permits a more direct input of the temperature distribution into the model of stress generation - the same mesh/grid may be used in both models; and secondly, it allows for a more general handling of different shapes/geometries (in an industrial setting the ability to easily handle different shapes is critical). Owing to the basic geometry of the problem, a three-dimensional heat-transfer model has been required in order to investigate the stresses which give rise to both longitudinal and transverse cracks in Monofrax-S refractories. Where appropriate, a two-dimensional analysis also has been employed in order to reduce the computational size of the problem. For example, based on the results of the industrial measurements Figures 4.4 and 4.9, a two-dimensional heat-transfer analysis would appear to be adequate for the zone at roughly mid-height in the mould.

Owing to the time-dependent nature of the process, the mathematical model has had to be transient in order to predict the temperature distribution as a function of time. Moreover, the heat-flow model has had to calculate the temperature distribution in the moulding material as well as in the refractory casting. The moulding material includes both the bonded sand mould and the surrounding annealing sand. The mild steel flasking has been neglected because its thermal resistance is negligible in comparison to the sand moulding - see Figure 1.3 mould/flasking lay-up.

5.1.1 Formulation

Based on the above description of the problem, the governing equations for two- and three-dimensional heat-flow in the refractory and surrounding mould fall into the general category of time-dependent field problems, or more precisely, "quasi-harmonic" equations with a time derivative^{35,36,37}. For the general three-dimensional case, the governing differential equation is then:

$$\frac{\partial}{\partial x} \left(k_x \frac{\partial T}{\partial x} \right) + \frac{\partial}{\partial y} \left(k_y \frac{\partial T}{\partial y} \right) + \frac{\partial}{\partial z} \left(k_z \frac{\partial T}{\partial z} \right) + Q - \rho C_p \frac{\partial T}{\partial t} = 0 \quad (5.1)$$

with the boundary conditions of the form;

$$T = \phi(x, y, z, t) \text{ on surface } S_1, \text{ for } t > 0 \quad (5.2)$$

and

$$k_x \frac{\partial T}{\partial x} n_x + k_y \frac{\partial T}{\partial y} n_y + k_z \frac{\partial T}{\partial z} n_z + q(x, y, z, t) + h(x, y, z, t)T = 0$$

on surface S_2 , for $t > 0$ (5.3)

and initial conditions;

$$T = T_o(x, y, z) \text{ in domain } \Omega, t = 0 \quad (5.4)$$

where, S_1 and S_2 represent surfaces of an arbitrary domain Ω on which the boundary conditions are imposed. The terms n_x , n_y and n_z represent the directional cosines of the normal to the surface. For the case where the material is isotropic and the thermal conductivity is independent of direction, the directional subscripts on the thermal conductivity, k , can be dropped. The approach that has been taken for solution of the problem described by equation (5.1) employs a finite-element discretization of the spatial derivatives only. The resulting system of ordinary differential equations is non-linear and is then solved by a step-by-step recurrence scheme.

5.1.1.1 Finite Element Discretization of Spatial Derivatives

The procedure for finite element discretization of the spatial derivatives is based on the assumption that within a typical element the temperature may be expressed as:

$$T^e(x, y, z) = \sum_{i=1}^n N_i(x, y, z) T_i(t) \quad (5.5)$$

where, N_i are the nodal interpolation functions and n is the total number of nodes per element. In general, the interpolation or shape functions are polynomials of a degree which is dependent on the number of nodes per element (element type). (For the purposes of discussion the form of the shape functions is left general at this time. Discussion on the selection of a specific type of element is left until the generalities have been covered.) Based on the trial expansion function, Equation (5.5), the finite element solution^[1] of Equation (5.1)

1 For a detailed discussion on the derivation of the finite element solution (application of the Galerkin criterion to the heat conduction equation) the reader is referred to a good text on the subject^{35,36,37}.

yields the following system of differential equations at the elemental level:

$$C^e \frac{dT}{dt} + K^e T + f^e = 0 \quad (5.6)$$

where,

$$K_{i_j}^e = \int_V B_i^T k B_j dV + \int_{A_2} h_i N_i N_j dA_2 \quad (5.7)$$

$$C_{i_j}^e = \int_V N_i \rho C_p N_j dV \quad (5.8)$$

$$f_i = \int_V Q N_i dV + \int_{S_2} N_j q_i dS_2 + \int_{S_2} N_j h_i T_{amb} dS_2 \quad (5.9)$$

In Equation (5.6), the K matrix is recognized as the temperature stiffness or temperature influence matrix which is, in turn, dependent on the B matrix, defined by Equations (5.10)-(5.11), and the k or thermal conductivity matrix, Equation (5.12).

$$B_i^T = \nabla^T N_i \quad (5.10)$$

$$B_j = \nabla N_j \quad (5.11)$$

$$k = \begin{pmatrix} k_x & 0 & 0 \\ 0 & k_y & 0 \\ 0 & 0 & k_z \end{pmatrix} \quad (5.12)$$

Note also the dependence or "stiffness increase" on those boundaries where a heat-transfer coefficient h is specified. Also in Equation (5.6), the heat capacitance matrix C , Equation (5.8), is recognized as the "dampening" matrix as it acts to dampen the response of the sys-

tem. Finally, the force vector f , Equation, (5.9), includes those terms which drive the system such as internal sources of heat, Q , and/or external sources of heat, q , and/or heat-transfer coefficients, h , applied to boundaries.

5.1.1.2 Solution

Assembly of the elemental system of Equations (5.6) results in a global system of ordinary differential equations of the following form:

$$C \frac{dT}{dt} + KT + f = 0 \quad (5.13)$$

Since these equations are non-linear they must be solved by a step-by-step recurrence scheme similar to finite-difference or Runge-Kutta procedures. Based on a review²⁶ of time-marching schemes for complex two-dimensional heat-conduction problems, the following three-point recurrence scheme, originally proposed by Dupont et al.²⁹, was adopted for model formulation:

$$\frac{K(3T_{i+1} + T_{i-1})}{4} + \frac{C(T_{i+1} - T_i)}{\Delta t_i} = f \quad (5.14)$$

where, T_i represents the temperature at the i th time step. Of the schemes tested, the Dupont time-stepping technique was reported²⁶ to produce the best accuracy and stability.

Since Equation (5.14) requires the temperature to be known at two successive time steps, a two-point recurrence scheme must be employed initially to start the process of time integration. Following Thomas et al²⁶, the Crank-Nicolson³⁹ technique, Equation (5.15), was utilized for the first time-step:

$$\frac{K(T_i + T_{i-1})}{2} + \frac{C(T_i - T_{i-1})}{\Delta t_i} = f \quad (5.15)$$

Equation (5.14) then can be manipulated into the form:

$$\mathbf{AT}_{i+1} = \mathbf{B} \quad (5.16)$$

which can be solved explicitly. The \mathbf{A} matrix is dimensioned $n \times n$, where n is the total number of nodes in the system, and is generally banded and symmetric about its diagonal.

Numerous banded, symmetric matrix solvers are available and can be employed to solve the system of Equations (5.15) efficiently. Owing to the computational severity of the Monofrax-S casting problem - three-dimensional, large geometry - a compact in-core profile solver was employed for solution. This algorithm, taken from Bathe³⁸, stores and manipulates only those numbers interior to the leading edge or profile of the band thus further reducing the computational size of the problem over the banded solvers.

5.1.1.3 Selection of Element Type.

The element types chosen for the heat flow model were selected based on their overall accuracy and their ability to easily handle different shapes/geometries. In addition, suitability for application to a stress analysis also figured importantly in selection of the temperature element since both the temperature and stress analyses would employ the same element (as mentioned previously this would permit the output from the thermal model to be input into the stress model in a straightforward manner). Based on a review of the element types available^{35,36,37}, the curve-sided, isoparametric, quadratic temperature element was selected. Eight-node (Figure 5.1) and twenty-node (Figure 5.2) versions were chosen for the two and three-dimensional analyses, respectively. This class of element provides C_0 compatibility (continuity of temperature across element boundaries), gives good accuracy with a minimum number of elements and is capable of easily handling geometries of arbitrary shape.

The key to this element being able to handle curved shapes easily lies in its isoparametric formulation. In essence this formulation employs the interpolation functions used for approximating the temperature distribution to also carry out a coordinate transformation from a local system (u, v, w) to a global system³⁵ (x, y, z) such that, for an element of arbitrary shape in the global system, the element is always rectilinear and of dimension (u,v,w) , $u = -1,0,1$, $v = -1,0,1$ and $w = -1,0,1$ in the local system - refer to Figures 5.1 and 5.2. The element interpolation functions employed in the formulation are for the local rectilinear coordinate system only. Their mathematical formulation is therefore relatively simple and easily coded and while being general in its applicability. There is a slight computational penalty for this procedure since numerical integration must be used for evaluation of Equations (5.7) - (5.9). However, in general, the increase in utility will outweigh the added computational costs.

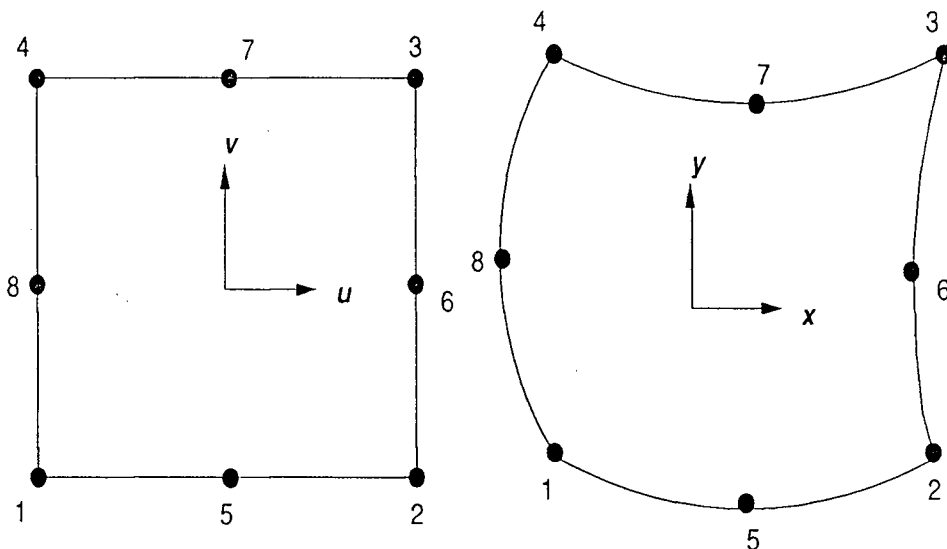


Figure 5.1. Eight-node isoparametric quadratic element depicted in rectilinear form in local coordinate system (u,v,w) and in global coordinate system (x,y,z) .

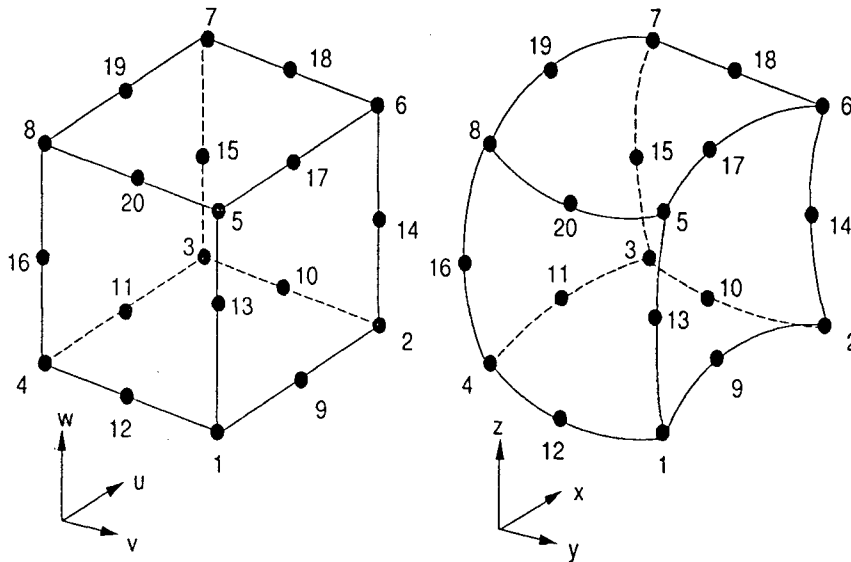


Figure 5.2. Twenty-node isoparametric quadratic element depicted in rectilinear form in local coordinate system (u, v, w) and in global coordinate system (x, y, z) .

For a detailed discussion on the mathematical formulation of the eight- and twenty-node quadratic isoparametric elements, the reader is referred to a good text on the subject³⁵⁻³⁷.

5.1.1.4 Numerical Integration

Various procedures for numerical integration of Equations (5.7) - (5.9) over the domain of the element exist and are well documented³⁵⁻³⁷. Of these, the Gaussian Quadrature or Legendre-Gauss procedures are particularly well suited to the finite-element technique since they require the least number of evaluations of the functions. Thus the overall computational effort is kept to a minimum. For numerical integration of a function in two- and three-dimensions the expressions are then:

$$\int_{-1}^1 \int_{-1}^1 f(u, v) du dv = \sum_{j=1}^m \sum_{i=1}^m W_i W_j f(u_i, v_j) \quad (5.17)$$

$$\int_{-1}^1 \int_{-1}^1 \int_{-1}^1 f(u, v, w) du dv dw = \sum_{k=1}^m \sum_{j=1}^m \sum_{i=1}^m W_i W_j W_k f(u_i, v_j, w_k) \quad (5.18)$$

where, W_i , W_j and W_k are the weighting coefficients at locations i , j and k , respectively, and m is the number of integration points (gauss points) within the domain of the element. For most applications involving quadratic temperature elements, 2×2 (two-dimensional) or $2 \times 2 \times 2$ (three-dimensional) Gauss points are adequate³⁵ for integration of the interpolation functions.

5.1.1.5 Temperature-Dependent Material Properties

Based on the information available at the time of model formulation, it was recognized that temperature dependencies in thermophysical properties would have to be accounted for in the model in order to predict the thermal behaviour of the Monofrax-S casting process correctly, particularly in view of the large temperature range involved (25 - 1800°C). Therefore, in addition to the fact that the basic heat-transfer formulation is non-linear, a further non-linearity is introduced by the temperature dependent behaviour of the material properties. The standard procedure⁴⁰ is to incorporate this temperature dependency by simply evaluating the thermophysical properties at the gauss-point temperatures within each element during the assembly procedure - refer to Equations (5.6)-(5.15). Various numerical procedures for handling time-independent problems with material non-linearities have been discussed in the literature^{35,37}. In general, the procedures involve some type of iteration scheme whereby successively better approximations are obtained until a residual error is reduced to an acceptable level. The Newton-Raphson method³⁵ is a good example of this type of procedure. Unfortunately, due to the computational size of the Monofrax-S problem, incorporation of this type of iterative technique into the time-stepping scheme was deemed impractical.

In an attempt to address both material non-linearities and the non-linear nature of the transient heat-flow formulation, an algorithm was developed which dynamically sets the time-step, Δt (see Equation 5.14), dependent on the rate of change of temperature in the previous two time-steps such that the temperature change within a time-step will not exceed a user specified maximum. For highly non-linear material problems this maximum temperature change is set to a relatively small value. Hence the material properties are updated over small temperature intervals. This procedure also lends itself to highly non-linear transient problems with rapidly changing temperatures. For this class of problem, a small user specified maximum change in temperature ensures an accurate integration in time. Finally, in order to better resolve temperature-dependent variations over the domain of an element, a three-point Gauss-Quadrature integration scheme was adopted.

Note: the results of the programme (previously described) for thermophysical property evaluation together with the application of these results to the Monofrax-S casting process are presented in Chapter 6.

5.1.1.6 Latent Heat Evolution

Owing to the fact that Monofrax-S undergoes solidification in the process under study, accounting for the latent heat of fusion (heat of crystallization) must also figure importantly in model formulation. Numerical methods, in general, tend to have difficulty handling latent heat evolution, particularly in those cases where the heat is released at a unique temperature/or over small temperature intervals⁴¹. Consequently, the topic has received considerable attention in the literature⁴¹⁻⁵⁰. For example, in problems dominated by latent heat removal, sophisticated finite-element techniques have been developed employing dynamically deforming grids which track the solidification front in order to ensure a fine mesh in the zone undergoing solidification⁴².

For those problems not dominated by latent heat evolution, such as casting processes, fixed grid techniques⁴³⁻⁵⁰ are adequate and avoid the added computation involved in deforming the grid. In the fixed grid techniques the location of the solidification front is not explicitly tracked and may lie between nodes at any given time. Generally, these techniques may be grouped into two categories. In the first group, the latent heat is treated as a heat source term Q - see Equation (5.9). Overall, these methods tend to be more prone to stability problems as the latent heat appears in the driving term, f , of Equation (5.6). In the other category, a different approach is adopted that accounts for the latent heat by artificially raising the heat capacity over the liquidus-solidus temperature range in the material undergoing solidification according to the following equation:

$$C_p^{eff} = \frac{\Delta H_f}{T_{liquidus} - T_{solidus}} + C_p \quad (5.19)$$

where ΔH_f represents the latent heat per unit mass. In this method, the effect of latent heat evolution is added to the dampening term, C , of Equation (5.6) and hence is inherently more stable. Unfortunately, although more stable, this method is not without its own problems. The difficulty lies in the shape of the modified heat capacity function which approximates the evolution of latent heat by a rapid increase in heat capacity over what is often a small liquidus-solidus temperature range. As the phase change zone passes through a particular element, accurate values for the modified heat capacity are required for input at the integration points. For conditions where the temperature change in a given time step is large in comparison to the liquidus-solidus temperature interval, individual integration points can miss the peak in the heat capacity curve associated with the phase change. The latent heat is then unaccounted for.

Based on a review of the literature²⁶ the so-called enthalpy techniques⁴⁵⁻⁵⁰ seem to be best suited to deal with this problem. The approach, originally adopted by Comini et al⁴⁵, employs enthalpy, which is the integral of heat capacity with respect to temperature, thus yielding a smooth function even over the phase change interval. A version of this technique adopted by Lemmon⁴⁷ and originally proposed by Morgan et al.⁴⁶ has been employed in model formulation. In this method, an average of the enthalpy and temperature gradients is taken over the domain of the element to yield an expression for the effective heat capacitance. This averaging process gives a representative value of the heat capacity while preserving the heat balance by avoiding the possibility of missing the peak in the modified heat-capacity function. The resulting expressions for the effective heat capacitance per unit volume in two and three-dimensions, employing the enthalpy method are then:

$$C_p^{eff} = \left(\frac{(dH/dx)^2 + (dH/dy)^2}{(dT/dx)^2 + (dT/dy)^2} \right)^{1/2} \quad (5.20)$$

$$C_p^{eff} = \left(\frac{(dH/dx)^2 + (dH/dy)^2 + (dH/dz)^2}{(dT/dx)^2 + (dT/dy)^2 + (dT/dz)^2} \right)^{1/2} \quad (5.21)$$

This technique lends itself easily to the iso-parameteric formulation with the above expressions evaluated at the appropriate Gauss integration points.

5.1.1.7 Boundary Conditions.

To this point, the description of the formulation of the mathematical model, including boundary conditions, has been kept general. To a large extent this is a consequence of the nature of the finite-element method. As formulated, the model is capable of being applied to a whole host of transient heat-transfer problems including the Monofrax-S casting process.

The finite element-method lends itself particularly well to this type of approach. The specifics of the application of this model to the Monofrax-S casting process, including a detailed description of the boundary conditions employed, will be left until Chapter 6.

5.1.2 Verification of Basic Model Formulation and Computer Code.

Once formulated, coded and debugged the next task was to verify the basic mathematical formulation and computer code. The technique employed was straightforward in principle and involved comparison of model predictions to exact mathematical solutions for specific cases. For this purpose, a problem must be selected for analysis for which an analytical or exact solution is available. Owing to the restrictive nature of the problems suitable for this task, more than one problem must be utilized to verify the basic components of the model.

The accuracy or performance of finite-element techniques, in general, is problem dependent and can be influenced by parameters such as boundary conditions, material properties, mesh density (whether a fine or course discretization of space is employed), and, for transient analysis, size of the time step²⁶. For the purpose of verification the problems have been chosen on the basis of their similarity to aspects of the Monofrax-S casting problem. Moreover, to assess the performance of the model further, the mesh densities used in the verification are typical of those employed for the full-scale Monofrax-S analysis. In this manner, the problems employed for comparison will examine aspects of the model which are relevant to its eventual application to the casting problem.

5.1.2.1 One-Dimensional Heat Conduction with Heat-Transfer Coefficient Boundary Condition.

The first problem examines transient heat conduction in a solid convectively or radiatively cooled from the surface. In the analysis of the casting problem, this type of boundary condition will be applied to describe heat transfer both at the refractory/mould interface and at the mould/ambient-air interface (a full description of the boundary conditions is presented in Chapter 6). An analytical solution from Kreith and Black⁵¹ was selected for the purpose of comparison. The basic geometry of the problem is illustrated schematically in Figure 5.3. The finite-element representation of this problem employing four, eight-node two-dimensional elements is presented in Figure 5.4. The appropriate boundary condition for this type of problem is then

$$q = -k \frac{\partial T}{\partial x} = h_c (T - T_{amb}) \quad (5.22)$$

where, h_c is the convective and/or "radiative" heat-transfer coefficient.

The analytical solution to the one-dimensional, transient heat conduction problem illustrated in Figure 5.3, subject to the initial condition $T(x,0) = T_0$ and boundary condition, Equation (5.22), is given⁵¹ by

$$\frac{T(x,t) - T_0}{T_{amb} - T_0} = 1 - \operatorname{erf}\zeta - \{\exp(Bi + \eta) (1 - \operatorname{erf}(\zeta + \sqrt{\eta}))\} \quad (5.23)$$

where

$$\zeta = \sqrt{\frac{x^2}{4\alpha t}} = \frac{F_o^{-1/2}}{2} \quad (5.24)$$

$$F_o = \frac{\alpha t}{x^2} \quad (5.25)$$

$$Bi = \frac{h_c x}{k} \quad (5.26)$$

$$\eta = \frac{h_c^2 \alpha t}{k^2} = (Bi)^2 (F_o) \quad (5.27)$$

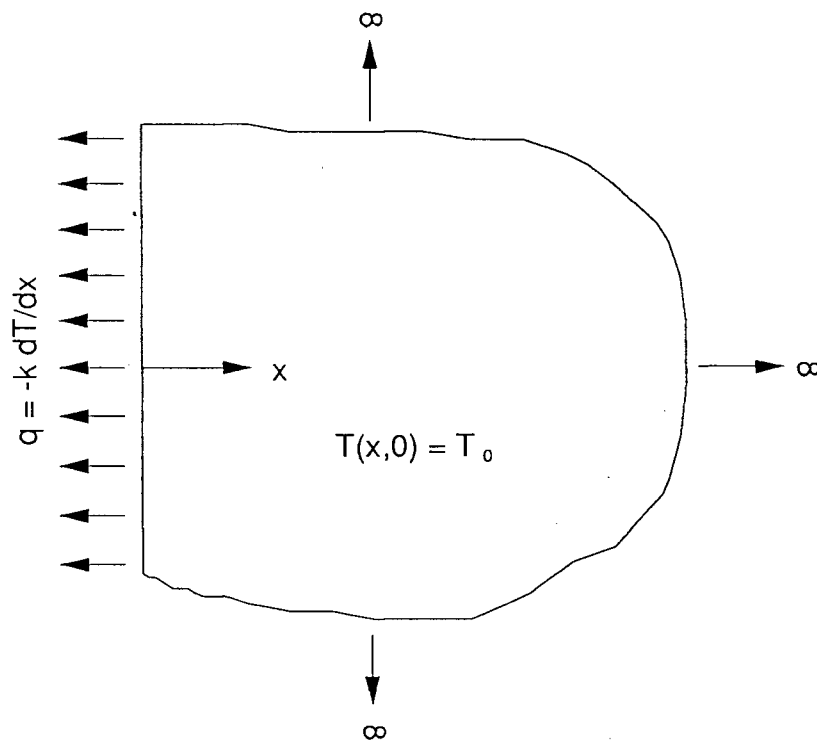


Figure 5.3. Schematic illustration of one-dimensional, semi-infinite, transient heat conduction problem.

For the analytical solution, the thermophysical properties are constant (independent of temperature), and heat conduction is one-dimensional. The problem parameters, initial condi-

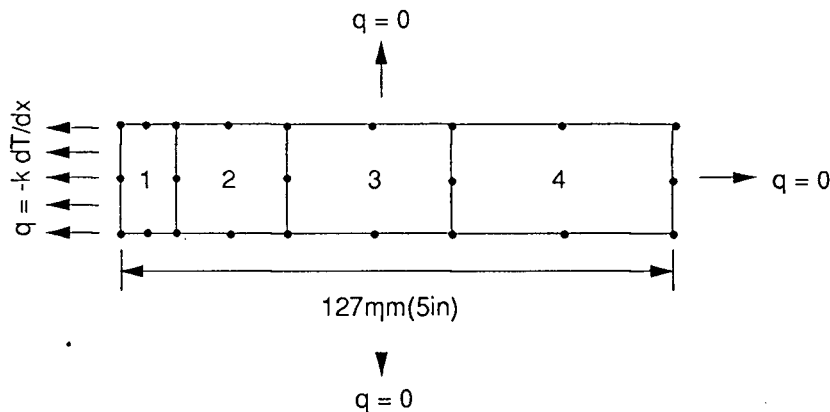


Figure 5.4. Schematic illustration of finite element representation of one-dimensional, semi-infinite, transient heat-conduction problem.

tions and heat-transfer coefficient are presented in Table 5.1. For the mathematical model, the time-step optimization algorithm described earlier was implemented. A maximum temperature change per time step of 10°C was input for this procedure. The duration of the analysis was limited to 300 s in order to maintain a portion of the grid at T_0 , consistent with the semi-infinite constraint of the analytical solution.

The results of a comparison of the model predictions to the exact solution for the one-dimensional transient heat conduction problem are presented in Figure 5.5. The numerical output from three nodes located at 0mm (0in), 6.4mm (0.25in) and 12.7mm (0.5in) from the heat-transfer coefficient boundary were selected for the purpose of comparison. As can be seen, there is good agreement between the model predictions and the exact solution. The spatial discretization employed for this analysis, Figure 5.4, is fully capable of resolving the transient behaviour of the solid described in Table 5.1 subject to the conditions outlined above. To investigate any directional dependencies in the computer code, the problem was

analyzed with heat conduction in the x and y direction, separately, for the two-dimensional elements, and in the x, y, and z directions, separately, for the three-dimensional elements. In all cases, the results were identical to those presented in Figure 5.5.

TABLE 5.1
Model Input Parameters and Initial Conditions

Parameter	Value
k, thermal conductivity (Monofrax-S)	1.0 W/m·°C
ρ , density (Monofrax-S)	3650.0 kg/m ³
C_p , heat capacity (Monofrax-S)	0.879 kJ/kg·C
h_c , heat transfer coeff.	100.0 W/m ² ·°C
T_0	1000.0 °C
T_{amb}	25.0 °C

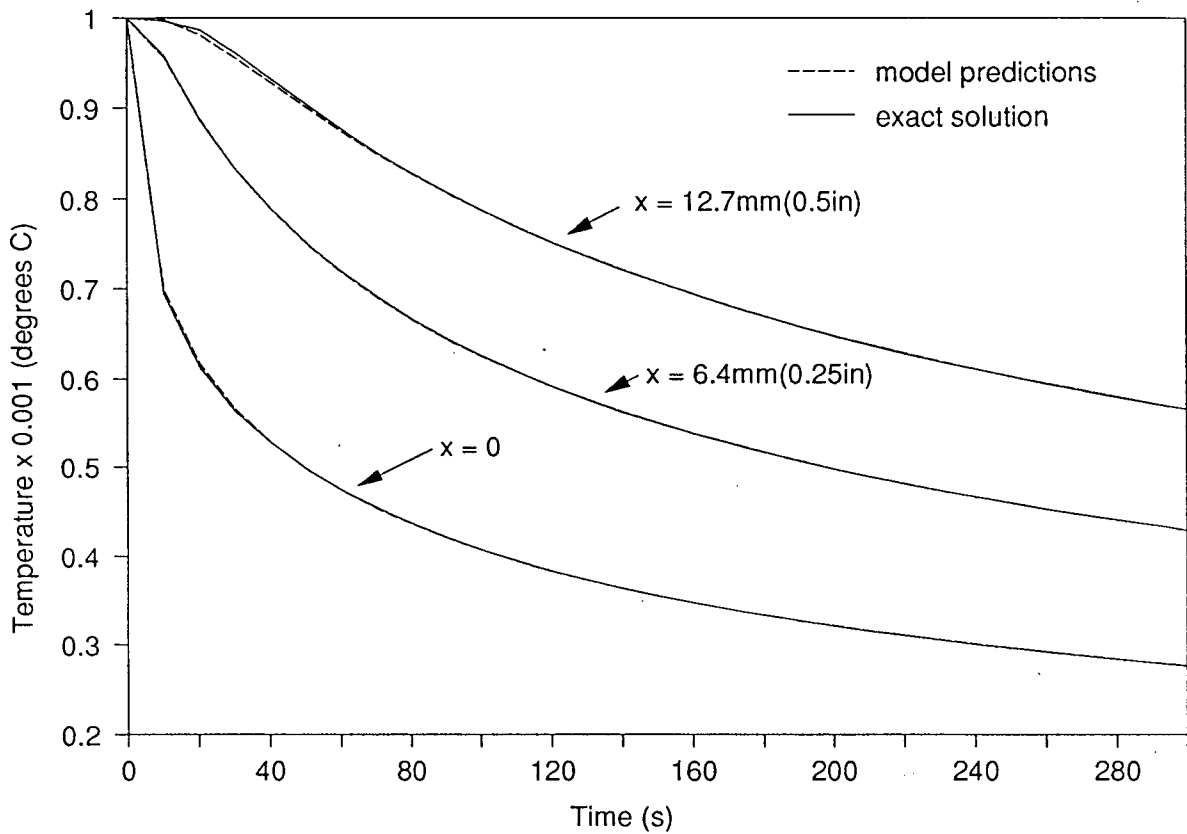


Figure 5.5 Comparison of model-predicted temperature response to the exact solution for one-dimensional transient heat conduction with a specified heat transfer coefficient boundary condition.

5.1.2.2 One-Dimensional Heat Conduction with Phase Change.

The second problem examines transient heat conduction in a solid undergoing a phase change with release of latent heat. The ability to analyze this problem accurately will assess

the capability of the model to simulate the casting process during the early stages of solidification. An analytical solution to a one-dimensional heat conduction problem with phase change from Szekely and Themils⁵² was selected for comparison. The basic geometry is illustrated schematically in Figure 5.6. The finite-element representation of this problem employing four, eight-node elements is presented in Figure 5.7. The boundary conditions and initial condition subject to which the analytical solution has been developed are

$$T_s = T_{s,0} \text{ at } x = 0, t \geq 0 \quad (5.28)$$

$$T_{liquid} = T_{mp} \text{ at all values of } x, t = 0 \quad (5.29)$$

The analytical solution to the one-dimensional, heat conduction problem with phase change illustrated in Figure 5.6, subject to boundary condition, Equation (5.28), and initial condition; Equation (5.29), is given⁵² as

$$T(x, t) = T_{s,0} + \frac{(T_{mp} - T_{s,0})}{\text{erf}\lambda} \text{erf}\left(\frac{x}{2\sqrt{\alpha_s t}}\right) \quad (5.30)$$

where

$$\lambda e^{\lambda^2} = -C_{p,s} \frac{(T_{mp} - T_{s,0})}{\pi^{1/2} \Delta H_{fusion}} \quad (5.31)$$

For the analytical solution, the thermal conductivity, density and heat capacity are constant (independent of temperature), and the latent heat of fusion is released at a fixed melting point temperature, T_{mp} . The problem parameters, initial conditions and latent heat of fusion are presented in Table 5.2.

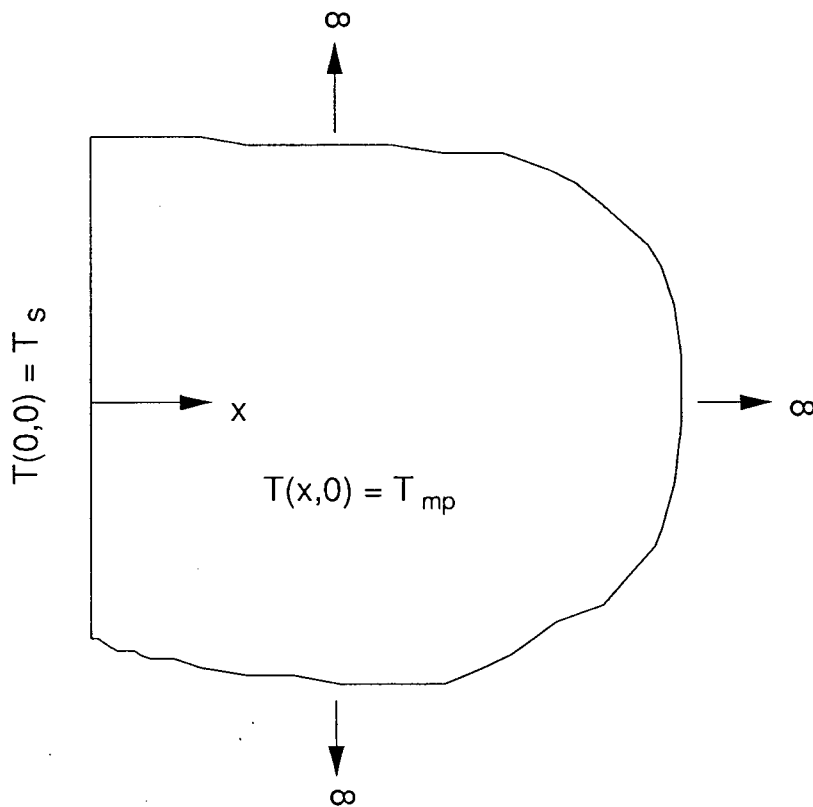


Figure 5.6. Schematic illustration of one-dimensional transient heat conduction problem.

In contrast to the analytical solution which specifies a unique solidification temperature, the mathematical model requires that the latent heat of solidification be released over a finite temperature range (this is a requirement of the enthalpy method for latent heat evolution). In order to permit a valid comparison to be made, a small liquidus/solidus temperature range must be used in the numerical analysis. Consequently, a reduced liquidus/solidus solidification range and proportionally scaled heat of fusion for Monofrax-S were adopted. In essence, an attempt has been made to maintain the same heat released per unit temperature change in both the moving boundary problem and Monofrax-S casting problem. Monofrax-S nominally undergoes solidification over a temperature range estimated to be approximately 30°C , from $1810\text{-}1780^\circ\text{C}$ (based on the Alumina-Zirconia-Silica ternary phase diagram²⁴

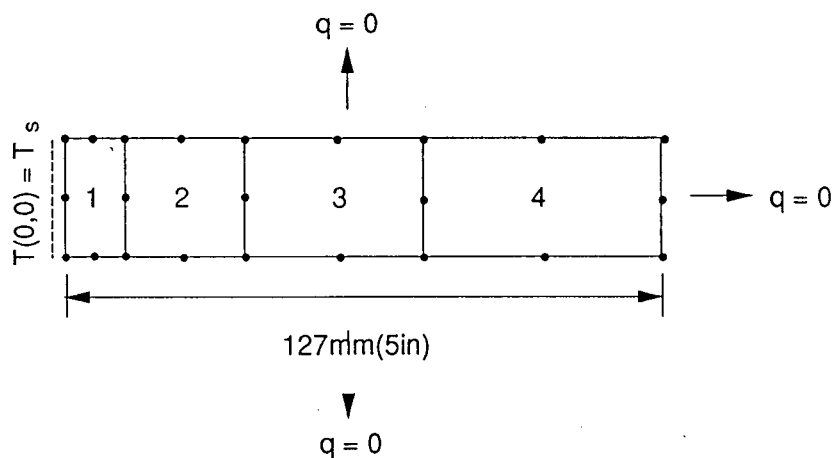


Figure 5.7. Schematic illustration of finite-element representation of one-dimensional transient heat conduction problem.

presented in Chapter 2), releasing an estimated 760 kJ/kg of heat (based on weighted average of heats of crystallization of Al_2O_3 ⁵³ and ZrO_2 ⁵⁴ neglecting the SiO_2 component which was assumed to remain in a glassy state). For the sake of this comparison, the solidification temperature range is reduced from 30 to 1°C by effectively increasing the solidus temperature to 1809°C and the latent heat of fusion proportionally scaled from 760 to 25 kJ/kg. These values appear in Table 5.2.

In addition, the time-step optimization algorithm described earlier was implemented. A maximum temperature change per time step of 0.25°C was employed. The duration of the analysis was limited to 1200 seconds in order to maintain a portion of the grid at T_0 consistent with the semi-infinite constraint of the analytical solution.

The results of a comparison of the model predictions to the exact solution for the one-dimensional moving boundary problem are presented in two stages. First, a comparison is made between the model predictions and the exact solution for the case where the material undergoing solidification does not release any latent heat. This provides a means of assessing

TABLE 5.2
Model Input Parameters and Initial Conditions

Parameter	Value
k ; thermal conductivity (Monofrax-S)	1.0 W/m·°C
ρ , density (Monofrax-S)	3650.0 kg/m ³
$C_{p,s}$, heat capacity (Monofrax-S)	0.879 kJ/kg·°C
ΔH_{fusion} , Heat of Fusion (Monofrax-S <i>scaled</i>)	25.0 kJ/kg
T_{liquidus} , (Monofrax-S)	1810.0°C
$T_{\text{mp}} = T_{\text{solidus}}$, (Monofrax-S <i>increased</i>)	1809.0°C
T_0	1810.0°C
$T_{s,0}$	1700.0°C

the ability of the model to handle the fixed temperature boundary condition. The numerical output from three nodes located at 6.4mm (0.25in), 12.7mm (0.5in) and 25.4mm (1.0in) from the fixed temperature boundary were selected for the purpose of comparison. The results are presented in Figure 5.8. As can be seen, there is good agreement between the model predictions and the exact solution⁵² apart from an initial, minor, short-term oscillation which occurs in one of the nodes. This is associated with the introduction of the fixed temperature boundary condition which initially gives a rapid step change in temperature across the first element resulting in some numerical error. For the most part, however, the spatial discretization employed for this analysis, Figure 5.7, is fully capable of resolving the transient behaviour of the solid described in Table 5.2 (with heat of fusion set to zero) subject to the conditions outlined above. To investigate any directional dependencies in the computer code, the problem was analyzed with heat conduction in the x and y directions, separately, for the two-dimensional elements, and in the x, y, and z directions, separately, for the three-dimensional elements. In all cases, the results were identical to those presented in Figure 5.8.

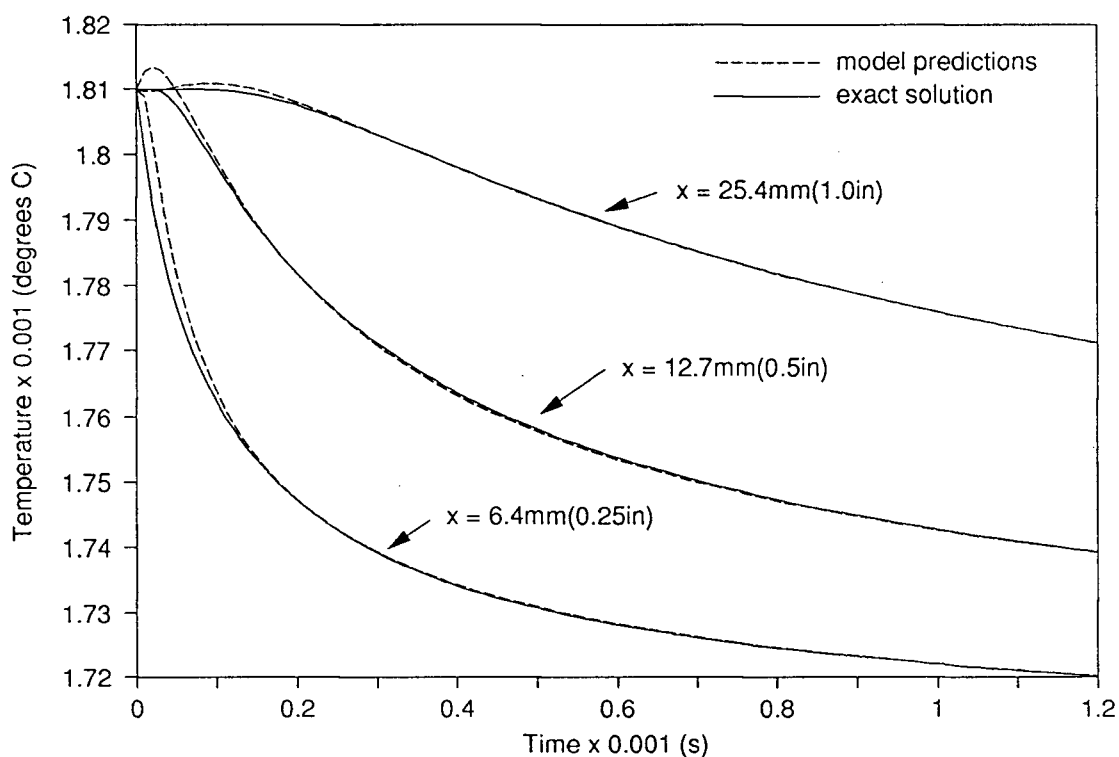


Figure 5.8. Comparison of model-predicted temperature response to exact solution⁵² for one-dimensional transient heat conduction problem with fixed temperature boundary condition.

Second, a comparison was made between the model predictions and the exact solution for the case where the material undergoing solidification releases latent heat - the moving boundary problem. The numerical output from three nodes located at 6.4mm (0.25in), 12.7mm (0.5in) and 25.4mm (1.0in) from the fixed temperature boundary were again selected for the purpose of comparison. The results are presented in Figure 5.9. As can be seen from this comparison the incorporation of latent heat evolution into the problem has a negative impact on the accuracy of the model which is significantly reduced over the previous conduction only case. At a distance of 6.4mm(0.25in) from the fixed temperature boundary the model first underpredicts the temperature by as much as 20°C, at approximately

50s elapsed time, then later, slightly over predicts the temperature by 2°C at roughly 350s elapsed time. The reason for this reduction in predictive capability is directly related to the way in which latent heat is accounted for in the numerical formulation. The enthalpy method adopted in the formulation employs an integral averaging technique over the domain of the element to determine a value for the modified heat capacity without explicitly tracking the location of the solidification front. As a result of this, in problems utilizing a relatively coarse grid, there is a "smearing out" of the effects of solidification. The model is incapable of accurately resolving the location where the heat of solidification should be released. This inaccuracy is particularly acute in those instances where the material releases its latent heat over a narrow temperature range as is the case in the example problem.

Based on the above argument, it can be anticipated that the results would be sensitive to the spatial discretization employed. To test this hypotheses, the problem was re-analyzed with a finer mesh. A regular grid with an element size of 6.4mm(0.25in) was selected for the finer mesh. This represents a factor of two increase in mesh density over element 1 in the original mesh - see Figure 5.7 for original mesh. The results are present in Figure 5.10. As suspected, these results clearly show a significant improvement in the accuracy of the model predictions. The maximum error is now down to approximately 5°C. On the basis of this comparison, it may be concluded that the original mesh, Figure 5.7, is barely adequate to resolve this problem, particularly if a priority were to be placed on accurately tracking the solidification front.

Finally, to investigate any directional dependencies in the computer code, this problem was also analyzed separately with heat conduction in the x and y directions for the two-dimensional elements, and in the x, y, and z directions for the three-dimensional elements. In all cases, results were identical to those presented in Figures 5.9 and 5.10.

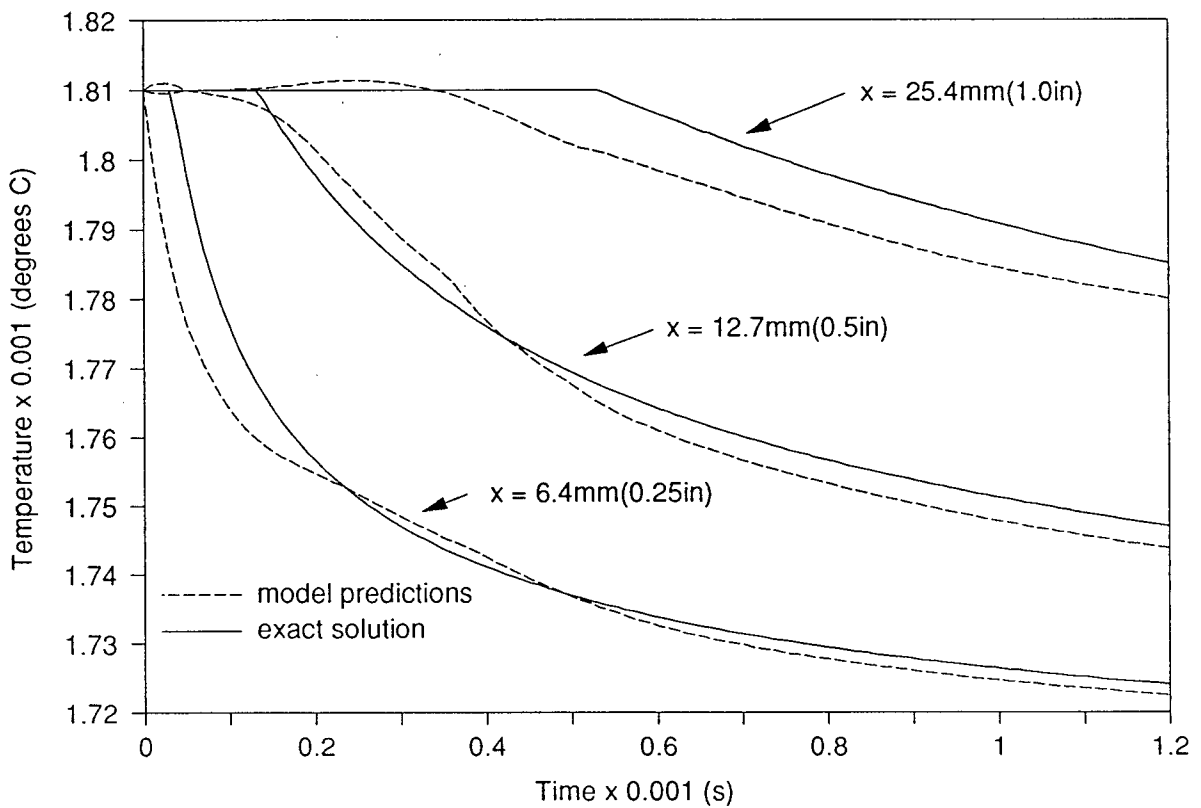


Figure 5.9. Comparison of model-predicted temperature response to exact solution⁵² for one-dimensional transient heat conduction problem with phase change and fixed temperature boundary condition.

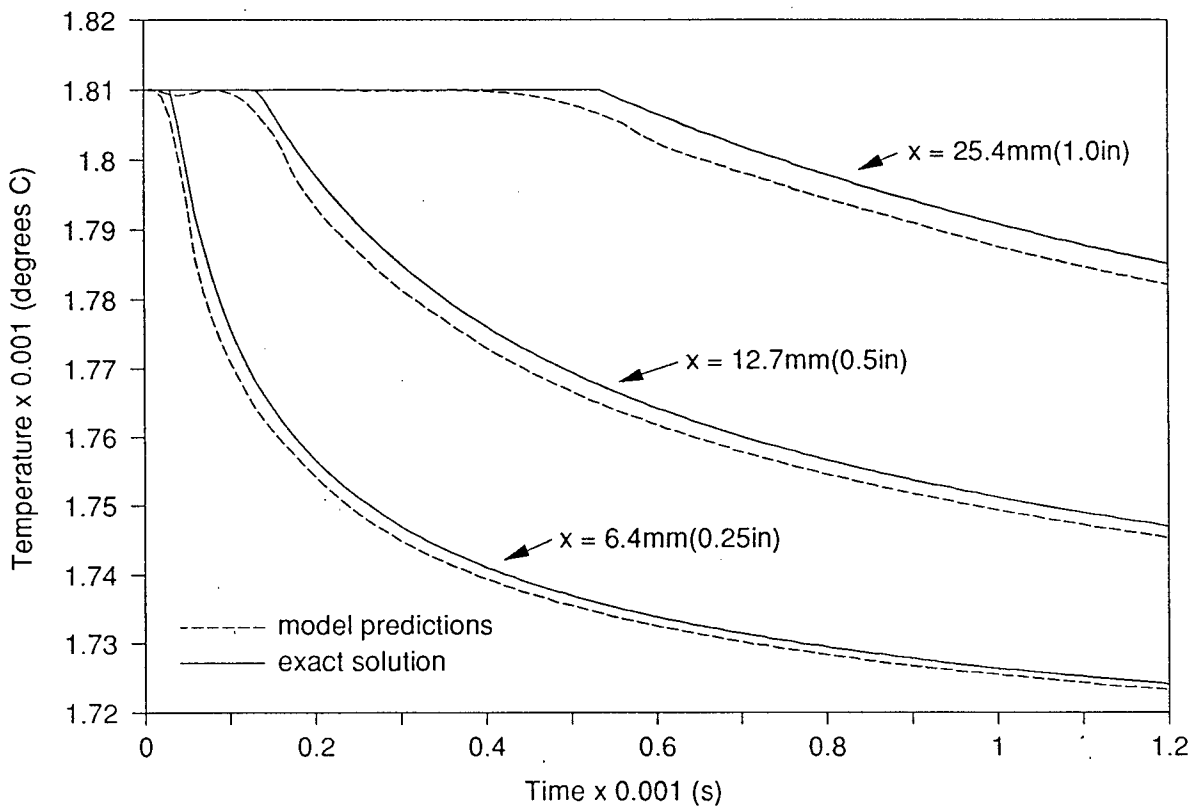


Figure 5.10. Comparison of model predicted temperature response to exact solution⁵² for one-dimensional transient heat conduction problem with phase change and fixed temperature boundary condition. Note: for this analysis the mesh density has been increased over the standard case.

5.1.2.3 Two-Dimensional Heat Conduction with Fixed-Temperature Boundary Condition.

The third and final problem analyzed examines heat conduction in two-dimensions in the corner of a transverse section of the Monofrax-S casting. An analytical solution from Rathjen and Jiji³¹ was selected for the purpose of comparison. The basic geometry of the problem is illustrated schematically in Figure 5.11. The finite element representation of this problem employing 24, eight-node two-dimensional elements is presented in Figure 5.12. The appropriate boundary conditions and initial conditions for which the analytical solution³¹ has been developed are

$$T_s = T_{s,0} \text{ at } x = 0, y = 0, 228.6\text{mm}(9\text{in}), t \geq 0 \quad (5.32)$$

$$T_s = T_{s,0} \text{ at } x = 0, 127\text{mm}(5\text{in}), y = 0, t \geq 0 \quad (5.33)$$

$$T = T_0 \text{ at } x = 127\text{mm}(5\text{in}) \text{ and } y = 0, 228.6\text{mm}(9\text{in}), t \geq 0 \quad (5.34)$$

$$T = T_0 \text{ at } x = 0, 127\text{mm}(5\text{in}) \text{ and } y = 228.6\text{mm}(9\text{in}), t \geq 0 \quad (5.35)$$

$$T = T_0 \text{ at all values of } x \text{ and } y, t = 0 \quad (5.36)$$

The analytical solution to the two-dimensional, transient heat conduction problem illustrated in Figure 5.11, subject to boundary conditions (5.32) - (5.35) and initial conditions (5.36) is given³¹ as

$$T(x, y, t) = T_{s,0} + (T_0 - T_{s,0}) \operatorname{erf}\left(\frac{x}{2\sqrt{\alpha_s t}}\right) \operatorname{erf}\left(\frac{y}{2\sqrt{\alpha_s t}}\right) \quad (5.37)$$

For the analytical solution, the thermal conductivity, density and heat capacity are constant (independent of temperature). The problem parameters and initial conditions are presented in Table 5.3.

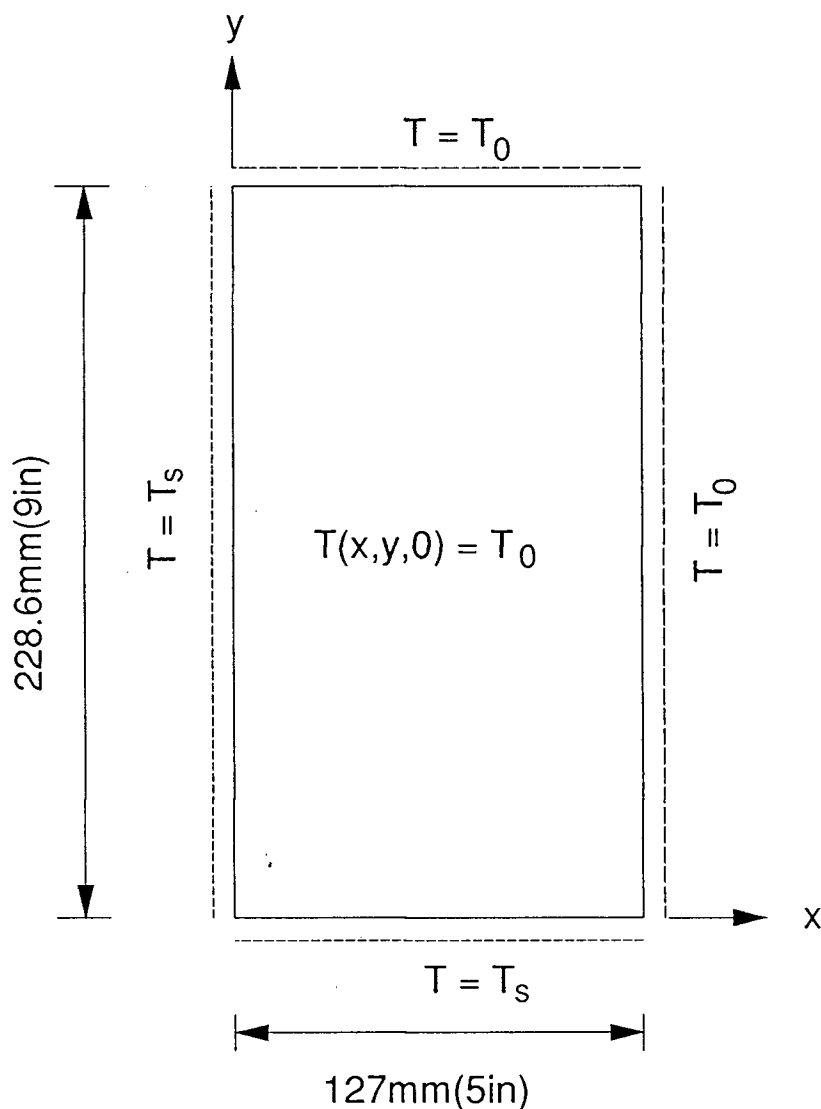


Figure 5.11. Schematic illustration of two-dimensional, transient heat conduction problem with fixed-temperature boundary conditions.

In addition, the time-step optimization algorithm described earlier was implemented. A maximum temperature change per time-step of 1.0°C was input for this procedure. The duration of the analysis was limited to 600 seconds in order to maintain a portion of the grid at T_0 consistent with the conditions of the analytical solution.

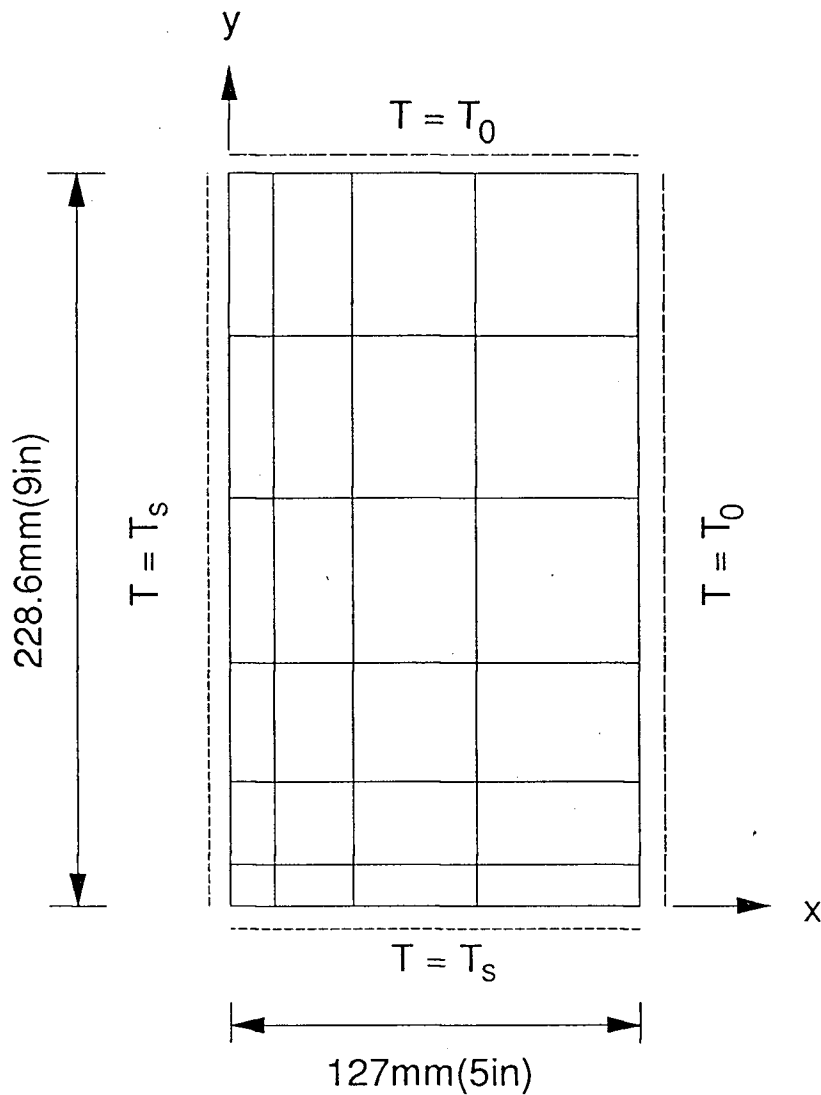


Figure 5.12. Schematic illustration of finite-element representation of two-dimensional transient heat-conduction problem with fixed-temperature boundary conditions.

The results of a comparison of the model predictions to the exact solution for the two-dimensional transient heat conduction problem are presented in Figure 5.13. The numerical output from three nodes located at $x = 12.7\text{mm}$ (0.5in), $y = 12.7\text{mm}$ (0.5in); $x = 12.7\text{mm}$

TABLE 5.3
Model Input Parameters and Initial Conditions

Parameter	Value
k, thermal conductivity (Monofrax-S)	1.0 W/m·°C
ρ , density (Monofrax-S)	3650.0 kg/m ³
C_p , heat capacity (Monofrax-S)	0.879 kJ/kg·°C
T_0	1810.0°C
$T_{s,0}$	1700.0°C

(0.5in), $y = 38.1\text{mm}$ (1.5in); and, $x = 38.1\text{mm}$ (1.5in), $y = 12.7\text{mm}$ (0.5in) - refer to Figure 5.12 - were selected for the purpose of comparison. As can be seen from Figure 5.13, there is good agreement between the model predictions and the exact solution. The maximum error is about 1°C. The spatial discretization employed for this analysis, Figure 5.12, is fully capable of resolving the transient behaviour of the solid described in Table 5.3 subject to the conditions outlined above. To investigate any directional dependencies in the computer code, this problem was also used to investigate conduction in the x/y , x/z and y/z directions, separately, for the three-dimensional elements. The results were identical to those presented in Figure 5.13.

5.1.2.4 Summary of Basic Heat-Flow Code Verification

Generally these analyses verify that the mathematical model is capable of simulating transient heat flow behaviour in a series of problems which comprise some of the basic aspects of the Monofrax-S casting process. Comparisons between model predictions and the exact solution for transient conduction problems without liberation of latent heat, indicate that a relatively coarse mesh is capable of accurately solving this class of problem under the conditions examined. For problems involving latent heat evolution over a small temperature interval, finer meshes than those utilized for the Epic-3 casting problem are required. It remains to be determined if the coarse mesh, Figure 5.12, is adequate for problems involving

latent heat evolution in materials, such as Monofrax-S, which exhibit a broader phase change temperature interval. Unfortunately, no exact mathematical solutions are available as a basis for comparison for this class of problem. A sensitivity analysis conducted on the model, as applied to the Monofrax-S casting process, will help to address this question. The results of this sensitivity analysis will be presented in Chapter 6.

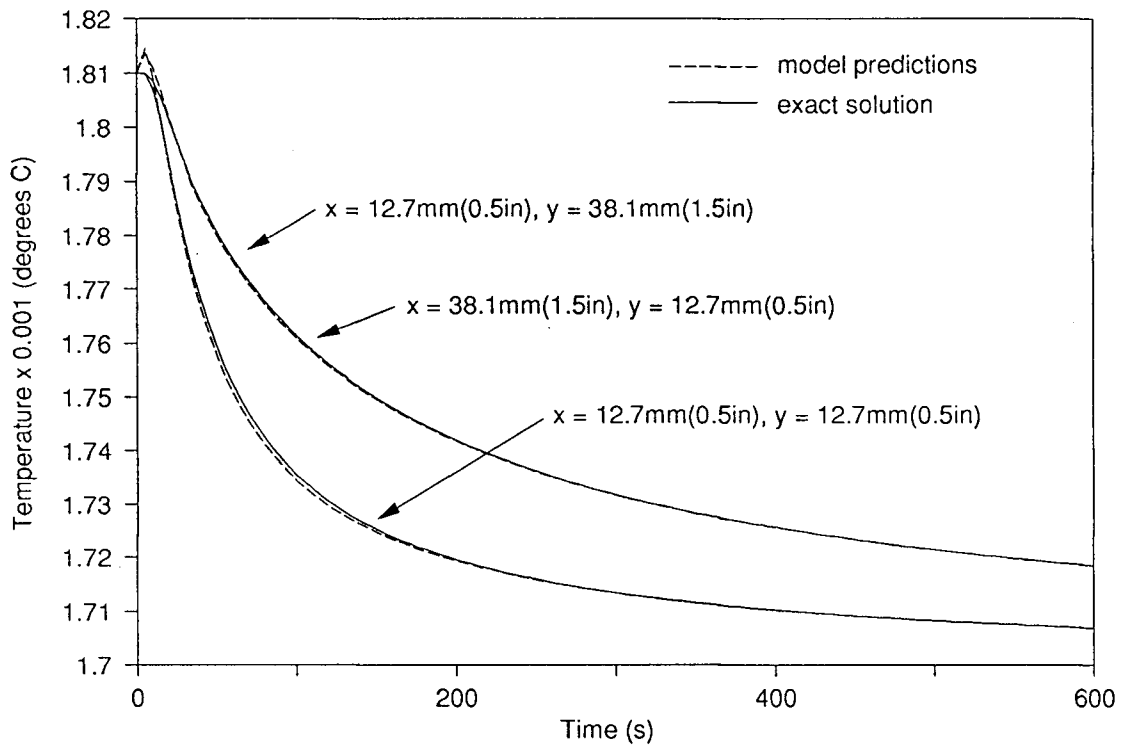


Figure 5.13. Comparison of model-predicted temperature response to exact solution for two-dimensional transient heat conduction problem with fixed temperature boundary conditions. Note: distances are measured from $x = 0, y = 0$.

5.2 Development of Mathematical Model of Stress Generation

The second distinct module of the overall heat-flow/stress model is the model of stress generation. For reasons outlined previously, a time-independent, elastic formulation was cho-

sen for the stress model despite evidence² that Monofrax-S behaves more in a time-dependent, visco-elastic manner at elevated temperatures. It is accepted that this approach will result in a reduction in the overall ability of the model to predict stresses quantitatively. At elevated temperatures the model will tend to over-predict stress and therefore will calculate a maximum stress. On the positive side, the model formulation is simplified and the computational severity of the problem is reduced. In contrast to the thermal analysis, only the refractory is considered in the stress analysis. The generation of stress in the moulding material is assumed to be of no consequence and interaction with the surrounding moulding material is ignored.

As indicated in the development of the mathematical model of heat-flow, where appropriate a two-dimensional analysis has been employed. Following Thomas et al.²³, a state of plane-stress, usually applied to thin plates, was assumed for the two-dimensional elastic analysis of the transverse quarter-section. At mid-height in the casting, the stresses that form the longitudinal mid-face cracks, such as the Type-B, will act parallel to the transverse plane and be independent of height. The plane stress-approximation is applicable to this situation with the exception that there are σ_z stresses acting normal to the plane in the refractory. However, as a first approximation, the impact of the σ_z stresses on the transverse stress distribution can be neglected.

5.2.1 Formulation

The governing differential equations of equilibrium for an elastic solid in a state of stress can be derived by conducting a force balance on an elemental volume. In two- and three-dimensions the resulting Equations are³⁵⁻³⁷

$$\frac{\partial \sigma_x}{\partial x} + \frac{\partial \tau_{xy}}{\partial y} + F_x = 0 \quad (5.38)$$

$$\frac{\partial \sigma_y}{\partial y} + \frac{\partial \tau_{xy}}{\partial x} + F_y = 0 \quad (5.39)$$

$$\frac{\partial \sigma_x}{\partial x} + \frac{\partial \tau_{xy}}{\partial y} + \frac{\partial \tau_{xz}}{\partial z} + F_x = 0 \quad (5.40)$$

$$\frac{\partial \sigma_y}{\partial y} + \frac{\partial \tau_{xy}}{\partial x} + \frac{\partial \tau_{yz}}{\partial z} + F_y = 0 \quad (5.41)$$

$$\frac{\partial \sigma_z}{\partial z} + \frac{\partial \tau_{xz}}{\partial x} + \frac{\partial \tau_{yz}}{\partial y} + F_z = 0 \quad (5.42)$$

where, σ_x , σ_y and σ_z are the stresses (force per unit area) acting on planes with normals in the x, y, and z directions, respectively; the τ_{ij} , are the shear stresses acting on planes with normals i in direction j, and the F_x , F_y and F_z are body forces acting in the x, y, and z directions, respectively. Boundary conditions for the equilibrium equations may be found by considering the surface forces acting on the body in question.

The resulting equilibrium equations for the general three-dimensional case, Equations (5.40)-(5.42), cannot be solved alone as there are six unknown components of stress and only three independent equations³⁶. In order to solve this system of equations subject to the surface force boundary conditions, the displacement field and its relationship to strain in the body also must be taken into account. These are the so-called "compatibility conditions" which must be satisfied. Combined, these equations make up the differential statements for equilibrium and compatibility for linear elastic bodies in a state of stress. The finite-element solution instead relies on the integral statements which must also hold for these bodies. In essence, focus is shifted from the relationships that must hold at any point in the system to

those that hold for the entire system. These integral relationships are the variational principles which apply to solid mechanics problems. For solution of the Monofrax-S problem, the "minimum potential energy principle" or "principle of virtual displacement" is adopted.

5.2.1.1 Finite-Element Solution by Displacement Method

In the displacement technique, the potential energy of an elastic body of general shape deformed by the action of body forces and surface tractions is defined as the energy of deformation of the body (strain energy) minus the work done on the body by the external forces³⁶. The theorem of minimum potential energy states that³⁶:

"The displacement (u, v, w) which satisfies the differential equations of equilibrium, as well as the conditions at the bounding surface, yields a smaller value for the potential energy than any other displacement which satisfies the same conditions at the bounding surface"

Expressing this mathematically, at equilibrium we have

$$\delta\Pi(u, v, w) = \delta U_p(u, v, w) - \delta V_p(u, v, w) = 0 \quad (5.43)$$

where, $\Pi(u, v, w)$ is the potential energy, $U_p(u, v, w)$ is the strain energy and $V_p(u, v, w)$ is the work done by applied loads during displacement changes. For equilibrium to prevail, the same expression must also hold for individual components or elements of the discretized solid. Therefore, the focus can be shifted to the level of an individual element.

For the general case, the strain energy of an individual element e of a linear elastic solid is then

$$U_p^e = 1/2 \int_{V^e} \{\epsilon\}^T \mathbf{D} \{\epsilon\} dV + \int_{V^e} \{\epsilon\}^T \mathbf{D} \{\epsilon\}_0 dV - \int_{V^e} \{\epsilon\}^T \{\sigma\}_0 dV \quad (5.44)$$

where, $\{\varepsilon\}$ is the strain vector, \mathbf{D} is the elasticity matrix containing the appropriate material properties, $\{\varepsilon_0\}$ is the initial strain vector and $\{\sigma_0\}$ is the initial stress vector.

The second component of the right hand side of Equation (5.43) is the work done by the external forces. This is given by

$$V_p^e(u, v, w) = \int_{V_e} \mathbf{F}\{\delta\} dV + \int_{A_e} \mathbf{T}\{\delta\} dA \quad (5.44)$$

where \mathbf{F} is the body force vector containing the x, y, and z components of the distributed body force acting on the element and \mathbf{T} is the surface traction force vector containing the x, y, and z components of the traction forces acting on the surface of boundary elements.

Substituting the differentiated expressions for the strain energy and the work done by external forces into the equation for potential energy, Equation (5.43), and rearranging yields the following expression which can be applied to each element individually:

$$K^e \{\delta\}^e + f^e = 0 \quad (5.46)$$

The individual components of this equation must now be evaluated within the context of the finite-element approximation - ie. an assumed variation in the field variable over the domain of the element.

In the displacement formulation, the potential energy of each element is evaluated in terms of the individual nodal displacements - u_i , v_i , w_i - based on an assumed variation of the displacement over the domain of the element. The same polynomial interpolation (shape) functions used in the thermal analysis are employed to describe the spatial variation in displacement, as follows

$$\{\delta^e\} = \begin{Bmatrix} u(x, y, z) \\ v(x, y, z) \\ w(x, y, z) \end{Bmatrix}^e = \begin{Bmatrix} \sum_{i=1}^n N_i(x, y, z) u_i \\ \sum_{i=1}^n N_i(x, y, z) v_i \\ \sum_{i=1}^n N_i(x, y, z) w_i \end{Bmatrix}^e \quad (5.47)$$

Based on these relationships the terms of Equation (5.46) now be expressed as

$$K_{ij}^e = \int_{V^e} B_i^T D B_j dV \quad (5.48)$$

and for the general case

$$f_i^e = - \int_{A^e} N_i^T T_i dA - \int_{V^e} N_i^T F_i dV - \int_{V^e} B_i^T D \{\epsilon\}_{0_i} dV + \int_{V^e} B_i^T \{\sigma\}_{0_i} dV \quad (5.49)$$

where, B , the matrix of differential operators is defined by

$$B_i^T = \nabla^T N_i \quad (5.50)$$

$$B_j = \nabla N_j \quad (5.51)$$

and N_i are the nodal interpolation shape functions. For one node i of element e the displacement vector $\{\delta\}$ is then

$$\{\delta\}_i^e = \begin{Bmatrix} u_i \\ v_i \\ w_i \end{Bmatrix} \quad (5.52)$$

In Equation (5.46), the matrix, K , is usually referred to as the elemental stiffness matrix and is of dimension $(n_e)(n.d.o.f.) \times (n_e)(n.d.o.f.)$, where n_e is the number of nodes per element and n.d.o.f. is the number of degrees of freedom per node (the number of degrees of freedom per node is equal to the dimension of the analysis i.e. 2-D \rightarrow n.d.o.f = 2). The force or load vector, f , is dimensioned $(n_e)(n.d.o.f.)$.

As illustrated in Equation (5.49), the overall force vector may be comprised of several components/loads dependent on the nature of the problem. These include, the effects of surface tractions, body forces, initial strains and initial stresses, respectively. For problems involving thermal stresses, such as the Monofrax-S casting analysis, an additional load must be considered which accounts for the effect of differential thermal strains on the body. The expression for the thermal load vector is identical to that for the load due to an initial strain, $\{\epsilon\}_0$, except that the strain is now associated with the temperature field. For node i , the thermal load is then

$$F_{T_i} = \int_{V_e} B_i^T D \{\epsilon\}_{T_i} dV \quad (5.53)$$

where, F_T is the thermal load vector and $\{\epsilon\}_T$ is the strain associated with the thermal field.

In Equation (5.53), the thermal strain vector for the general three-dimensional case is then

$$\{\epsilon\}_{T_i} = \begin{Bmatrix} \epsilon_x \\ \epsilon_y \\ \epsilon_z \\ \gamma_{xy} \\ \gamma_{xz} \\ \gamma_{yz} \end{Bmatrix} = \begin{Bmatrix} \alpha \Delta T \\ \alpha \Delta T \\ \alpha \Delta T \\ 0 \\ 0 \\ 0 \end{Bmatrix} \quad (5.54)$$

where, α is the thermal linear expansion coefficient and ΔT is the change in temperature relative to some datum.

5.2.1.2 Solution

Assembling the elemental system of equations, Equation (5.46), results in a global system of equations of the form of Equation (5.55) which can then be solved for the nodal displacements δ . The global \mathbf{K} or "stiffness" matrix is dimensioned $(n)(n.d.o.f.) \times (n)(n.d.o.f.)$, where n is the total number of nodes in the system, and is banded and symmetric about its diagonal. As in the case of the thermal model, to minimize the computational size of the problem, a profile solver³⁸ is employed to solve the system of equations.

$$\mathbf{K}\{\delta\} + \mathbf{f} = 0 \quad (5.55)$$

Once the nodal displacements have been determined, the associated stress distribution can be calculated in a straightforward manner with Hooke's law

$$\{\sigma\}_i = (\mathbf{B}_i\{\delta\}_i - \{\epsilon\}_{T_i})\mathbf{D} \quad (5.56)$$

Note that for problems involving thermal stress, the thermal strain, $\{\epsilon\}_T$, is removed from the total strain prior to multiplication by the elasticity matrix \mathbf{D} .

5.2.1.3 Selection of Element Type

For reasons outlined in the Chapter 3, the equivalent element types (same number of nodes) are employed in both the heat-flow and stress analyses. These are the eight and twenty-node isoparametric, quadratic, temperature and displacement elements for two- and three-dimensional heat-flow and stress analyses, respectively. For the stress analysis, this element type results in a linear variation in stress over the domain of the element since stress is proportional to the first derivative of displacement. For a general discussion of the reasons for selecting this element type the reader is referred to the original treatment - see Section 5.1.1.3.

As indicated in Section 5.1.1.3, numerical integration must be employed with this element for evaluation of Equations (5.48) and (5.49). This procedure is described in the next section.

5.2.1.4 Numerical Integration

The technique for integration of the quadratic displacement elements is identical to that employed in the heat transfer analysis for the quadratic temperature elements (Gaussian Quadrature procedure - see Section 5.1.1.4). However, the procedure for implementation of this technique is slightly different.

According to Zienkiewicz³⁵, a two-point Gauss Quadrature integration yields more accurate results for stress than the three-point scheme when applied in the formation of the elemental matrices - Equations (5.48)-(5.49). Moreover, once the displacements have been determined, further gains in accuracy are realized if the stresses are evaluated at the Gauss points. If evaluation at the nodes is desired, a simple bilinear extrapolation from the Gauss-point values should be employed. Based on these recommendations, reduced or two-point integration is adopted for formation of the matrices in the model for stress analysis. Furthermore, the procedure for evaluation of nodal stress values suggested by Zienkiewicz³⁵ is also utilized. (By comparison, for reasons outlined in Section 5.1.1.4, a three-point scheme is employed for integration in the thermal analysis.)

5.2.1.5 Temperature-Dependent Material Properties

Material property temperature dependencies are incorporated into the model of stress generation by evaluating the relevant mechanical properties at the Gauss point temperatures within each element during formation of the elemental matrices. The procedure⁴⁰ is identical

to that utilized in the heat-flow model - see Section 5.1.1.5. for details. The specifics of the application of this model to the Epic-3 Monofrax-S casting process, including a description of the thermomechanical properties employed in the analysis, are presented in Chapter 6.

5.2.1.6 Boundary Conditions

In an manner analogous to the heat-flow model, the mathematical formulation of the elastic-stress model, including boundary conditions, has been kept general. As formulated, the model can be applied to the analysis of numerous elastic thermal stress problems including the Monofrax-S process. The specifics of the application of this model to the Monofrax-S casting process together with a detailed description of the boundary conditions employed are presented in Chapter 7.

5.2.2 Verification of Basic Model Formulation and Computer Code

Once coded and debugged, the basic mathematical formulation and computer code again had to be verified. The approach is identical to that employed for the heat-flow model and involves comparison of the elastic-stress model predictions to exact solutions. A series of simplified problems, for which analytical or exact solutions are available have been selected for this task. Owing to the restrictive nature of these problems, more than one problem must be utilized to verify the basic components of the stress model.

As discussed previously, the performance, or accuracy, of the finite-element technique is very much problem dependent. Bearing this in mind, where possible, the problems selected for verification have been chosen on the basis of their similarity to aspects of the Monofrax-S casting process. Moreover, the mesh densities employed in the verification are typical of those used in the full-scale Monofrax-S analysis. In this manner, the problems utilized for comparison will examine aspects of the elastic-stress model which are relevant to its

eventual application to the casting process.

5.2.2.1 Iso-Thermal Beam Deflection Problem

The first problem examined the ability of the model to predict displacements correctly in an isothermal beam subject to an external loading at one end. Unfortunately, this particular problem bears little practical resemblance (other than mechanical properties) to the Monofrax-S casting problem. Nevertheless, it serves to verify the basic load-deflection calculation.



Figure 5.14. Schematic illustration of beam bending problem employed for verification of load-deflection calculation.

An analytical solution from beam theory³² was selected for comparison. The basic problem geometry, loading and boundary conditions are presented in Figure 5.14. The finite element representation employing four eight-node two-dimensional elements in the analysis is presented in Figure 5.15. The plane-stress approximation is utilized as mentioned earlier.

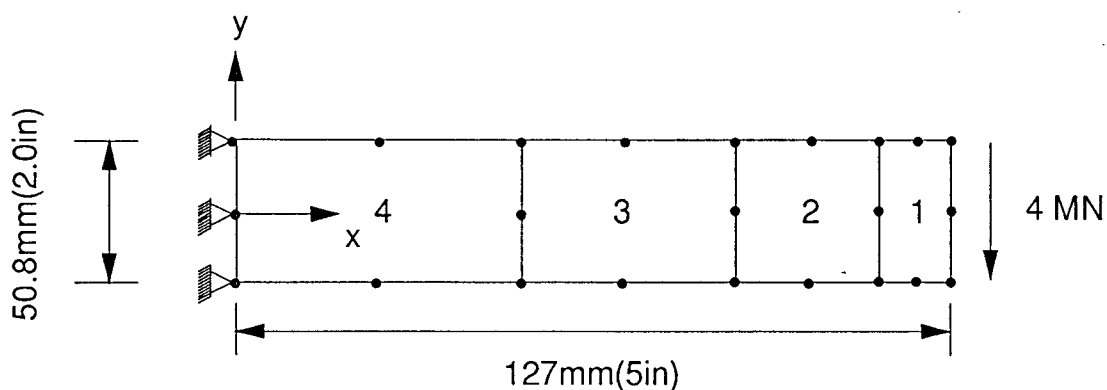


Figure 5.15. Schematic illustration of finite-element representation of beam bending problem employed for verification of load-deflection calculation.

Referring to Figure 5.15, the appropriate boundary conditions for the problem are then

$$u = 0, v = 0 \text{ at } x = 0 \quad (5.57)$$

$$F_{load} = 4\text{MN} \text{ at } x = 127\text{mm} (5.0\text{in}) \quad (5.58)$$

where, u and v are the displacements in the x and y directions respectively. A load of 4MN was chosen in order to give a moderate deflection of the beam.

From beam theory³², the equation for deflection of the beam illustrated in Figure 5.14, subject to the above boundary conditions, is

$$\delta = \frac{F_{load}x^3}{3EI} \quad (5.59)$$

where, E is the elastic modulus and

$$I = \frac{1}{12}th^3 \quad (5.60)$$

The t and h terms in Equation (5.60) are the thickness and height of the beam respectively.

The mechanical properties are presented in Table 5.4.

TABLE 5.4
Mechanical Properties for Beam Deflection Problem

E, Elastic Modulus (Monofrax-S)	100,000.MPa
ν , Poisson's Ratio (Monofrax-S)	0.15

In order to assess the performance of the model a comparison was made between the beam deflection predicted with the model and the analytical value from beam deflection theory. The vertical deflection at the tip of the beam ($x = 127\text{mm}(5.0\text{in})$) serves as the basis for this comparison. From the numerical analysis, the deflection for the three nodes located at the end of the beam, bottom to top are -2.6 , -2.54 and -2.46mm , respectively. These may be compared with the value of -2.5mm from beam theory.

As can be seen from this comparison the model is capable of predicting the load-deflection relationship in this particular problem. The difference in the model-predicted values for the three nodes located at the tip can be attributed to shear deformation. For the node located in the middle of the beam, $y = 0$, the shear deformation is near zero and hence the deflection predicted for this node is identical, to three significant figures, to the value from beam deflection theory. In order to check for any directional dependencies in the code, the problem was analyzed with the load applied in the x and y directions, separately, for the two-dimensional analysis and in the x , y and z directions, separately, for the three-dimensional analysis. For the two-dimensional case the results are identical for the two load directions examined, and for the three-dimensional case, the results were identical for the three load directions examined. There was a slight difference, as expected, between the results of the two-dimensional, plane-stress approximation and the fully three-dimensional case.

5.2.2.2 Non-isothermal Body Problem

The second problem examined the basic thermal-load/thermal-stress calculation in the model. The problem involves the application of a known temperature distribution to a section of the Monofrax-S casting subject to specific displacement boundary conditions. These boundary conditions are dictated by the limitations of the analytical solution which has been developed by applying the method of thermal strain suppression⁵⁵.

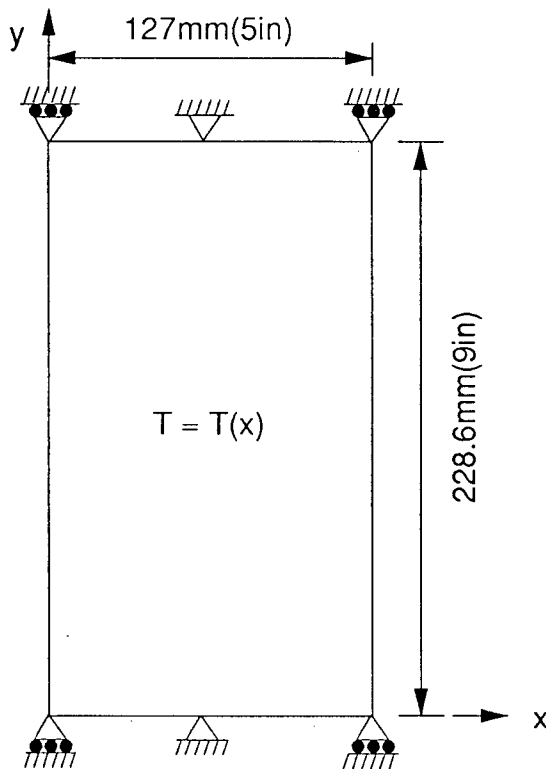


Figure 5.16. Schematic illustration of non-isothermal problem employed for verification of thermal-load/thermal-stress calculation.

The basic geometry of the problem is illustrated in Figure 5.16. The finite element representation of the same problem employing 24, eight-node, two-dimensional elements is presented in Figure 5.17. The plane-stress approximation is again adopted. The performance

of the model with this particular grid has been assessed because it is typical of those employed in the application of the model to the Monofrax-S casting analysis. Moreover, the temperature distribution was selected to produce variations in stress typical in a qualitative sense of those predicted by the model in the actual application to the Epic-3 casting process.

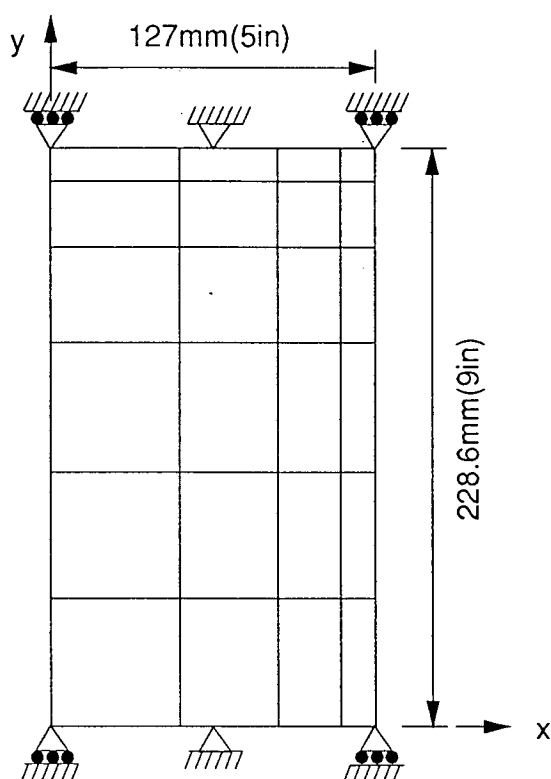


Figure 5.17. Schematic illustration of finite element representation of non-isothermal problem employed for verification of thermal-load/thermal-stress calculation.

Given the following boundary conditions and temperature distribution:

$$v = 0, \text{ at } y = 0, x = 0 - 127\text{mm}(5\text{in}),$$

$$y = 228.6\text{mm}(9\text{in}), x = 0 - 127\text{mm}(5\text{in}) \quad (5.61)$$

$$u = 0, \text{ at } x = 63.5(5\text{in}), y = 0, y = 228.6\text{mm}(9\text{in}) \quad (5.62)$$

$$T = 1000.0 - (x^2) \quad (5.63)$$

where, x is in units of millimeters and T is °C. The stress distribution in the x -direction, σ_x , is then

$$\sigma_x = \alpha E(x^2) \quad (5.64)$$

Equation (5.64) has been derived based on the assumption that the Monofrax-S is in a zero state of stress at 1000°C. The thermomechanical properties for the problem are presented in Table 5.5.

TABLE 5.5
Thermomechanical Properties for Non-isothermal Problem

Parameter	Value
E, Elastic Modulus (Monofrax-S)	100,000. MPa
ν , Poisson's Ratio (Monofrax-S)	0.15
α , Thermal Linear Expansion Coefficient	8.0×10^{-6} (°C ⁻¹)

The results of a comparison between the σ_x distribution predicted by the model and the analytical solution are presented in Figure 5.18. The output from nine nodes located over a range of x values from $x = 0.0$ to 127mm(5in) at $y = 114.3$ mm(4.5in) has been selected for the comparison. The analytical results appear as discrete points.

Based on the comparison in Figure 5.18, the model is capable of predicting the resulting stress distribution for the non-isothermal problem outlined above. As is evident from this comparison, the accuracy of the stress prediction is dependent on mesh density. For the zone with the lowest mesh density, the accuracy is reduced in comparison to that observed with the higher mesh density. This is a consequence of attempting to reproduce the quadratic variation in stress, Equation (5.64), with a linear variation in stress over the domain of the element. In order to investigate any directional dependencies, the problem was analyzed with

the boundary conditions and temperature distribution conducive to generating tensile stresses in the x and y directions, separately, for the two-dimensional analysis and x, y and z directions, separately, for the three-dimensional analysis. The results were identical to those presented in Figure 5.18.

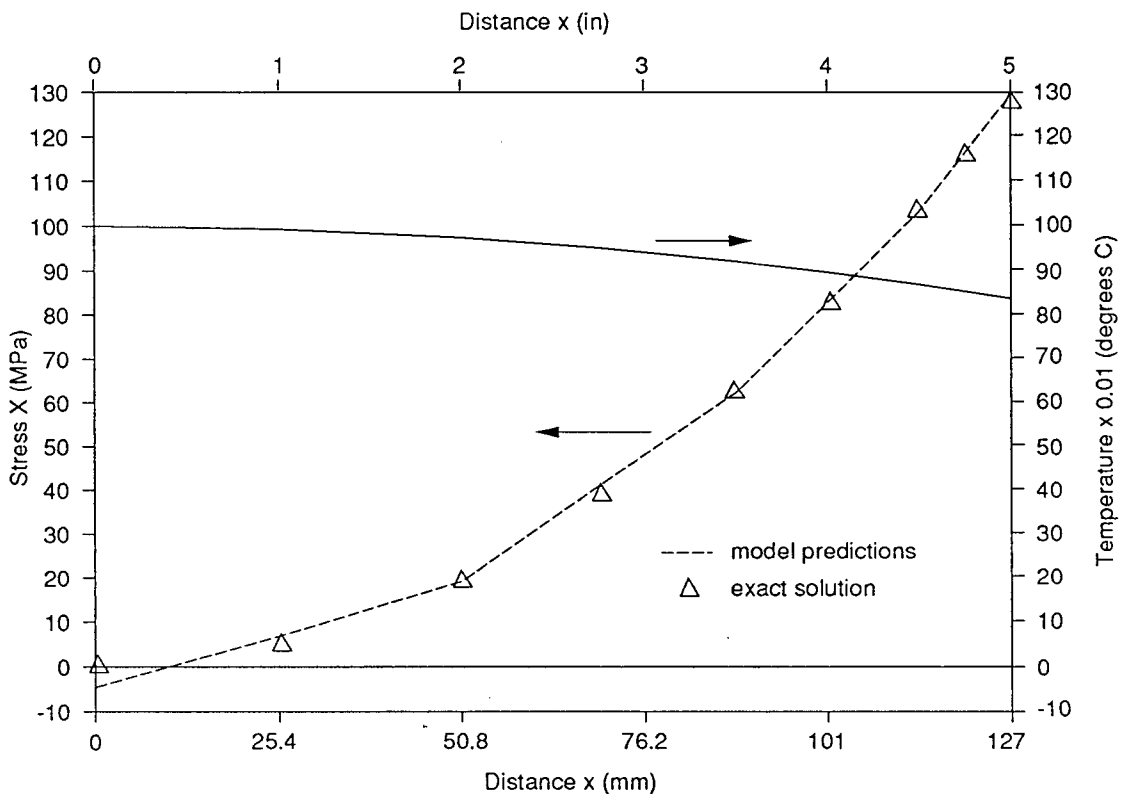


Figure 5.18. Comparison of model predictions of σ_x distribution to results of analytical solution. Note: the temperature distribution is also shown on this graph.

5.2.2.3 Summary on Basic Stress Analysis Code Verification

The results of the two previous analyses have verified the basic mathematical formulation and computer code utilized in the model stress generation. In addition, the second problem served as a means of assessing the performance of the model for the Epic-3 casting

application.

CHAPTER 6

ANALYSIS OF EPIC-3 MONOFRAX-S CASTING PROCESS

The focus of the discussion can now be shifted to the manner in which the models of heat-flow and stress generation have been applied to the analysis of the Epic-3 Monofrax-S casting process. As mentioned previously, the Epic-3 casting technique has been selected for study owing to its high propensity for crack formation. Moreover, since a statistical crack survey has been completed for this casting process (see Chapter 1) a good data base is available and can be employed, in conjunction with the numerical investigation, to develop mechanisms for crack formation.

Since the mathematical models of heat-flow and stress generation are uncoupled and distinct, the analysis was done in two stages.

6.1 Application of Thermal Model

In essence, the task of applying the thermal model requires that the Epic-3 casting process be described in mathematical terms. The resulting mathematical problem then can be analyzed with the general finite-element model developed in Chapter 5. The procedure for description of the problem includes characterization of the boundary conditions, initial conditions and material properties. Once these had been specified, an appropriate finite element spatial discretization was selected. Finally, model input parameters relevant to execution of the mathematical algorithm were input.

6.1.1 Epic-3 Boundary Conditions

In the Epic-3 casting technique, heat flows via conduction within the refractory and the mould, and is removed from the exterior surface of the mould by radiation and natural convection. To predict the thermal history in the refractory correctly, the model must therefore

consider heat flow in the surrounding mould material as well as in the casting. The principal boundary conditions are then: the refractory surface; the mould surface adjacent to the refractory (combined they make up the refractory/mould interface); and, the mould exterior.

In order to analyze this problem efficiently, heat transfer symmetry has been assumed to reduce the computational effort required. For heat flow in a transverse plane, symmetry about the x- and y-centre planes has been assumed. The resulting transverse quarter-section is illustrated schematically in Figure 6.1 - see plan view. On the symmetry boundaries a zero heat-flow or adiabatic boundary condition, Equation (6.1), has been specified.

$$q = -k \frac{\partial T}{\partial n} = 0 \quad (6.1)$$

For the fully three-dimensional problem, a third boundary of zero heat flow may be applied in the region near mid-height in the casting. Based on the results of the in-mould temperature measurements (see Chapter 4, Figure 4.4), there is little or no heat flow in the axial or z-direction for a large region which is centered about mid-height in the casting. Depending on the region of interest, the computational size of the problem can therefore be reduced to the analysis of either the top or bottom quarter section of the casting.

Initially, it is likely that heat flows across the boundary between the refractory and the mould by conduction as there is good physical contact between the liquid Monofrax-S and the mould. For some time, any shrinkage occurring in the refractory due to cooling, which could lead to formation of a gap at refractory/mould interface, will tend to be offset by thermal expansion of the mould. Eventually, however, depending on the relative rates of thermal contraction in the refractory and expansion/contraction of the mould, there could potentially be a net displacement of the refractory relative to the mould giving rise to an air gap at the

According to Thomas et al.²², the high heat-transfer rates at the interface prior to gap formation must be accounted for to predict the thermal behaviour within the cooling ingot correctly. Moreover, the thermal resistance due to air-gap formation also has a significant impact on cooling and solidification⁵⁶. Based on these findings, a time-dependent heat-transfer coefficient has been adopted for the Monofrax-S casting process. To approximate the behaviour of this interface prior to gap formation, a conductive heat transfer coefficient is utilized consistent with high heat transfer rates. Once t_{gap} has been reached (the time of gap formation), the conductive heat transfer coefficient is then reduced linearly, as a function of time, until its value is exceeded by an effective heat transfer coefficient due to radiation which then is assumed to become the dominant mode of heat transfer.

The boundary condition which has been employed to describe heat transfer at the refractory/mould interface is

$$q = -k \frac{\partial T}{\partial n} = h_{gap} (T_s - T_\infty) \quad (6.2)$$

where for elapsed times less than t_{gap}

$$h_{gap} = h_{cond} \quad (6.3)$$

and for elapsed times greater than t_{gap} , h_{coeff} is the larger of

$$h_{gap} = h_{cond} - f_{ramp} (t - t_{gap}) \quad (6.4)$$

or

$$h_{gap} = \frac{1}{\left(\frac{1-\epsilon_1}{\epsilon_1} + \frac{1-\epsilon_2}{\epsilon_2} + 1 \right)} \sigma \frac{(T_s^4 - T_\infty^4)}{(T_s - T_\infty)} \quad (6.5)$$

Note that Equation (6.5) applies for two parallel plates exchanging radiation that are in close proximity with one another (edge effects can be neglected) and are behaving as gray radiative bodies.

To serve as a starting point, a value of $4000 \text{ W/m}^2 \cdot ^\circ\text{C}$ was assumed for the conductive heat-transfer coefficient, h_{cond} , which is consistent with values reported in the literature⁵⁶ for metal castings. The time for gap formation, t_{gap} was assumed to be 3600 s or 1 hr. The rate of decrease of h_{cond} (which is dictated by the magnitude of f_{ramp}) was assumed to be $1.1 \times 10^{-03} \text{ W/m}^2 \cdot ^\circ\text{C} \cdot \text{s}$ in order to result in a change in h_{cond} of about $4000 \text{ W/m}^2 \cdot ^\circ\text{C}$ in about 10 hrs. The normal emissivities for Monofrax-S and silica sand, ϵ_1 and ϵ_2 respectively, are assumed to be equal to that of fused rough quartz, 0.93⁵¹. The validity of these assumptions and the validity of the application of information from metals casting processes will be examined later in Section 6.1.5. where the sensitivity analysis and the comparison between industrial data and model predictions are discussed.

To implement this heat-transfer coefficient boundary condition, duplicate nodes have been specified at the refractory/mould interface for those element faces which lie on the boundary. Hence, the driving force for heat conduction across the interface is the temperature difference between pairs of nodes located at the same location belonging to either a refractory element or mould element. In Equations (6.2) and (6.5), the terms T_s and T_∞ then represent either the refractory surface and mould surface temperatures or mould surface and refractory surface depending on whether the element forms part of the refractory surface or mould surface, respectively. Within the elemental integration scheme these temperatures are evaluated at the appropriate Gauss integration points on the boundary element surfaces.

The final boundary condition which has been characterized for the Epic-3 casting process is the mould exterior. On this boundary, heat is conducted from the mould to its surroundings by natural convection and radiation. The boundary condition which is applied to the mould exterior is

$$q = -k \frac{\partial T}{\partial n} = h_{ext}(T_s - T_\infty) \quad (6.6)$$

where, h_{ext} is the overall heat transfer coefficient due to radiation and natural convection:

$$h_{ext} = h_{conv} + h_{rad} \quad (6.7)$$

The first term in Equation (6.7) has been evaluated based on an empirical expression for free-convection for vertical planes and cylinders^{51,69}.

$$h_{conv} = k_{air} \frac{\overline{Nu}_L}{L} \quad (6.8)$$

where, the Nusselt number under conditions of laminar flow is

$$\overline{Nu}_L = 0.555(Gr_L Pr_L)^{1/4} \quad (6.9)$$

and L is defined as the characteristic length of the system. It was verified that the product of the Grashof and Prandtl numbers did not exceed 10^9 indicating the onset of turbulent flow. For the Epic-3 casting process L is assumed to be equal to half of the height of one of the lower flasking segments, approximately 150mm(6in), owing to the presence of the horizontal ridges separating the segments - see Figure 6.1. The expressions for the Prandtl and Grashof numbers are, respectively,

$$Pr = \frac{C_{p,air} \mu_{air}}{k_{air}} \quad (6.10)$$

$$Gr_L = \beta g \rho_{air}^2 \frac{(T_{surface} - T_{\infty})}{\mu_{air}^2} L^3 \quad (6.11)$$

where,

$$\beta = \frac{\rho_{\infty} - \rho}{\rho(T_{surface} - T_{\infty})} \quad (6.12)$$

In Equations (6.8), (6.10) and (6.11) the thermophysical properties of air are evaluated at the mean film temperature.

In the three-dimensional analysis, where the top and bottom external surfaces of the mould must be considered, the above relationships for natural convection for vertical plates and cylinders are assumed to hold. The second term in Equation (6.7), h_{rad} , is evaluated from the expression

$$h_{radiation} = \varepsilon \sigma \frac{(T_{surface}^4 - T_{\infty}^4)}{(T_{surface} - T_{\infty})} \quad (6.13)$$

where, ε is the emissivity of the mild steel mould flasking and is assumed to be equal to 0.94⁵¹. The mild steel flasking is assumed to behave as a gray radiative body.

The above expressions, Equations (6.1) - (6.13), complete the mathematical description of the boundary conditions utilized in the thermal model to describe the Monofrax-S casting process.

6.1.2 Initial Conditions

In the Epic-3 casting technique, molten or liquid Monofrax-S is poured from the electric furnace directly into the mould which is at ambient temperature. As mentioned earlier, after pouring is completed, the casting is left to cool for a period of time until a re-pour is

carried out. In this procedure, the casting is re-positioned under the furnace pour spout and liquid Monofrax-S is added to the top of the casting to reduce the size of the shrinkage cavity. The casting is then moved to a location where it is left to cool.

To avoid the added complexity of modelling the actual pouring event, the numerical analysis commences with the pour complete. The Monofrax-S is assumed to be initially at the pour temperature and the surrounding moulding material at ambient temperature. In addition, the re-pour event and any effect that it has on the thermal history of the refractory has been ignored. From the industrial measurements made on the instrumented Epic-3 (see Chapter 4) the initial conditions are then

$$T_{Monofrax-S} = 1875^{\circ}C, t = 0 \quad (6.14)$$

$$T_{Mould} = 25^{\circ}C, t = 0 \quad (6.15)$$

$$T_{\infty} = 25^{\circ}C, t \geq 0 \quad (6.16)$$

6.1.3 Material Properties

Having completed the characterization of the boundary and initial conditions, the focus is now shifted to material property characterization. For the thermal analysis, thermophysical data is necessary for both the Monofrax-S and the surrounding mould materials. For those data which are a function of temperature, the model has been formulated to accept the data in the form of a polynomial.

As outlined in Chapter 3, owing to a paucity of thermophysical and thermomechanical data for Monofrax-S in the literature, a parallel programme for material property evaluation was initiated by Carborundum at the beginning of the research programme. Unfortunately, the extreme temperatures involved presented a significant obstacle to data generation and not all of the necessary information could be obtained within the time frame of the project. In

those instances where data is not available, or is only partially available (limited temperature range), estimates and extrapolations have had to be made, respectively. In general, the extrapolations have been made on the basis of the low-temperature behaviour of the material.

6.1.3.1 Thermophysical Properties of Monofrax-S (AZS-CS3)

For Monofrax-S (AZS-CS3), the thermal diffusivity, heat capacity and density have been evaluated as a function of temperature. The source for thermal diffusivity and heat capacity data is Virginia Polytechnic Institute⁷⁰, and for the density data, Harrop Industries⁷¹. (The information from these reports was provided in the form of a summary by Lebold⁷⁶. Unfortunately, the summary did not contain reference to the techniques employed for measuring these data nor to an estimate of the accuracy of the measurements.) This data has been utilized to calculate a thermal conductivity which is employed in the model. The approach taken for this calculation was to assume that the density was constant and independent of temperature consistent with the requirement of the fixed mesh utilized in the analysis. In this manner, the combination of density, heat capacity and thermal conductivity yield the correct value for the thermal diffusivity.

The measured thermal diffusivity, heat capacity, density and calculated effective thermal conductivity for Monofrax-S (AZS-CS3) are presented in Table 6.1 as a function of temperature. Based on these data, a series of polynomials have been developed which describe the variation in the material properties with temperature from 0 to 1900°C. The correlations, which serve as input to the thermal model, are presented in Equations (6.17)-(6.21) with temperature in °C. An average value of 3650.0 kg/m³ was adopted for the density. A comparison between the original measured data and the model input data obtained from the correlations is shown in Figures 6.2-6.5.

TABLE 6.1
Thermophysical Properties of Monofrax-S (AZS-CS3)

Temperature (°C)	Thermal Diffusivity ⁷⁰ α (m ² /s)	Heat Capacity ⁷⁰ C_p (kJ/kg·°C)	Density ⁷¹ ρ (kg/m ³)	Thermal Conductivity $k^{70,71}$ (W/m·°C)
25	26.8x10 ⁻⁷	.666	3702	6.52
100	23.5x10 ⁻⁷	.762	3695	6.53
200	18.42x10 ⁻⁷	.838	3691	5.63
300	15.7x10 ⁻⁷	.885	3682	5.07
400	13.67x10 ⁻⁷	.930	3674	4.64
500	11.08x10 ⁻⁷	.947	3664	3.83
600	8.97x10 ⁻⁷	.962	3655	3.15
700	8.15x10 ⁻⁷	.975	3644	2.90
800	7.27x10 ⁻⁷	.986	3631	2.62
900	7.02x10 ⁻⁷	.996	3621	2.55
1000	7.41x10 ⁻⁷	1.005	3615	2.72
1100	7.94x10 ⁻⁷	1.013	3630	2.93
1200	8.22x10 ⁻⁷	1.020	3626	3.06
1300	8.41x10 ⁻⁷	1.026	3615	3.15
1400	8.49x10 ⁻⁷	1.032	3604	3.20
1500	8.19x10 ⁻⁷	1.038	3594	3.10

Heat Capacity (kJ/kg·°C)For temperature range $0 \leq T \leq 500^\circ\text{C}$

$$C_{P_{\text{Monofrax-S}}} = 0.65 + 1.16 \times 10^{-3}T - 1.15 \times 10^{-6}T^2 \quad (6.17)$$

For temperature range $500 < T \leq 1900^\circ\text{C}$

$$C_{P_{\text{Monofrax-S}}} = 0.91 + 8.85 \times 10^{-5}T \quad (6.18)$$

Density (kg/m³)For temperature range $0 \leq T \leq 1900^\circ\text{C}$

$$\rho_{\text{Monofrax-S}} = 3650 \quad (6.19)$$

Thermal Conductivity (W/m·°C)For temperature range $0 \leq T \leq 650^\circ\text{C}$

$$k_{\text{Monofrax-S}} = 6.90 - 6.08 \times 10^{-3}T \quad (6.20)$$

For temperature range $650 < T \leq 1900^\circ\text{C}$

$$k_{\text{Monofrax-S}} = 3.0 \quad (6.21)$$

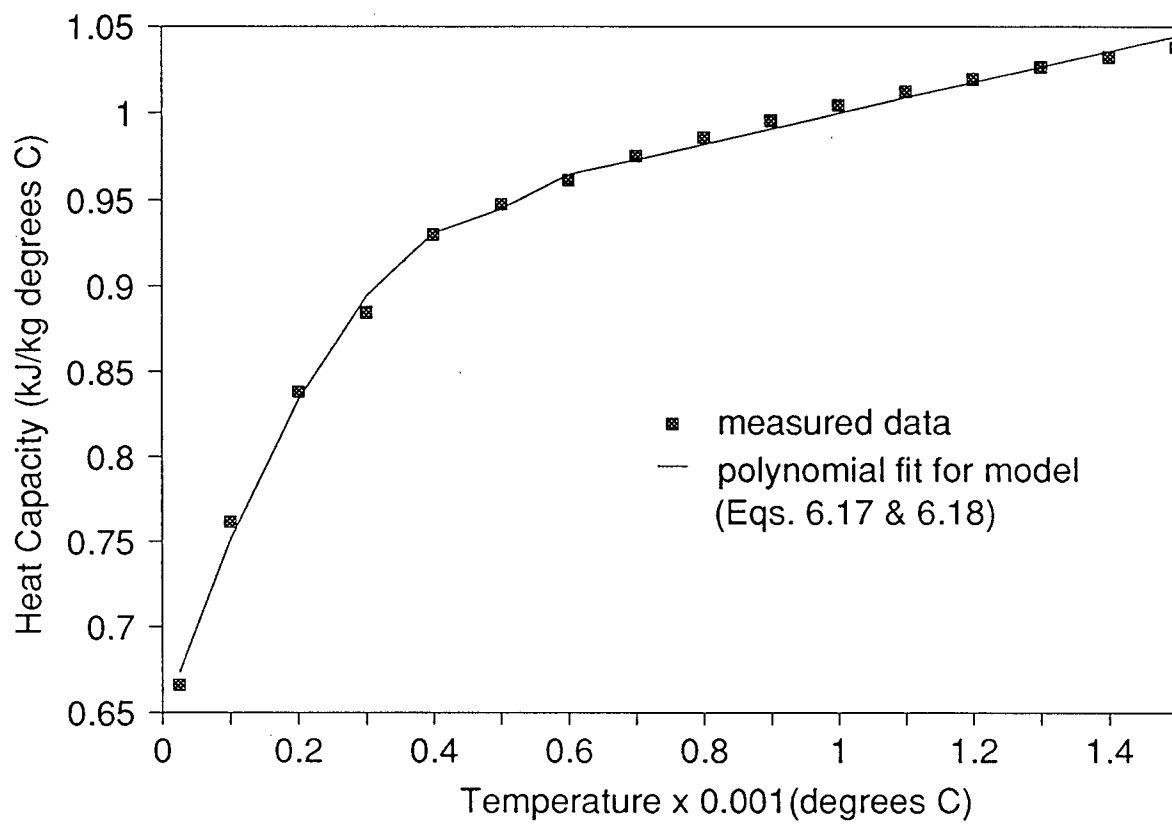


Figure 6.2. Measured heat capacity data as a function of temperature and polynomial fit for Monofrax-S(AZS-CS3).

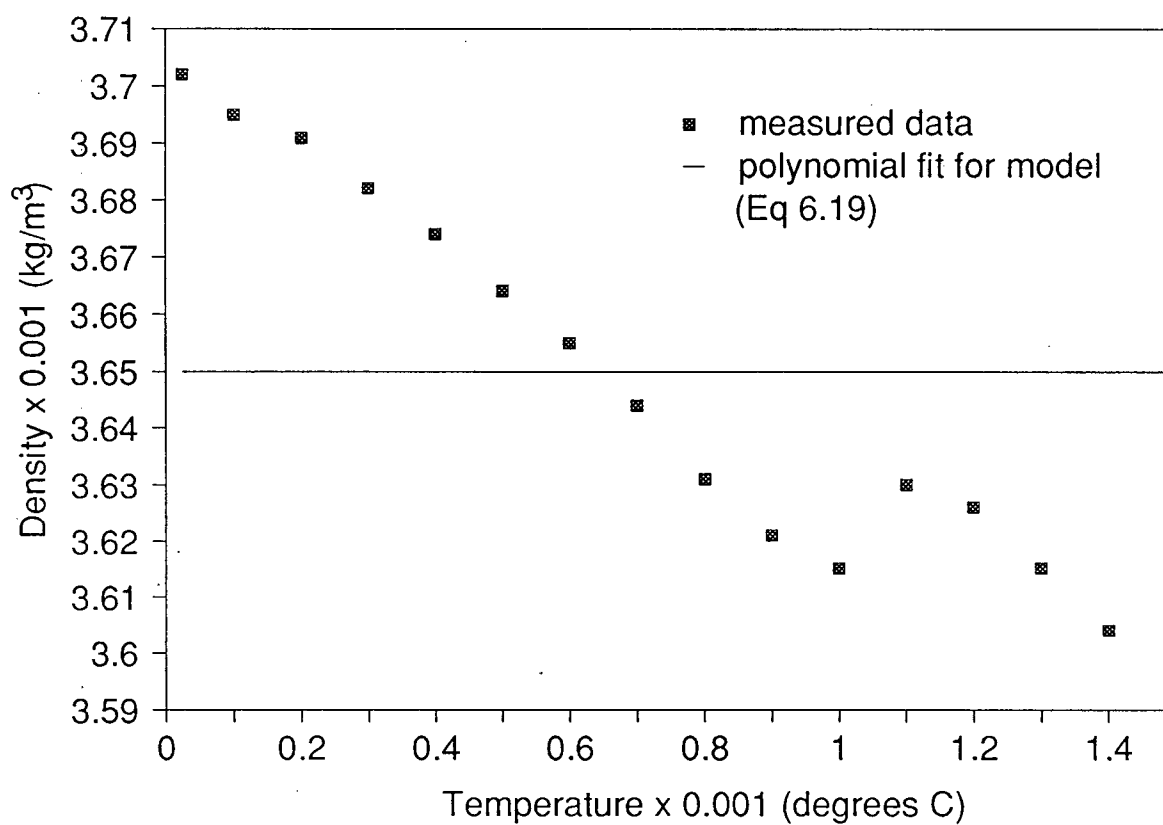


Figure 6.3. Measured density data as a function of temperature and polynomial fit for Monofrax-S(AZS-CS3).

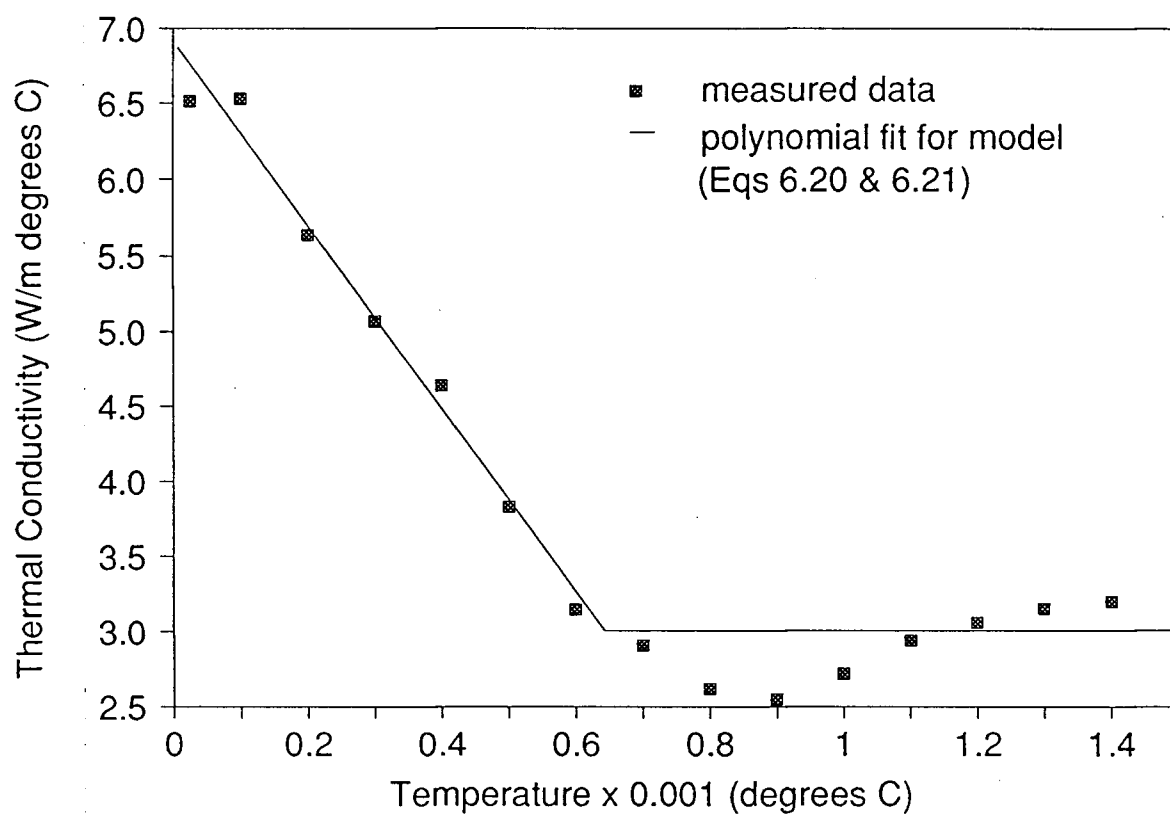


Figure 6.4. Measured thermal conductivity data as a function of temperature and polynomial fit for Monofrax-S(AZS-CS3).

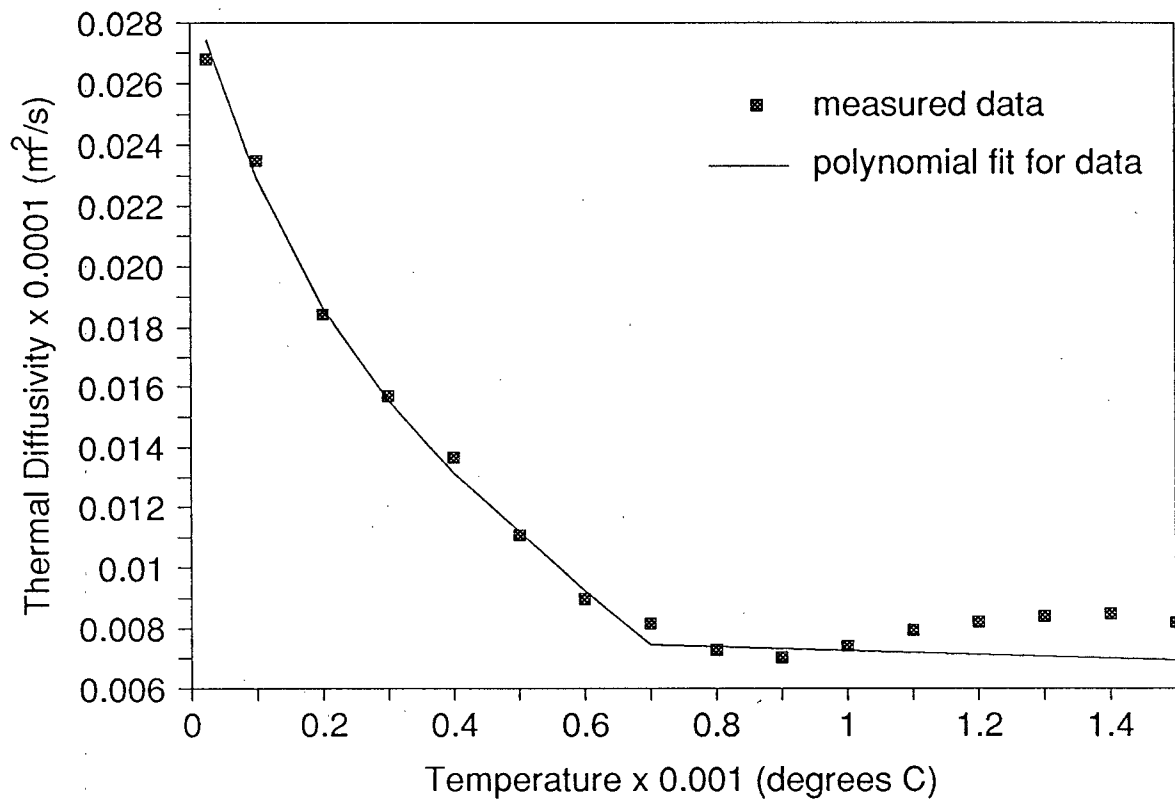


Figure 6.5. Measured thermal diffusivity data and as a function of temperature and polynomial fit for Monofrax-S(AZS-CS3).

As discussed in Chapter 5, Section 5.1.1.6, the enthalpy technique was employed for latent heat evolution. Within the model, the enthalpy method for calculation of a modified heat capacity is implemented for those elements which have a node above or within the liquidus-solidus temperature gap. Once through the phase change temperature range, the enthalpy technique is bypassed and the correlation for heat capacity is employed for evaluation of the heat capacity which requires less computational effort.

For evaluation of the enthalpy function, a heat capacity, solidus and liquidus temperature and latent heat of solidification are required. To simplify the calculation, a constant value of 1.03 (kJ/kg·°C) was adopted for the heat capacity of Monofrax-S over the phase change interval based on the data presented in Figure 6.2. Owing to a lack of data, the solidus and liquidus temperature and latent heat of solidification were estimated - refer to Section 5.1.2.2. Monofrax-S is assumed to solidify over a temperature range from 1810 to 1780°C and release 760 kJ/kg of heat. The resulting enthalpy function, Equations (6.22) - (6.24) is presented graphically in Figure 6.6.

Enthalpy Function (kJ/kg)

For temperature range $0 \leq T \leq 1780^\circ\text{C}$

$$H_{\text{Monofrax-S}} = -25.75 + 1.03T \quad (6.22)$$

For temperature range $1780 < T \leq 1810^\circ\text{C}$

$$H_{\text{Monofrax-S}} = -43285.8 + 25.3T \quad (6.23)$$

For temperature range $1810 < T \leq 1900^\circ\text{C}$

$$H_{\text{Monofrax-S}} = -703.35 + 1.03T \quad (6.24)$$

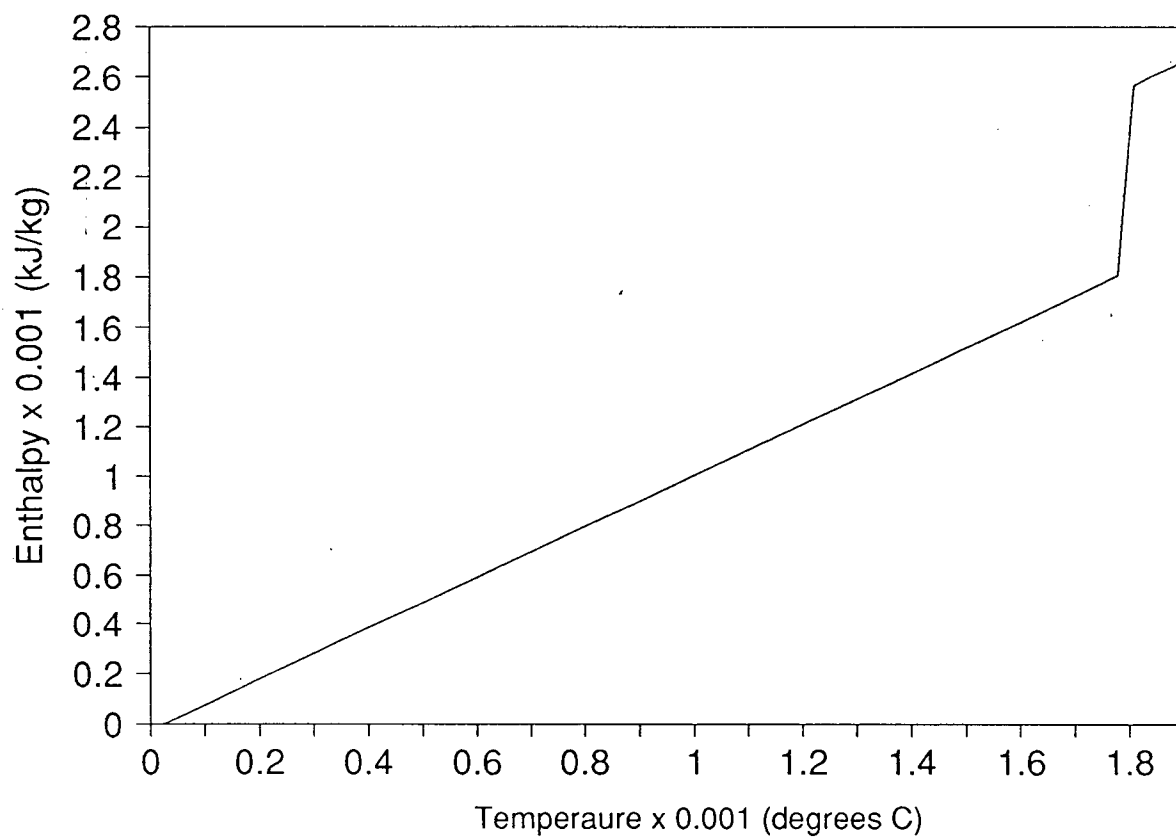


Figure 6.6. Enthalpy function for Monofrax-S(AZS-CS3) employed in the thermal model (Eqs.(6.22) to (6.24)).

6.1.3.2 Thermophysical Properties of Bonded and Annealing Sand

For the moulding materials (bonded and annealing sands) a combination of data obtained from the evaluation programme and from the literature⁷⁰ have been employed in the model. Tables 6.2 and 6.3 present the measured thermal conductivity data for bonded and annealing sands, respectively, obtained at the Ohio State University Refractories Research Center⁷². Unfortunately, the report⁷² does not include a description of the experimental technique employed or an estimate of the accuracy of the measurements. The bulk density for both the bonded sand and annealing sand was reported to be 1620 kg/m^3 . Typical chemical analysis of the base sand, which is used for both the bonded and annealing sand, is presented in Table 6.4. The assay indicates that the sand is almost pure silica. (For the bonded sand, an addition of sodium silicate is made to act as the binding agent.) During the Ohio State University analysis⁷², it was noted that both the bonded and annealing sands underwent a significant volume expansion with increasing temperature, to the extent that the lid of the container in which the sample was being held, was raised.

Based on the data presented in Tables 6.2 and 6.3, correlations have been developed to describe the temperature dependency of the thermal conductivity. A comparison between the original data and the correlations for the bonded and annealing sands, Equations (6.25)-(6.27), is presented in Figure 6.7 and 6.8, respectively. A constant density of 1620 kg/m^3 was assumed for both types of sand consistent with the requirements of the fixed grid analysis and is based on the Ohio State measurements⁷². Finally, a correlation for the variation in the heat capacity of silica sand with temperature has been obtained from the literature⁷³. The correlation, which serves as input to the model, is presented in Equations (6.29)-(6.30) and Figure 6.9.

Thermal Conductivity of Bonded Sand (W/m·°C)For temperature range $0 \leq T \leq 313^\circ\text{C}$

$$k_{\text{bonded sand}} = 0.251 \quad (6.25)$$

For temperature range $313 \leq T \leq 1900^\circ\text{C}$

$$k_{\text{bonded sand}} = -0.0425 + 8.82 \times 10^{-4}T \quad (6.26)$$

Thermal Conductivity Annealing Sand (W/m·°C)

$$k_{\text{annealing sand}} = 0.0996 + 6.39 \times 10^{-4}T \quad (6.27)$$

Density Bonded and Annealing Sand (kg/m³)

$$\rho_{\text{sand}} = 1620. \quad (6.28)$$

Heat Capacity of Bonded and Annealing Sand (kJ/kg·°C)For temperature range $0 \leq T \leq 750^\circ\text{C}$

$$C_{p_{\text{sand}}} = 0.821 + 8.51 \times 10^{-4}T - 5.40 \times 10^{-7}T^2 \quad (6.29)$$

For temperature range $750 \leq T \leq 1900^\circ\text{C}$

$$C_{p_{\text{sand}}} = 1.090 + 8.68 \times 10^{-5}T \quad (6.30)$$

TABLE 6.2
Thermal Conductivity of Bonded Sand⁷²

Temperature (°C)	Thermal Conductivity (W/m·°C)
88.9	0.251
313.3	0.256
673.9	0.510
1081.7	0.931

TABLE 6.3
Thermal Conductivity of Annealing Sand⁷²

Temperature (°C)	Thermal Conductivity (W/m·°C)
92.9	0.192
318.3	0.291
686.1	0.480
1089.4	0.832

TABLE 6.4
Typical Composition of Base Sand⁷²

Component	Weight %
SiO ₂	99.88
Fe ₂ O ₃	0.02
Al ₂ O ₃	0.10
TiO	0.015
CaO	0.015
MgO	0.005
LOI	0.080

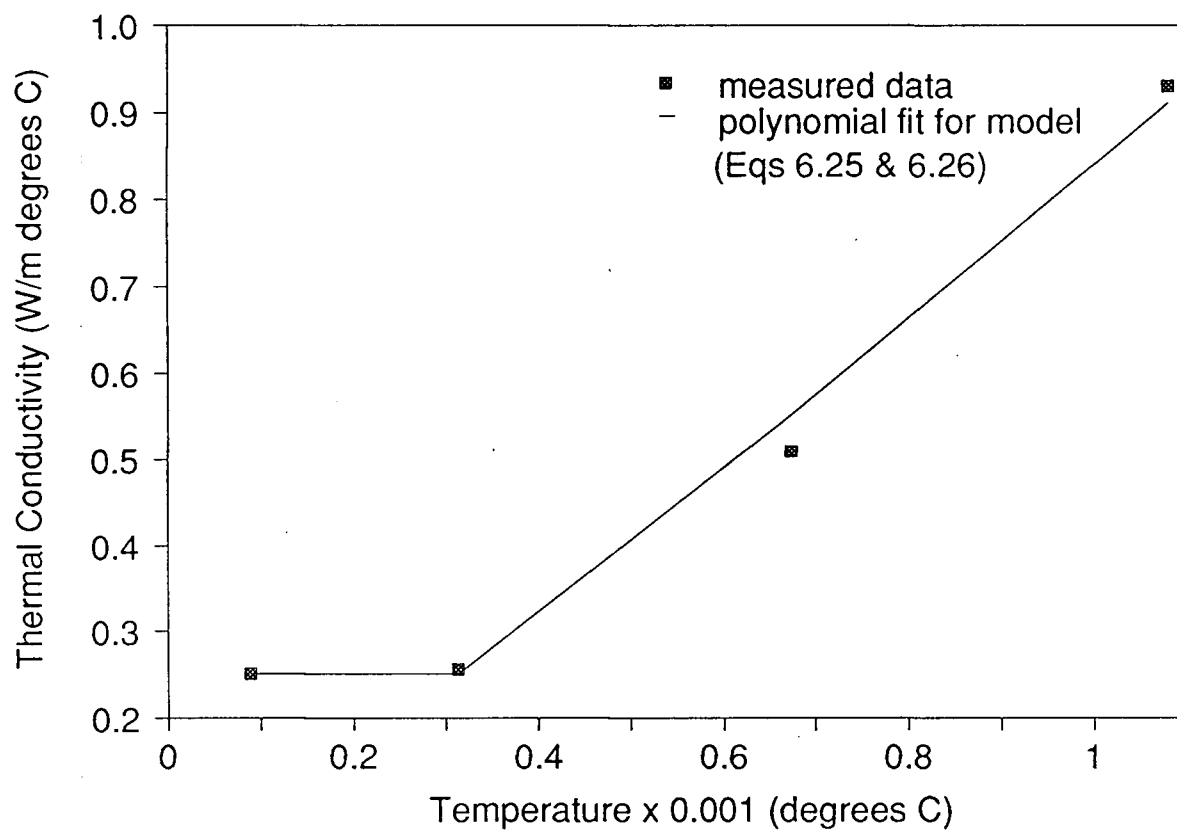


Figure 6.7. Measured thermal conductivity data as a function of temperature and polynomial fit for bonded sand.

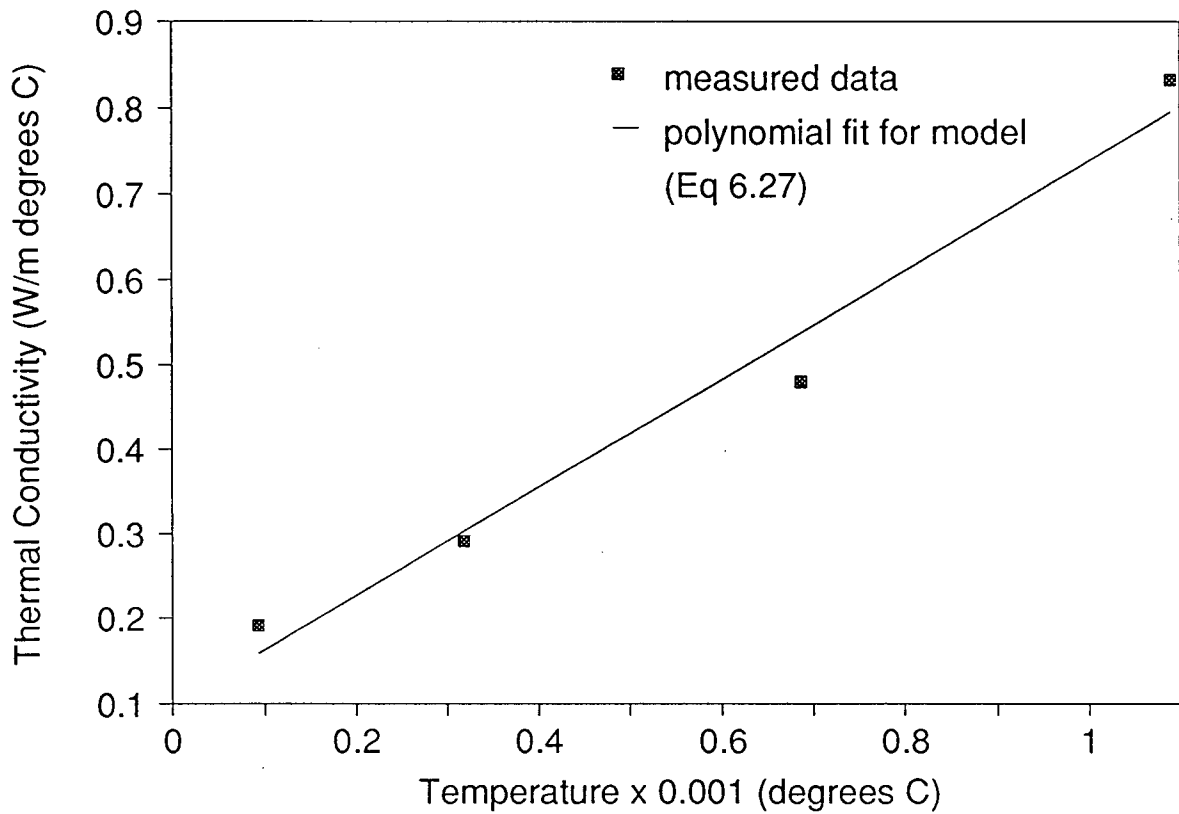


Figure 6.8. Measured thermal conductivity data as a function of temperature and polynomial fit for annealing sand.

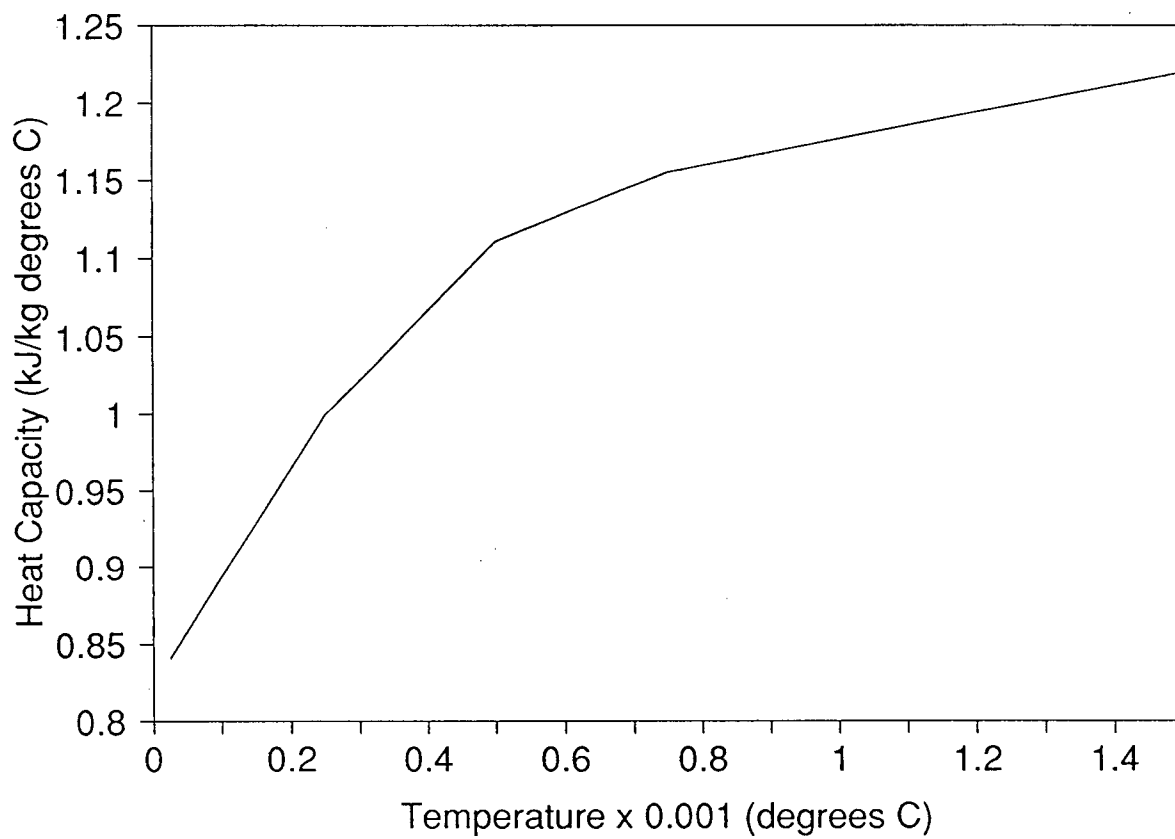


Figure 6.9. Heat capacity as a function of temperature for silica sand, input to the model (Eqs. (6.29) and (6.30)).

6.1.4 Finite-Element Spatial Discretization.

Once the region to be analyzed has been defined through specification of the boundary conditions and material properties, an appropriate spatial discretization, or mesh, can be selected. This final step completes the mathematical description of the problem.

Based on the frequency distribution of Type-A cracks (refer to Figure 1.4, Chapter 1), the lower quarter-section of the casting was selected for analysis. As can be seen from Figure 6.10, this region encompasses those zones where the Type-A1, A2, B and E cracks are routinely observed.

In geometrically large problems, such as the analysis of the lower quarter-section of the Epic-3 casting, selection of an appropriate spatial discretization often requires that a trade off is made between the desire for accuracy (high-density mesh) and need for computational efficiency (low-density mesh). Moreover, the upper limit in problem size is usually dictated by computational hardware constraints. In this application, in order to maintain reasonable job execution times, the problem size was limited to the amount of RAM memory available to the computational engine. For the lower quarter section, this limit (approximately 55 Mega-Bytes with the current facility) was reached when 24 layers of three-dimensional elements (in the pattern of the base grid illustrated in Figure 6.11) were stacked on top of one another. The resulting three-dimensional mesh contained a total of 3048 elements comprised of 14,771 nodes. Of these, 432 elements (2397 nodes) make up the refractory.

Given the practical constraint on mesh size, an attempt has been made to improve the accuracy through the utilization of a varying mesh density. As can be seen in Figure 6.11, higher mesh densities have been employed in those regions where temperature gradients are expected to be the largest, such as in the vicinity of the refractory/mould interface, where as, low densities have been utilized near the mould exterior where thermal gradients will be less

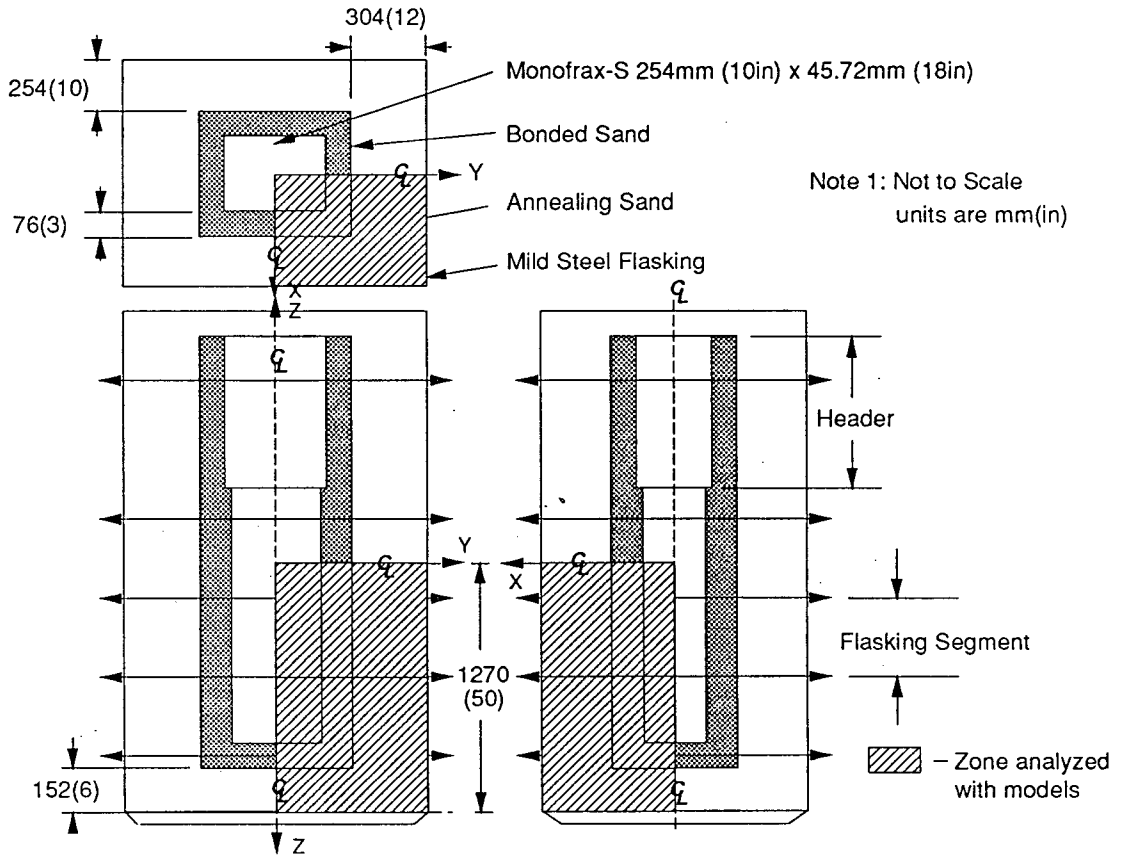


Figure 6.10. Schematic illustration of section of Epic-3 casting analyzed with heat-flow model.

severe. For the base of the mould, higher densities have been achieved at the refractory/mould interface by reducing the vertical distance between nodes while maintaining the same overall two-dimensional pattern of elements.

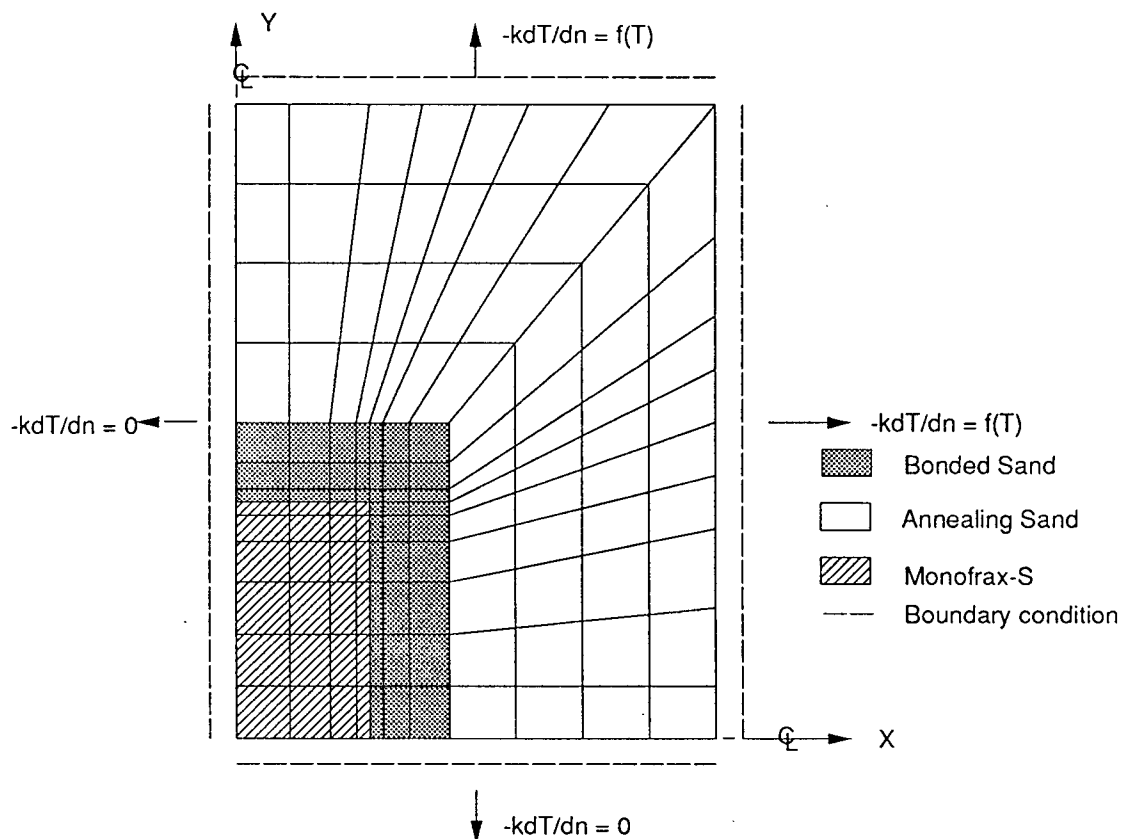


Figure 6.11. Schematic illustration of the transverse (x/y) section of the three-dimensional mesh employed in the thermal analysis.

6.1.5 Sensitivity Analysis, Comparison to Industrial Data and Alignment of the Heat-Flow Model to the Industrial Process.

The first few runs with heat-flow model were utilized to conduct a sensitivity analysis on model input parameters. On the basis of the results of this analysis, the model input parameters were then "fine tuned" in order to bring the model predictions more in line with the industrial measurements.

Owing to the fact that multiple executions of the program were made, the sensitivity analysis, comparison to the industrial data and model adjustment procedure have been restricted to two-dimensions in order to give a reasonable program execution time. A transverse section of the mesh utilized in the three-dimensional analysis, Figure 6.11, was employed in the two-dimensional analyses. The two-dimensional grid contained a total of 443 nodes and 127 elements.

6.1.5.1 Sensitivity Analysis

The focus of the investigation was on those parameters which are not well defined and on the identification of potential sources of error in the model predictions. The sensitivity analysis was conducted on the parameters which characterize the material properties and the boundary conditions, and, are relevant to execution of the numerical algorithm.

The sensitivity of the model has been assessed on the basis of comparisons to the standard case predictions for selected nodes - see Figure 6.12. The standard case serves as a point of reference and is defined to be a 24 hr simulation with the model employing the input parameters as defined thus far. The nodes have been selected to coincide with the locations of thermocouples. For execution of the standard simulation, the maximum temperature change per time-step, T_{\max} , has been set to 5°C - refer to Section 5.1.1.5 of model formulation for discussion of this parameter.

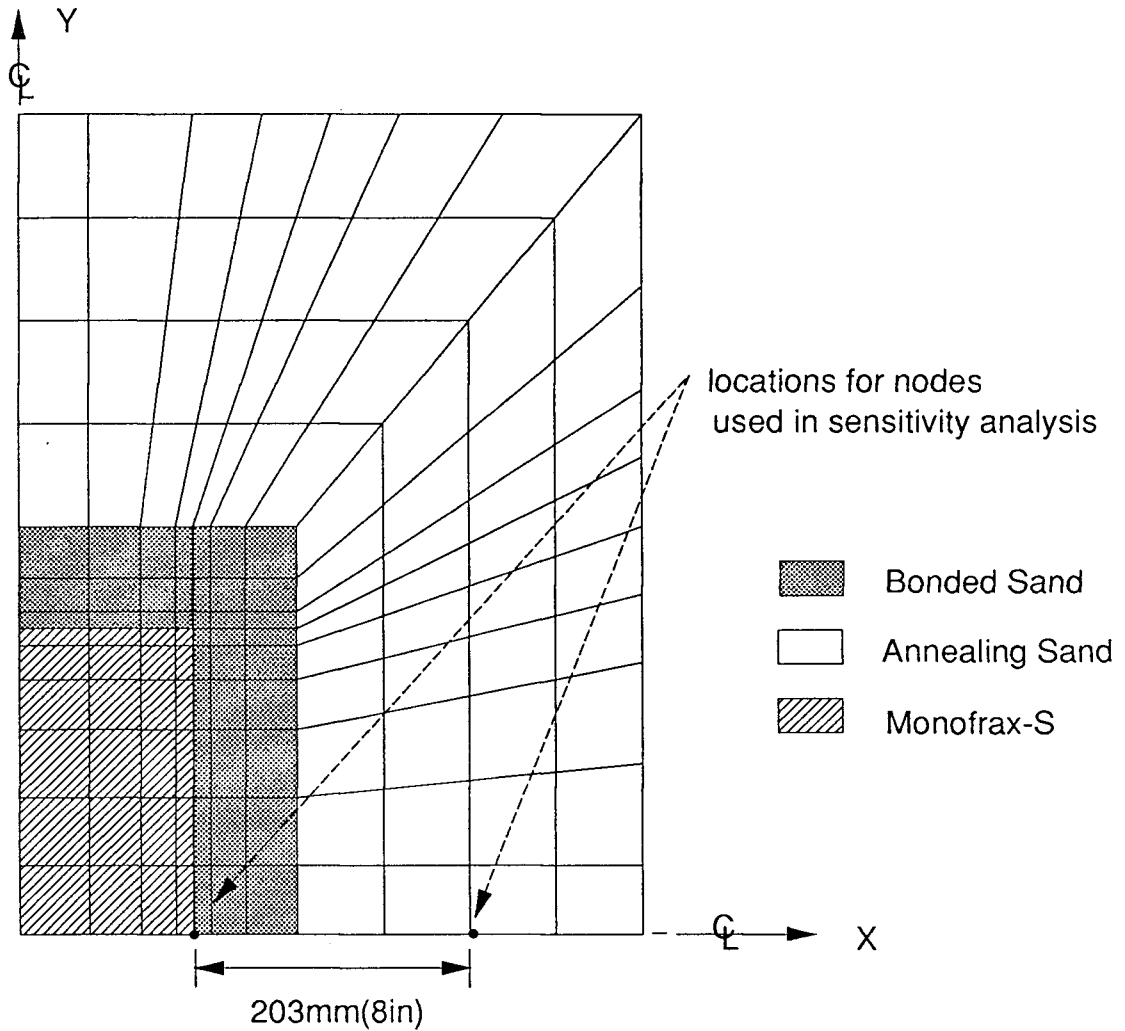


Figure 6.12. Location of nodes utilized in sensitivity analysis

[i] Heat of Solidification of Monofrax-S.

As discussed earlier, the latent heat of solidification of Monofrax-S was estimated with a crude rule of mixtures approach - see section 6.1.2.2. The solidified structure of Monofrax-S, however, suggests a complex solidification sequence. Thus the rule-of-mixtures

approach will yield only a rough estimate of the amount of heat released during solidification. To investigate the sensitivity of the model to this parameter, the input value has been varied arbitrarily by a factor two relative to the standard input value of 760 kJ/kg. The results for the three cases are shown in Figure 6.13.

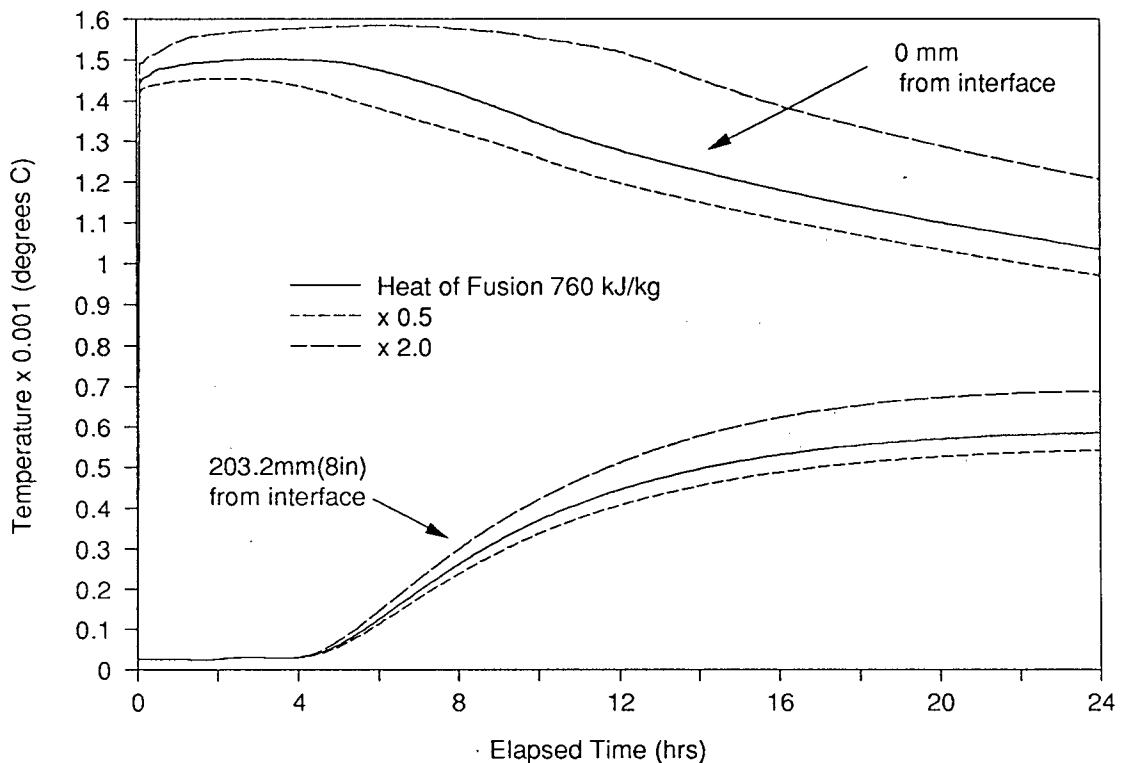


Figure 6.13. Model sensitivity to latent heat of fusion of Monofrax-S.

The behaviour exhibited in Figure 6.13 indicates a relatively high degree of sensitivity to this parameter. Doubling the latent heat of fusion results in roughly a 20% increase in the mould temperature at the refractory/mould interface at 24 hrs elapsed time. Alternatively, halving the heat of fusion decreased the mould temperature at the interface by less than 10%. As expected, the temperature responses predicted by the model are elevated with increasing

latent heat. Moreover, for the node located at the mould/refractory interface, there is a general broadening of the temperature peak as the latent heat is increased. Clearly, any error in the magnitude of this parameter will have a significant impact on the model predictions and therefore on the accuracy of the model.

[ii] Solidus-Liquidus Temperature Gap.

In addition to estimating the amount of latent heat, it has also been necessary to estimate the temperature range over which this heat is released. For Monofrax-S, the liquidus and solidus temperatures have been estimated from the $\text{Al}_2\text{O}_3\text{-ZrO}_2\text{-SiO}_2$ ternary phase diagram²⁴ to be 1810 and 1780°C, respectively. The sensitivity of the model to T_{gap} (the difference between the solidus and liquidus temperatures) has been investigated by holding the liquidus temperature constant and varying the solidus temperature such that T_{gap} is altered arbitrarily by a factor of two. The results of this comparison are presented in Figure 6.14.

As can be seen, the model predictions show a moderate sensitivity to the magnitude of T_{gap} . Doubling the solidification temperature range results in roughly a 10% increase in mould temperature at the refractory/mould interface at 24 hrs elapsed time. Alternatively, halving this temperature range reduces the mould temperature at the interface by less than 10%. The effect of decreasing T_{gap} is similar to that observed for a decrease in the latent heat of fusion - see Figure 6.13. Releasing the latent heat over a smaller temperature range should slightly increase temperature gradients within the refractory block and have only a small impact on the interfacial temperature. One plausible explanation for the observed behaviour, is error in the numerical technique which accounts for the release of latent heat. It is well documented⁴¹ that latent heat evolution becomes difficult to handle numerically when the phase change interval, T_{gap} , becomes small. The relationship between the size of T_{gap} and the

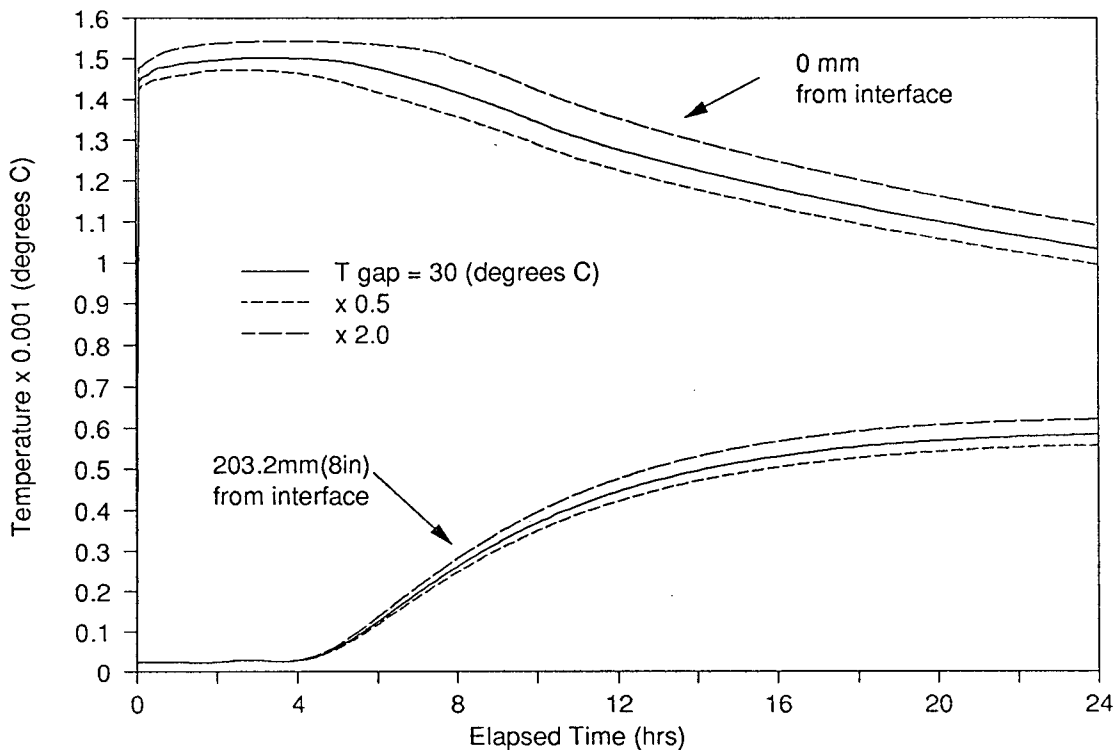


Figure 6.14. Model sensitivity to liquidus-solidus temperature gap, T_{gap} .

magnitude of the numerical error will be dependent on such factors as mesh density (see section 5.1.2.2) and the amount of latent heat released. It is likely that the enthalpy technique for latent heat evolution, utilized in the heat-flow model, is underestimating the latent heat released for values of T_{gap} less than 60°C . This hypothesis is supported by the fact that an increase in T_{gap} beyond 60°C does not result in an appreciable change in the model predictions (not shown).

[iii] Refractory/Mould Interface Boundary Condition.

In order to provide a starting point for the Monofrax-S casting analysis, several assumptions have been made about the manner in which heat flows across the refractory/mould interface. Referring to section 6.1.1, Equation (6.4), the key parameters are: h_{cond} ,

magnitude of heat transfer coefficient due to conduction; t_{gap} , time for gap formation, and; f_{ramp} , rate of decrease of h_{cond} . To determine the sensitivity of the model to these parameters, the magnitude of each, in turn, has been varied arbitrarily by a factor of two relative to the standard case. The results of the analysis are presented in Figures 6.15, 6.16 and 6.17.

Based on the comparison presented in Figure 6.15, model sensitivity to the magnitude of h_{cond} is relatively high. Most notably, a large change in model predictions are observed for the case where h_{cond} has been increased from 4000 to 8000 $\text{W/m}^2 \cdot ^\circ\text{C}$. Doubling h_{cond} results in a significant increase in the rate of supply of heat to the mould. This results in a 20% increase in the mould temperature at the refractory/mould interface at 24hrs elapsed time. It is also interesting to note that, until approximately 5 hrs. elapsed time, the model is not sensitive to variations in this parameter. The peak temperatures achieved in the mould at the refractory/mould interface are almost identical.

The effect of varying the time for gap formation, t_{gap} , is presented in Figure 6.16 where it is evident that, for the range of t_{gap} investigated, the model predictions are not sensitive to this parameter. An increase in t_{gap} to 2 hrs. results in roughly a 1% increase in the temperatures predicted by the model in the mould.

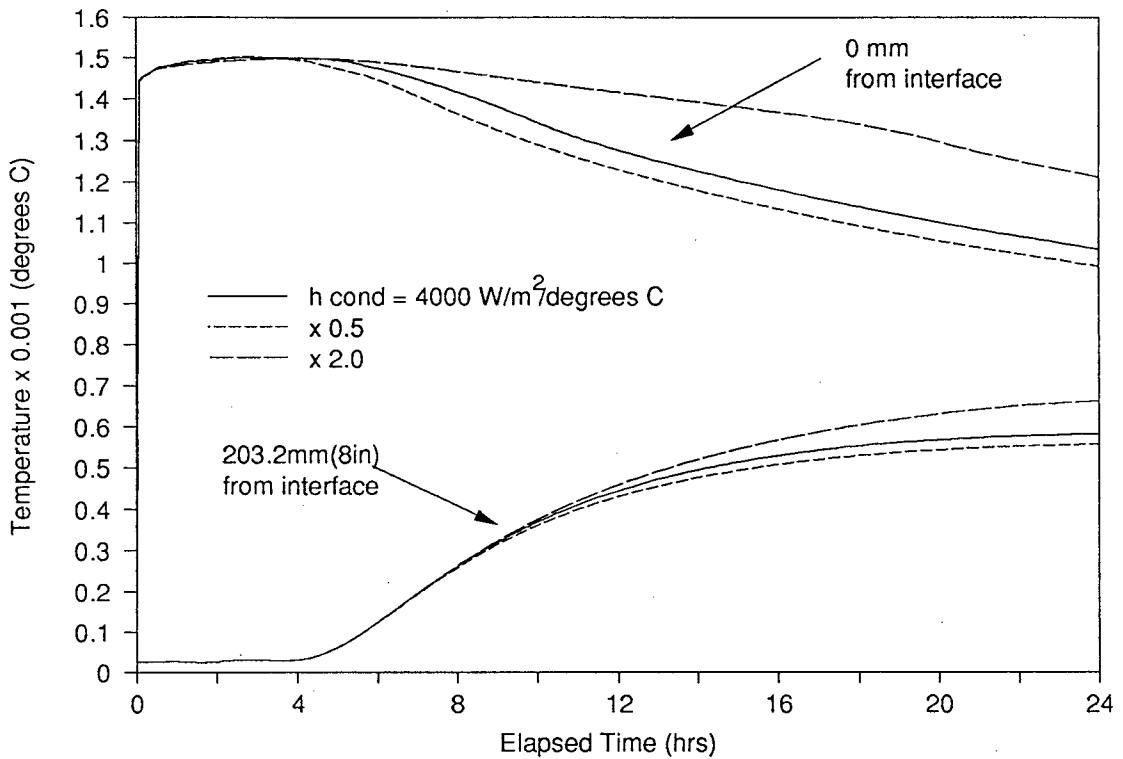


Figure 6.15. Model sensitivity to magnitude of refractory/mould interfacial heat-transfer coefficient, h_{cond} .

Model sensitivity to the rate of decrease of h_{cond} , which is determined by the magnitude of f_{ramp} , is presented in Figure 6.17. Reducing f_{ramp} by a factor of two from 1.1×10^{-5} to $0.55 \times 10^{-5} \text{ W/m}^2 \cdot \text{C} \cdot \text{s}$ results in a 20% increase in the temperatures predicted by the model in the mould at the refractory/mould interface at 24 hrs elapsed time.

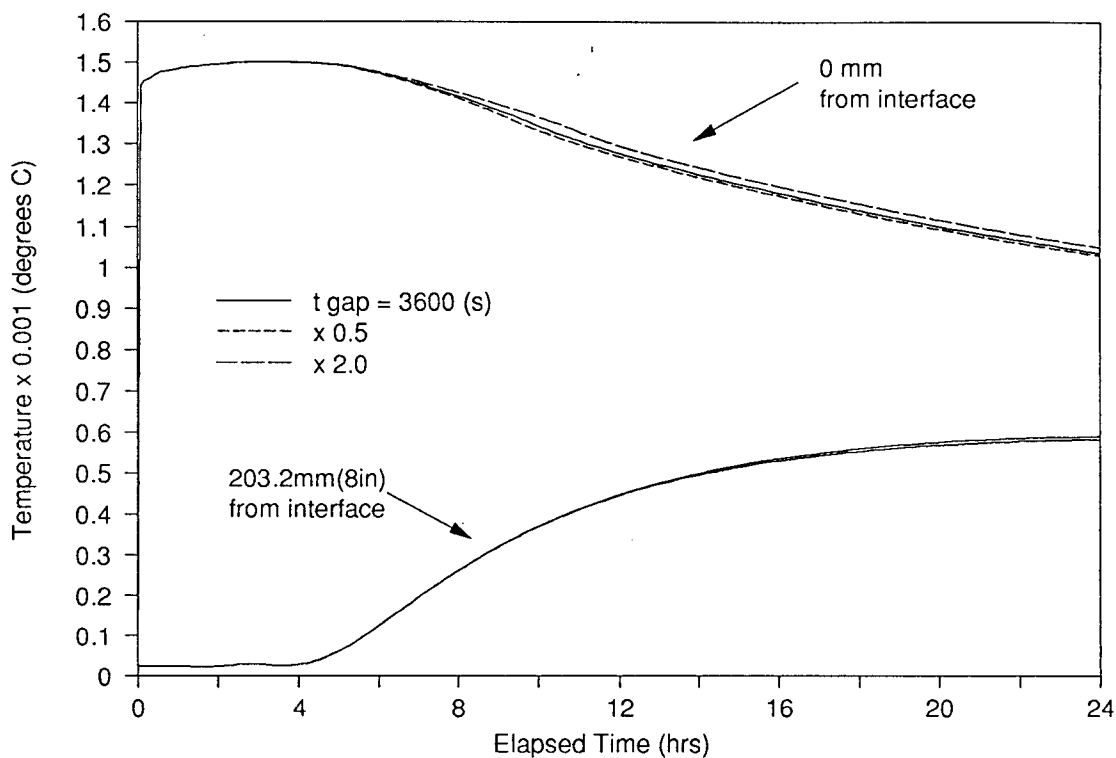


Figure 6.16. Model sensitivity to time of gap formation at refractory/mould interface.

Overall, the results presented in Figures 6.15-6.17 indicate a high degree of model sensitivity to the parameters utilized in the characterization of the refractory/mould interfacial boundary condition. As formulated, heat transfer across this interface is a function of the temperature differential across the boundary (driving force) and the magnitude of the specified heat transfer coefficient. Initially heat is transferred rapidly owing to the large temperature difference between the refractory and mould. While the temperature difference remains large the model exhibits little sensitivity to changes in h_{cond} owing to the high rates of heat flow. During this period the sand is likely the dominant resistance to heat flow from the casting. At times beyond t_{gap} , h_{cond} is gradually decreased until radiation becomes the dominant mechanism of heat-transfer across the gap - refer to Section 6.1.1. At some point during this transition, the resistance to heat transfer becomes large enough to impact on the temperature

profiles within the mould. The time at which this occurs is dictated by the magnitude of h_{cond} and f_{ramp} and hence the model exhibits a high degree of sensitivity to these parameters. Moreover, the model will obviously be sensitive to t_{gap} if it is increased to long enough times.

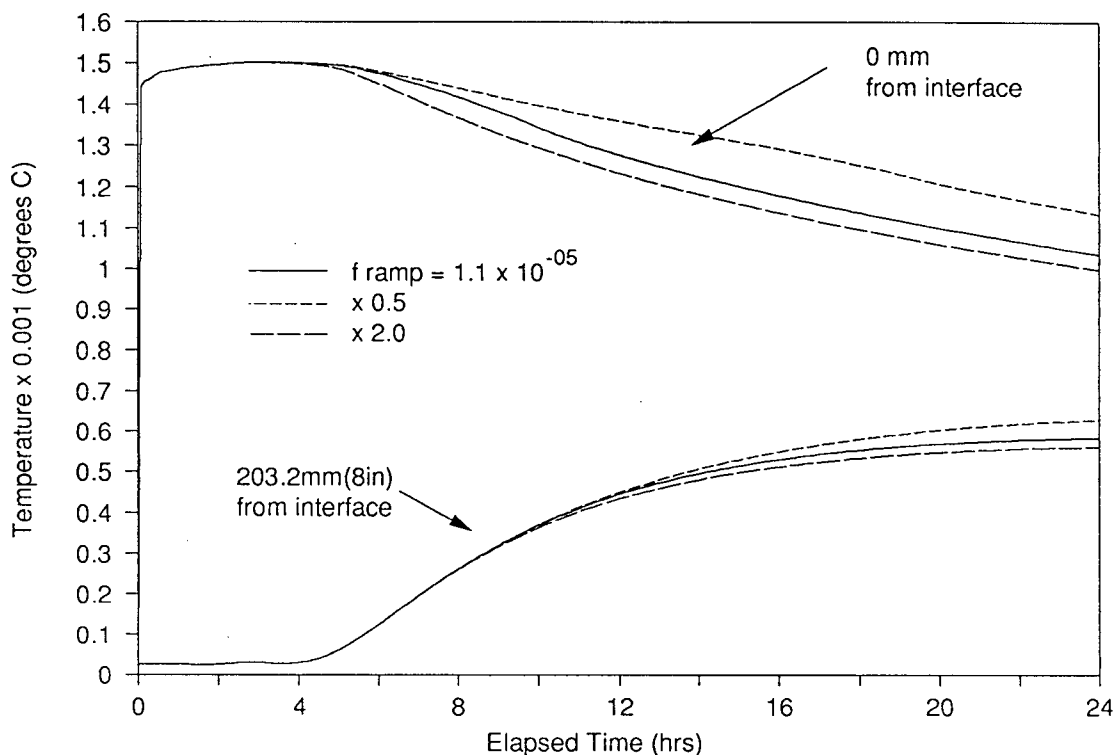


Figure 6.17. Model sensitivity to magnitude of rate of decrease of refractory/mould interfacial heat-transfer coefficient, f_{ramp} .

[iv] Thermal Conductivity of Sand.

For the investigation of the thermal conductivity of bonded and annealing sand, the thermal conductivity of both materials was arbitrarily varied by a factor of two relative to the measured data. The results of the comparison are presented in Figure 6.18 where it is evident that the model is highly sensitive to this parameter. Doubling the thermal conductivity

reduces the peak temperature achieved at the refractory/mould interface by 10% and evidently has a major impact on the temperature profiles throughout the mould. Moreover, at 203.2 cm (8") from the interface, the time at which the heat-pulse is predicted to arrive, is decreased from 4 to 2 hrs elapsed. Combined, the bonded and annealing sands obviously represent a major resistance to heat flow in the Epic-3 casting process. A crude comparison of the resistances to heat flow within the casting confirms that the sand represents the dominant resistance. (At mid-height in the casting, the resistances to heat flow are approximately: $R_{AZS} = 0.04 \text{ } ^\circ\text{C/W}$, $R_{\text{refractory/mould gap}} = 0.0003\text{-}0.01 \text{ } ^\circ\text{C/W}$, $R_{\text{sand}} = 1.5 \text{ } ^\circ\text{C/W}$ and $R_{\text{mould exterior}} = 0.01 \text{ } ^\circ\text{C/W}$.) Any errors in the quantification of the thermal conductivity of these sands will lead to significant errors in model predictions.

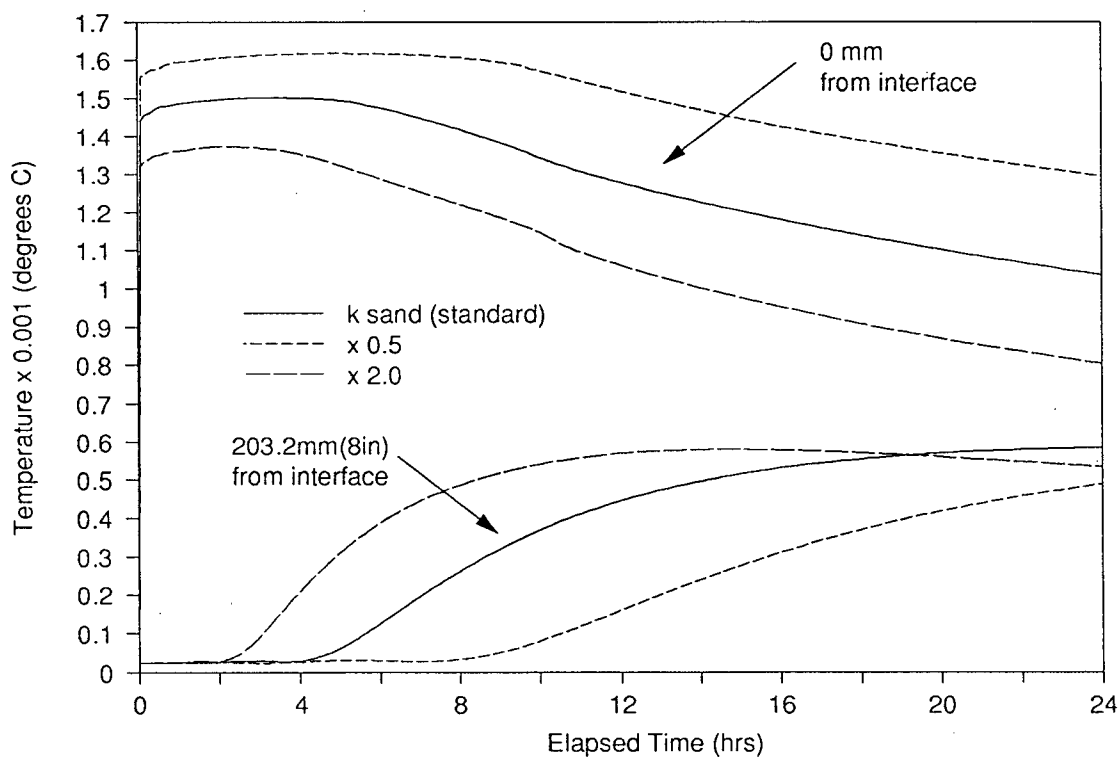


Figure 6.18 Model sensitivity to the thermal conductivity of the moulding sand.

[v] Maximum Temperature Change per Time-Step.

One of the potential sources of numerical error in non-linear transient heat transfer analyses is improper selection of the integration time-step. Model sensitivity to this parameter has been investigated to establish whether or not a reasonable value is being employed in the calculation.

Within the heat-flow model, the integration time-step is controlled dynamically so as to keep the change in temperature, for an increment in time, within a user-specified maximum, T_{\max} . With this technique, the time-step is adjusted in accordance with the rate at which the temperature is changing in the casting process. The time-step is therefore not explicitly set by the user, but instead, is dynamically controlled as a function of T_{\max} and the conditions prevailing in the model. Model sensitivity to integration time-step has been investigated indirectly through a sensitivity analysis of the parameter T_{\max} , which has been varied by a factor of two from the standard value of 5°C . The results are presented in Figure 6.19 and indicate that the model is relatively insensitive to the magnitude of T_{\max} . A factor of two decrease in T_{\max} results in roughly a 5% decrease in the temperature profiles predicted for the selected nodes at 24 hrs elapsed time. The effect becomes obvious beyond 5 hrs. elapsed time. Presumably, this behaviour is due to the frequency with which the material properties and temperature dependent boundary conditions are up-dated within the model. It follows, therefore, that the smaller T_{\max} will yield the more accurate results. However, not without an added computational cost as a larger number of iterations are carried out. For this analysis, it is felt that $T_{\max} = 5^{\circ}\text{C}$ serves as a reasonable compromise.

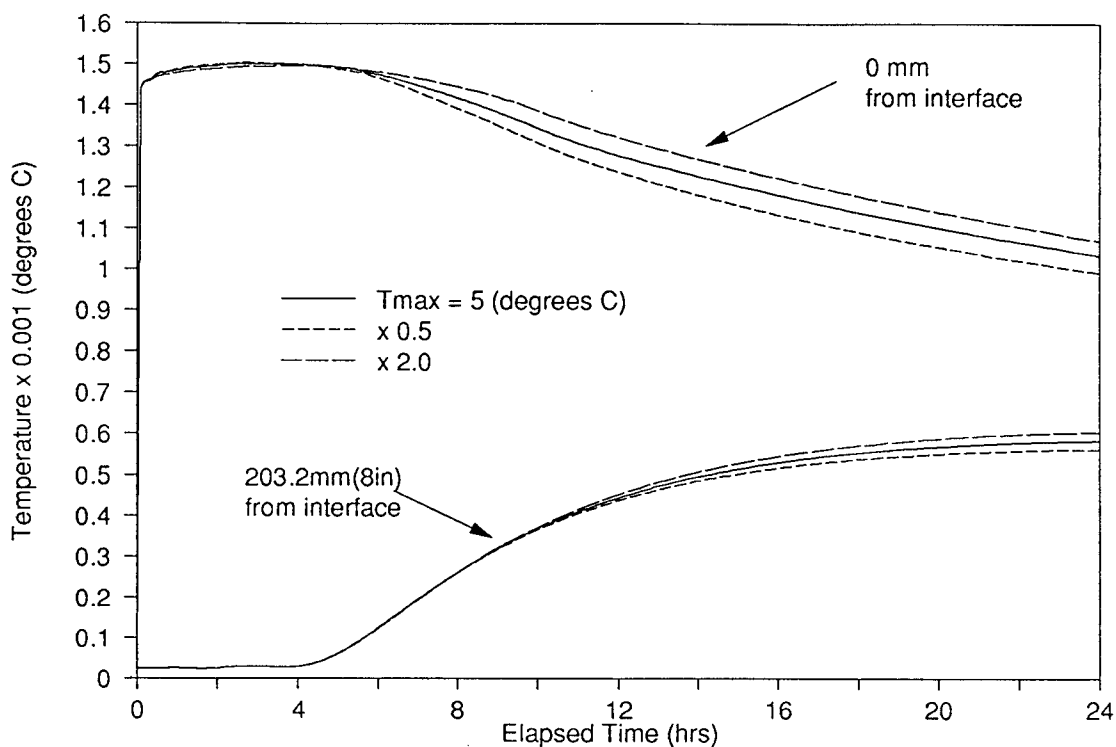


Figure 6.19. Model sensitivity to maximum temperature change per time step.

6.1.5.2 Comparison of Model Predictions to Industrial Data

A comparison then was made between the model predictions and the industrial thermocouple measurements. Through this comparison, the performance of the model has been assessed and the validity of the more questionable input parameters ascertained. The thermocouples used in the comparison are located at roughly mid-height in the casting consistent with the restrictions imposed by the two-dimensional analysis. Figure 6.12 illustrates their locations relative to the refractory/mould interface. Note that these positions are identical to those utilized in the sensitivity analysis. The results of the comparison are presented in Figure 6.20.

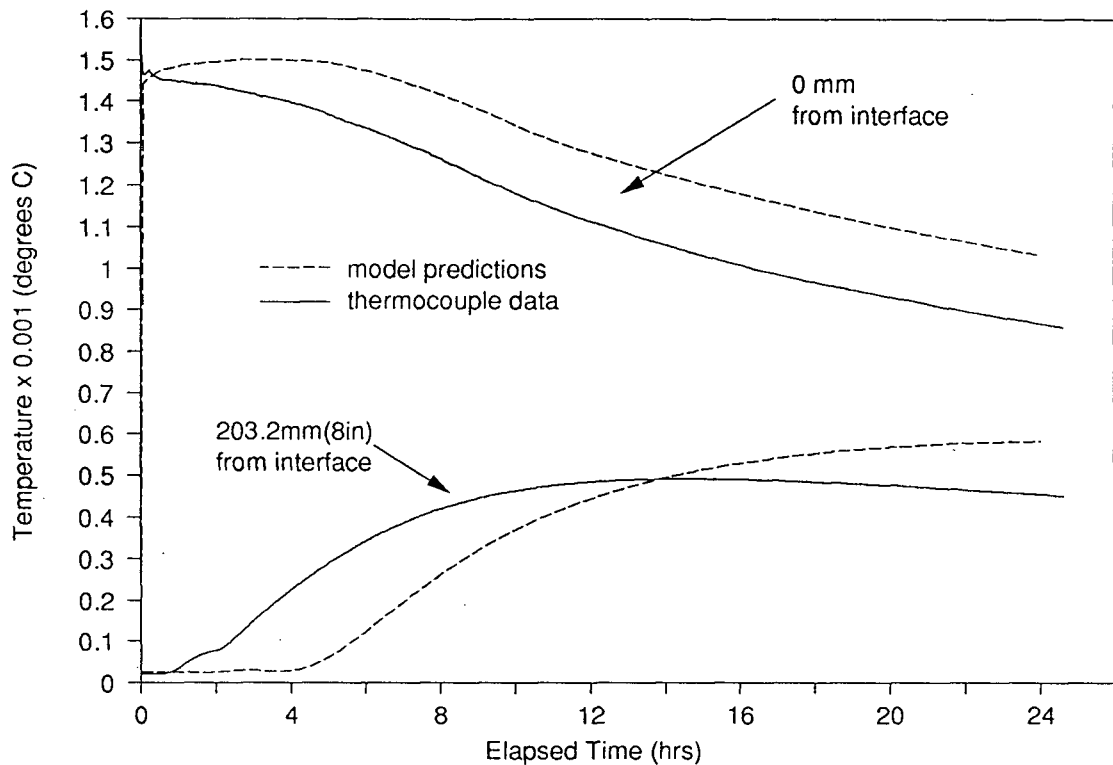


Figure 6.20. Comparison between model predictions and industrial thermocouple data.

It is evident from Figure 6.20 that the model predictions do not agree well with the industrial data. For example, there is a significant discrepancy in the time it takes for the heat pulse to arrive 203.2mm(8in) into the mould. The thermocouple data indicates that the temperature at this location first begins to rise approximately one hour after pouring. In contrast, the model predicts this time to be closer to four hours. Moreover, model predictions for the interfacial temperature also exhibit poor agreement with the industrial measurements. In this case, the model is over-estimating the temperature at the refractory/mould interface by as much as 150°C.

6.1.5.3 Alignment of Model to the Epic-3 Casting Process.

Given the uncertainty surrounding the evaluation of some of the input data and the characterization of certain boundary conditions, the poor agreement exhibited in Figure 6.20 is not unexpected. Bringing to bear the results of the sensitivity analysis, it was possible to employ the thermocouple data to help better define some of the more questionable input parameters. In this manner, the model was "tuned" or "aligned" to the Epic-3 casting process.

The sensitivity analysis identified two material-related parameters which warrant close inspection: the thermal conductivity of sand and the latent heat of solidification of the refractory. A comparison between the thermocouple data, Figure 6.20, and the results of the sensitivity analysis to the thermal conductivity of sand, Figure 6.18, revealed that an increase in the thermal conductivity of the sand will result in a better overall alignment of the model predictions to the industrial data. The effect is two fold: firstly, the time it takes for the heat to reach 203.2mm(8in) into the mould decreases with increasing thermal conductivity; and secondly, the prediction for the interfacial temperature is reduced as the conductivity of the mould material is increased. It was felt, therefore, that the thermal conductivity for the mould material (bonded and annealing sands) is too low and required adjustment. This inconsistency may be in part due to differences in the packing density. It is well documented⁷⁴ that bulk density can have a significant impact of the conductivity of granular materials. The sand within all but the top regions of the Epic-3 mould is probably much more densely packed by the burden than the samples used by Ohio State for evaluation⁷². Unfortunately, the bulk density within the mould was not measured for comparison. Moreover, the impact of compaction on the thermal conductivity of sand was not investigated.

Following the assumption that the sand within the mould is more densely packed, the thermal conductivity of the sand was increased. The strategy was to increase the conductivity

at room temperature while keeping the conductivity at high temperature consistent with the Ohio State measurements⁷². The rationale for this approach follows from observations made during the Ohio State measurements - refer to Section 6.1.3.2. During evaluation of the conductivity, it was reported that the sand samples exhibited a significant thermal expansion. Presumably, the impact of semi-constrained expansion would be to fill the void spaces in the sand resulting in an increase in the thermal conductivity. This would account for the factor of four increase in thermal conductivity observed during the Ohio State measurements - refer to Table 6.2. In the Epic-3 mould, the sand initially has a lower void-space due to the burden. Hence, the thermal conductivity at room temperature would be higher. The amount by which the conductivity is increased was established through a process of trial and error to align the model predictions to the industrial data. The primary criterion for assessing the degree of alignment or fit was the length of time for the heat pulse to reach 203.2mm(8in) into the mould. As can be seen from the results presented in Figure 6.21, the model predictions fall much more in-line with the industrial data when the sand conductivity was adjusted. The variation in sand thermal conductivity utilized to achieve this are as follows:

For temperature range $0 \leq T \leq 1000^{\circ}\text{C}$

$$k_{sand}(W/m \cdot ^{\circ}\text{C}) = 4.78 \times 10^{-1} + 1.00 \times 10^{-3}T - 5.4 \times 10^{-7}T^2 \quad (6.31)$$

For temperature range $1000 \leq T \leq 1900^{\circ}\text{C}$

$$k_{sand}(W/m \cdot ^{\circ}\text{C}) = 8.89 \times 10^{-1} + 6.52 \times 10^{-5}T \quad (6.32)$$

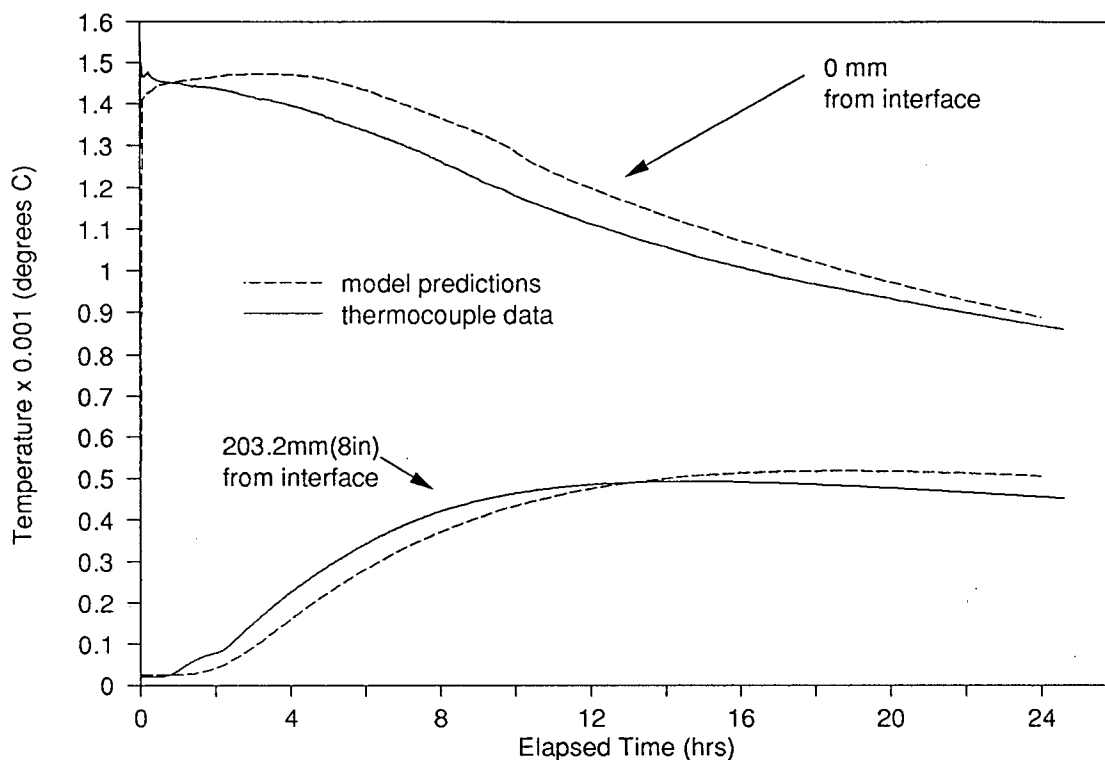


Figure 6.21. Model fit to industrial thermocouple data using an adjusted thermal conductivity of moulding sand.

Despite a marked improvement, there was still a tendency for the model to over-estimate the temperature observed in the mould. A comparison between the results presented in Figure 6.21 and the model sensitivity to the heat of solidification, Figure 6.13, reveals that the over-prediction in temperature could be attributed to error in this parameter. The latent heat of solidification appears to be the only parameter capable of having an impact on the peak temperature achieved at the interface other than the thermal conductivity of sand. Based on this observation, it was reasoned that the initial estimate for the latent heat of fusion of Monofrax-S employed in the model was too high. Through a process of trial and error the latent heat of fusion of Monofrax-S was determined to be closer to 400 kJ/kg. This represents close to a 50% reduction in the amount of latent heat evolved in comparison to the value of

760 kJ/kg estimated by the rule of mixtures. This reduction may be plausible if a significant portion of the mullite ($3\text{Al}_2\text{O}_3\cdot 2\text{SiO}_2$) forms as a metastable glass and does not release any latent heat. (According to the Al_2O_3 - ZrO_2 - SiO_2 phase diagram most of the alumina should form mullite.) Since 70% of the calculated latent heat is attributed to crystallization of Al_2O_3 in the rule of mixtures estimation, the reduction could be significant. The model predictions for the case where the latent heat has been reduced are presented together with the industrial data in Figure 6.22. As can be seen, the agreement is now quite reasonable.

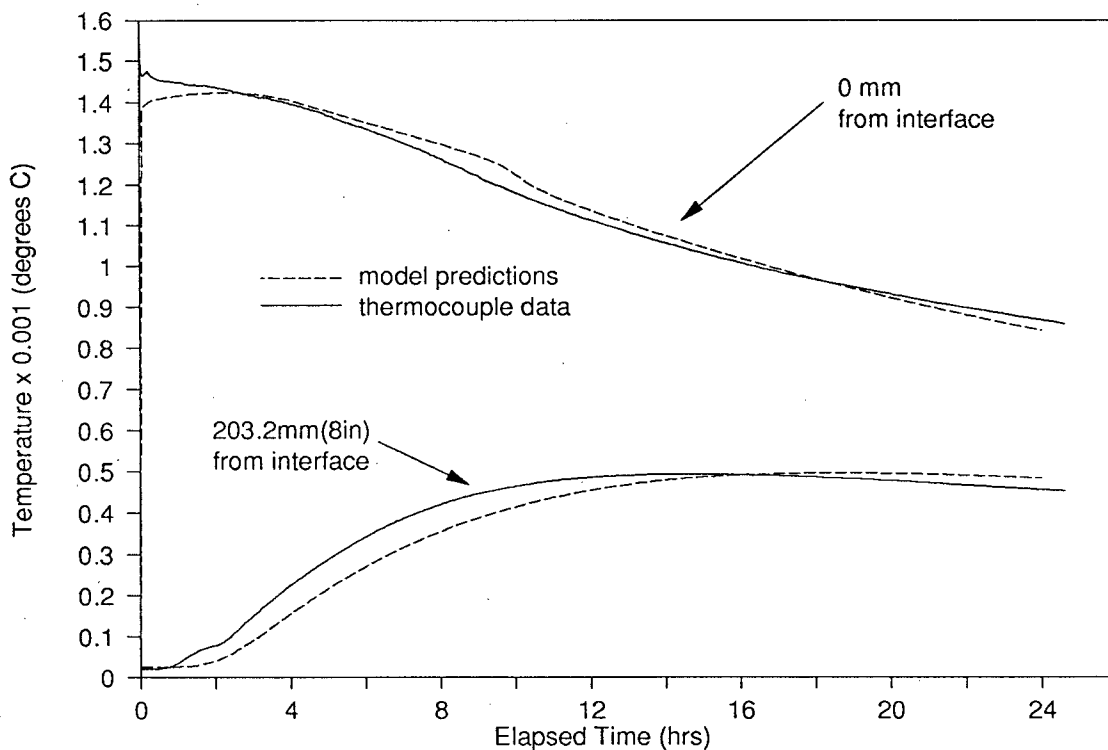


Figure 6.22. Model fit to industrial thermocouple data using an adjusted latent heat of fusion of Monofrax-S.

Together with the thermal conductivity of sand and the heat of solidification of Monofrax-S, the sensitivity analysis has identified other parameters associated with the char-

acterization of heat transfer across the refractory/mould interface as being potential sources of significant error. A comparison between the model predictions presented in Figure 6.22 and the results of the sensitivity analysis for these parameters, Figures 6.15-6.17, revealed that the estimated values for h_{cond} , t_{gap} and f_{ramp} are probably quite reasonable. Fine tuning of this boundary condition through the introduction of a time dependent f_{ramp} , resulted in only a small improvement in the performance of the model as indicated in Figure 6.23. In Figure 6.23, for elapsed times in the range of 1 to 4 hrs, f_{ramp} was set equal to $2.0 \times 10^{-3} \text{ W/m}^2 \cdot \text{C} \cdot \text{s}$ and for elapsed times greater than 4 hrs it was reduced to $5.0 \times 10^{-4} \text{ W/m}^2 \cdot \text{C} \cdot \text{s}$. A review of the literature⁵⁶ indicates that there is some justification for this type of behaviour. In metal casting processes utilizing sand-moulds, measured heat transfer coefficients are shown⁵⁶ to exhibit a rapid initial decrease in h_{cond} at the onset of gap formation which is then followed by a slower rate of decline. In light of some of the other modelling assumptions, this adjustment is probably slightly presumptuous. Nevertheless, it helps to fit to the industrial data.

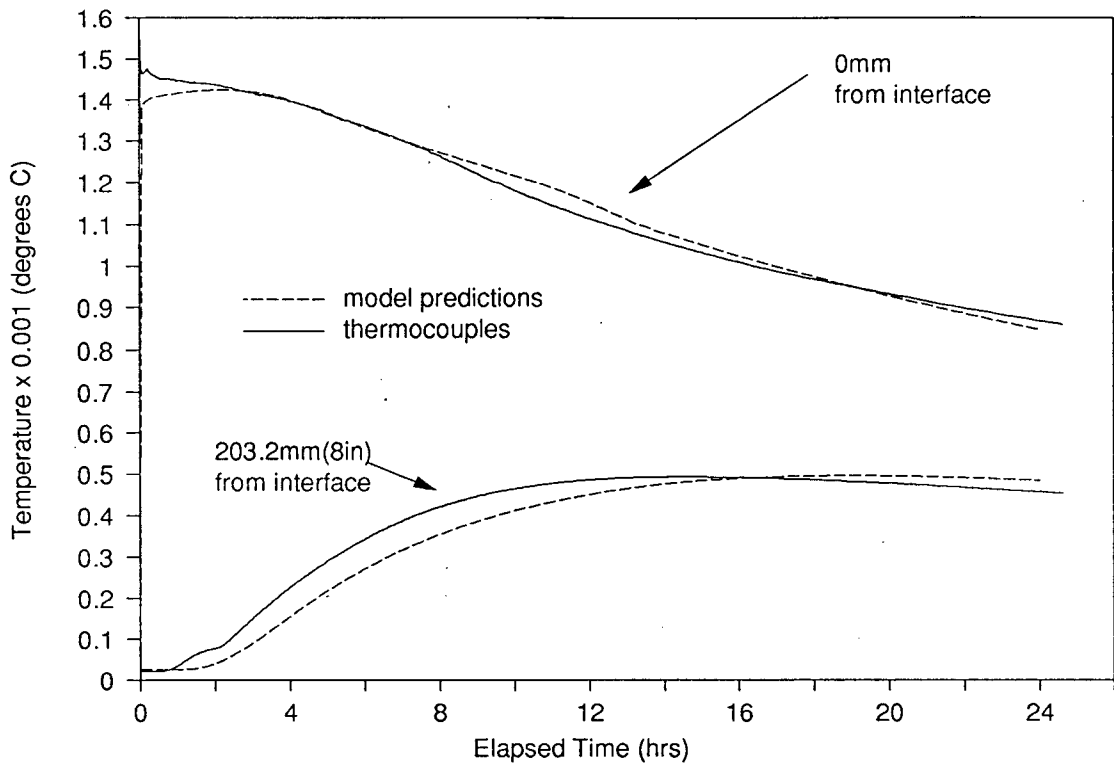


Figure 6.23. Model fit to industrial thermocouple data using adjusted value for f_{ramp} .

To this point, the comparisons to industrial measurements have been limited to nodes located 0 and 203.2mm(8in) from the broad-face. To present a more complete assessment of the predictive capabilities of the model, comparisons have been made between thermocouple measurements 51mm(2in) from the broad and narrow faces at mid-height and nodes located 57mm(2.25in) from the broad and narrow faces (the mesh does not contain nodes at the exact thermocouple positions). The results of the comparison are presented in Figure 6.24. Bearing in mind the difference in location, the results show reasonable agreement between the model predictions and the in-mould temperature responses adjacent to both the minor and major faces of the casting.

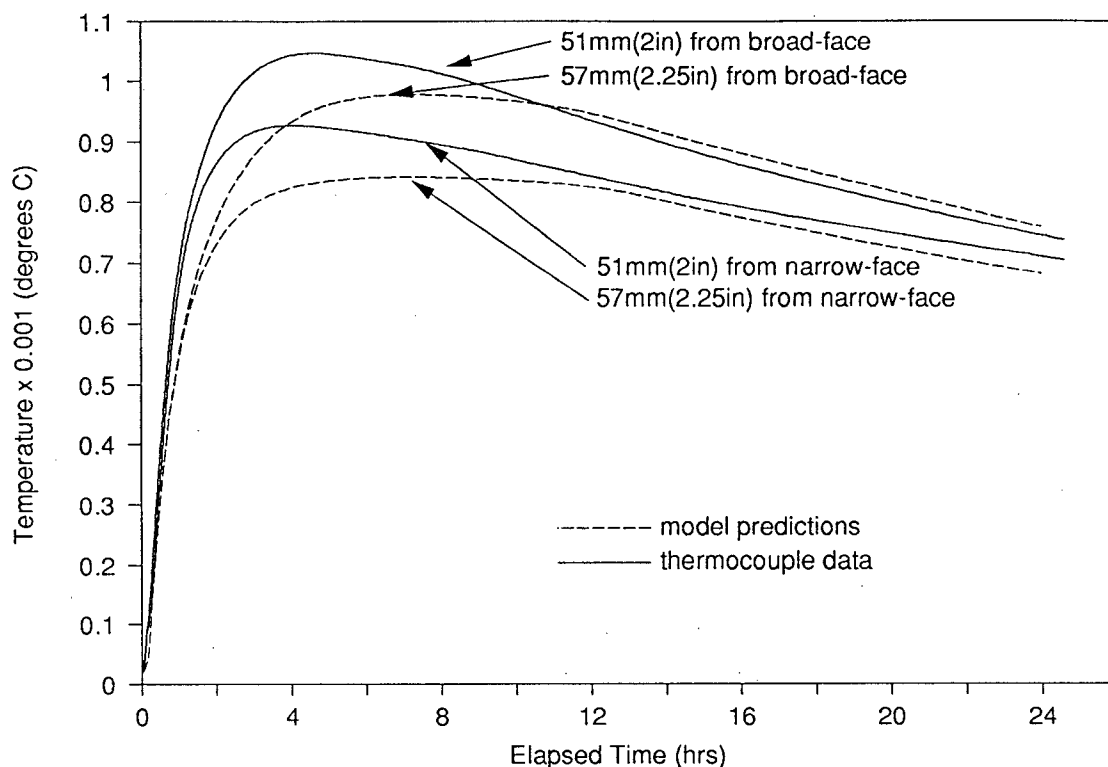


Figure 6.24. Model fit to industrial thermocouple data using adjusted values for input parameters.

6.2 Application of Stress Model.

As with the thermal model, the Epic-3 casting process must first be described in mathematical terms before the finite-element model of stress generation can be applied. This description involved the characterization of the boundary conditions, initial conditions and material properties. Once completed, an appropriate finite element spatial discretization was selected.

6.2.1 Boundary Conditions.

In contrast to the thermal analysis, which includes the mould, the stress analysis has been limited to the refractory only. Moreover, any interaction with the surrounding mould is neglected and the surfaces of the refractory are assumed to be traction free. From the standpoint of the stress analysis the Monofrax-S refractory is therefore assumed to solidify in an unconstrained fashion free of the mould.

In a similar fashion to the thermal model, axes/planes of symmetry have been adopted to reduce the computational effort. The symmetry boundaries utilized in the stress analysis follow directly from the assumption of symmetry in the flow of heat from the casting (see Section 6.1.1., Figure 6.1, for locations of axes/planes of symmetry in the thermal analysis). On the symmetry boundaries, displacement in the direction normal to the plane of symmetry has been suppressed. Since the thermal load/forces normal to the interior boundaries are assumed to be equal and opposite, the net displacement in the direction of these forces will be zero. Figure 6.25 illustrates schematically the boundary conditions applied to the two-dimensional transverse quarter-section of the refractory.

Referring to Figure 6.1, Section 6.1.1, the internal symmetry boundary conditions are then:

$$u = 0 \text{ at } x = 0; y = 0, 228.6\text{mm } (9\text{in}); z = 0, 952.5\text{mm } (37.5\text{in}) \quad (6.33)$$

$$v = 0, \text{ at } x = 0, 127\text{mm } (5\text{in}); y = 0; z = 0, 952.5\text{mm } (37.5\text{in}) \quad (6.34)$$

$$w = 0 \text{ at } x = 0, 127\text{mm } (5\text{in}); y = 0, 228.6\text{mm } (9\text{in}); z = 0 \quad (6.35)$$

where, u , v and w are the displacements in the x , y and z directions respectively.

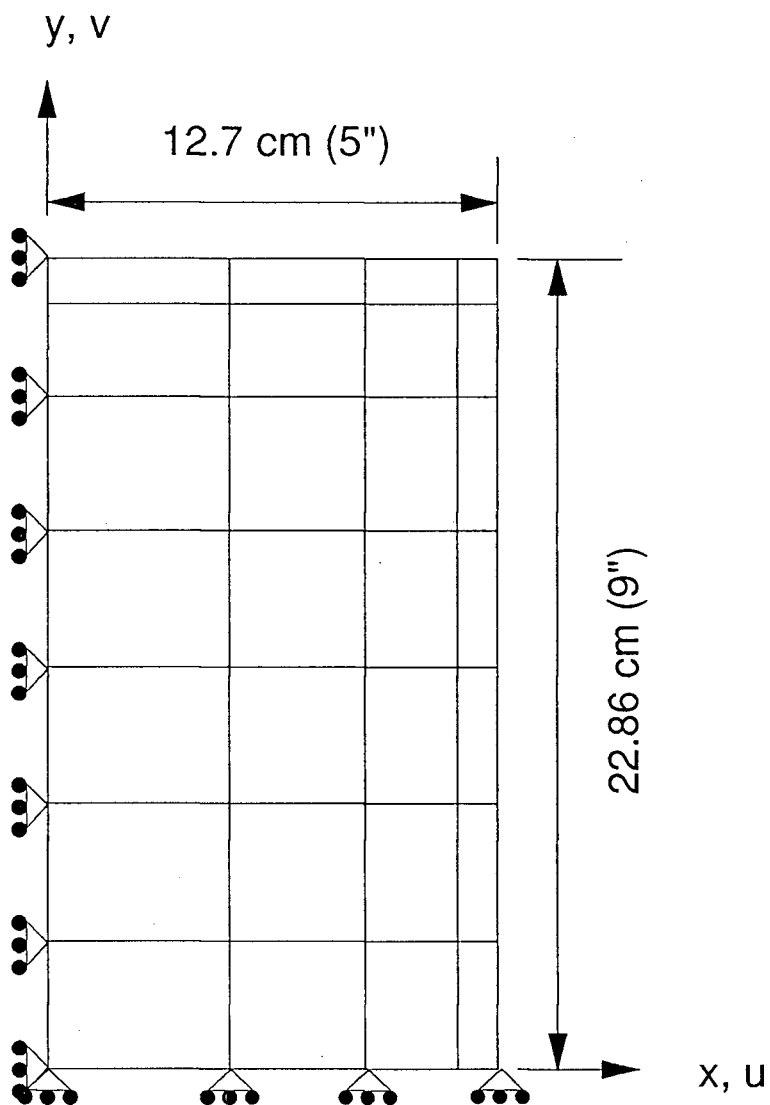


Figure 6.25. Schematic illustration of boundary conditions applied to the two-dimensional transverse quarter-section of Epic-3 refractory.

6.2.2 Initial Conditions

For the stress analysis the refractory was assumed to be in a state of zero stress at the beginning of the casting process. Hence all initial nodal displacements were set to zero. Since the Monofrax-S is initially in a liquid state this is a reasonable assumption. The initial conditions for the lower quarter section are thus

$$\begin{aligned}
 u = v = w = 0 \\
 \text{at } x = 0, 127\text{mm } (5\text{in}); y = 0, 228.6\text{mm } (9\text{in}); z = 0, 952.5\text{mm } (37.5\text{in}); \\
 t = 0
 \end{aligned}
 \tag{6.36}$$

6.2.3 Thermomechanical Properties of Monofrax-S (AZS-CS3)

As was the case with the thermal model, the principal source of thermomechanical data was the evaluation programme initiated at Carborundum^{71,75} (see outline of programme in the Methodology). Unfortunately, not all of the necessary data could be obtained within the time-frame of the project. In those instances where the thermomechanical data was incomplete (eg. limited temperature range), extrapolations have been made from the low temperature measurements. Furthermore, due to the lack of information describing the experimental techniques, no assessment of the error in the measurements has been made.

For the elastic thermal-stress formulation, the relevant material properties for Monofrax-S are the elastic modulus, Poisson ratio and thermal-linear expansion coefficient. The latter must be calculated from information on the thermal expansion/contraction behaviour of the material.

The elastic modulus, Poisson ratio and percentage change in length data ($\% \Delta L$) for Monofrax-S (AZS-CS3) are presented as a function of temperature in Table 6.5^{71,75} (the percentage change in length data has been established from a Thermal Dilatometric Analysis or

TDA). From this data correlations have been developed which describe the variation in elastic modulus and the Poisson ratio over a temperature range of 0 - 1900°C. The elastic modulus is assumed to decrease linearly from 1200°C to 1780°C at which point it is assumed to remain constant at 0.1 MPa through to 1900°C. A relatively small value of 0.1MPa was utilized to simulate the effect of the liquid/mushy material on the generation of stress which will be negligible (the stress model requires a finite elastic modulus). The Poisson ratio was assumed to remain constant at 0.15 above 900°C. These correlations are presented in Equations (6.37) - (6.41) and are shown in Figures 6.26 and 6.27.

The thermal-linear expansion coefficient was obtained by dividing the TDA data presented in Table 6.5 by 100 to convert it to units of $\Delta l/l$ (linear strain). From Figure 6.28 it is apparent that more than one thermal linear expansion coefficient will be necessary to describe the behaviour of Monofrax-S under cooling conditions (lower curve). Most notably, there is a departure from contraction to expansion during cooling as the ZrO_2 component of Monofrax-S undergoes the tetragonal-to-monoclinic phase transformation between 940 and 840°C. Three lines have been fitted to the cooling curve as illustrated in Figure 6.28. The slopes of these lines, Equations (6.42)-(6.44), are the thermal-linear expansion coefficients input to the model. For temperatures above 1780°C the thermal-linear contraction coefficient for Monofrax-S was assumed to be equal to zero.

Elastic Modulus (MPa)

For temperature range $0 \leq T < 1000^\circ\text{C}$

$$E_{\text{Monofrax-S}} = 100,000.0 \quad (6.37)$$

For temperature range $1000 \leq T < 1200^\circ\text{C}$

$$E_{\text{Monofrax-S}} = 473850 - 374.8T \quad (6.38)$$

For temperature range $1200 \leq T < 1780^\circ\text{C}$

$$E_{\text{Monofrax-S}} = 87825 - 157.6T \quad (6.39)$$

For temperature range $1780 \leq T < 1900^\circ\text{C}$

$$E_{\text{Monofrax-S}} = 0.1 \quad (6.40)$$

Poisson Ratio

For temperature range $0 \leq T < 1900^\circ\text{C}$

$$\nu_{\text{Monofrax-S}} = 0.15 \quad (6.41)$$

Thermal Linear Expansion/Contraction Coefficients ($\Delta l/l$)/ $^\circ\text{C}$

For temperature range $0 \leq T < 840^\circ\text{C}$

$$\alpha_{\text{Monofrax-S}} = -6.55 \times 10^{-6} \quad (6.42)$$

For temperature range $840 \leq T < 940^\circ\text{C}$

$$\alpha_{\text{Monofrax-S}} = 2.41 \times 10^{-5} \quad (6.43)$$

For temperature range $940 \leq T < 1780^\circ\text{C}$

$$\alpha_{\text{Monofrax-S}} = -1.15 \times 10^{-5} \quad (6.44)$$

For temperature range $1780 \leq T < 1900^\circ\text{C}$

$$\alpha_{\text{Monofrax-S}} = 0 \quad (6.45)$$

TABLE 6.5
Thermomechanical Properties of Monofrax-S (AZS-CS3)

Temperature (C)	Elastic Modulus ⁵ E (MPa)	Poisson Ratio ⁵ v	Thermal Dilatometric Analysis ⁷¹ , Heating (% Δ L)	Thermal Dilatometric Analysis ⁷¹ , Cooling (% Δ L)
20	112,600.	0.149	0.0000	-0.0938
100	111,700.	0.150	0.0375	-0.0375
150	111,000.	0.152		
200	110,100.	0.152	0.0938	0.0375
250	108,600.	0.151		
300	106,200.	0.150	0.1688	0.1125
350	103,800.	0.146		
400	101,300.	0.146	0.2438	0.1875
450	99,400.	0.141		
500	98,200.	0.141	0.3375	0.2625
550	97,600.	0.144		
600	97,100.	0.143	0.4125	0.3188
650	96,500.	0.145		
700	95,900.	0.146	0.5063	0.3750
750	95,000.	0.148		
800	94,100.	0.147	0.6375	0.4200
840			0.6750	0.4313
850	96,400.	0.154		
900	101,200.	0.166	0.7313	0.3000
940			0.7688	0.1875
950	107,800.			
980			0.7875	0.2063
1000	106,100.		0.7688	0.2250
1050	83,600.			0.3375
1100	59,500.		0.6563	0.3938
1140			0.6375	0.4688
1150	37,100.			
1200	29,600.		0.6750	0.4679
1300			0.7875	0.5625
1400			0.8625	0.6750
1500			0.9563	0.8063
1600			0.9375	0.9375

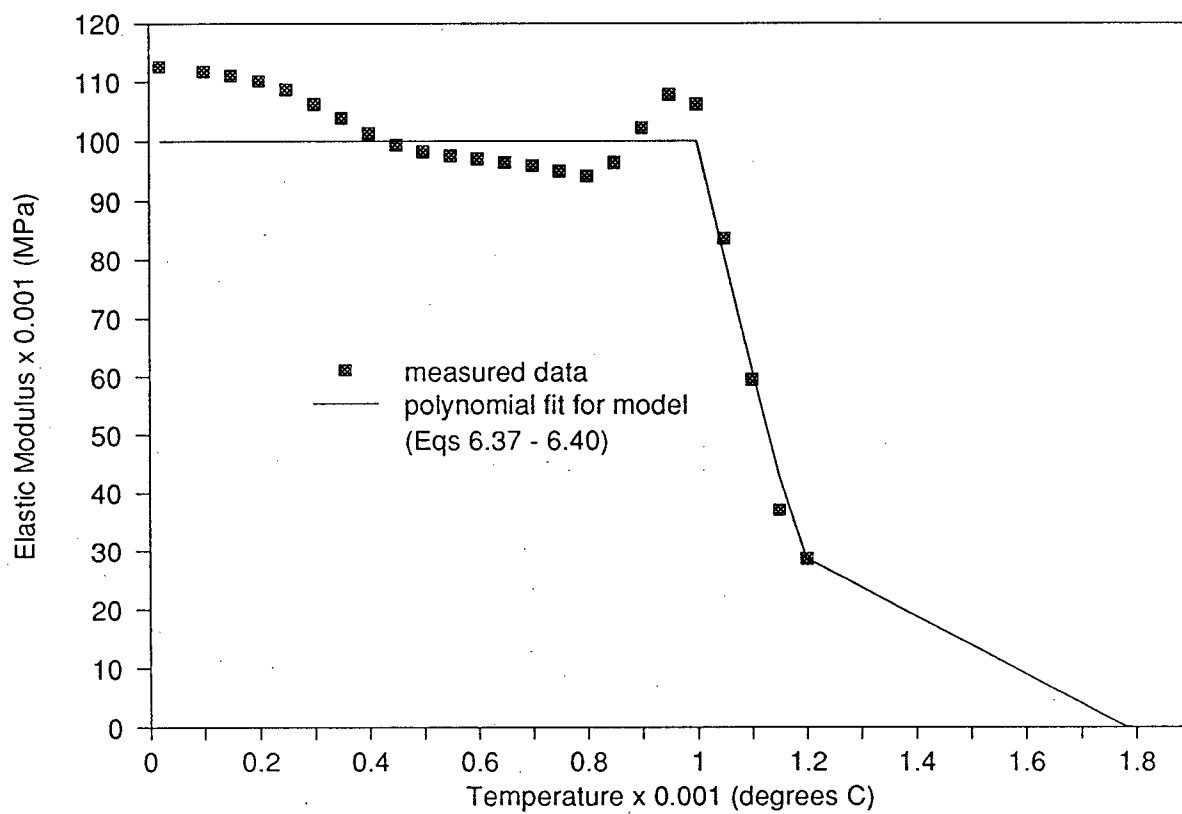


Figure 6.26. Measured elastic modulus data as a function of temperature and polynomial fit for Monofrax-S (AZS-CS3).

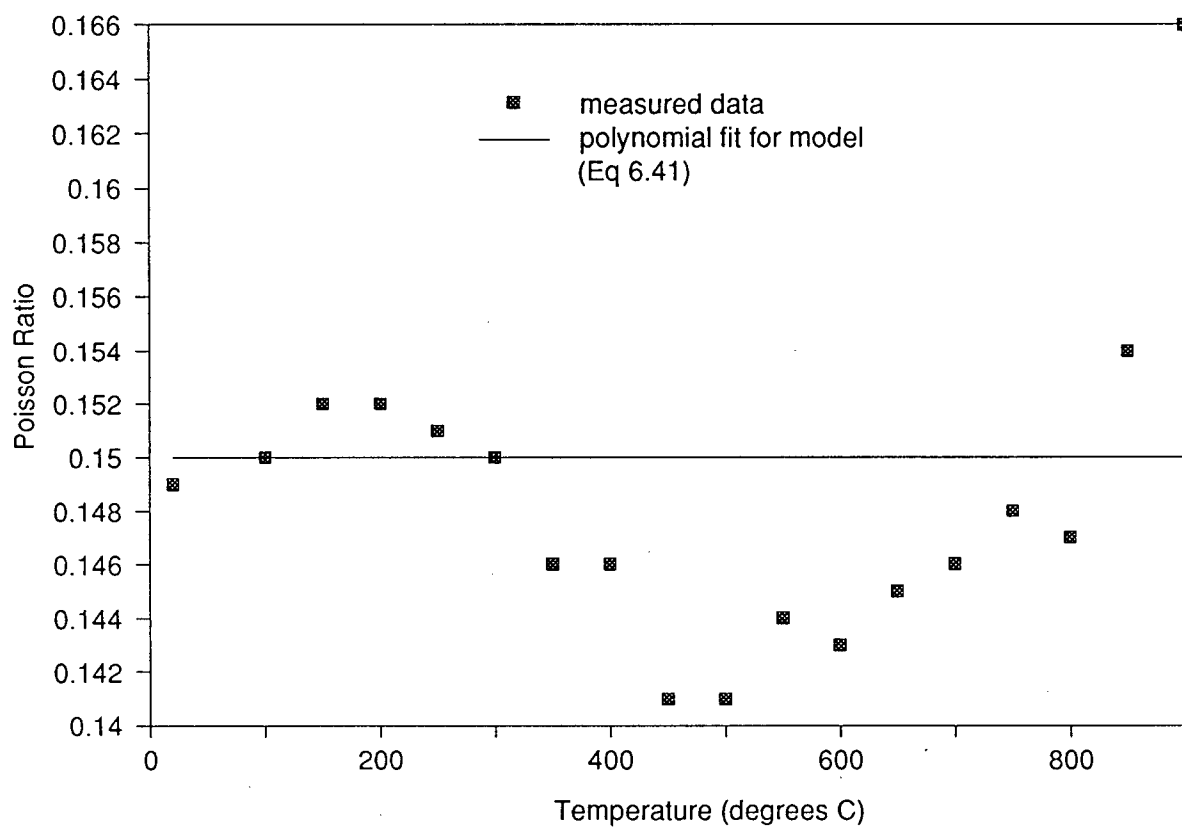


Figure 6.27. Measured Poisson ratio data as a function of temperature and polynomial fit for Monofrax-S (AZS-CS3).

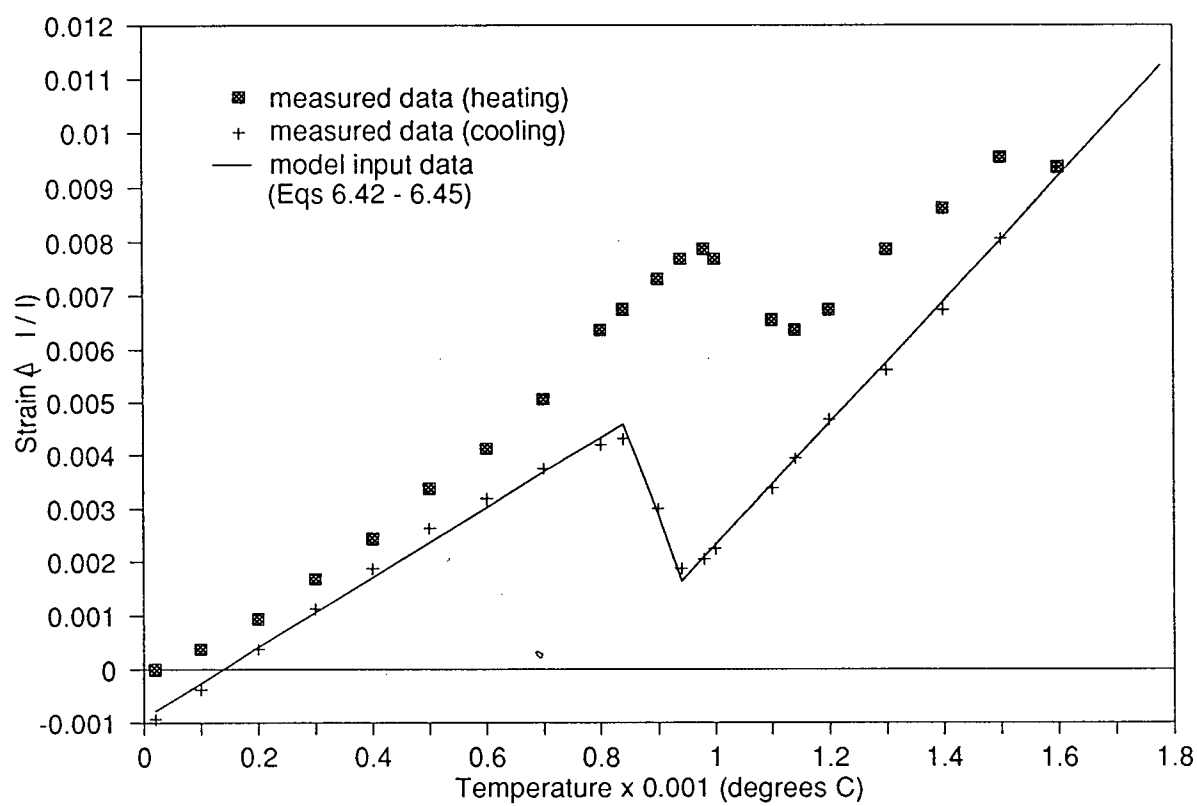


Figure 6.28. Measured thermal-linear strain as a function of temperature and polynomial fit for Monofrax-S (AZS-CS3).

6.2.4 Finite Element Spatial Discretization.

In order to permit the results of the thermal analysis to be input directly into the stress model, the mesh utilized for the refractory in the thermal analysis has been adopted for the stress analysis. The reader is referred to section 6.1.4 for a description of the spatial discretization utilized in the stress model for both the two-dimensional and three-dimensional analysis.

6.2.5 Sensitivity Analysis.

The focus of the sensitivity analysis was identification of potential sources of error in the model predictions. The two-dimensional plane-stress approximation was utilized in order to give reasonable job execution times. The results of a two-dimensional heat-flow analysis were input to the stress model. The sensitivity of the model has been assessed by varying individual parameters such as the elastic modulus and the Poisson ratio and comparing the results to the standard case predictions for selected nodes - see Figure 6.29. The standard case serves as a point of reference and is defined to be a 34 hr simulation with the models of heat-flow and stress generation utilizing the input parameters as defined thus far. It was necessary to extend the standard simulation to 34 hrs from 24 hrs (used in the thermal model sensitivity analysis) in order to encompass the effect of the tetragonal-to-monoclinic phase transformation. Stresses acting parallel to the respective faces on which the selected nodes lie were chosen for output from the model in the sensitivity analysis. These are σ_y and σ_x for the nodes located on the broad and narrow faces, respectively. Tensile stresses at these locations would be necessary to initiate longitudinal cracks. On the broad-face, the result would be a Type-B crack.

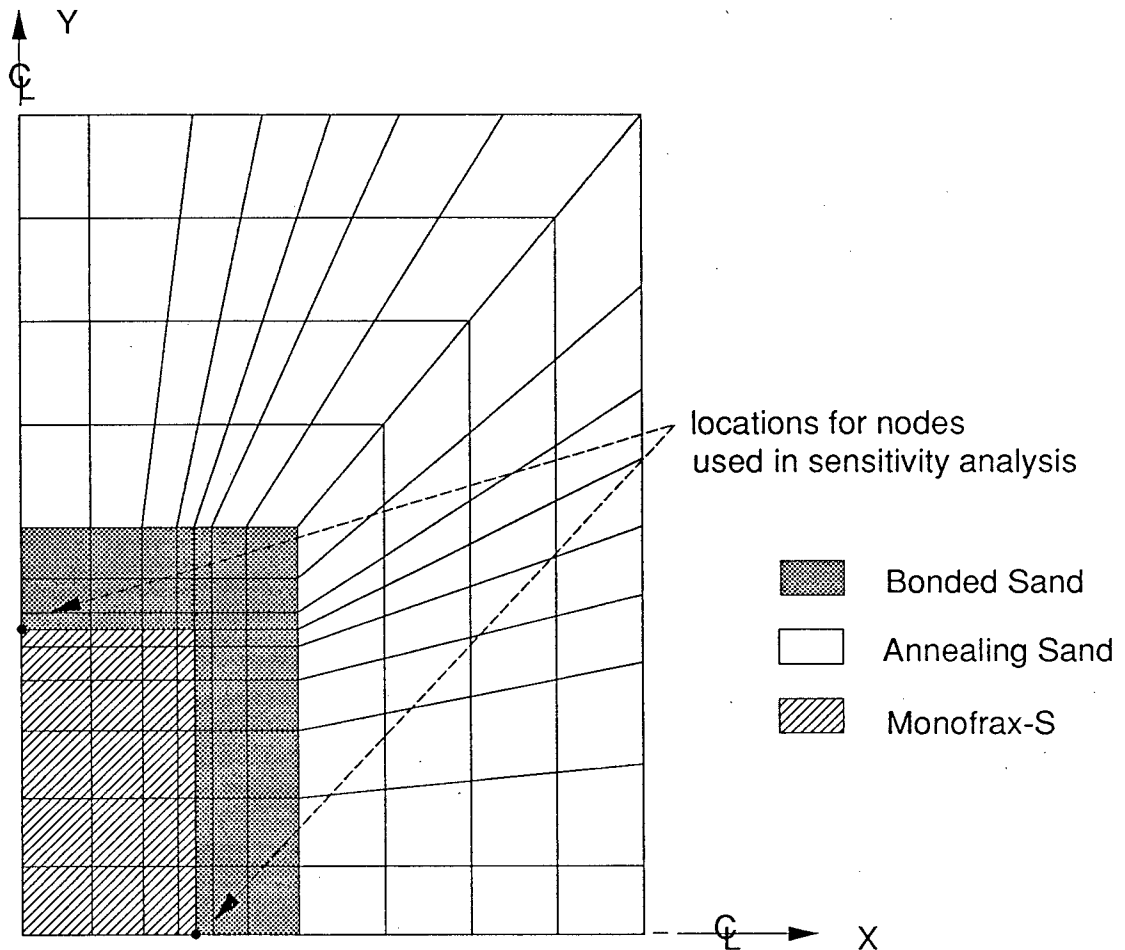


Figure 6.29. Location of nodes utilized in the sensitivity analysis.

[ii] Elastic Modulus

Model sensitivity to the elastic modulus has been examined to better understand the influence of varying this parameter as a function of temperature. Figures 6.30 and 6.31 show a comparison between the stress predicted by the model for the standard case, Equations (6.37)-(6.39), and for the case where the range of Equation (6.37) has been extended above 1000 up to 1900°C. In this manner the influence of reducing the elastic modulus at temperatures above 1000°C can be deduced. The results indicated that the model is highly sensitive

to variations in this parameter. For the σ_y stress response, the effect of decreasing the elastic modulus is to reduce the predicted peak tensile stress from 350MPa to 50MPa, approximately 85% - see Figure 6.30. A similar effect is observed in Figure 6.31, which shows the predicted σ_x response. For both the σ_y and σ_x responses, the predictions for the modified case become equal to the standard case at roughly 17 hrs elapsed time after both nodes have dropped below 1000°C - refer to temperature response for mid-face nodes presented in Figure 6.32. The behaviour implies an interaction between the development of stress on the two faces. At the centre-line of both faces, the material is placed in compression between 940°C and 840°C (tetragonal-to-monoclinic phase transformation) as it tries to expand but is constrained by the surrounding material. Based on these results, any errors in the quantification of the elastic modulus will obviously have a significant bearing on the predictions of the model.

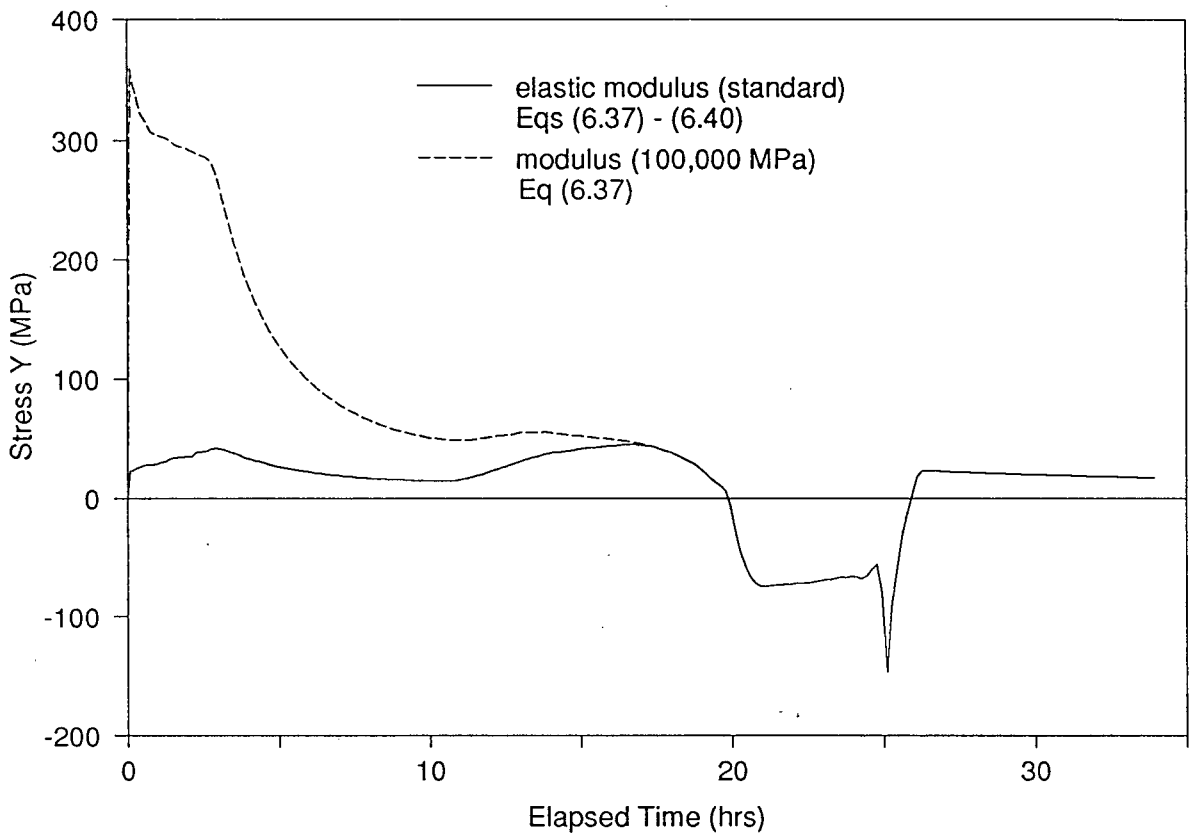


Figure 6.30. Model sensitivity to elastic modulus (σ_y at centre of broad face).

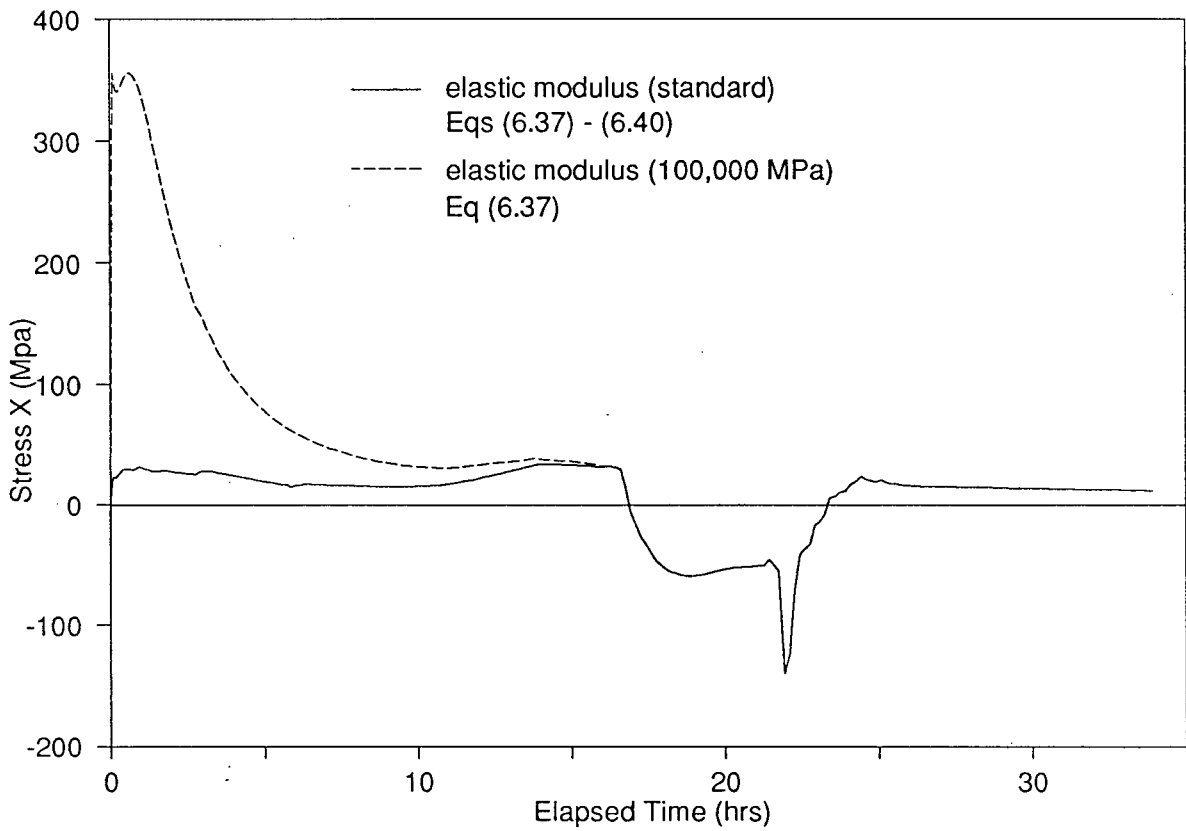


Figure 6.31. Model sensitivity to elastic modulus (σ_x at centre of narrow face).

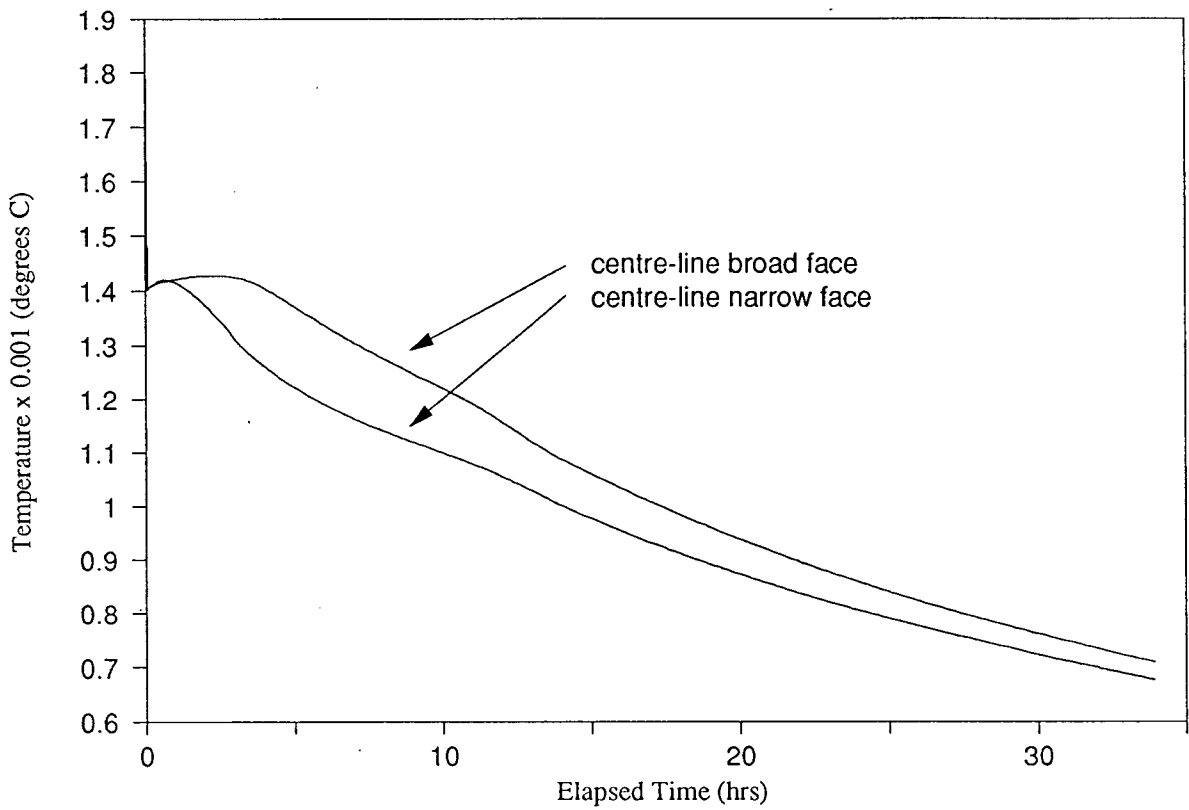


Figure 6.32. Predicted temperature response at centre of broad and narrow face.

[ii] Poisson Ratio

Model sensitivity to the Poisson ratio has been explored to establish the impact of employing a temperature independent average value for this parameter. The sensitivity of the model has been examined by varying this parameter by a factor of two relative to the standard value. The magnitude of this variation exceeds the measured variations in this parameter with temperature - refer to Table 6.5 and Figure 6.27. The results are presented in Figures 6.33 and 6.34 and indicate a low sensitivity.

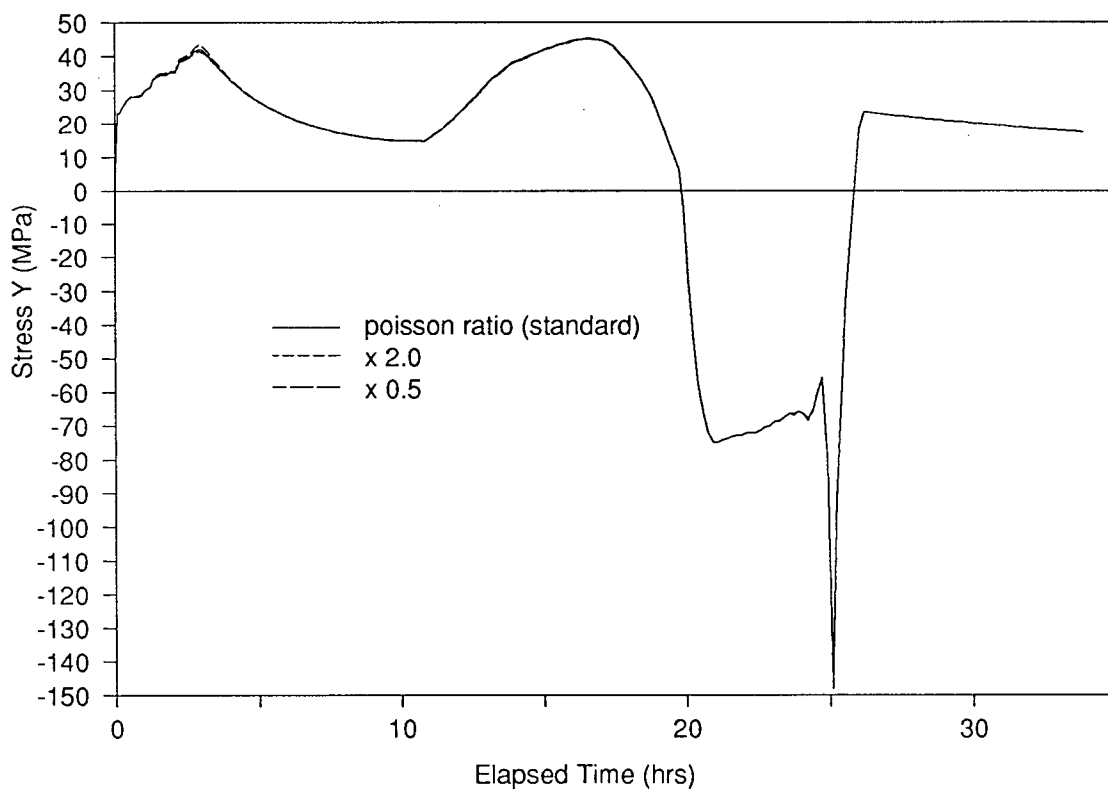


Figure 6.33. Model sensitivity to Poisson ratio (σ_y at centre of broad face).

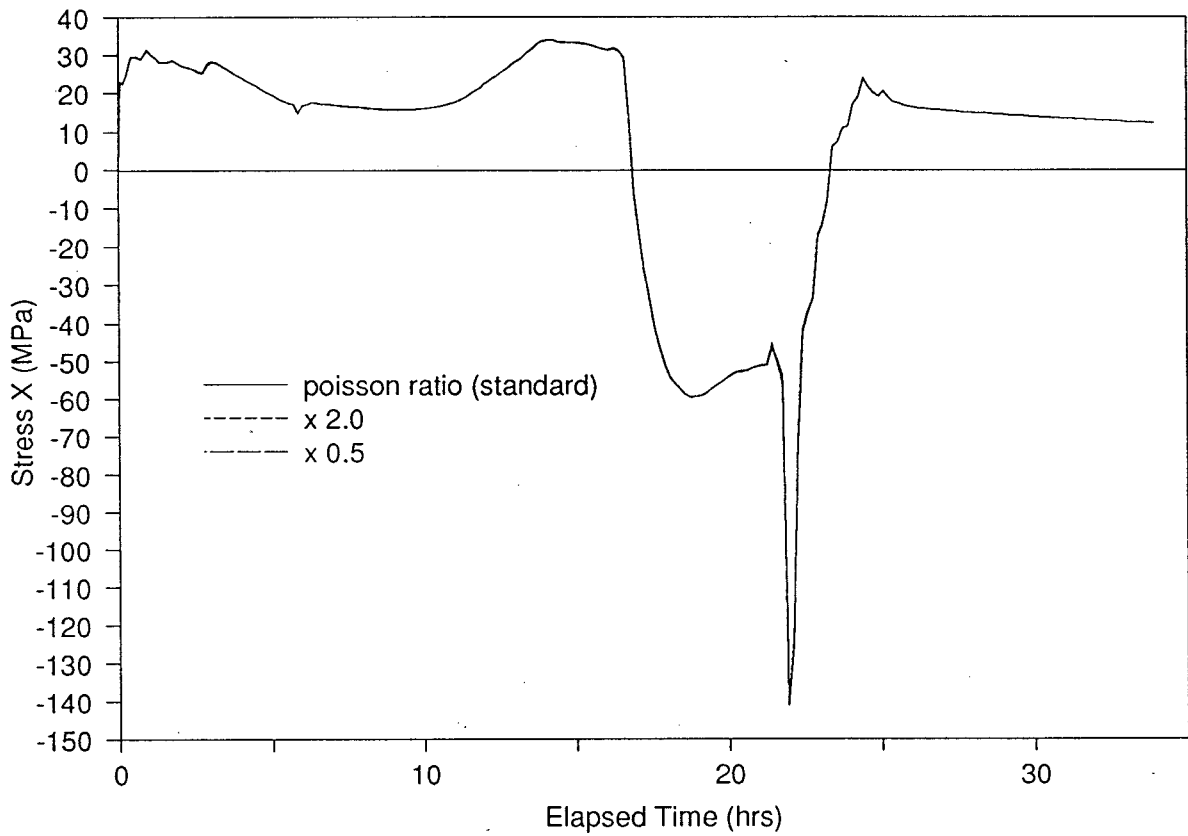


Figure 6.34. Model sensitivity to Poisson ratio (σ_x at centre of narrow face).

CHAPTER 7

MODEL PREDICTIONS AND DISCUSSION

This chapter contains the results of the three-dimensional analysis of the lower quarter-section of the Epic-3 casting. From the model predictions, mechanisms for the formation of the various crack types have been developed and a strategy for their prevention has been recommended.

7.1 Model Predictions

The volume of predictions from a 34-hr three-dimensional simulation of the Epic-3 casting process with the models of heat flow and stress generation is formidable. From the thermal analysis, this includes the temperature at each node within the refractory and sand at discrete time steps over the course of the simulation, and from the stress analysis, the three components of normal stress, σ_x , σ_y and σ_z , and the three components of shear stress τ_{xy} , τ_{yz} , and τ_{zx} at each node within the refractory. In total, this represents a significant volume of information which must be processed and interpreted. The chore of presenting this information in a manner which facilitates its interpretation is a challenging one. Fortunately, recent advances in the technology of data visualization are well suited to the task.

Employing a high-speed SiliconGraphics workstation it has been possible to display the temperature, σ_x , σ_y and σ_z distributions side-by-side and to examine the evolution of each of these variables with time in three dimensions. With this presentation technique, developed in conjunction with the University Computing Services staff, it has been possible to link regions of tensile thermal stress visually with the location of cracks in the refractory. Thermal phenomena then may be connected with stress phenomena in the casting in order to develop an understanding of thermal stress generation. Overall, this visualization technique has proved

to be critical in interpreting the predictions from the three-dimensional analysis.

Visualization of the results, as illustrated in Figure 7.1, has revealed a complex dynamic picture of the manner in which stresses develop and evolve with time in the Epic-3 casting process. Early in the solidification process, heat is extracted from the surfaces of the refractory at a high rate as the liquid Monofrax-S first contacts the mould at ambient temperature. The large temperature gradients which arise near the surface of the block generate large tensile thermal stresses due to differential contraction (the material on the cooler exterior attempts to contract relative to material in the hotter interior). These stresses can be seen acting parallel to the surfaces and edges of the refractory. The most severe stresses are generated at the refractory edges where the temperature drops rapidly. As heat continues to be lost, the temperature within the mould adjacent to the block increases leading to a reduction in the flow of heat from the refractory. This results in a gradual moderation in temperature gradients within the refractory and a reduction in the tensile stresses associated with differential contraction.

For some time this reduction in the differential strains due to contraction progresses. As the casting continues to cool, however, regions of refractory eventually begin to move through the 940 to 840°C temperature range where the zirconia component of Monofrax-S expands as it transforms from a monoclinic to tetragonal structure - refer to Figure 6.28. For the section of the refractory analyzed, the phase transformation begins first at the corners between the base and sides of the refractory; then moves along the corner between the narrow face and base; broad face and based; up the vertical edge between the faces; across to encompass the narrow face; then the broad face and finally through the centre section of the refractory. As material passes through this phase transformation it attempts to expand and in so-doing is placed in compression by the material above 940°C which acts to suppress the

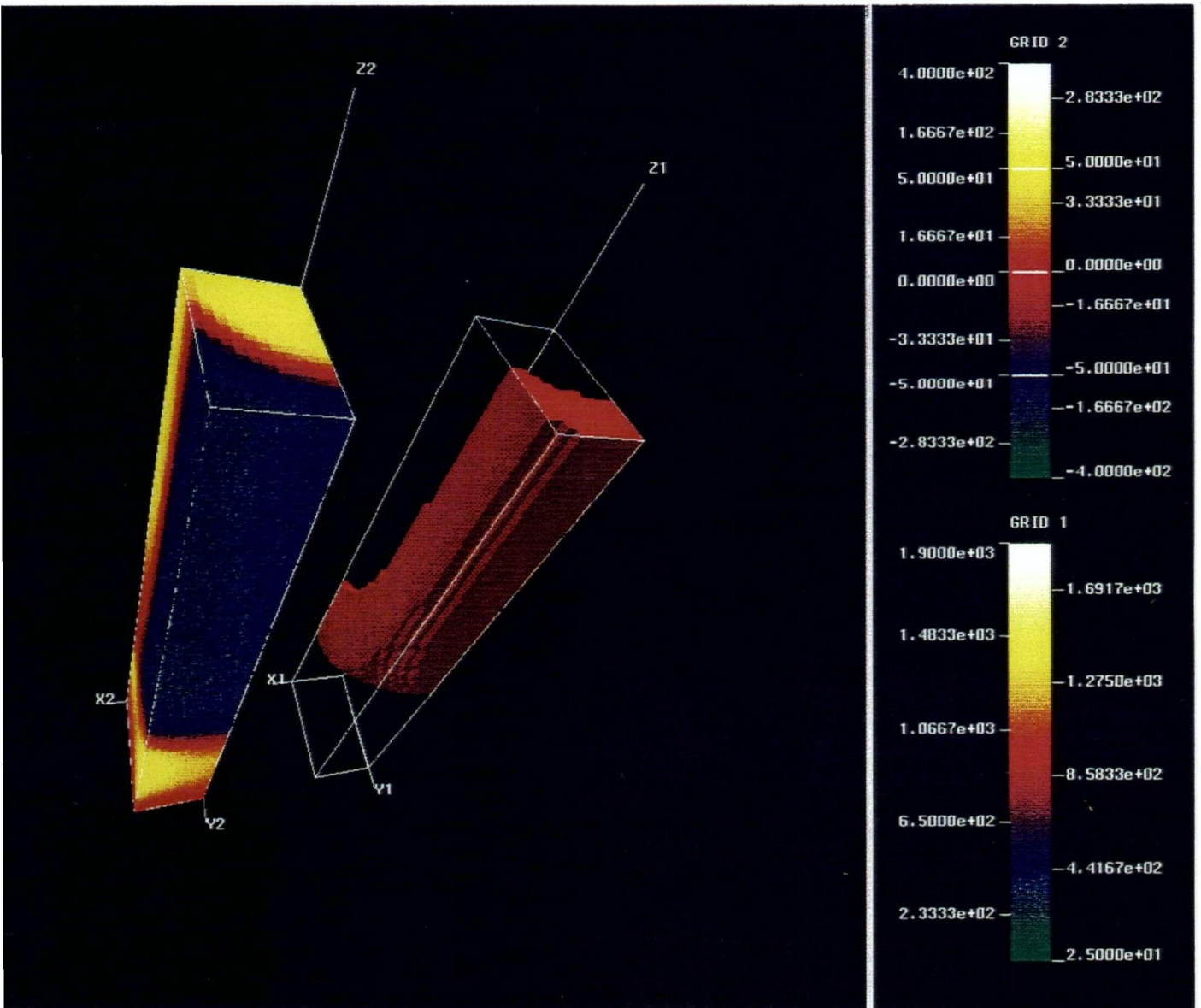


Figure 7.1. Predicted distributions of temperature and axial stress (σ_z) on the surface of the lower quarter-section of the Epic-3 cast refractory at 23 hrs elapsed time.

Note: The three-dimensional image on right (grid 1) shows a 940-840°C iso-surface (tetragonal-to-monoclinic phase transformation temperature range). The scale for grid 1 is in degrees C. The three-dimensional image on the left (grid 2) is the axial stress (σ_z) distribution. The scale for grid 2 is in MPa.

expansion and is then placed in tension. Animation of the results with the visualization tools illustrates clearly the zones of tension which are generated ahead of the tetragonal-to-monoclinic phase transformation as it moves through various regions of the cooling refractory. Despite moderation of temperature gradients it is apparent that the tensile stresses associated with the phase transformation are quite high. In the interior of the refractory near mid-height, severe tensile stresses form in the axial, or z direction, as the vertical edge and narrow face pass through the phase transformation. The tensile stresses are seen to act normal to the temperature gradients through which the phase transformation is moving. The severity of these stresses can be attributed to the relative magnitude of the thermal-linear expansion coefficients before and during the phase transformation which are: -6.55×10^{-6} and 2.41×10^{-5} $\Delta l/l \cdot ^\circ\text{C}$, respectively. Overall, these findings are in agreement with the conclusions of Thomas et al.^{22,23} which have linked major regions of tensile and compressive stress in steel casting to the γ - α phase transformation in steel.

In contrast to the behaviour of axial stress, there is a marked absence of transverse tensile stresses generated ahead of the phase transformation at the surface of the refractory. This behaviour may be attributed to the direction of the temperature gradients through which the transformation is moving. As the transformation moves from the corner toward the centre of the face, the gradients run parallel to the block surfaces and hence are incapable of generating stresses in an orientation parallel to that face. Once the transformation begins to move toward the interior however, the orientation of the gradient is perpendicular to the face and can give rise to transverse tensile stress ahead of the transformation.

7.1.1 Mechanisms for Crack Formation.

To help develop mechanisms for the formation of the various cracks types, the focus is shifted from a general description of the evolution of stress to one specific to those regions of

the casting prone to cracking. For each of the crack types, an attempt has been made to identify tensile stresses capable of causing initiation and propagation of the crack. To assess the severity of the tensile stresses predicted by the model, comparisons have been made with the measured modulus of rupture (MOR) of Monofrax-S throughout this chapter. Once formed, the presence of cracks will obviously have a significant impact on the stress distribution within the refractory. This effect has been ignored in the current analysis.

The measurements of the MOR of Monofrax-S were obtained as part of the parallel programme for thermophysical and thermomechanical data evaluation undertaken at Carborundum and are presented as a function of temperature in Table 7.1. Unfortunately, the summary of this data presented by Lebold⁷⁶ did not contain information on the experimental technique or an estimate of the error. The data is assumed to represent a reasonable assessment of the ultimate tensile strength of Monofrax-S.

Crack Type-A1 - Examination of the results of the three-dimensional analysis reveals large axial tensile thermal-stresses generated in the region of the casting prone to Type-A1 (transverse) cracks. Figure 7.1 shows the axial stress distribution on the surface of the lower quarter-section of the Epic-3 refractory at 23 hrs elapsed time. Tensile stresses, indicated by yellow, on the x-y centre-plane (top surface) are consistent with the propagation of the Type-A1 cracks through the thickness of the block. Examination of the axial stress distribution in the interior along the y-z centre-plane, presented in Figure 7.2, reveals that this region of tensile stress extends down in a column through roughly two-thirds of the refractory. This region is surrounded first by a band of red (zero stress) and then by blue indicating compression. The zone of compression extends out to encompass the narrow face and corner of the refractory. The temperature distribution, also shown in Figure 7.1, indicates that this blue compressive zone is associated with the tetragonal-to-monoclinic phase transformation

TABLE 7.1
 Modulus of Rupture of Monofrax-S (AZS-CS3) in Tension
 as a Function of Temperature⁷⁶

Temperature °C	Modulus of Rupture (MPa)
20	88.5
400	89.6
600	88.5
700	86.4
800	81.0
900	72.5
950	36.8
1000	21.3
1100	14.9
1200	10.7
1300	7.5
1400	4.3

in ZrO_2 and that the tensile stresses are generated ahead of this phase transformation.

To develop an understanding of the manner in which a Type-A1 crack might initiate and then propagate through the refractory, the predicted time-dependent variation in axial stress for three nodes located along the centre-line normal to the broad face at roughly mid-height in the refractory has been examined together with the axial stress variation for a node located at the centre of the narrow face. The location of the nodes along the centre-line normal to the broad face, see in Figure 7.3, has been chosen to coincide with a zone of the refractory through which Type-A1 cracks are routinely observed to propagate. The predictions, presented in Figure 7.4, indicate that the material along the proposed propagation path is subjected to a complex cyclic loading of tension and compression. The most predominant features in the figure are the large tensile peaks which occur at between 15 and 30 hrs

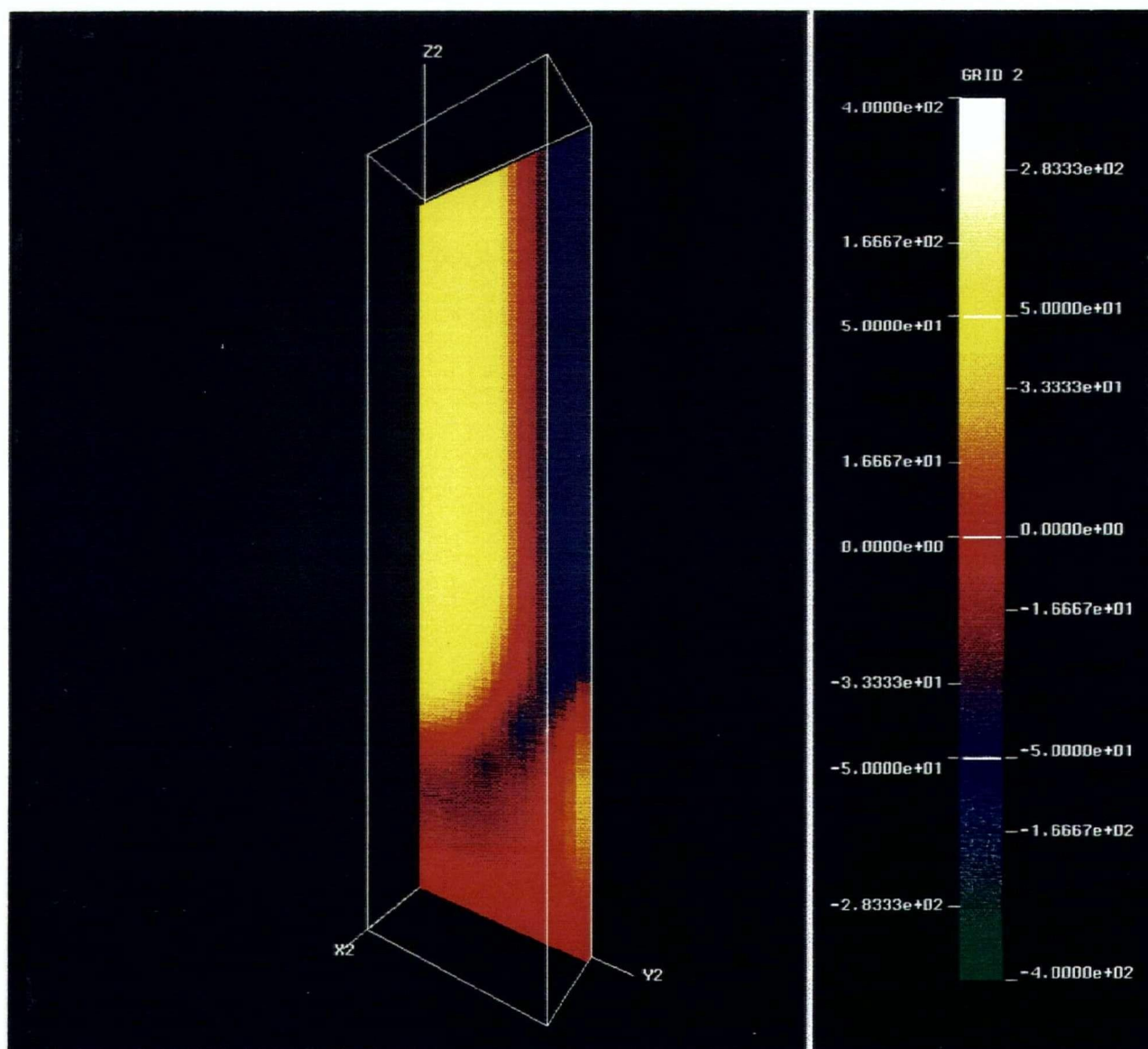


Figure 7.2. Predicted distribution of axial stress (σ_z) on the y-z centre-plane of the lower quarter-section of the Epic-3 cast refractory at 23 hrs elapsed time.

Note: The three-dimensional image (grid 2) is the axial stress (σ_z) distribution on the y/z centre-plane. The scale for grid 2 is in MPa.

elapsed time. At greater depths below the surface the peak increases from 60 to 110MPa, approximately 90%. In contrast, for the first smaller peak (0 - 5 hrs), the trend is opposite and decreases in magnitude with depth. All of the peaks shift in position to longer times with increasing depth.

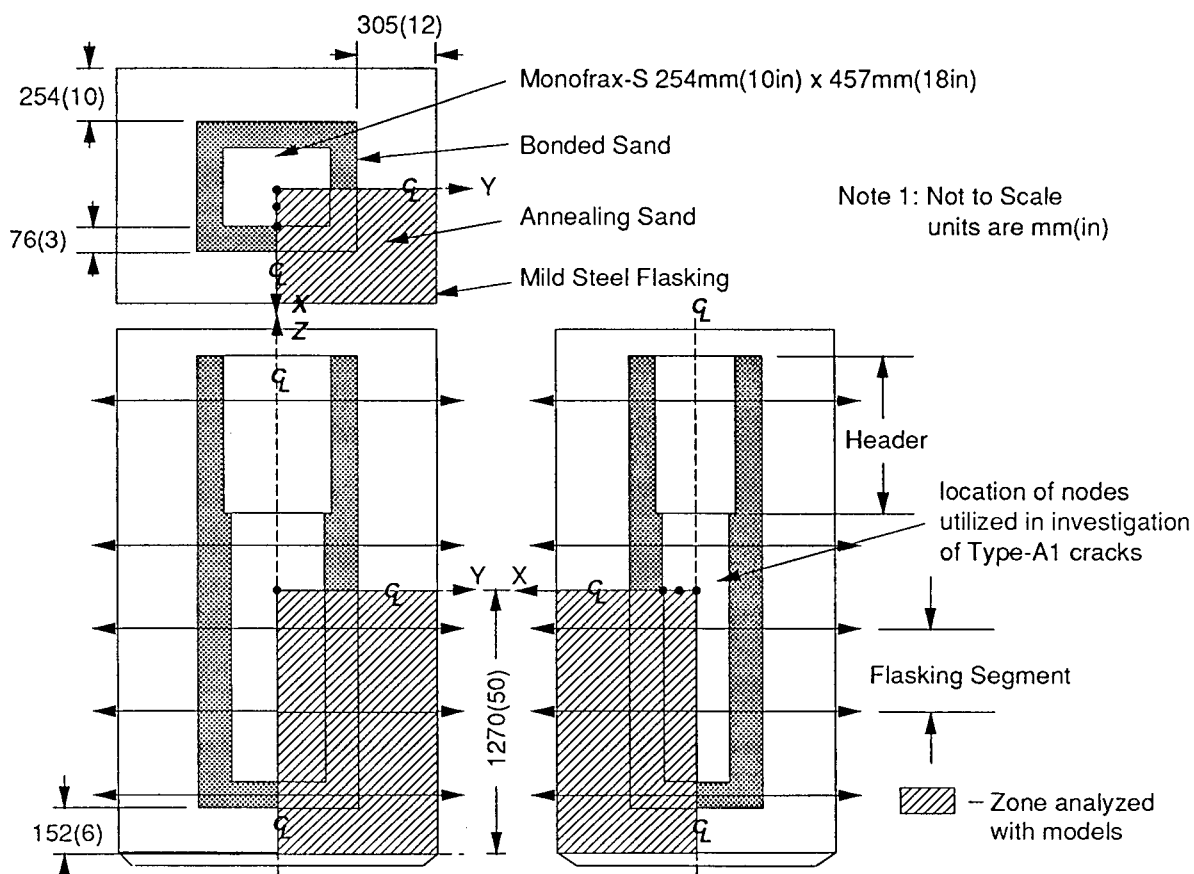


Figure 7.3. Schematic illustration of mould/flasking lay-up showing the region of casting analyzed with heat-flow model and location of nodes utilized in the investigation of Type-A1 cracks. Distances are in units of mm(in).

The behaviour exhibited in Figure 7.4 is obviously complex but can be resolved. As described earlier, the first tensile peaks at the surface of the broad and narrow faces arise from rapid cooling and contraction of the exterior relative to the interior and hence really only develops at the surface of the refractory. As the temperature gradient normal to the surface moderates there is a tendency for the tension to ease. On the broad face, the decline in tensile stress is accelerated by the behaviour of the vertical edge and narrow face of the refractory which are cooling more rapidly and hence have contracted to a greater extent and are in tension. The response at the centre of the narrow face is shown in Figure 7.4. By roughly 5 hrs elapsed time, predictions indicate that the material along the proposed fracture propagation path, 0mm, 51mm(2in) and 127mm(5in) from the surface of the broad face of the refractory, is in compression. If a crack were to have formed on the surface of the broad face during the period of tensile stress early in the solidification process, it could conceivably re-join or "heal" providing the glassy phase is viscous. The increase in tension on the narrow face and compression on the broad face predicted between roughly 14 and 20 hrs elapsed time is associated with the elastic modulus which increases significantly between 1200 and 1000°C. (A high degree of model sensitivity to this parameter was demonstrated in Chapter 6.) Beginning at around 20 hrs elapsed time material 0mm, 51mm(2in) and 127mm(5in) from the surface of the broad face is sequentially placed in tension as the edge and narrow face (shown in Figure 7.4) pass through the tetragonal-to-monoclinic phase change temperature range and begin to expand. The large compressive stresses generated on the narrow face as a result of the phase transformation are clearly shown in Figure 7.4.

As discussed in Chapter 5, there are limitations to the ability of an elastic stress analysis to predict stresses quantitatively in this application at elevated temperatures. It has been documented² that the siliceous matrix in Monofrax-S softens at temperature as low as 650°C helping to dampen thermally induced stresses visco-elastically. Time-dependent deformation

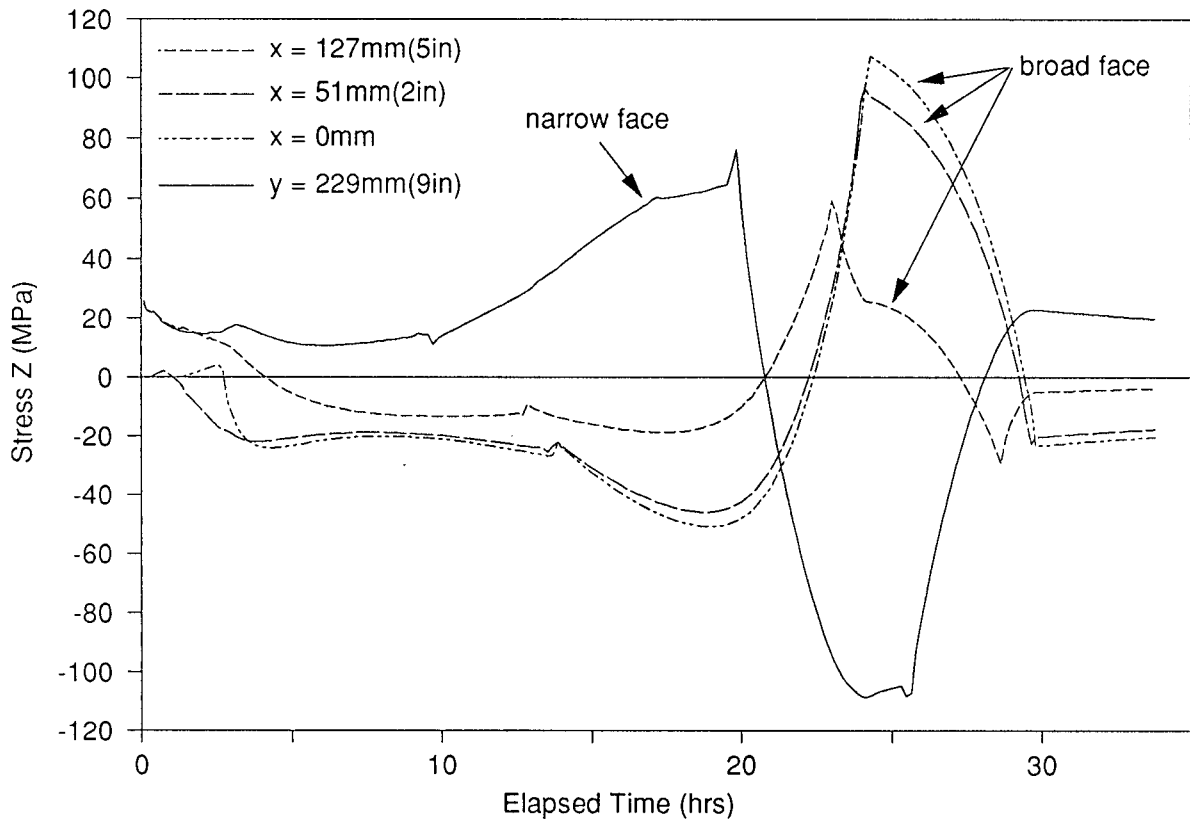


Figure 7.4. Axial stress (σ_z) predicted by the model for three nodes located along a line perpendicular to the centre of broad face and one node located at the centre of the narrow face at roughly mid-height in the refractory. Distances are measured from the vertical centre-line of the refractory.

at elevated temperatures would have to be considered and accounted for to provide a more quantitative analysis. In light of these arguments, an upper temperature limit has been placed on the ability of the model to predict stress in this application quantitatively. This threshold is assumed to be between 900 and 1000°C. Both the measured elastic modulus and modulus of rupture decrease rapidly in this temperature range which is taken to reflect significant softening of the glassy matrix in Monofrax-S. Above this limit the elastic analysis will likely over-predict stress. Moreover, the relative error will be exacerbated with increasing temperature.

Bearing in mind these limitations, an attempt has been made to assess the severity of the tensile stresses predicted by the model. To facilitate this, the predicted axial stress at positions 0mm, 51mm(2in) and 127mm(5in) from the block face has been plotted as a function of temperature together with the measured variation in the modulus of rupture (MOR) of Monofrax-S in Figure 7.5. This comparison indicates that the tensile stresses are capable of causing failure. Moreover, they suggest that the Type-A1 cracks initiate first at the surface early in the solidification process and then propagate toward the centre of the refractory driven by the tetragonal-to-monoclinic phase transformation in ZrO_2 . However, in view of the fact that the first peak at the surface occurs at a temperature above the upper limit for quantitative predictions and is likely over-predicted it is not certain that it is responsible for crack initiation. The second peak associated with the zirconia transformation could also be responsible. The issue of initiation is further clouded by comparing the predicted variation in axial stress at the centre of the broad and narrow faces. These predictions, presented in Figure 7.6, would suggest at least an equal propensity for Type-A1 crack initiation on the narrow face. Yet industrial experience indicates that the Type-A1 cracks occur only on the broad face. The development of stress suggested in Figures 7.4 and 7.5 is obviously incomplete or misleading.

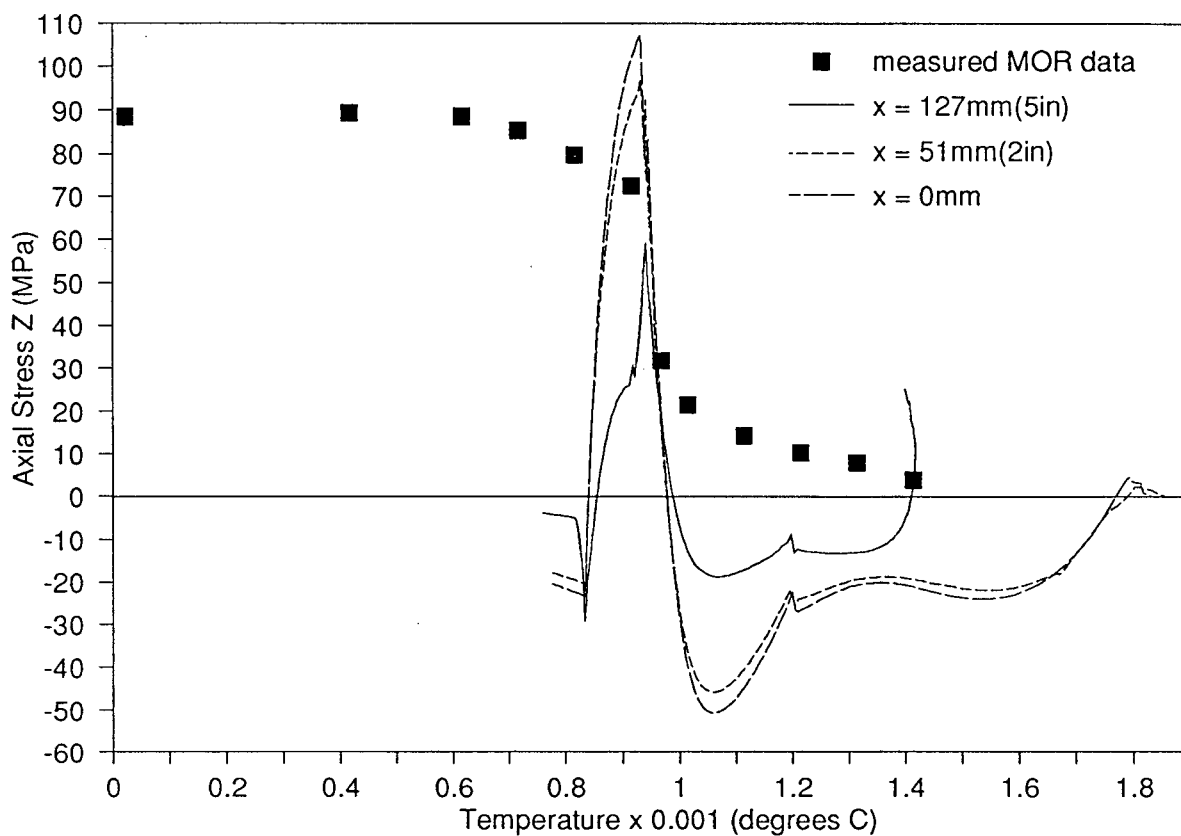


Figure 7.5. Comparison between axial stress (σ_z) predicted by the model and the modulus of rupture of Monofrax-S plotted as a function of temperature. Distances are measured from the vertical centre-line of the refractory.

Re-examination of the results of the autopsy on the instrumented Epic-3 block, Figure 4.8, Chapter 4, helps to develop one possible explanation for preferential crack initiation on the broad face. These results, which show three Type-A1 cracks in a region between the header ledge and the mould seam strongly suggest that mechanical interaction between the refractory and the mould (neglected in the model) plays a role in the formation of Type-A1 cracks. Zones between lines where the refractory is pinned to the mould will be placed in tension as the refractory contracts during cooling. The tensile stresses will be generated early in the solidification process and will act with the tensile thermal stresses. Once initiated the cracks are then driven deep into the block by the tetragonal-to-monoclinic phase transformation occurring on the narrow face and edge. Obvious points where pinning between the casting and the mould can occur are the header ledge and the mould seam (intrusion of molten Monofrax-S into the seam can produce a second smaller ledge). As indicated in Figure 4.8, the mould seam appears only on the broad face and hence could be responsible for occurrence of the crack on the major face consistent with industrial experience. The significance of this mechanism in the generation of Type-A1 cracks will be discussed later in Section 7.2.3.

In addition to factors relating to mould construction, sticking can also arise from fusion between the refractory and the mould. Excessive liquid super-heat could result in re-melting of the initial chill layer leading to bonding of the refractory to the mould and the generation of axial tensile stresses. A comparison of the predicted temperature at the centre-line of the broad and narrow faces, Figure 7.7, reveals that the broad face cools more slowly increasing the propensity for this type of pinning. This prediction is consistent with the thermocouple measurements which have revealed a lower in-mould temperature adjacent to the narrow face despite a greater thickness of annealing sand - refer to Figure 7.3. In view of the fact that the heat-transfer coefficients used to characterize the interfacial boundary condition

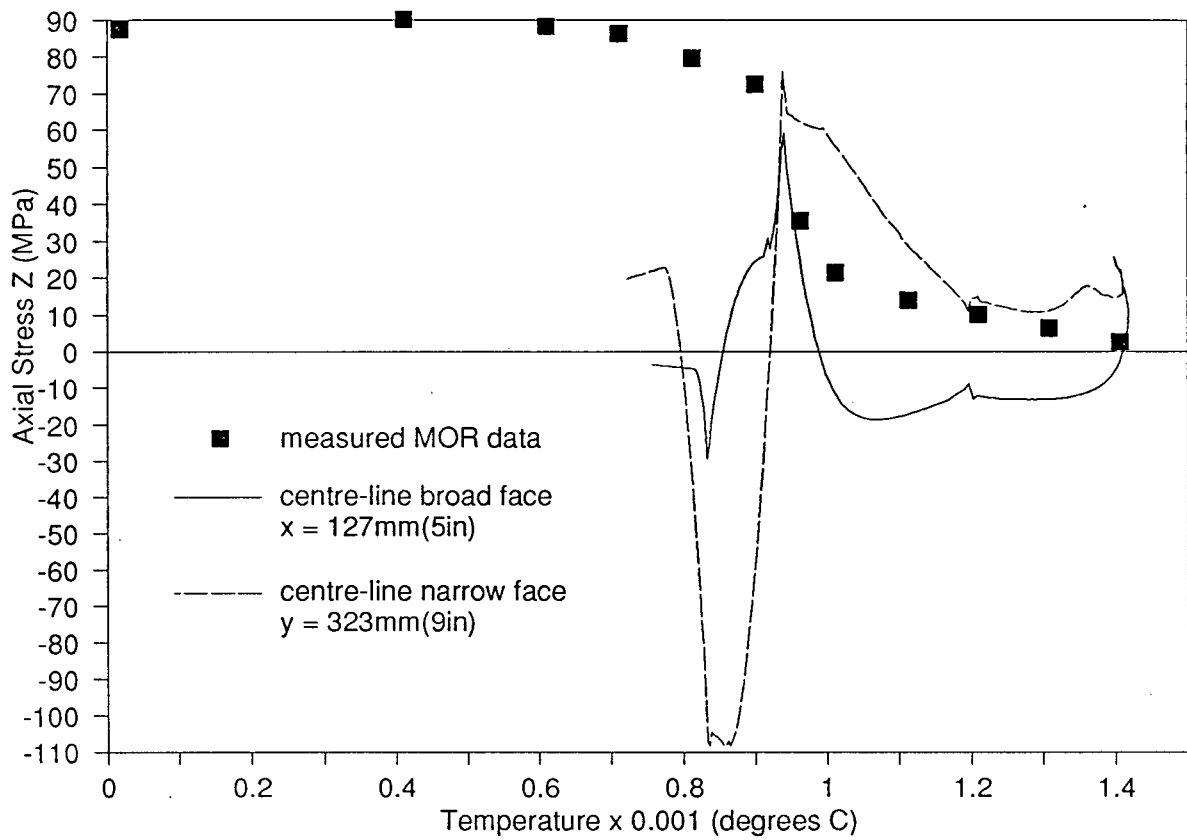


Figure 7.6. Comparison between axial stress (σ_z) predicted by the model at the centre of the broad and narrow faces and the modulus of rupture of Monofrax-S as a function of temperature.

are identical on the broad and narrow faces, this behaviour must be related to the aspect ratio of the block. The shorter corner-to-midface distance causes the narrow face to cool more rapidly than the broad face.

An alternative possibility, is that the Type-A cracks are linked to the use of graphite chills. As mentioned earlier, graphite chills (large boards of graphite) are routinely embedded in the Epic-3 mould at various locations to add structural strength and prevent bulging. According to Carborundum personnel³⁴, the graphite chills are typically placed adjacent to the broad face both within the bonded sand mould and against the outside of the bonded sand mould. The presence of a material adjacent to the broad face with a high thermal conductivity (50 W/m·°C for graphite vs. 0.5 W/m·°C for sand), will obviously increase the flow of heat from the broad face and enhance tensile thermal stresses associated with rapid heat removal from the face early in the solidification process. Confirmation of this effect with the mathematical models is presented later in this chapter in Section 7.2.1. Unfortunately, this mechanism does not account for the Type-A1 cracking which occurred in the instrumented Epic-3 mould which did not contain any graphite chills.

A final possibility which must be considered is that the evidence presented in Figure 7.4 is misleading both in terms of the sequence of events and the quantitative accuracy of the predictions. Re-interpretation of the results presented in this figure leads to the conclusion that the Type-A1 cracks could be propagating from the inside out. It is conceivable that the fracture first occurs at the centre of the block at the time of peak axial stress at roughly 24 hrs elapsed time. Once formed, the crack then propagates out toward the surface of the broad face which is in tension. The crack is inhibited from reaching the narrow face owing to the fact it is in a high state of compression due to the tetragonal-to-monoclinic phase transformation. In addition, it is likely that the tensile stress predicted on the narrow face is too high. As

shown in Figure 7.4, the tensile stress on the narrow face gradually build up over a period of time as the refractory cools. These stresses are a result of differential strains which accumulate beginning at high temperatures early in the solidification process. At high temperatures significant time dependent viscous relaxation is likely to occur. In contrast, the differential strains which give rise to the tensile stresses at the centre of the block build up quickly at a lower temperature just prior to the phase transformation. Overall these differential strains are less likely to be viscously reduced and over predicted by the model. This accounts for the preferential occurrence of the Type-A1 cracks on the broad face. The proposed mechanism is also consistent with the results of the autopsy on the instrumented Epic-3 casting, Figure 4.8, which revealed an internal Type-A1 crack. Moreover, the predicted vertical distribution of axial tensile stress associated with the phase transformation, Figure 7.2, is in agreement with the statistical crack survey which found that the Type-A1 cracks usually occur in the middle two-thirds of the refractory. Unfortunately, the results of the study of crack surface morphology do not help to conclusively prove or refute this crack formation mechanism. The results of this study presented in Chapter 1, Figures 1.5 - 1.9, show evidence of viscous flow (indicating high temperature failure) on the surface of Type-A1 cracks both near the face and interior of the refractory. The proposed mechanism suggests that failure occurs due to the tensile stresses generated ahead of the phase transformation and therefore above 940°C. The evidence from the literature² and from the thermomechanical property evaluation^{75,76}, suggests that Monofrax-S is capable of deforming in a visco-elastic manner at these temperatures which could account for the fracture morphology.

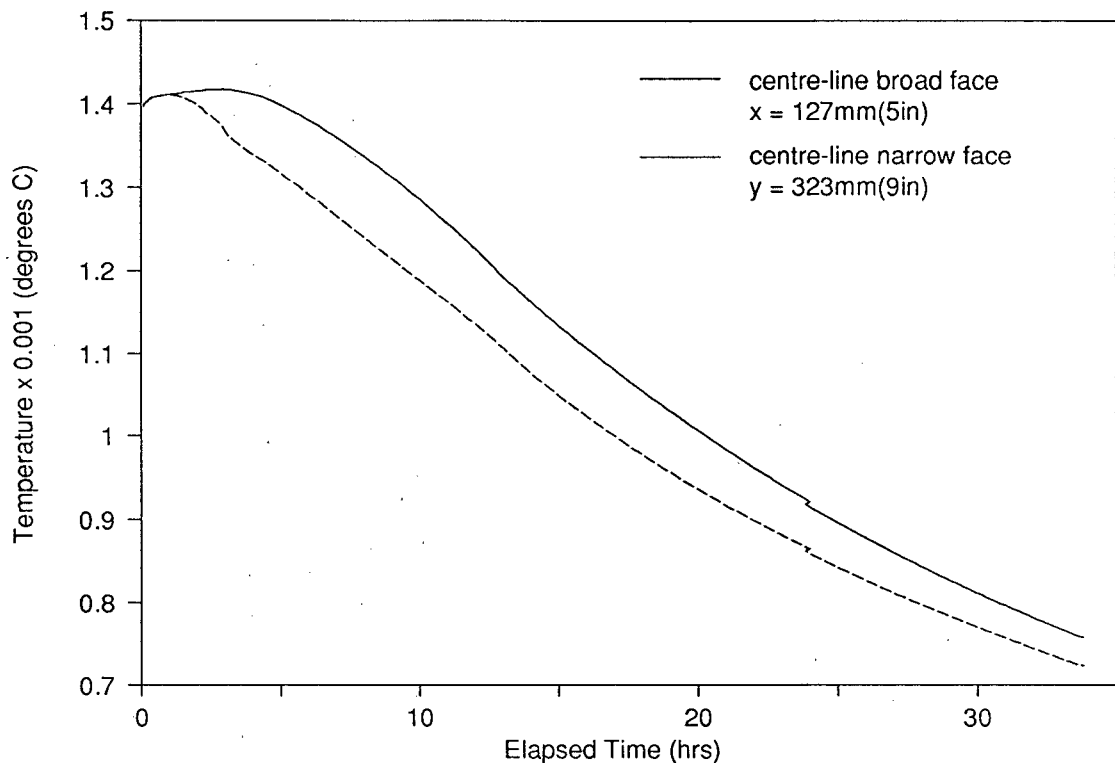


Figure 7.7. Comparison between temperature predicted by the model at the centre of the broad and narrow faces.

Crack Type-A2 - Large axial tensile thermal stresses are also predicted by the model in the zone near the base of the casting which is prone to Type-A2 cracks. In Figure 7.8, the zone of tensile stress appears as a yellow band on the broad-face near the base at 20 hrs elapsed time. The presence of a blue band (indicating compression) above this zone of tension indicates that the tensile stress is generated in the wake of the tetragonal-to-monoclinic transformation of ZrO_2 . The phase transformation occurs within the 940 - 840°C isotherms which, at the base of the refractory, curve down towards the centre of the each face due to axial heat flow. An examination of the axial stress distribution 25.4mm(1in) below the surface of the broad-face at 20 hrs elapsed time, as shown in Figure 7.9, reveals that the band of tensile stress is

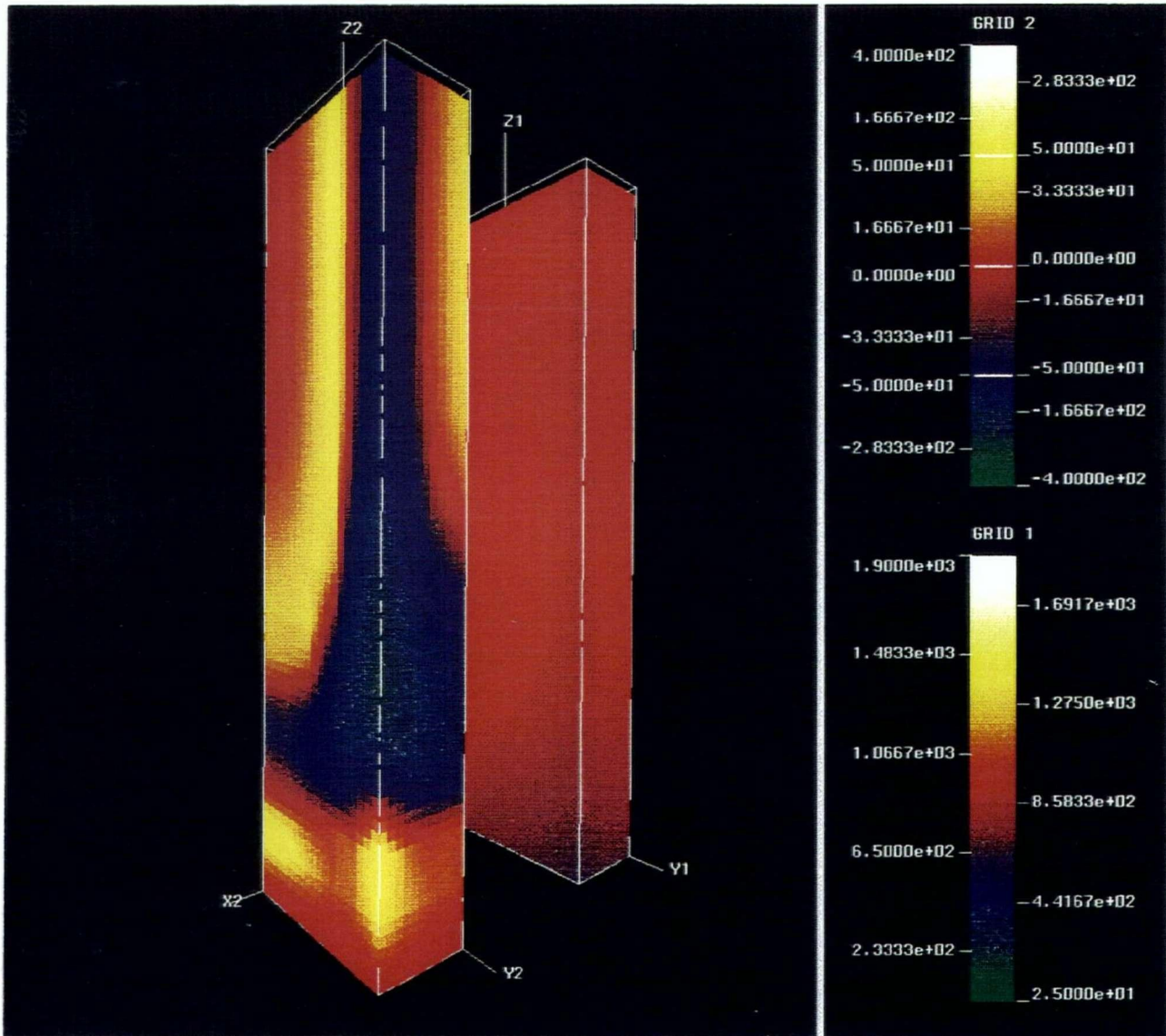


Figure 7.8. Predicted distributions of temperature and axial stress (σ_z) on the surface of the lower quarter-section of the Epic-3 cast refractory at 20 hrs elapsed time.

Note: The three-dimensional image on right (grid 1) shows the temperature. The scale for grid 1 is in degrees C. The three-dimensional image on the left (grid 2) is the axial stress (σ_z) distribution. The scale for grid 2 is in MPa.

shallow in depth and is limited to the surface of the refractory. This observation appears consistent with the results of the autopsy, Figure 4.8, Chapter 4, which show the Type-A2 to be shallow in depth of penetration.

To follow the development of stress, the output from three nodes located on the broad-face at varying distances from the base of the refractory (see Figure 7.10 for locations) has been plotted as a function of time. The predictions for all three nodes, presented in Figure 7.11, exhibit a pattern of cyclic thermal loading beginning first with tension. The largest tensile stresses are predicted to occur between 15 and 20 hrs elapsed time and are induced in the wake of the phase transformation in ZrO_2 via the mechanism outlined earlier. As the distance from the base is increased the impact of the phase transformation is delayed to longer times. A comparison between the relative magnitude of the peaks indicates that the largest tensile stresses are generated in a region centred about 14mm (5.5in) from the base of the refractory between 22 and 23 hrs elapsed time.

To assess the severity of the tensile stresses, a comparison has been made between the axial stress at the centre of the broad-face, 14mm (5.5in) from the base, and the measured modulus of rupture data (MOR) - see Figure 7.12. The results suggest that the fracture initiates early in the solidification process and is caused by the first tensile peak associated with rapid cooling of the surface. The crack surface morphology, presented in Chapter 1, confirms this indicating viscous glassy material in the zone where the crack intersects the block face at the time of crack formation. The crack presumably then is driven below the surface, likely by the tensile stresses which are generated in the wake of the tetragonal-to-monoclinic phase transformation.

A comparison between the stress predicted by the model at the centre of the broad and narrow faces near the base and near mid-height in the refractory, shown in Figure 7.13,

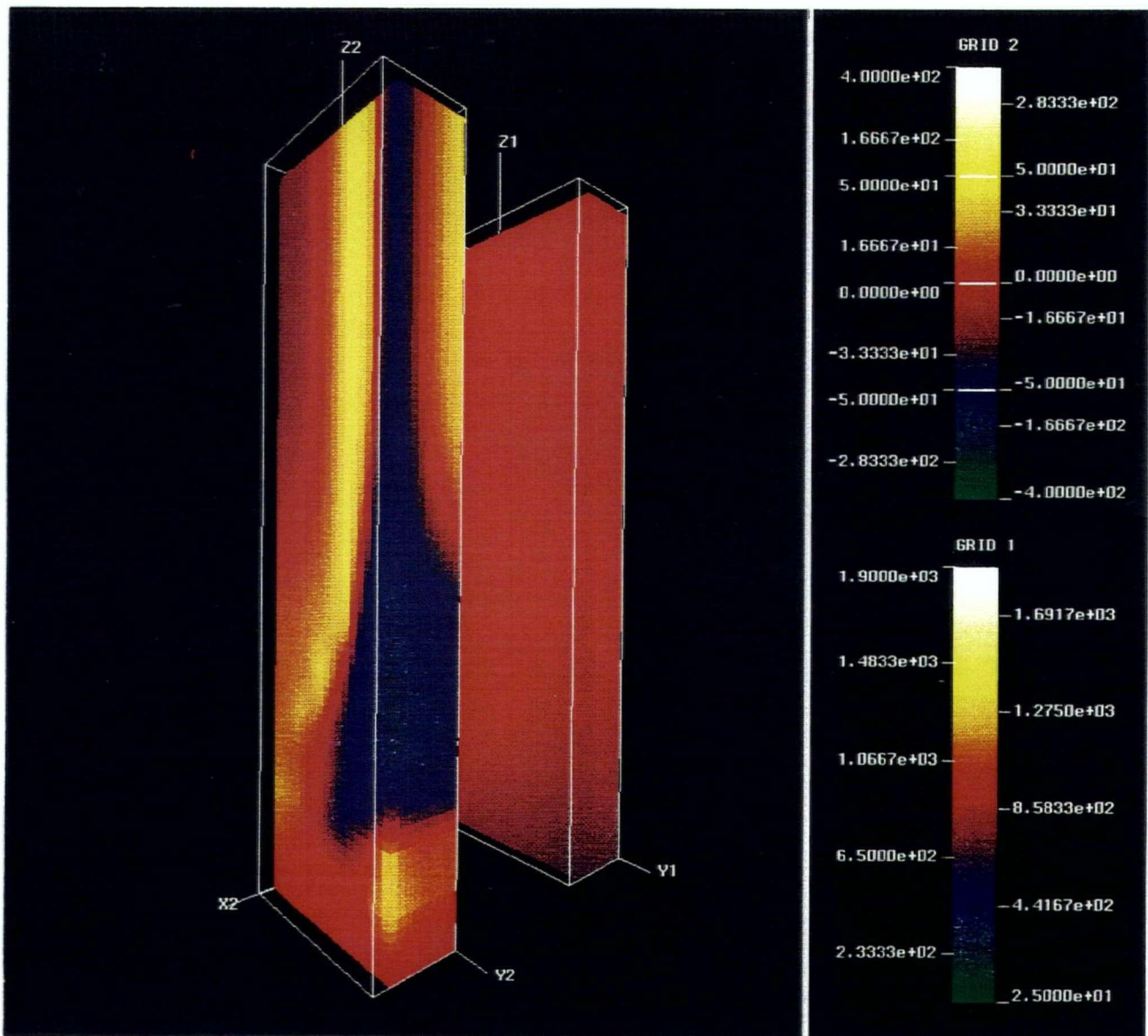


Figure 7.9. Predicted distributions of temperature and axial (σ_z) stress on the surface of the lower quarter-section of the Epic-3 cast refractory at 20 hrs elapsed time. The quarter-section has been truncated by removing 25.4mm (1in) in a direction normal to the broad-face.

Note: The three-dimensional image on right (grid 1) shows the temperature. The scale for grid 1 is in degrees C. The three-dimensional image on the left (grid 2) is the axial stress (σ_z) distribution. The scale for grid 2 is in MPa.

reveals that the initial tensile peak in stress at the near the base is significantly larger and longer in duration. A peak is reached at approximately 2 hrs elapsed time when the material in the proximity of the base is fully solidified. Axial heat flow leads to a focusing of tensile stresses 140mm (5.5in) above the base at the centre of the broad face. This is consistent with the Epic-3 autopsy, Figure 4.11, which shows the Type-A2 crack occurring about 150mm(6in) from the base. The point of focus follows the isotherms across the face and leads to a curved or "smile-shaped" crack profile.

The tensile stresses generated in this region of the casting via the proposed mechanism may be sufficient to initiate a Type-A2 crack without the added effect of interaction with the mould. The diminished role of mechanical bonding of the refractory to the broad face is anticipated since temperatures will not remain elevated for as long due to additional heat flow from the base as shown in Figure 7.14. The model predictions also suggest that the Type-A2 crack may occur before the Type-A1. As with the Type-A1 crack, the presence of a graphite chill adjacent to the broad-face will likely increase the magnitude of the first tensile peak. Once formed, the cracks then propagate inward toward the centre of the refractory in the wake of the tetragonal-to-monoclinic phase transformation. The model predictions suggest that the depth of penetration will be shallow.

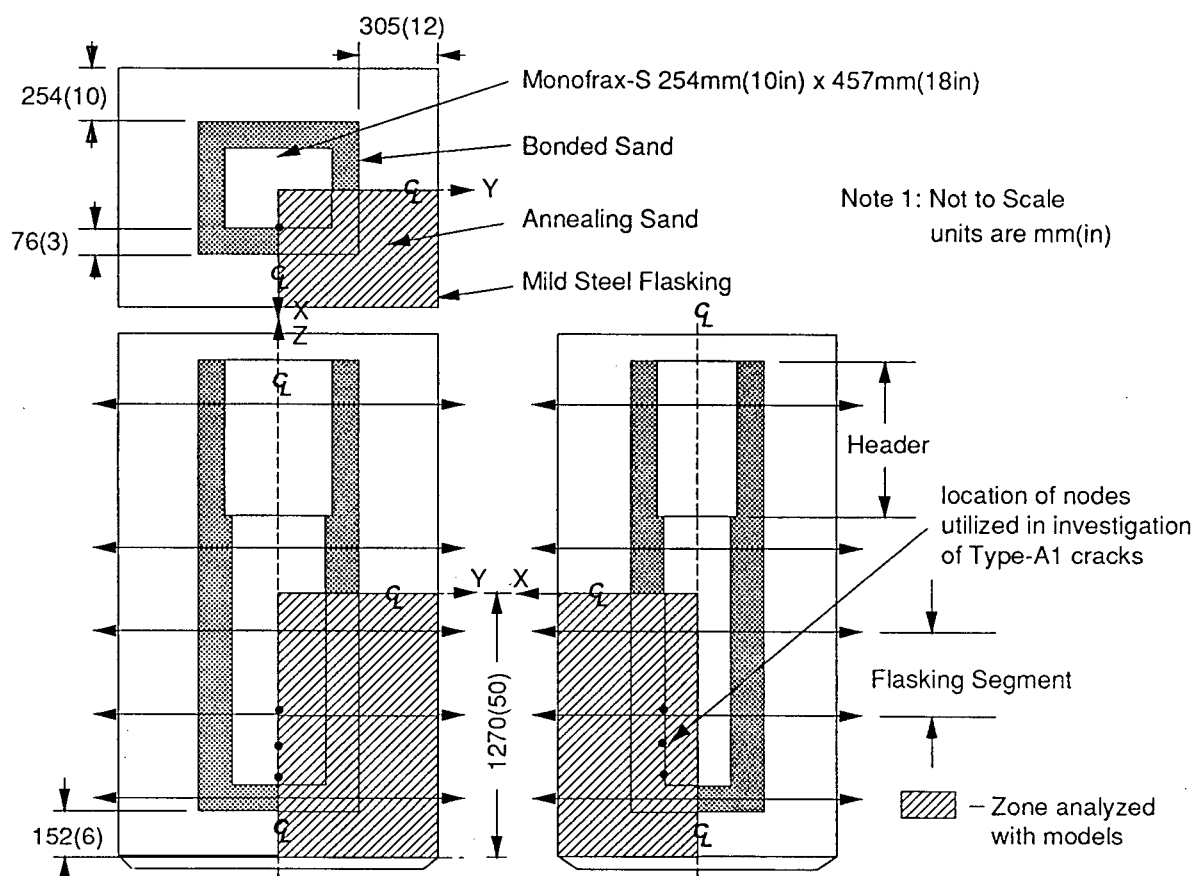


Figure 7.10. Schematic illustration of mould/flasking lay-up showing region of casting analyzed with heat-flow model and location of nodes utilized in the investigation of Type-A2 cracks. Distances are in units of mm(in)

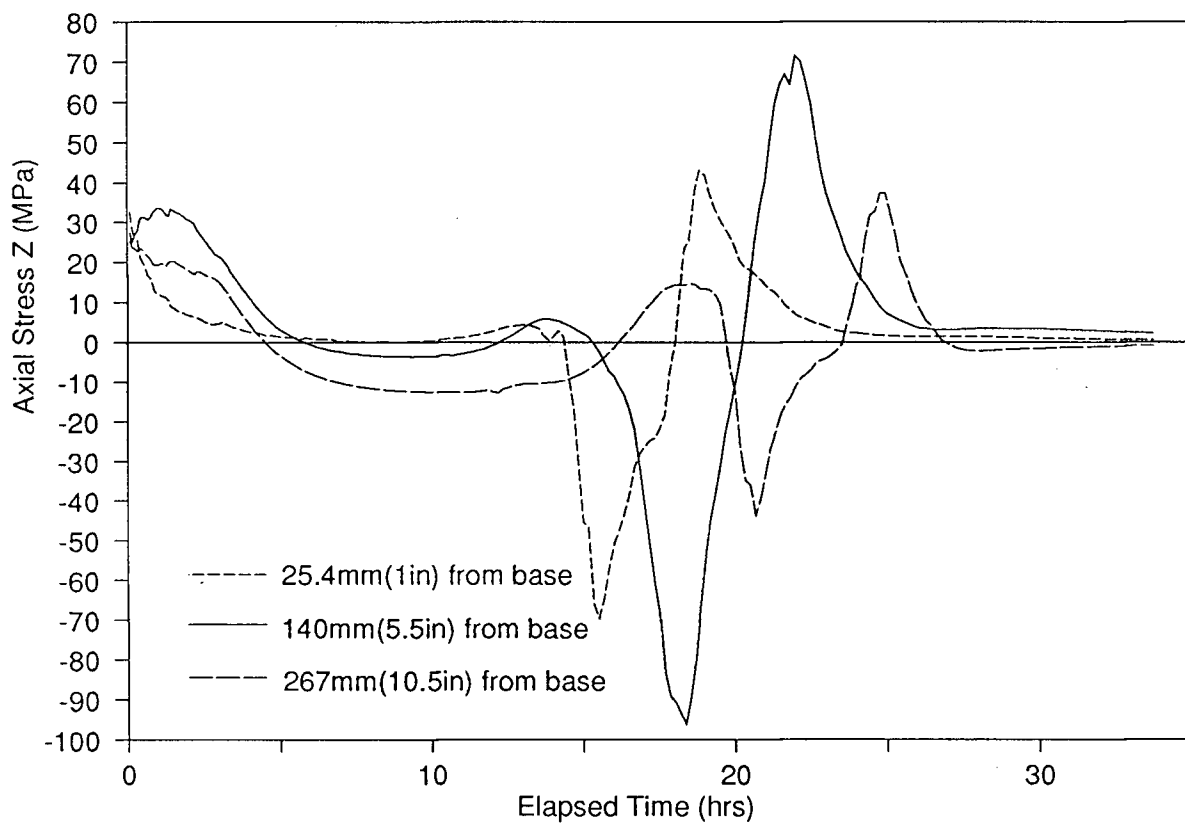


Figure 7.11. Axial stress (σ_z) predicted by the model at the centre of the broad face at varying distances from the base.

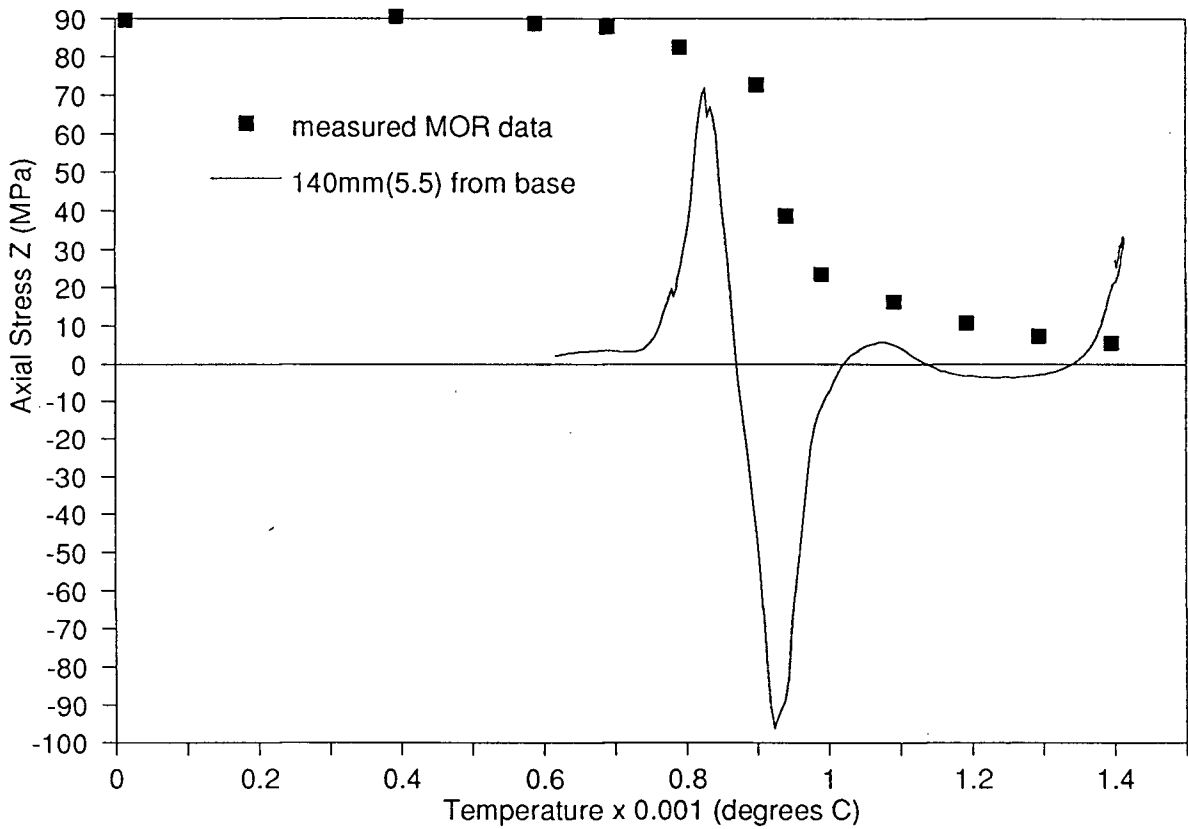


Figure 7.12. Comparison between axial stress (σ_z) predicted by the model and measured modulus of rupture data for Monofrax-S for node located at the centre of the broad face 14mm (5.5in) from the base.

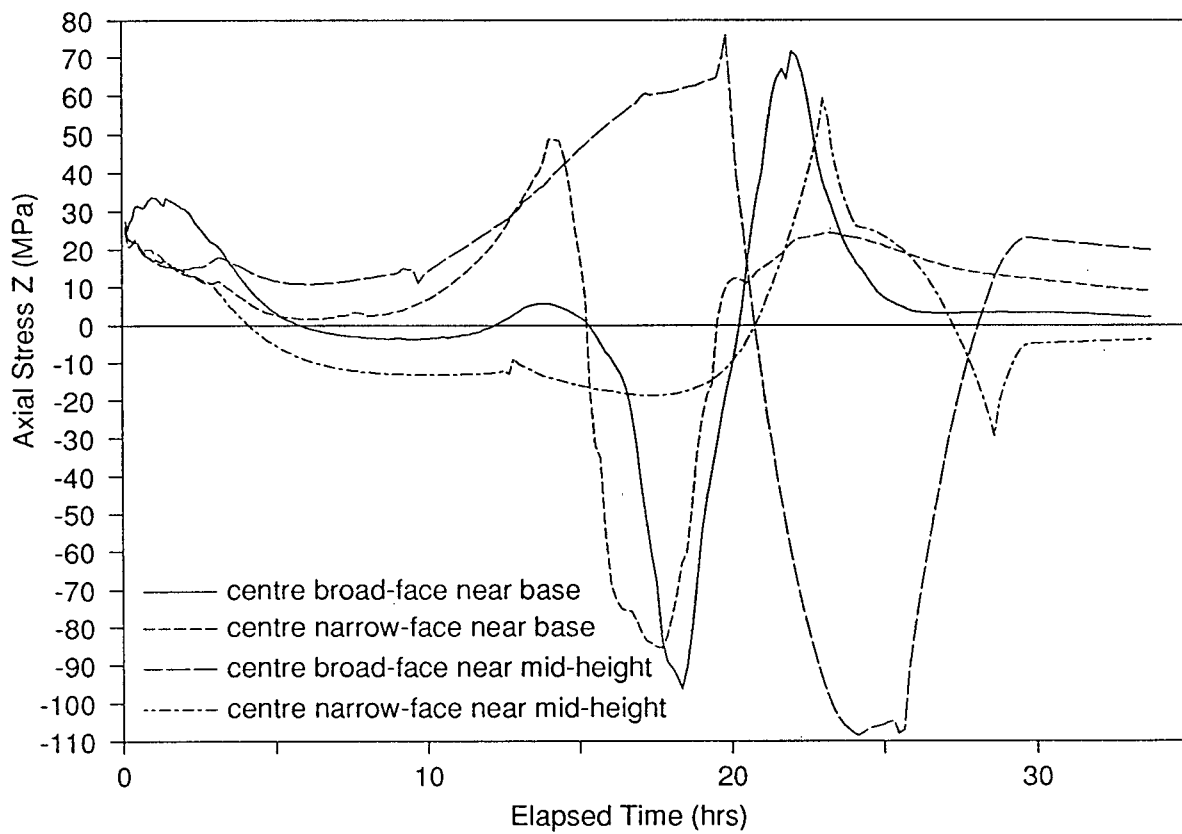


Figure 7.13. Comparison between axial stress (σ_z) predicted by the model at the centre of the broad and narrow faces near the base and near mid-height.

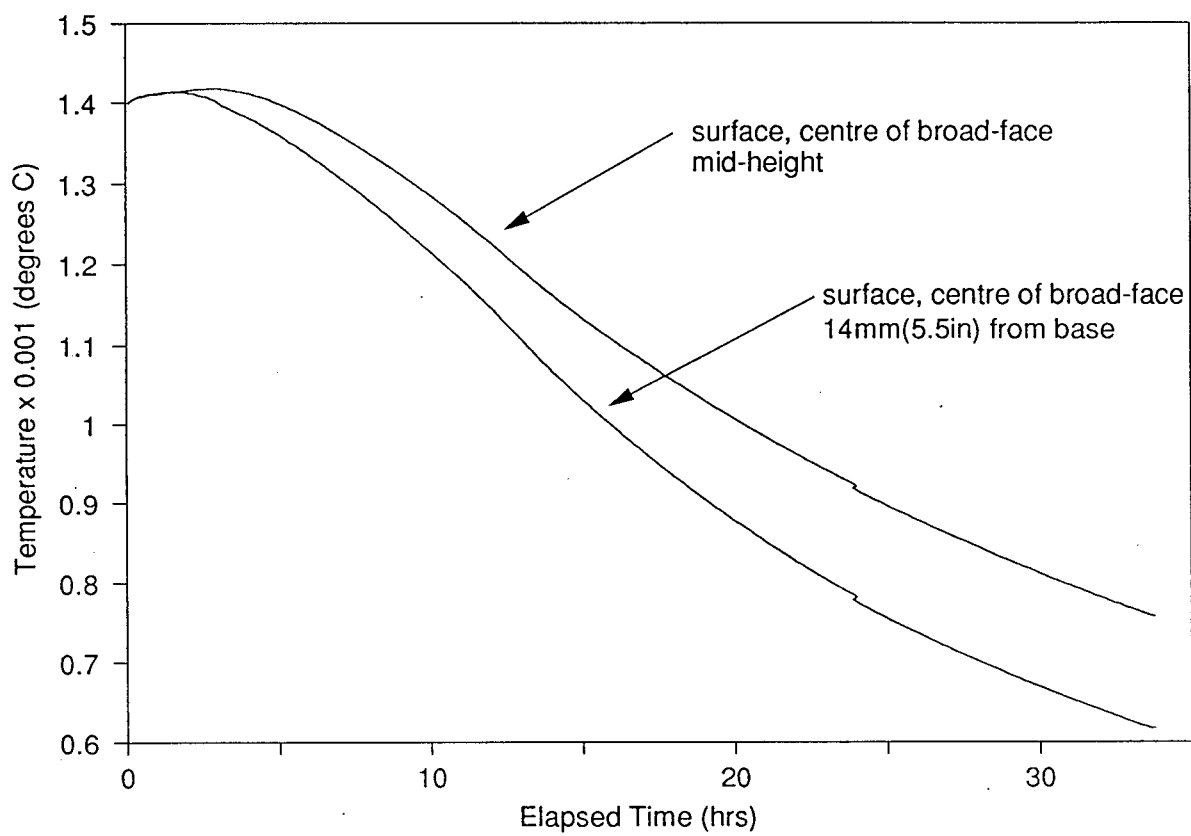


Figure 7.14. Comparison between temperatures predicted by the model at centre of the broad face near the base and near mid-height.

Crack Type-B - A review of the results reveals significant tensile stresses predicted by the model in the y-direction parallel to the broad-face and in the x-direction parallel to the narrow-face. An example of the surface σ_x and σ_y distributions at 20 hrs elapsed time is presented in Figure 7.15. The tensile stresses appear as a yellow band distributed about the centre of each face. The region of tension extends over roughly the top three-quarters of the lower quarter-section of the refractory and can be seen to increase in depth of penetration toward the centre of the face. The orientation and location of these tensile stresses is consistent with the formation of longitudinal mid-face cracks.

To examine the development of stress, a comparison has been made between the transverse stresses acting parallel to the broad and narrow faces at mid-height in the refractory. The predictions, presented in Figure 7.16, indicate that the centre of both faces is subject to peaks in tension early in the solidification process (between 0 - 5 hrs elapsed time) and again later, between 17 and 22 hrs elapsed time. The largest peaks are predicted at the centre of the broad face, consistent with the preferential occurrence of Type-B cracks on the wider face. It is interesting to note that the largest stresses are generated parallel to the face with the lower through-thickness temperature gradient contrary to what would be anticipated. A more in-depth examination reveals that differential displacements occurring on one face are transmitted through to the other face in order to preserve internal equilibrium within the structure. Figure 7.17 illustrates schematically this loading as it might apply to the shell of a partially solidified Epic-3 casting cooled alternately from the broad and narrow faces. The resulting thermal loading that arises is analogous in many respects to a beam bending problem. The thermal loads are equal and act parallel to each face. These loads induce a bending moment on the opposite face which in turn gives rise to tensile stresses concentrated at the centre of the face. Owing to the fact that the moment arm is larger for the broad-face it is subject to the largest tensile stresses.

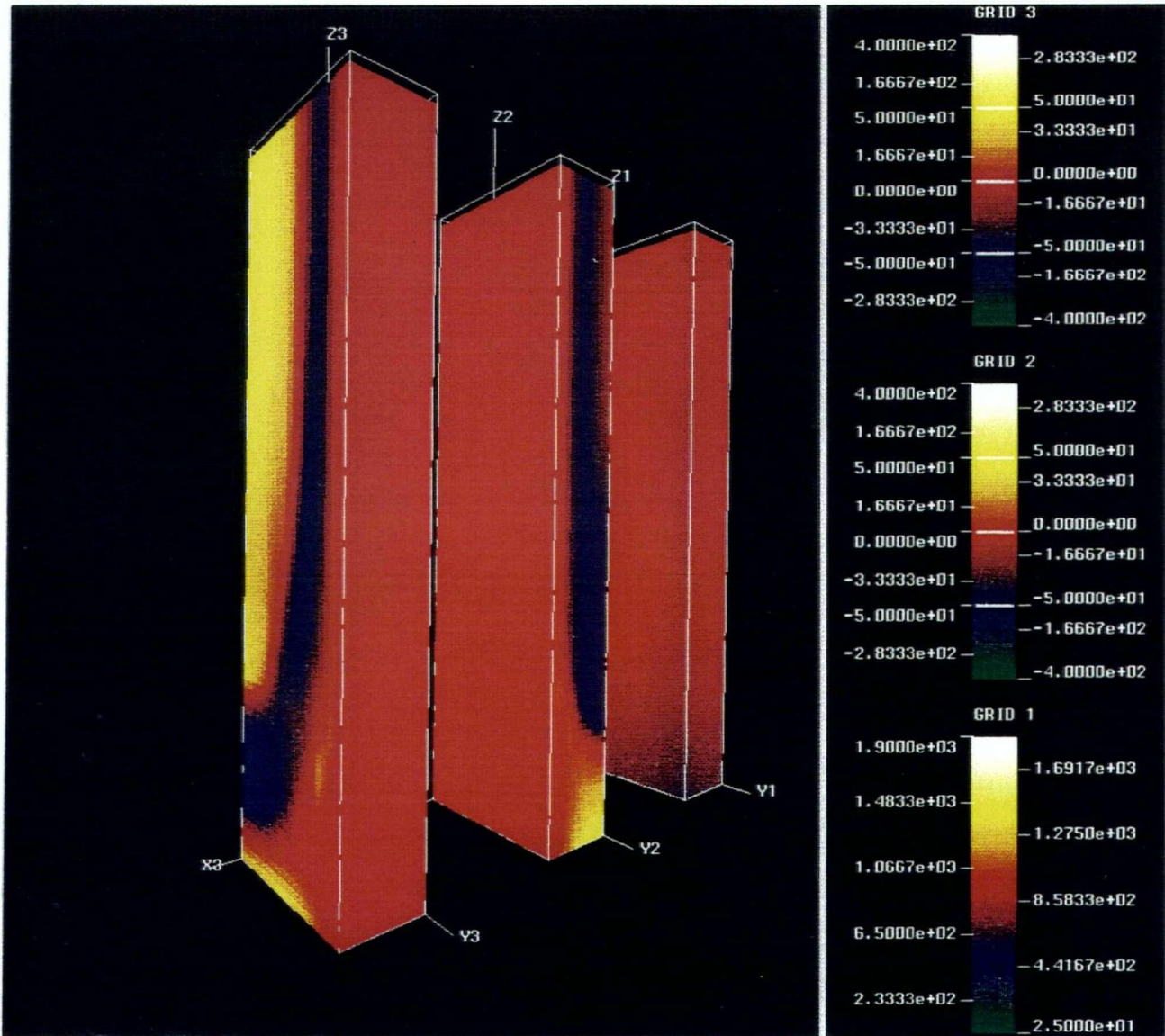


Figure 7.15. Predicted distribution of temperature, σ_x and σ_y on the surface of the lower quarter-section of the Epic-3 cast refractory at 20 hrs elapsed time.

Note: The three-dimensional image on right (grid 1) shows the temperature. The scale for grid 1 is in degrees C. The three-dimensional image in the centre (grid 2) is the σ_x distribution. The scale for grid 2 is in MPa. The three-dimensional image on the left (grid 3) is the σ_y distribution. The scale for grid 3 is in MPa.

The increase in tensile stress observed in Figure 7.16 at 10 hrs elapsed time, despite moderation of temperature gradients, can be attributed to the behaviour of the elastic modulus which exhibits a rapid increase between 1200 and 1000°C. Cooling further, the material then moves through the tetragonal-to-monoclinic phase transformation and is quickly placed into compression as it attempts to expand. To illustrate the impact of the phase transformation on the generation of transverse stresses, the variation in σ_y with depth below the surface of the broad face has been examined. The results presented in Figure 7.18 show a tensile peak in stress generated 51mm (2") below the surface as the exterior moves through the phase transformation (indicated by compressive peak). This may help to drive the crack below the surface. Once through the transformation temperature range, the tensile hoop-stress returns. Beyond 34 hrs elapsed time there is a gradual reduction in tensile stress as temperature gradients continue to moderate.

A comparison between the predicted stress at the centre of the broad-face and the MOR data is presented in Figure 7.19. The comparison suggests that there is an opportunity for Type-B cracks to initiate throughout the early stages of the casting process while the broad face is in the temperature range of 1400 to 1000°C. Bearing in mind the quantitative limitations of the model, the predictions suggest the formation of a high temperature fracture surface. An examination of crack surface morphology conducted earlier in Chapter 1, reveals evidence of both low- and high-temperature fracture and is inconclusive. However in general, the evidence suggests a lower temperature failure in the vicinity of the block face changing to one more indicative of hot tearing deeper into the refractory. The model predictions also suggest that the Type-B cracks are not likely to occur after the Type-A1 but may occur after the Type-A2. Industrial experience indicates that the Type-B crack is the last to form (at points where Type-A and B cracks intersect the Type-B crack is discontinuous). However, it is not clear from Walrod's study⁸ whether this applies to the Type-A1 or -A2 transverse crack. The

fact that no Type-B fracture was observed in the instrumented Epic-3 casting, Figure 4.11, indicates that the conditions examined in the model may not be conducive to the formation of Type-B cracks. It is possible that the Type-B cracks are linked to the addition of graphite chills to the mould adjacent to the broad face - see earlier description for chill placement. The graphite chill would likely increase the tensile hoop stresses associated with differential thermal contraction since heat would be extracted from the broad face more rapidly. Confirmation of this effect with the mathematical models is presented later in this chapter in Section 7.2.1.

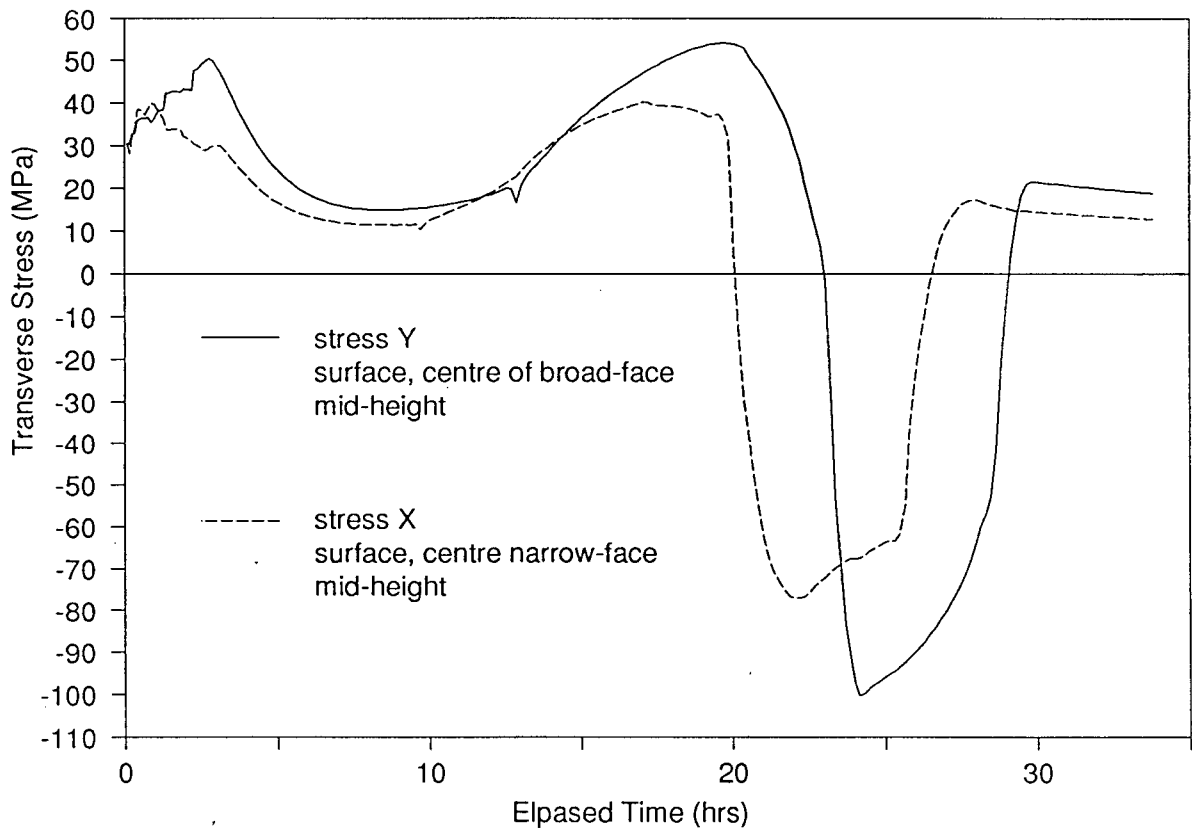


Figure 7.16. Predicted transverse stresses acting parallel to the broad and narrow faces. The nodes are located at the centre of each face at mid-height in the refractory.

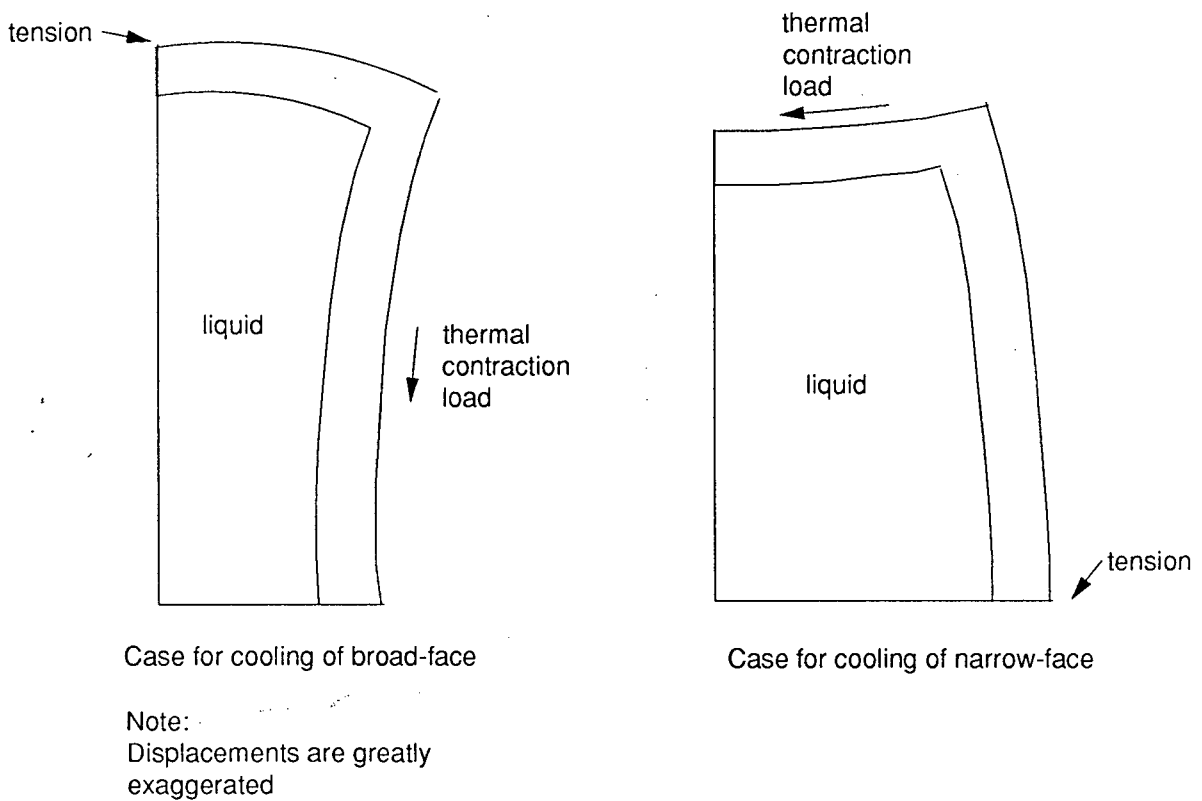


Figure 7.17. Schematic illustration of beam bending analogy as applied to a quarter transverse-section of Monofrax-S refractory. The refractory is depicted as being only partially solidified.

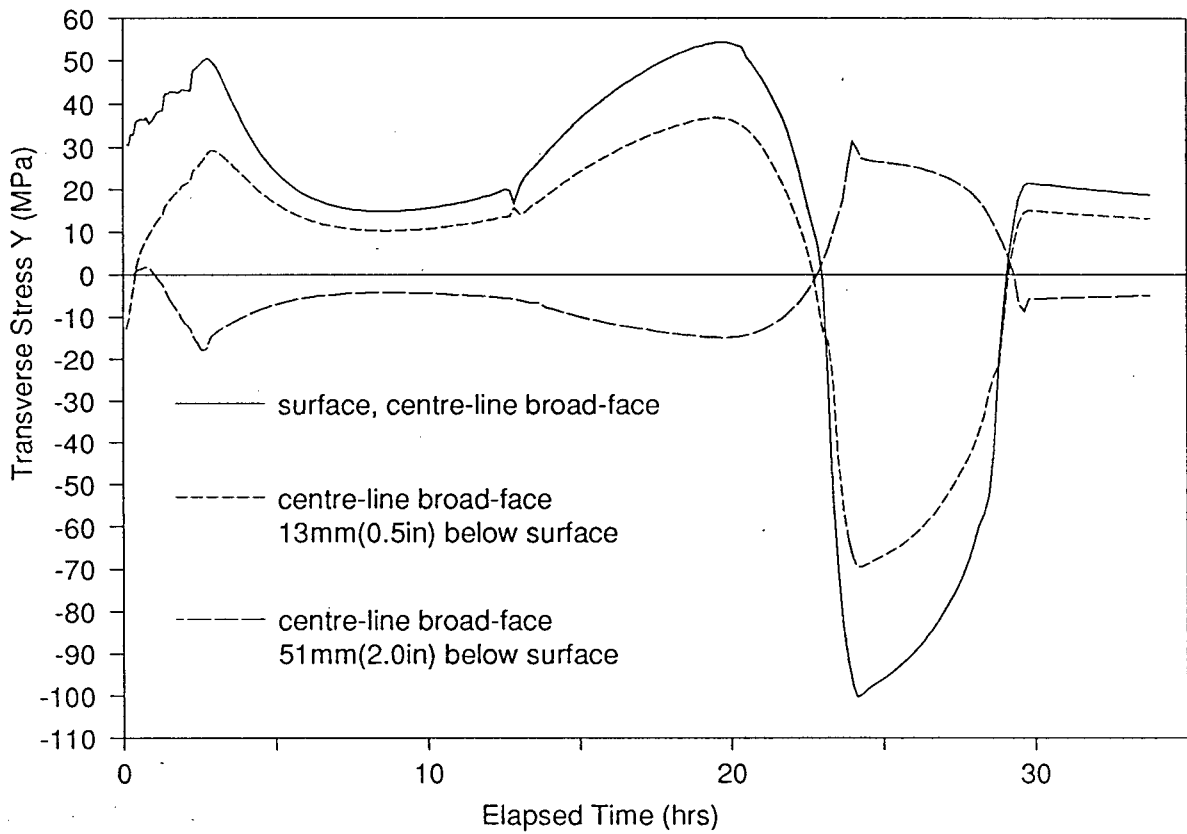


Figure 7.18. Predicted σ_y variation at centre of the broad-face at (0)mm, 13mm(0.5in) and 51mm(2in) below the surface at mid-height in the refractory.

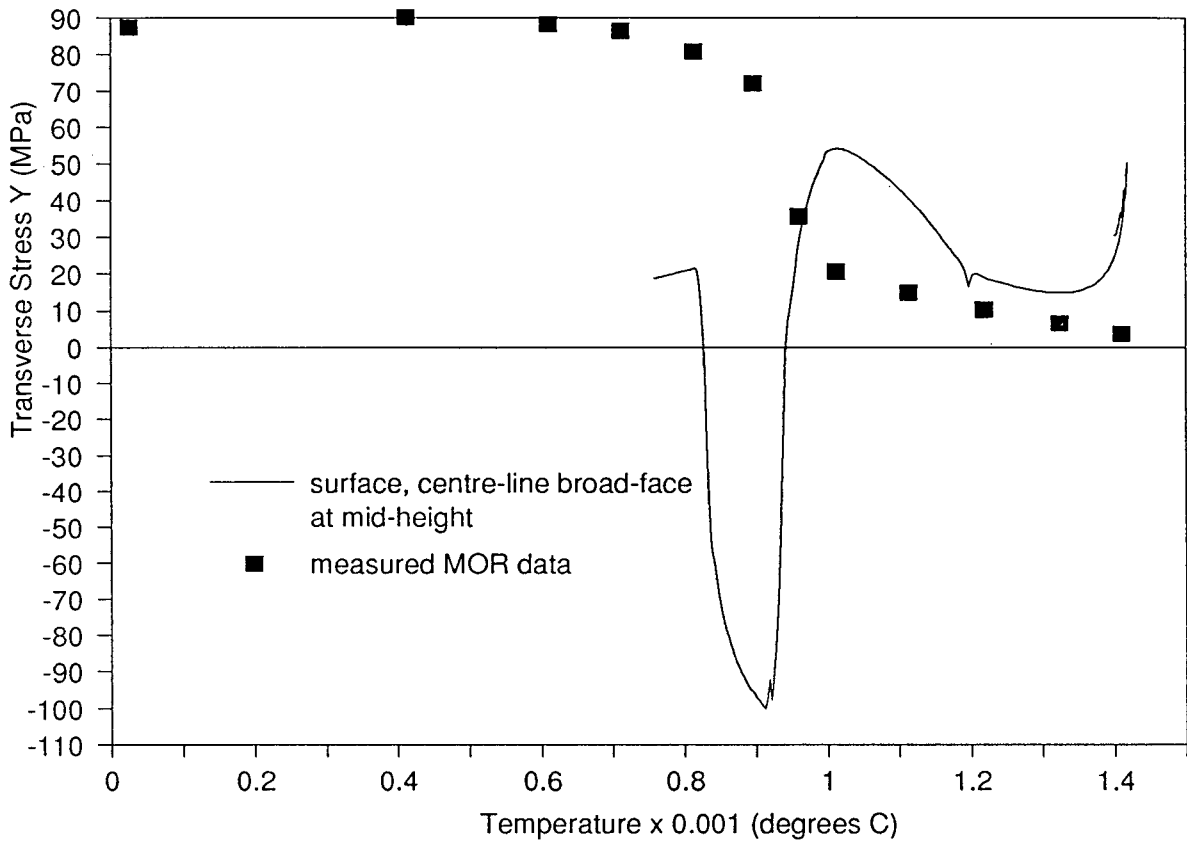


Figure 7.19. Comparison between σ_y predicted by the model at centre of the broad face at mid-height and the measured modulus of rupture data for Monofrax-S as a function of temperature.

Crack Type-E - Examination of model predictions for the vertical edge of the refractory reveals a significant tensile thermal stress in the axial or z-direction consistent with the occurrence of Type-E edge tears in Epic-3 castings. In Figure 7.20, these stresses appear as the bright yellow region located on the vertical edge of the z orientated stress distribution. Excessive rates of heat removal from this zone and the resulting large temperature gradients are responsible for the generation of these stresses.

The development of axial stress at the exterior edge at mid-height in the casting can be seen in Figure 7.21. The predictions indicate that large axial thermal stresses are generated at the vertical edges early in the solidification process due to differential contraction. The stresses are predicted to peak at approximately 1/2 hr elapsed time and then begin a slow decline as thermal gradients within the refractory moderate. Between 15 and 20 hrs elapsed time the corner is predicted to move through the tetragonal-to-monoclinic phase transformation and into a state of compression. Beyond 30 hrs the corner is back in tension which continues to moderate with time.

A comparison to the measured MOR data, presented in Figure 7.22, reveals that the axial stresses predicted at the edge are more than adequate to initiate the formation of a Type-E crack. At 1000°C, the tensile stresses are predicted to exceed the modulus of rupture by roughly a factor of three. This represents the most severe tensile stresses encountered in the analysis and is consistent with the fact that the Type-E edge tears are the most prevalent crack type.

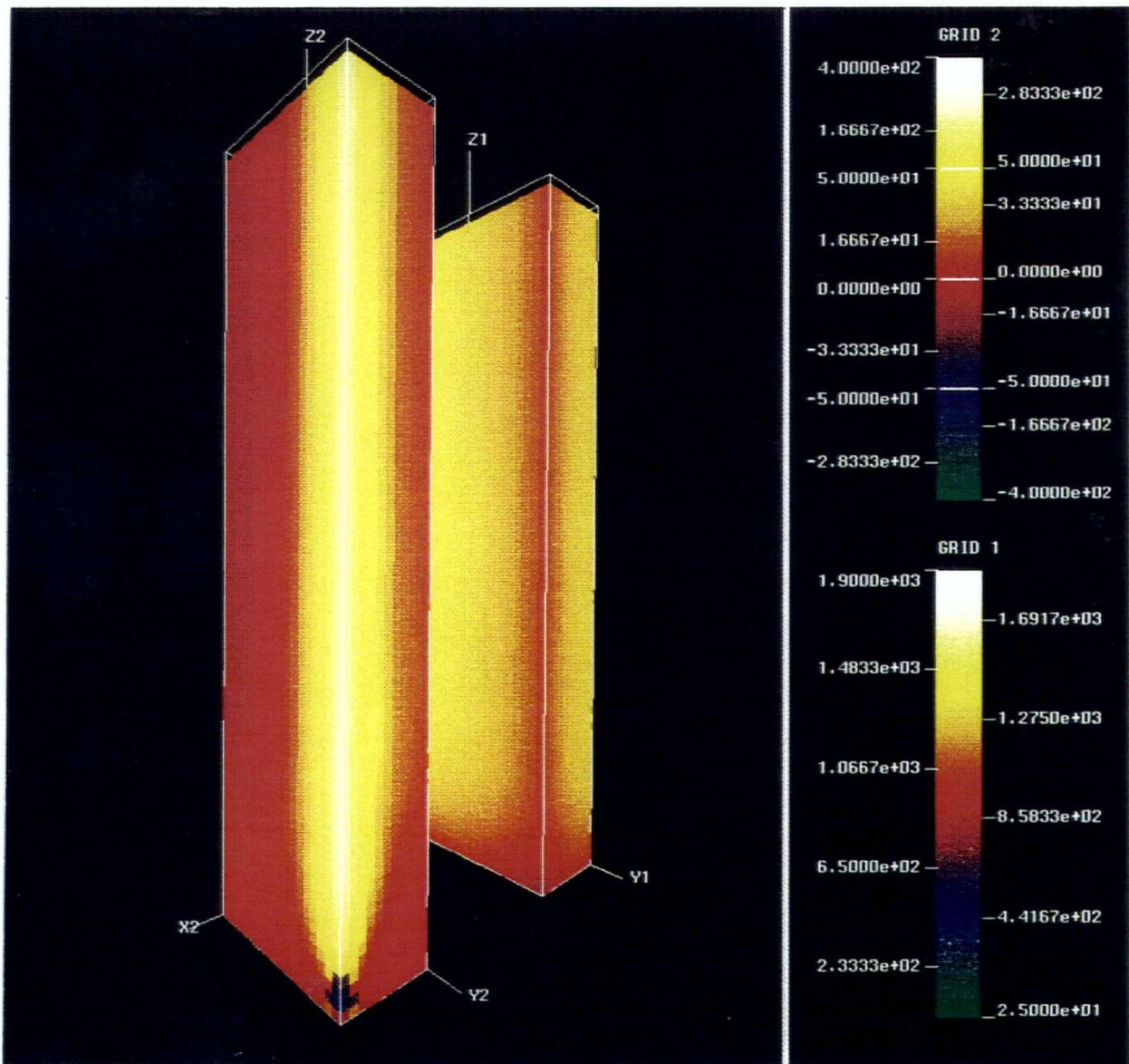


Figure 7.20. Predicted distributions of temperature and axial stress (σ_z) on the surface of the lower quarter-section of the Epic-3 cast refractory at 5 hrs elapsed time.

Note: The three-dimensional image on right (grid 1) shows the temperature. The scale for grid 1 is in degrees C. The three-dimensional image on the left (grid 2) is the axial stress (σ_z) distribution. The scale for grid 2 is in MPa.

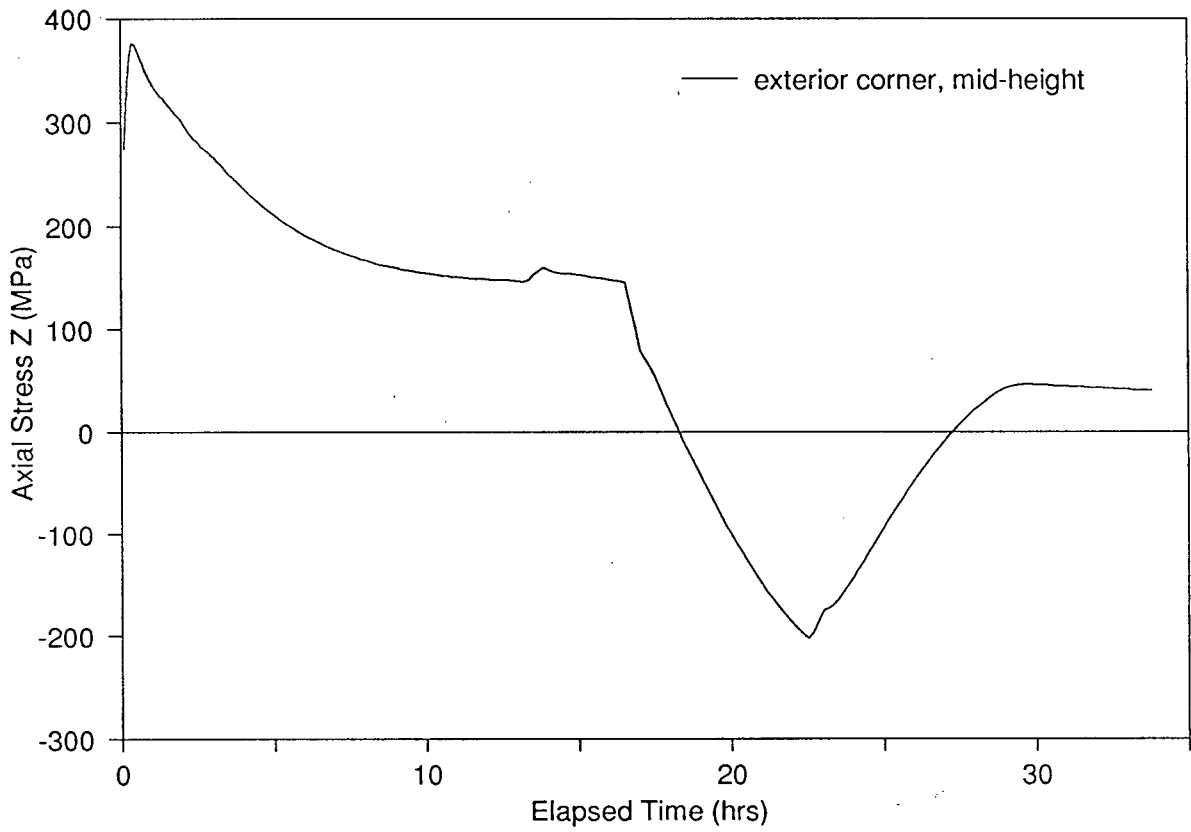


Figure 7.21. Predicted σ_z at intersection between broad and narrow faces at mid-height of the refractory.

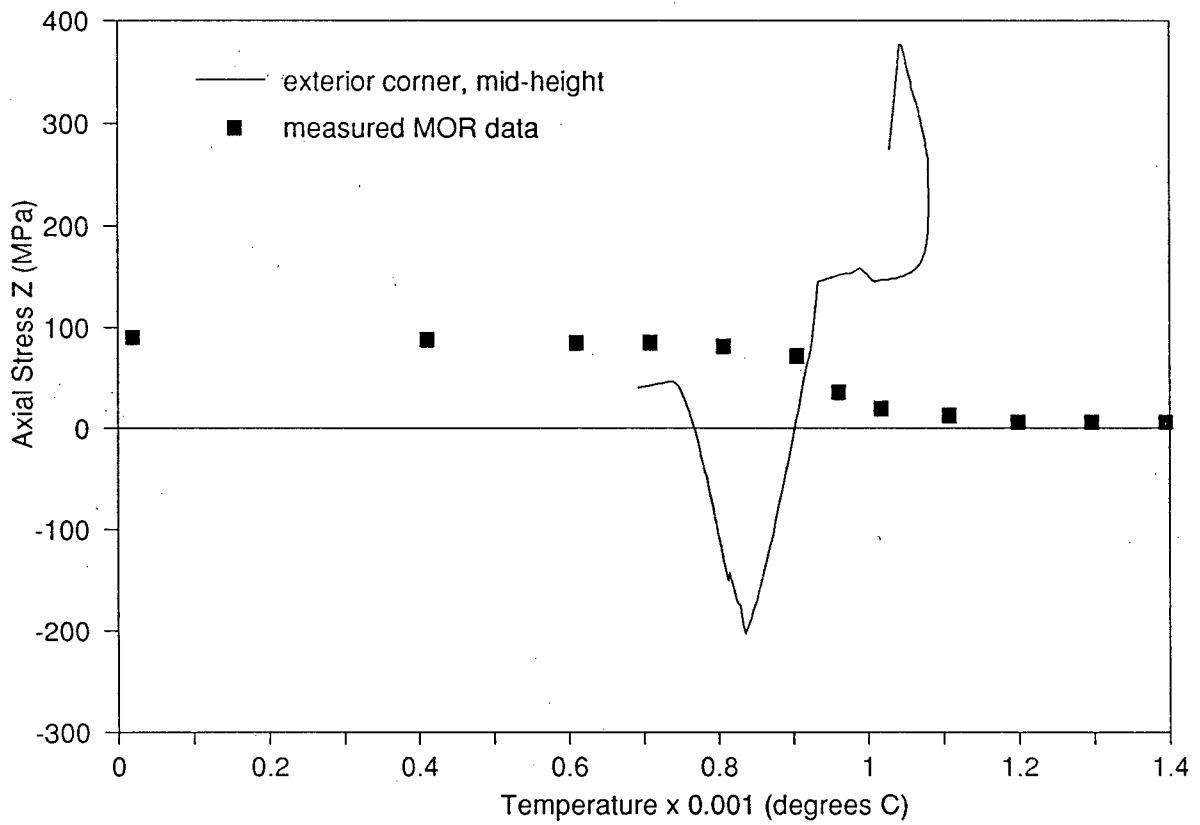


Figure 7.22. Comparison between σ_z predicted by the model at the intersection of the broad and narrow faces at mid-height and the measured modulus of rupture data for Monofrax-S as a function of temperature.

7.2 Recommendations for the Control of Cracking.

The recommendations for control of cracking follow directly from a mechanistic understanding of the generation of tensile stresses in the Epic-3 casting process. It has been shown that tensile stresses arise due to excessive temperature gradients within the refractory and/or mechanical interaction with the mould. The control of cracking, therefore, requires modifications to the moulding and casting practice in order to minimize the propensity for these stresses to occur.

7.2.1 Critical Aspects of Mould Design.

First and most obvious, the autopsy on the instrumented Epic-3, Figure 4.8, has identified the header ledge and mould seam as two features of the mould which may act to inhibit the contraction of the refractory during cooling. Mechanical pinning of the refractory at these sites could lead to the generation of large axial tensile stresses and eventually to the initiation of Type-A1 cracks. Both of these features should be removed on a trial basis to ascertain their impact on cracking. Insulation around the upper part of the casting or header could be employed as an alternative to a larger cross-section. This would permit the removal of the ledge entirely while helping to maintain a supply of liquid to minimize shrinkage cavities within the solidifying casting. Mould construction should also be modified to employ continuous bonded sand moulds on the faces of the casting. As indicated previously, intrusion of molten Monofrax-S into the seams can produce a second smaller ledge. Combined, these modifications should act to remove one of the proposed mechanisms by which tensile stresses can be generated in the Epic-3 casting.

The strategy for control of tensile stresses which arise due to excessive thermal gradients is more complex and requires that a balance be achieved between the desire to reduce

temperature gradients within the refractory and the need to minimize the likelihood of fusion between the refractory and the mould. The thermal analysis has identified regions of accelerated heat flow within the refractory which lead to the formation of large thermal gradients. In order of severity they are: the corners between the base and sides, the corners between the sides, the base of the refractory and the narrow face. The obvious strategy would be to encompass these areas in insulation in order to retard the flow of heat and reduce thermal gradients (a zone about the centre-line of the broad face is to be kept free of insulation). However, excessive amounts of insulation adjacent to the refractory interface will promote the re-melting of the initial chill layer leading to fusion and bonding of the refractory to the mould. In a manner analogous to the header ledge and mould-seam these sites may then act to inhibit the refractory from contracting mechanically. Therefore, the insulation should be placed on the outside of the bonded sand mould. At this distance from the refractory face the insulation will not interfere with the formation of the initial chill layer. The flow of heat is retarded by the insulation later in the solidification process after a stable chill layer has been permitted to form. The target is to reduce temperature gradients specifically within the refractory as the zirconia component of Monofrax-S passes through the tetragonal-to-monoclinic phase transformation. Analysis with the stress model has identified large axial tensile stresses associated with this phase transformation which are likely responsible for the formation of Type-A cracks. Moreover, the strategy will also reduce the temperature gradients which can act to propagate Type-B cracks - see Section 7.1.1 .

In contrast to the use of insulation, graphite chills may be needed within the bonded sand mould adjacent to the broad face. The rationale is to accelerate the flow of heat from the centre of the broad face early in the solidification process in order to reduce the propensity for fusion. Fusion and bonding between the refractory and the mould have been identified as a possible mechanism for preferential initiation of Type-A1 cracks on the broad-face.

To verify the basic philosophy behind these recommendations, the Epic-3 casting process was re-analyzed with a modified mould in place. The results of this analysis were then compared to the results of the analysis with the standard mould to determine if the desired effect on the generation of thermal stresses was achieved. The proposed mould design serves as a preliminary attempt at an improved mould and does not represent an optimum. A schematic illustration of the modified mould is presented in Figure 7.23. To impact on the Type-A1 transverse cracks, insulation has been placed on the outside around the narrow faces and edges of the of the bonded sand mould adjacent to the narrow face and edges of the refractory. The objective is to reduce the flow of heat preferentially from the narrow face thereby reducing temperature gradients which exist in the casting as the vertical edges and narrow face pass through the tetragonal-to-monoclinic phase transformation. This should reduce the axial thermal stresses which are believed to be responsible for the Type-A1 cracks. Moreover, this should also help to decrease the hoop stresses which give rise to the Type-B cracks. For the lower Type-A2 transverse cracks, insulation is placed adjacent to the base of the bonded sand mould to reduce axial heat flow. The strategy here also is to moderate the temperature gradients specifically when the zirconia component phases through the phase transformation. Finally, to promote the formation of a stable chill layer on the broad face, a small graphite board is inserted into the bonded sand mould adjacent to the major face of the casting. The width, thickness, length and location of the insulation and graphite have had to coincide with the boundaries of elements employed in the three-dimensional mesh. The thermophysical properties of the graphite chill and insulating board employed in the modified mould are presented in Table 7.2. These materials have been selected in conjunction with Carborundum operations personnel. The insulating material is currently produced

by Carborundum and the thermophysical properties have been obtained from a product brochure⁷⁸. As mentioned earlier, graphite chills are routinely employed in the current casting practice to add structural strength to the mould.

Crack Type-A1. A series of comparisons between the model predictions for the standard mould and for the modified mould are presented in Figures 7.24 - 7.26. The predictions indicate that the desired effect has been achieved. At the surface of the broad face and at the centre of the refractory, the peaks in axial tensile stress associated with the tetragonal-to-monoclinic phase transformation in zirconia have been reduced - see Figures 7.24 and 7.25. Also at the surface of the broad face, the formation of a stable chill layer early in the solidification process has been promoted by causing the temperature to initially decrease more rapidly - see Figure 7.26. The mechanism for initiation of the Type-A1 cracks has been affected in a manner conducive to a reduction in cracking. On the negative side, the tensile stress associated with initial rapid cooling of the broad face have been exacerbated. These stresses are believed to act in conjunction with the stresses which arise due to mechanical bonding to help initiate the crack. Based on this result, the addition of a graphite chill adjacent to the broad face is perhaps at best only a stopgap measure for control of cracking in lieu of accurate control of pour super-heat (the potential effect of excess super heat has been described earlier).

Crack Type-A2. In the region of the casting prone to Type-A2 cracks, the modifications to the mould are predicted to have a significant impact on the axial tensile peak which forms in the wake of the zirconia phase transformation. This effect can be seen from the comparison of axial tensile stress profiles presented in Figure 7.27. It is also worth noting that, in the vicinity of the base of the refractory, the impact of the graphite chill on the first tensile peak is predicted to be minimal.

Crack Type-B. A comparison between the transverse stresses acting parallel to the broad-face for the two moulds, Figure 7.28, reveals both an increase and a decrease in the tensile stress relative to the standard mould. Early in the solidification process, the tensile stresses are predicted to increase due to the graphite chill, and then later, to be reduced as the insulation on the exterior of the bonded sand mould begins to take effect. On the basis of this result, the propensity for Type-B cracks to initiate has been increased with the addition of the graphite chill. As applied, the insulation will likely impact only on the propagation of these cracks.

Crack Type-E. Examination of the axial tensile stresses predicted by the model at the corner of the refractory, presented in Figure 7.29, reveals that the modifications have had a significant impact in reducing the stress levels beyond 5 hrs elapsed time. Prior to this time, the insulation is ineffective at reducing temperature gradients within the refractory. To impact on the peak tensile stress which arise early in the solidification process the insulation would have to be moved closer to the refractory/mould interface adjacent to the edges.

Table 7.2
Thermophysical Properties of Additional
Moulding Materials Employed in the
Re-designed Mould

Material	Thermal Conductivity (W/m·°C)	Heat Capacity (kJ/kg·°C)	Density (kg/m ³)
Graphite ⁷³	50.	1.4	1920
Insulation ⁷⁸	8.7(10 ⁻²)	1.13	268

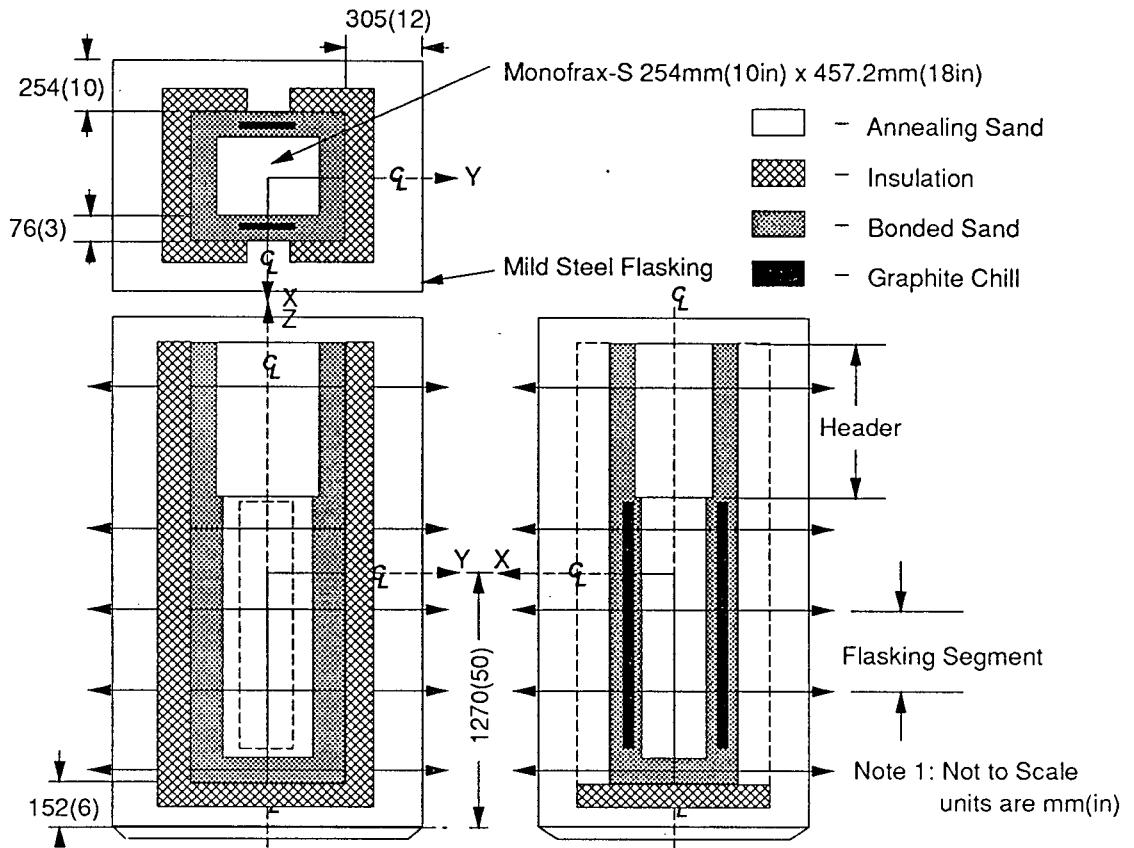


Figure 7.23. Proposed mould design for control of cracking in the Epic-3 casting process.

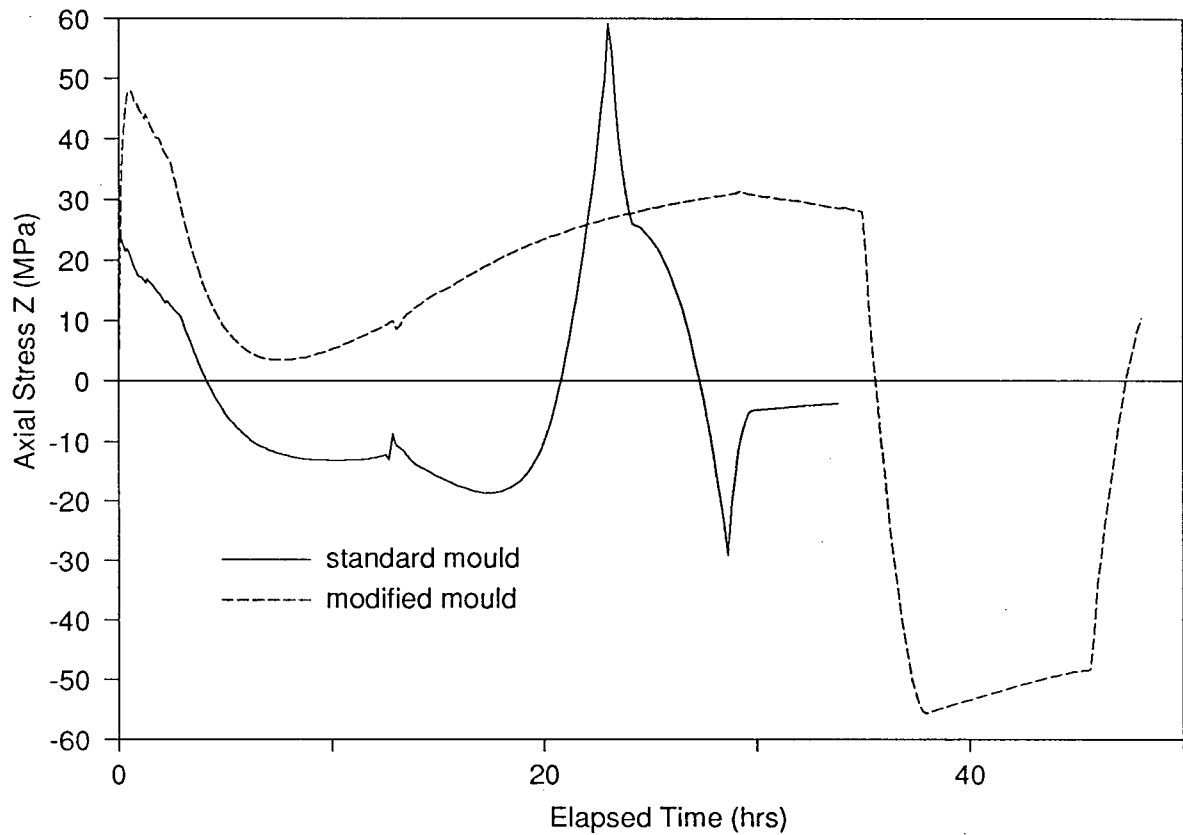


Figure 7.24. Comparison between axial stresses predicted by the model at the centre of the broad face at mid-height in the refractory for the standard mould and for the modified mould (refer to Figure 7.3).

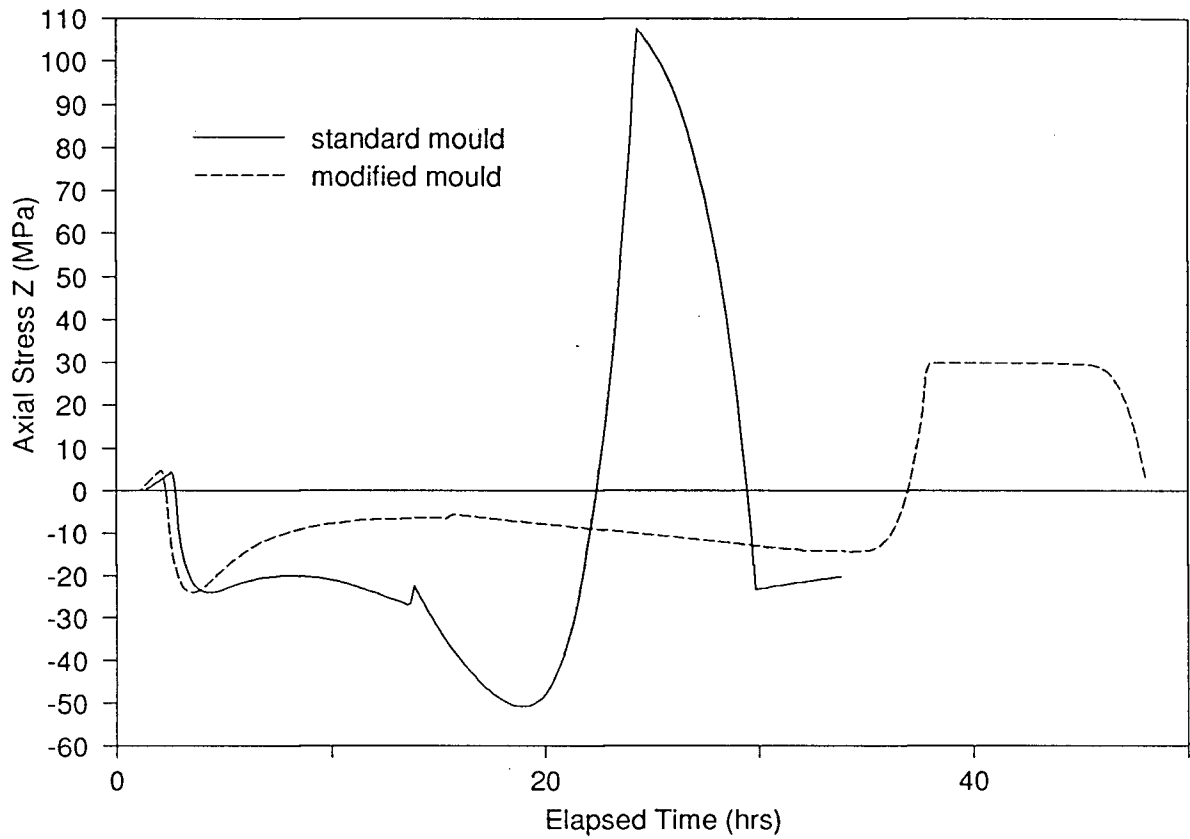


Figure 7.25. Comparison between axial stresses predicted by the model at the centre of the refractory at mid-height for the standard mould and for the modified mould (refer to Figure 7.3).

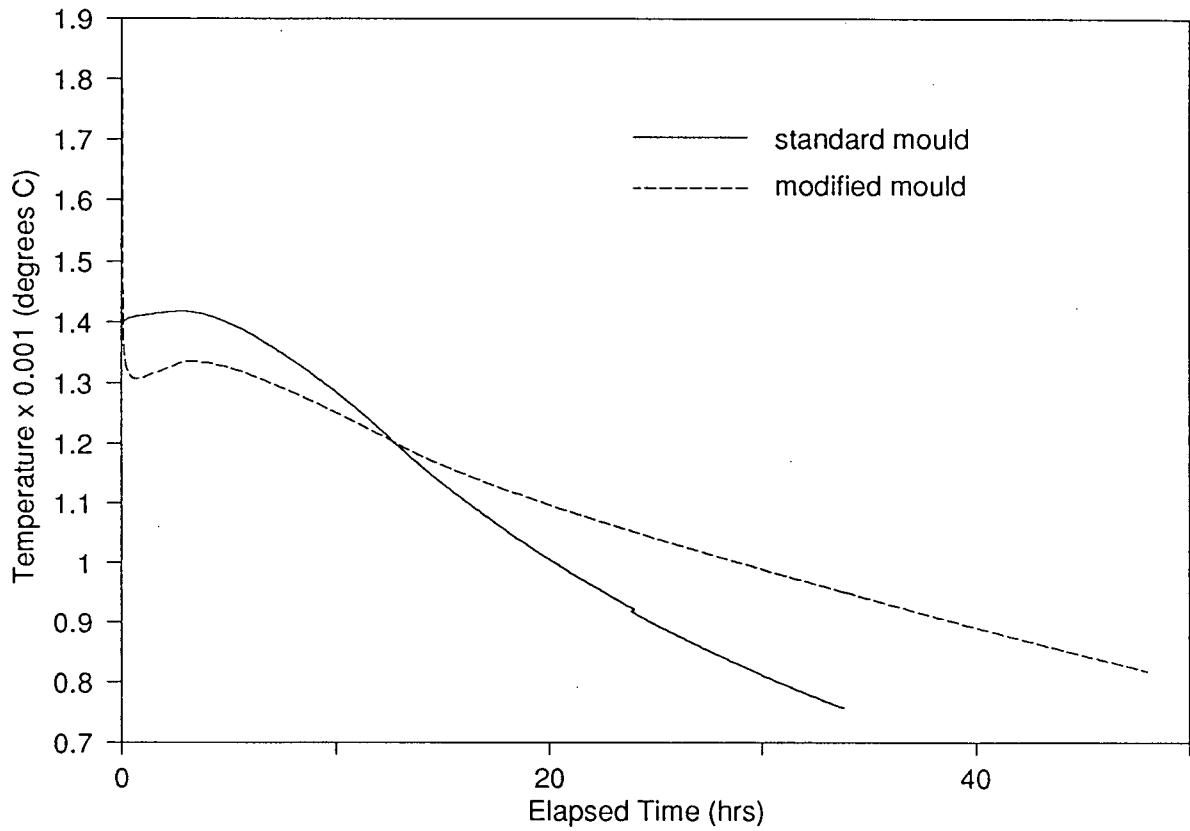


Figure 7.26. Comparison between temperature responses predicted by the model at the centre of the broad face at mid-height in the refractory for the standard mould and for the modified mould (refer to Figure 7.3).

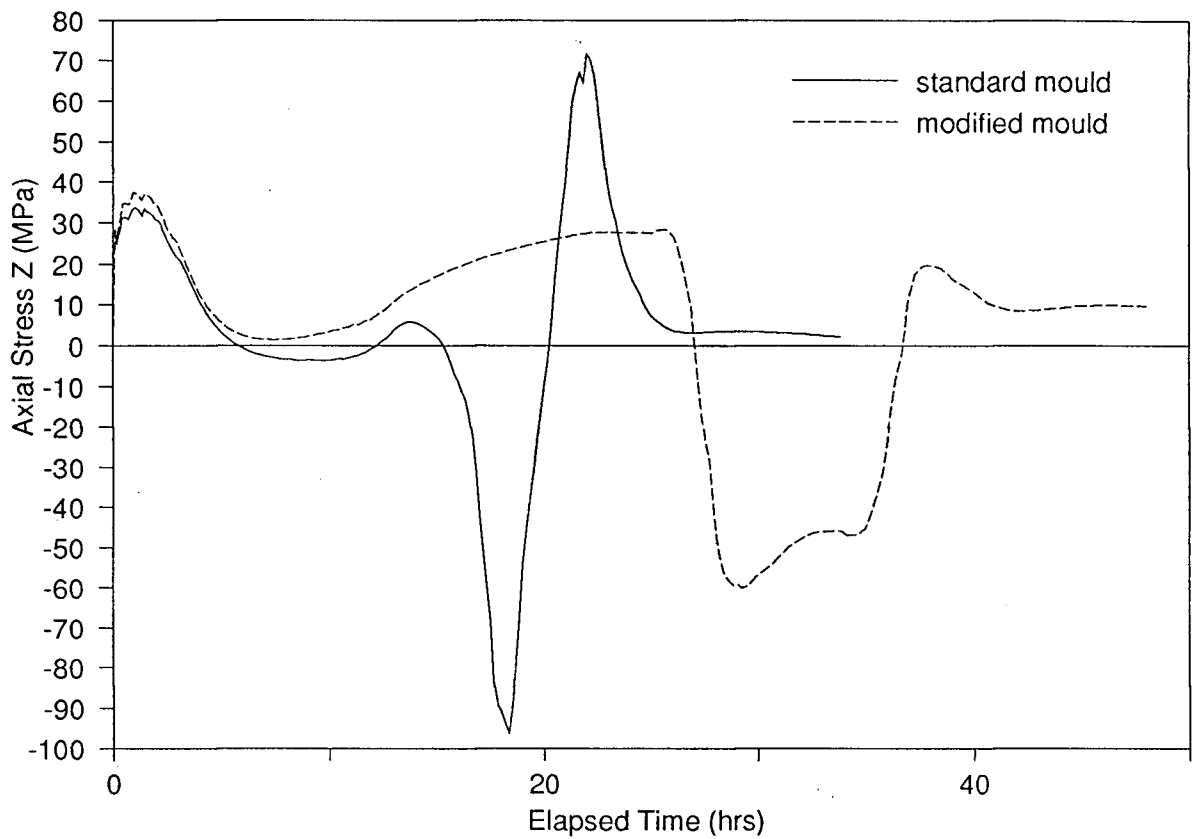


Figure 7.27. Comparison between axial stresses predicted by the model at the centre of the broad face 140mm(5.5in) from the base of the refractory for the standard mould and for the modified mould (refer to Figure 7.9).

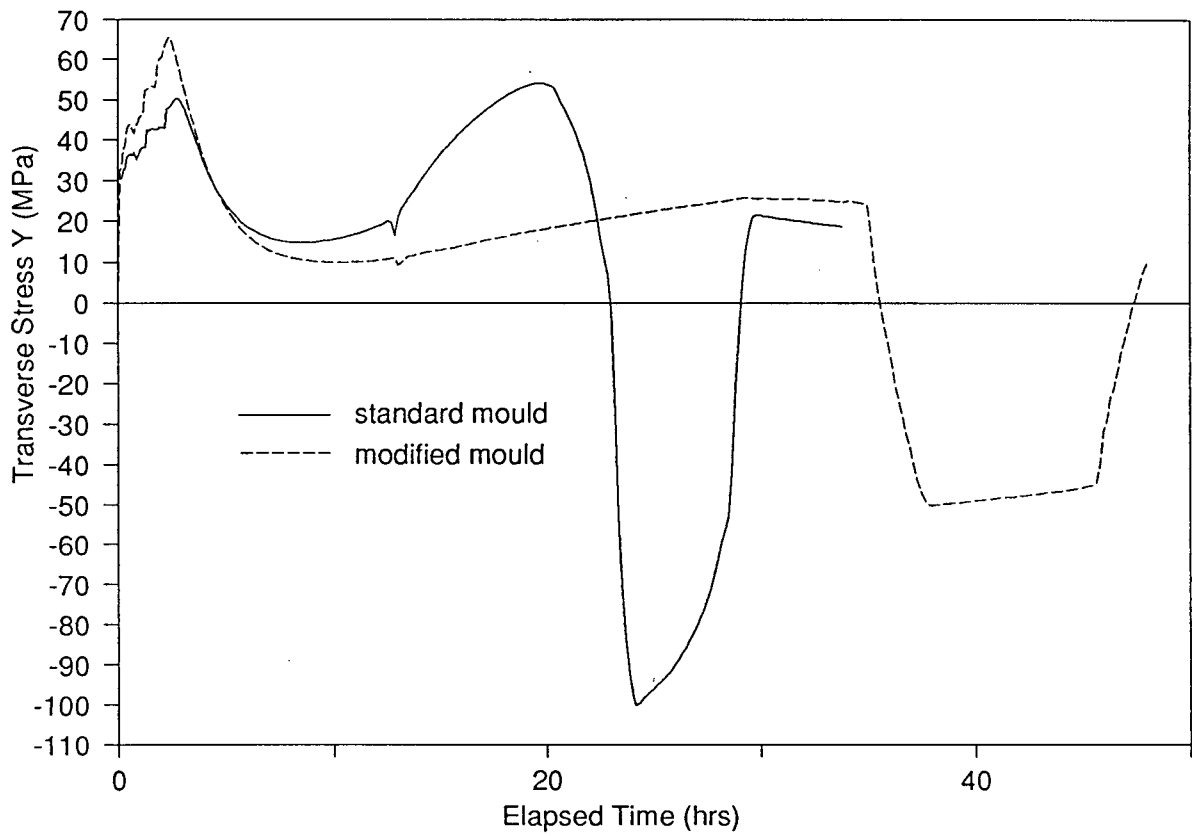


Figure 7.28. Comparison between transverse (σ_y) stresses predicted by the model at the centre of the broad face at mid-height in the refractory for the standard mould and for the modified mould (refer to Figure 7.3).

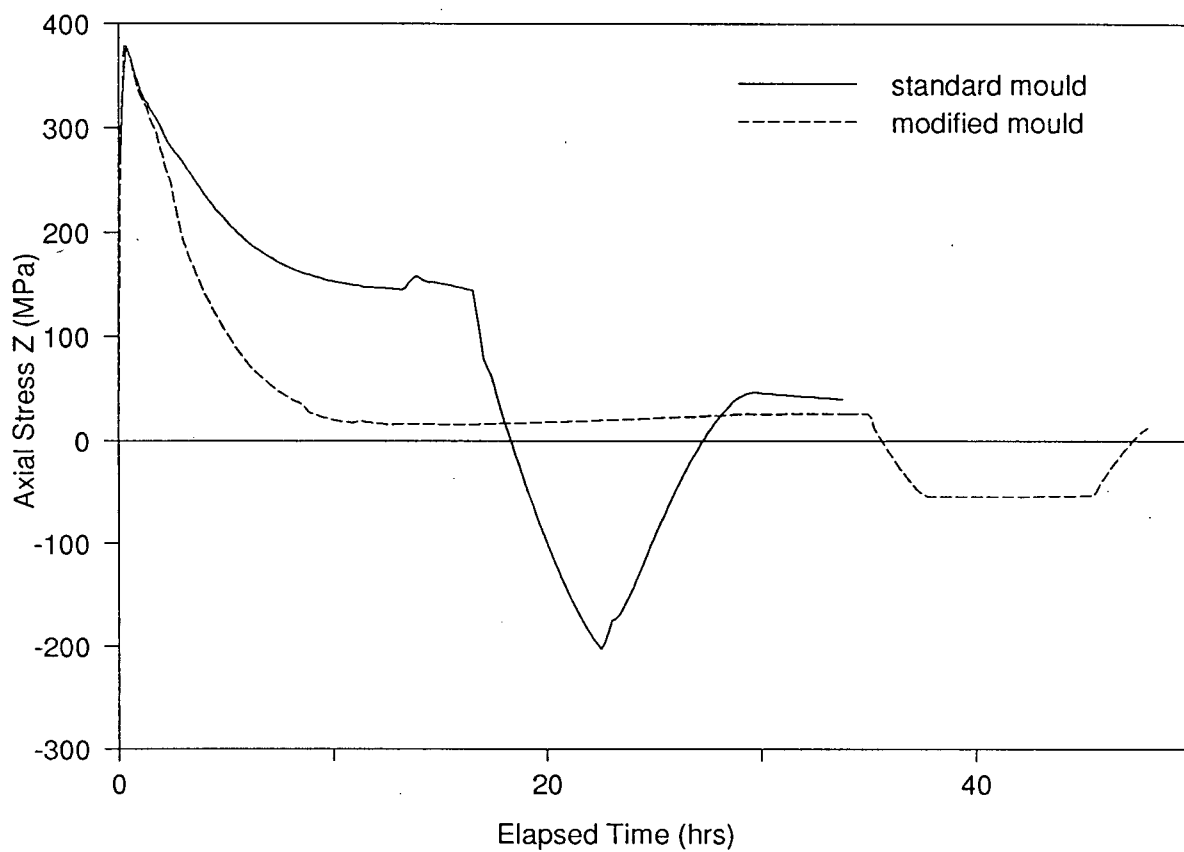


Figure 7.29. Comparison between axial stresses predicted by the model at the edge between the faces at mid-height in the refractory for the standard mould and for the modified mould.

7.2.2 Critical Casting Variables.

Control of pour temperature has been identified from the analysis as a key casting variable. Excess super-heat levels may act to re-melt the initial chill layer leading to bonding, fusion of the refractory to the mould and eventually the initiation of Type-A1 cracks. It is critical therefore that pour temperature be accurately controlled in order to minimize excess super-heat. In light of the detrimental aspects of the addition of a graphite chill adjacent to the broad face, this is the preferred manner for control of fusion and bonding. Unfortunately, it is difficult to quantitatively estimate the optimum amount of super-heat particularly in view of the uncertainty in the latent heat of solidification and solidification temperature range. Too small an amount obviously will impact negatively on castability. This parameter will have to be determined through trial and error in practice.

7.2.3 Industrial Trials with Modified Mould.

Based on the recommendations for control of cracking, a series of preliminary industrial trials have been completed with modified moulds by Carborundum. Since the industrial trials were conducted exclusively by Carborundum personnel and are beyond the scope of the original research programme only a summary of the results has been presented below.

Mould Seam Removed: One casting has been completed with the mould seam removed from the broad face. Visual inspection of the block after cooling and removal from the mould has revealed Type-A and Type-E cracks, and no Type-B cracks.

Header Ledge Removed: One casting has been completed with the header ledge removed. Visual inspection of the block after cooling and removal from the mould has revealed Type-A and Type-E cracks, and no Type-B cracks.

Mould Insulation and Graphite Chill: Three castings has been completed with the modified mould, Figure 7.23. Visual inspection of the block after cooling and removal from the mould has revealed only Type-E cracks (edge tears).

On the basis of one casting it appears that removal of the mould seam alone will not alleviate the Type-A or -E cracking problem. Similarly, removal of the header ledge alone does not appear to bring about a reduction in axial tensile stresses sufficient to stop transverse cracks from forming. Combined, these results suggest that the proposed mechanisms for generation of mechanical tensile stress are not a major factor in transverse cracking. It appears instead that the key tensile stresses are thermally induced. The strategy of applying insulation to the narrow face and base in order to manipulate the flow of heat and reduce the tensile stresses has proven to be a successful means of controlling transverse cracking. The interaction between the flow of heat from the narrow face and the generation of tensile stresses in the centre and broad face of the refractory is a novel and surprising result. It is in direct agreement with the predictions of the mathematical models and the proposed mechanism for formation of transverse cracks in Epic-3 Monofrax-S casting. Owing to the limited number of trials completed, these results are arguably statistically insignificant. Nevertheless, they are encouraging.

CHAPTER 8

SUMMARY AND CONCLUSIONS

The scope of the present work has involved an in depth study of the Epic-3 Monofrax-S fused-cast casting process. Mathematical models of heat-flow and elastic stress generation based on the finite element method have been developed and utilized to analyze the casting process. Industrial thermocouple measurements of in-mould temperatures have also been made to help to validate the mathematical model of heat flow.

The three-dimensional mathematical analysis has revealed a complex and dynamic picture of the evolution of thermal stresses in cooling Epic-3 castings. Major regions of tensile stress have been identified and have been linked to: firstly, rapid cooling of the refractory surface early in the solidification process and secondly, to the tetragonal-to-monoclinic phase transformation in zirconia which occurs later as regions of the cooling refractory move through the 940 to 840°C temperature range. The patterns of tensile stress that are induced by the changing thermal field suggest a strong interaction between remote regions of the casting. For example, axial thermal loads induced by the tetragonal-to-monoclinic phase transformation on the vertical edge and narrow face of the refractory result in axial tensile stresses in the centre region and broad face. Moreover, transverse thermal loads parallel to the narrow face act to induce transverse thermal strains parallel to the broad face and vice-versa.

To resolve the cracking problem, the evolution of stress in various regions of the refractory prone to cracking has been examined closely. From this examination and from information from the statistical crack survey⁸, mechanisms for the formation of the various cracks types have been developed. Based on an overall understanding of the generation of tensile stresses, recommendations have been made for modifications to the moulding and casting procedures in order to reduce the propensity for cracking to occur. The modifications

have included changes to the mould geometry and construction to reduce the generation of axial mechanical stress, and changes to the moulding materials, to impact on the flow of heat at key times during solidification and cooling. To control cracking in the transverse direction on the broad face at mid-height (Type-A1), a novel approach has been adopted whereby insulation is applied to the outside of the bonded sand mould adjacent to the narrow face and vertical edge along the length of the refractory. At this location, the insulation acts to reduce thermal gradients in the narrow face and edge as they move through the tetragonal-to-monoclinic phase transformation. This approach serves also to reduce the transverse tensile stresses believed to be responsible for Type-B longitudinal cracks occurring in the middle of the major face. To control the Type-A2 crack (transverse broad face near base) insulation is placed on the outside of the bonded sand mould adjacent to the base to reduce axial heat flow.

With the recommendations for modifications to the mould in place, the casting process has been re-examined with the mathematical models. The predictions indicate that modifications have acted on the generation of tensile stresses in a manner conducive to a reduction in the frequency of crack occurrence. Based on these results, a series of preliminary industrial trials have been completed with modified moulds by Carborundum personnel. The results of the industrial trials suggest that the strategy for control of tensile thermal stresses is effective in stopping the formation of Type-A cracks. Moreover, the results also suggest that mechanical interaction between the mould and refractory does not play a major role in the generation of axial tensile stresses.

8.1 Recommendations for Future Work.

One of the more troublesome aspects of the research programme has been the need to rely on incomplete and in some cases questionable thermophysical and thermomechanical

data. As a starting point, it is recommended that the thermal conductivity of sand be reevaluated under conditions more in-line with those occurring within the mould. As well, it would be a great benefit to know more accurately the latent heat of solidification and liquidus and solidus temperatures of Monofrax-S. Furthermore, to permit a more complete and thorough interpretation of the results of the stress analysis, future work should include also characterization of the stress/strain behaviour of Monofrax-S as a function of temperature and at varying strain rates.

In addition to benefiting from better thermophysical and thermomechanical data, the thermal analysis would benefit greatly from further industrial trials aimed at better characterizing the behaviour of the mould/refractory interface boundary condition. Evaluation of a time dependent heat-transfer coefficient for this boundary condition would greatly improve the predictive capabilities of the thermal model.

The most notable limitation of the mathematical model of stress generation is the inability to account for time dependent deformation at elevated temperatures. This shortcoming has influenced the ability of the model to quantitatively predict stress at temperatures above 900 - 1000°C. Improved capabilities at these temperatures will help to better resolve questions surrounding the tensile thermal stresses which are generated in association with rapid cooling of the refractory surface early in the solidification process. This improvement would require both modifications to the formulation of the stress model and a better understanding of the high temperature mechanical behaviour of Monofrax-S.

Finally, for future work, it is also recommended that the Epic-3 casting be reanalyzed utilizing only two-fold symmetry in the transverse plane. It is clear that the assumption of axial symmetry about the centre plane, particularly in the stress analysis, is a poor one.

REFERENCES

1. Standard Oil Engineered Materials Product Advertisement Brochure.
2. Chan et al., Am. Ceramic Soc. Bulletin, Vol. 57, No. 2, 1978, pp. 226-229.
3. "Science and Technology of Zirconia", Eds. A.H. Heuer and L.W. Hobbs, Advances in Ceramics, Vol. 3, Am. Cer. Soc., 1981.
4. L.L. Fehranbacher and L.A. Jacobson, "Metallographic Observation of Monoclinic-Tetragonal Phase Transformation in ZrO_2 ", J. American Ceramic Society, Vol. 48, No. 3, March 1965.
5. R.N. Patel and E.C. Subbarao, J. Appl. Crystallogr., 2, 281-88 (1969).
6. R.N. Patel and E.C. Subbarao, Acta Crystallogr., 26, 535-42 (1970).
7. Engineering Properties of Selected Ceramic Materials, Ed., J.K. Lynch, Am. Cer. Soc., 1966.
8. D.G. Walrod, Standard Oil Crack Survey Report, unpublished.
9. W.D. Kingery, J. Am. Ceramic Soc., 1955, Vol. 38 (1), pp. 3-15.
10. V.S. Kienow, Ber. Dt. Kerman. Ges., 1970, Vol. 47, pp. 426-430.
11. D.P.H. Hasselman, J. Am. Ceramic Soc., 1963, Vol. 46 (11), pp. 535-540.
12. D.P.H. Hasselman, J. Am. Ceramic Soc., 1969, Vol. 52 (11), pp. 601-664.
13. D.P.H. Hasselman, "Ceramics in Severe Enviroments", W.W. Kriegel and H.Palmour, III Eds., PLenum Press, New York, N.Y., 1971, pp. 89-103.

14. W.S. Chang, C.E. Knight, D.P.H. Hasselman and R.G. Mitchiner, "Analysis of Thermal Stress Failure of Segmented Thick-Walled Refractory Structures", *Journal of Am. Cer. Soc.*, Vol. 66, No. 10, Oct., 1983, pp. 708-713.
15. F. Bradley, A.C.D. Chaklader and A. Mitchell, "Thermal Stress Fracture of Refractory Lining Components: Part 1. Thermoelastic Analysis", *Met. Trans. B*, Vol. 18B, June 1987, pp. 355-363.
16. V. Venkateswaran, "Three-Dimensional Heat Flow in the Direct-Chill Casting of Non-Ferrous Metals", Ph.D., U.B.C., 1980.
17. G. Van Drunen, J.K. Brimacombe and F. Weinberg, "Internal Cracks in Strand Cast Billets", *Ironmaking and Steelmaking*, 1975, Vol. 2, pp. 125-133.
18. J.K. Brimacombe and K. Sorimachi, "Crack Formation in the Continuous Casting of Steel", *Metall. Trans. B*, 1977, Vol. 8B, pp. 489-505.
19. J.K. Brimacombe, F. Weinberg and E.B. Hawbolt, "Formation of Longitudinal, Mid-Face Cracks in Continuously Cast Steel Slabs", *Metall. Trans. B*, 1979, Vol. 10B, pp. 279-292.
20. B.G. Thomas, J.K. Brimacombe, and I.V. Samersekera, "The Formation of Panel Cracks in Steel Ingots: A State-of-the-Art Review, Part I. Hot Ductility of Steel", *ISS Transactions*, 1986, Vol. 7, pp. 7-20.
21. B.G. Thomas, J.K. Brimacombe, and I.V. Samersekera, "The Formation of Panel Cracks in Steel Ingots: A State-of-the-Art Review, Part II. Mid-Face and Off-Corner Cracks", *ISS Transactions*, 1986, Vol. 7, pp. 21-29.

22. B.G Thomas, I.V. Samarasekera and J.K. Brimacombe, "Mathematical Model of Thermal Processing of Steel Ingots: Part I. Heat Flow Model", Metall. Trans B, Vol. 18B, March 1987, pp. 119-130.
23. B.G Thomas, I.V. Samarasekera and J.K. Brimacombe, "Mathematical Model of Thermal Processing of Steel Ingots: Part II. Stress Model", Metall. Trans B, Vol. 18B, March 1987, pp. 131-147.
24. E.M. Levin, H.F. McMurdie and F.P. Hall, Phase Diagrams for Ceramists, The American Ceramic Society, 1956.
25. W.D. Kingery, "Introduction to Ceramics", Pub. J. Wiley and Sons Inc., 1960.
26. B.G Thomas, I.V. Samarasekera and J.K. Brimacombe, "Comparison of Numerical Modelling Techniques for Complex, Two-Dimensional, Transient Heat-Conduction Problems", Metall. Trans. B, Vol. 15B, June 1984, pp. 307-318.
27. A.F. Emery and W.W. Carson, "An Evaluation of the Use of the Finite-Element Method in the Computation of Temperature", Trans. ASME, Journal of Heat Transfer, May 1971, pp. 136-145.
28. K. Ho and R.D. Pehlke, "Comparison of Finite Element and General Finite Difference Methods for Transient Heat Flow", Material Sci. and Tech., Vol. 3, June 1987, pp. 466-.
29. T. Dupont, G. Fairweather and J. Johnson, Siam J. Numerical Analysis, 1974, Vol. II, pp.392-410.
30. A. Luikov, Analytical Heat Transfer Diffusion Theory, Academic Press, New York, N.Y., 1968, pp. 214-40.

31. K. Rathjen and L. Jiji, *Journal of Heat Transfer*, Trans. ASME, 1971, Vol. 93, pp. 101-109.
32. E.P. Popov, *Introduction to Mechanics of Solids*, Prentice Hall Inc., Englewood Cliffs, N.J., 1968.
33. R.H. Kennedy, "Selecting Temperature Sensor", *Chemical Engineering*, Aug 8, 1983, pp. 54-71.
34. Private communication Carborundum personnel.
35. O.C. Zienkiewicz, "The Finite Element Method", 3rd ed., McGraw-Hill, 1977.
36. K.H. Huebner, "The Finite Element Method for Engineering", John Wiley and Sons, New York, N.Y., 1975.
37. R.D. Cook, "Concepts and Application of Finite Element Analysis", 2nd ed., John Wiley and Sons, New York, N.Y., 1974.
38. K.J. Bathe, "Finite Element Procedures in Finite Element Analysis", Prentice Hall, New Jersey, 1982.
39. J. Crank and P. Nicolson: *Proc. Camb. Philos. Soc.*, 1947, vol. 43, pp. 50-67.
40. S. Del Giudice, G. Comini and R.W. Lewis, "Finite Element Simulation of Freezing Processes in Soils", *International Journal for Numerical and Analytical Methods in Geomechanics*, Vol. 2, 223-235 (1978)
41. V.Voller, M. Cross and P. Walton, "Numerical Methods in Thermal Problems", R. Lewis et al., eds., Pineridge Press, Swansea, U.K., 1979, vol. 1, pp.172-181. (... difficulties in modelling phase change)

42. D.R. Lynch and K. O'Neill, "Continuously Deforming Finite Elements for the Solution of Parabolic Functions, With and Without Phase Change", *International Journal For Numerical Methods In Engineering*, Vol. 17, 1981, pp.81-96.
43. W. Rolf and K. Bathe: *International Journal of Numerical Methods in Engineering*, Vol. 18, 1982, pp.119-134.
44. G. Guymon and J.Luthin: *Water Resources Research*, Vol. 10, 1974, p. 995
45. G. Comini, S.Del Giudice, R.W. Lewis and O.C. Zienkiewicz, "Finite Element Solution of Non-Linear Heat Conduction Problems with Special Reference to Phase Change", *Int. Journal of Numerical Methods in Engineering.*, Vol.8, 1974, pp.613-624.
46. K. Morgan, R.W. Lewis and O.C. Zienkiewicz, "An Improved Algorithm For Heat Conduction Problems With Phase Change", *Int. Journal for Numerical Methods in Engineering*, Vol. 12 #7, 1978.
47. E. Lemmon, *Numerical Methods in Heat Transfer*, R. Lewis et al., eds., John Wiley and Sons Ltd., New York, N.Y., 1981, pp. 201-13.
48. V. Voller and M. Cross, "Accurate Solutions of Moving Boundary Problems Using The Finite Element Method", *International J. Heat Transfer*, Vol. 24, 1981, pp.545-556.
49. V.R. Voller and C. Prakash, "A Fixed-Grid Numerical Modelling Methodology For Convective-Diffusion Mushy Region Phase Change Problems", *International J. of Heat and Mass Transfer*, Vol. 30 No. 8, 1987, pp. 1709-1719.

50. V.R. Voller, M. Cross and N.C. Markatos, "An Enthalpy Method for Convection-Diffusion Phase Change", *International J. of Numerical Methods in Engineering*. Vol. 24, 1987, pp.271-284.
51. F. Kreith and W.Z. Black, "Basic Heat Transfer", Harper & Row, New York, 1980, p. 144.
52. J. Szekely and N.J. Themelis, "Rate Phenomena in Process Metallurgy", Wiley-Interscience, John Wiley and Sons, New York, 1974.
53. L. Brewer - *Chem. Rev.*, 52, 1, 1953
54. Turkdogan, "Physical Chemistry of High Temperature Technology", Academic Press., 1980.
55. Timoshenko and Goodier, "Theory of Elasticity", 3rd ed., McGraw-Hill, 1970
56. Y. Nishida, W. Droste and S. Engler, "The Air-Gap Formation at the Casting-Mold Interface and the Heat Transfer Mechanism through the Gap", *Met. Trans. B.*, Vol. 17B, Dec. 1986, pp. 833-844.
57. M.R. Ozgu, D.H. Bright and D.K. Watkins: *Steelmaking Proc.*, ISS, 1985, vol. 385, pp. 313-43.
58. V.A. Diener, A. Drastik and W. Haumann: *Archive fur das Eisenhüttenwesen*, July 1972, vol. 43, No. 7, pp. 525-33.
59. F. Kavicka: *Slevarenstvi*, B.I.S.I. 15540, 1976, vol. 24, No. 11, pp. 448-52. (...heat transfer across mould/ingot interface)
60. F. Oeters, K. Ruttiger and H.J. Selenz: *Casting and Solidification of Steel*, 1977, pp. 125-67 (... heat transfer across mould ingot interface)

61. V. Paschkis: AFA Transactions, 1944, vol. 52, pp. 649-70.
62. R.J. Sarjant and M.R. Slack: J. Iron and Steel Inst., 1954, vol. 177, pp. 428-44
63. C.C. Reynolds: AFS Transactions, 1944, vol. 72, pp. 342-47
64. G.E. Nero, R.F. Polich and M.C. Flemings: AFS Transactions, 1965, vol. 73, pp.1-13
65. S. Suzuki and Y. Nishida: Imono (J. Japan Found. Soc.), 1967, vol. 39, pp. 895-902.
66. Y. Nishida and S. Suzuki: J. Japan Inst. Met., 1968, vol. 32, pp. 882-86
67. Y. Nishida: J. Japan Inst. Met., 1970, vol. 34, pp. 1135-39.
68. H. Jones: J. Inst. Metals, 1969, vol. 97, pp. 38-43.
69. B. Gebhart, Heat Transfer, 2nd ed., McGraw-Hill, New York, 1970.
70. Virginia Polytechnic Institute, Unpublished, Aug. 8, 1987
71. Harrop Industries, Unpublished, Dec. 10, 1987
72. Ohio State University Refractories Research Centre, Unpublished, July 30, 1988
73. R.D. Pehlke, A. Jeyarajon and H. Wada, "Summary of Thermal Properties for Casting Alloys and Mould Materials", Ann Arbor, Michigan (Dec. 1982). National Technical Information Service (NTIS), No. PB83-211003.
74. Chemical Engineers Handbook, Perry and Chilton eds., 5th ed., McGraw-Hill.
75. Toshiba Monofrax Division, Unpublished, Sept. 26, 1989
76. A. Lebold, 'Summary of Physical Properties of Monofrax-S, CS3', Unpublished.
77. Fiberfrax Ceramic Fiber Insulation, Broduct Brochure Form C730, 1987, The Carborundum Company.

78. Private communication Carborundum personnel.